

UNIVERSIDADE DE LISBOA
FACULDADE DE CIÊNCIAS
DEPARTAMENTO DE FÍSICA



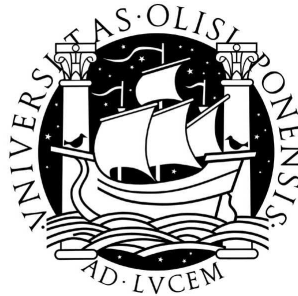
**PRECISION MEASUREMENT OF NEUTRINO OSCILLATION
PARAMETERS: COMBINED THREE-PHASE RESULTS OF THE
SUDBURY NEUTRINO OBSERVATORY**

Nuno Filipe Fiúza de Barros

DOUTORAMENTO EM FÍSICA

Lisboa, Dezembro de 2011

UNIVERSIDADE DE LISBOA
FACULDADE DE CIÊNCIAS
DEPARTAMENTO DE FÍSICA



PRECISION MEASUREMENT OF NEUTRINO OSCILLATION
PARAMETERS: COMBINED THREE-PHASE RESULTS OF THE
SUDBURY NEUTRINO OBSERVATORY

Nuno Filipe Fiúza de Barros

DOUTORAMENTO EM FÍSICA

Orientador: Prof. Doutora Amélia Maio
Doutor José Maneira

Lisboa, Dezembro de 2011

Abstract

The Sudbury Neutrino Observatory has successfully demonstrated neutrino flavour transformation of the neutrinos produced in the Sun. The use of heavy water as the detection medium allowed a measurement of both the total active solar neutrino flux and the pure electron neutrino component. This work presents the results of a neutrino oscillation analysis of the latest combined analysis of all phases of the experiment, aiming to obtain the most precise measurement of the neutrino mixing parameters relevant for solar neutrinos. The results obtained show a precision on $\tan^2 \theta_{12}$ better than 10% both on a two and three flavour analysis of all solar neutrino data. A three-flavor neutrino oscillation analysis combining the results of all solar neutrino experiments and the KamLAND experiment yielded $\Delta m_{21}^2 = (7.41_{-0.19}^{+0.21}) \times 10^{-5} \text{ eV}^2$, $\tan^2 \theta_{12} = 0.446_{-0.029}^{+0.030}$, and $\sin^2 \theta_{13} = (2.5_{-1.5}^{+1.8}) \times 10^{-2}$, which implies an upper bound of $\sin^2 \theta_{13} < 0.053$ at the 95% confidence level (C.L.). The newly obtained results also demonstrate a shift of the θ_{12} mixing angle towards lower values, increasing the tension with the KamLAND experiment slightly increasing the significance of a non-zero θ_{13} . A combined analysis of neutrino data from multiple sources was performed in an attempt to obtain an enhanced constrain on θ_{13} , with a result of a non-zero θ_{13} with a statistical significance of 3.2σ . This work also presents improvements in the optical calibration of the detector during the NCD phase, having reached a precision in the optical parameters comparable to the results of the previous phases, despite the added difficulty with the introduction of the *neutral current detector (NCD)* into the *heavy water (D₂O)* volume. These improvements permitted to reduce the systematic uncertainties on the energy reconstruction and therefore extract the most interesting physics from the full data set of SNO.

Keywords: Solar neutrinos; Neutrino oscillations; Low background detectors; Water Čerenkov detectors; Optical calibration.

Sumário

O *Sudbury Neutrino Observatory (SNO)* foi a primeira experiência a demonstrar a mudança de sabor nos neutrinos solares, resolvendo o denominado *Problema dos Neutrinos Solares*. Usando água pesada como meio activo, foi possível a SNO medir de forma independente o fluxo total de neutrinos de todos os sabores por intermédio da reacção de *correntes neutras (NC)*, e também o fluxo de neutrinos de electrão por intermédia da reacção de *correntes carregadas (CC)*. Neste trabalho são apresentados os resultados da análise de oscilação a dois e três sabores dos dados combinados das três fases da experiência, analisados simultâneamente como um conjunto único. Estes resultados demonstram uma melhoria na precisão do parâmetro de oscilação $\tan^2 \theta_{12}$ tendo-se obtido uma incerteza abaixo dos 10% em ambas as análises a dois e três sabores de todos os dados de neutrinos solares. Ao efectuar uma análise combinada dos dados de todas as experiências de neutrinos solares juntamente com a experiência de reactor KamLAND obtiveram-se os resultados de $\Delta m_{21}^2 = (7.41_{-0.19}^{+0.21}) \times 10^{-5} \text{ eV}^2$, $\tan^2 \theta_{12} = 0.446_{-0.029}^{+0.030}$, e $\sin^2 \theta_{13} = (2.5_{-1.5}^{+1.8}) \times 10^{-2}$, implicando um limite superior de $\sin^2 \theta_{13} < 0.053$ com 95% de grau de confiança. Verificou-se ainda que os novos dados de SNO induzem a uma variação no ângulo de mistura para valores mais baixos, o qual é propagado nas análises combinadas com dados de outras experiências, tendo como consequência um aumento da anti-correlação com os resultados de KamLAND levando a um ligeiro aumento da significância estatística de um valor de θ_{13} não nulo. Foi ainda efectuada uma análise combinada de dados de neutrinos de múltiplas fontes, de forma a obter o máximo de informação em relação à possibilidade de um valor de θ_{13} não nulo tendo-se obtido um resultado com uma significância estatística de 3.2σ . São ainda apresentados várias melhorias implementadas na calibração óptica de SNO, com particular ênfase na terceira fase da experiência. Estas melhorias levaram a uma precisão nos parâmetros ópticos comparável aos resultados obtidos na primeira

e segunda fase, apesar de na terceira fase haver a dificuldade adicional imposta pela introdução dos contadores proporcionais (NCDs) no detector. Esta precisão permitiu reduzir as incertezas sistemáticas na reconstrução em energia de forma a ser possível extrair os melhores resultados de Física possíveis dos dados de SNO.

Numa fase inicial deste trabalho (Capítulo 1) é feita uma introdução à física de neutrinos solares, enquadrando este trabalho no conhecimento actual e na motivação para a medição precisa dos parâmetros de oscilação. De seguida é efectuada uma introdução ao detector SNO (Capítulo 2), apresentando informação sobre a sua estrutura, os principais tipos de fundos e as diversas calibrações efectuadas, com particular incidência sobre a instrumentação da calibração óptica, que consiste num laser e uma esfera difusora quasi-uniforme. É então feito um enquadramento do trabalho desenvolvido no âmbito da calibração óptica (Capítulo 3), sendo apresentados os métodos e os princípios gerais, nomeadamente uma descrição dos diferentes objectivos da calibração óptica, do modelo óptico usado para efectuar a caracterização do detector e das optimizações a cortes de qualidade aplicados para obter a descrição mais fiável das propriedades do detector. De seguida são apresentados os dois métodos usados na análise de dados das diferentes fases da experiência. Após esta introdução são então apresentados os resultados das diversas actividades efectuadas na calibração óptica (Capítulo 4) focando nos resultados com influência directa na análise dos dados de neutrinos, tais como a implementação de novos cortes de qualidade. São também abordadas outras actividades que, não tendo influência directa na análise dos dados de neutrinos, serviram para testar outros elementos do modelo óptico (por exemplo o estudo da reflectividade dos contadores proporcionais e a assimetria cima-baixo) ou serviram para validar outras análises já efectuadas (como por exemplo o estudo da correcção de ocupância dos PMTs baseado em simulações de Monte Carlo). No final deste capítulo são descritos os resultados de um reprocessamento de uma selecção de dados de calibração óptica, sendo então efectuada uma avaliação quantitativa das propriedades ópticas do detector ao longo das três fases, assim como algumas considerações sobre a sua variação durante o tempo de vida da experiência. No capítulo seguinte (Capítulo 5) é explicado o método usado na análise dos dados de neutrinos. Neste capítulo são inicialmente explicados os diversos observáveis usados na análise dos dados de neutrinos. Posteriormente são explicados os métodos de análise focando sobretudo no novo método usado na análise combinada das três fases de SNO, em que é efectuada uma análise espectral obtando-se uma

parametrização funcional da distorção do espectro de neutrinos solares provenientes da reacção de ${}^8\text{B}$. É depois apresentada uma análise efectuada no âmbito desta tese para a determinação da melhor parametrização a usar para se poder extrair o máximo de informação dos dados. Finalmente são apresentados os resultados finais da análise dos dados de neutrinos usando a parametrização escolhida, sendo então efectuada uma breve análise dos resultados obtidos. Finalmente são apresentados os resultados da parte principal deste trabalho, que consiste na medição precisa dos parâmetros de oscilação dos neutrinos solares. É então efectuada uma pequena revisão da fenomenologia das oscilações de neutrinos, tanto no vácuo como assumindo efeitos de matéria. Neste âmbito é apresentada uma derivação da probabilidade de sobrevivência implementada na análise de oscilação de neutrinos de forma a melhorar a precisão na determinação dos parâmetros de oscilação. Esta implementação calcula a probabilidade de sobrevivência por intermédio de uma aproximação adiabática, a qual permite obter uma descrição analítica da mesma. Os diferentes dados necessários para obter a probabilidade de sobrevivência são então descritos, sendo efectuada uma avaliação quantitativa do efeito de cada parâmetro na probabilidade de sobrevivência. É então explicado o método de análise usado para os diferentes tipos de dados usados, focando sobretudo no método para SNO, em que se faz a análise do espectro de energia medido sob a forma de uma parametrização polinomial da probabilidade de sobrevivência. Tanto a parametrização como o método de análise são uma novidade em relação aos métodos usados no passado, sendo também demonstrados os resultados de estudos de validação do método. Finalmente são apresentados os resultados de diversas análises de oscilação efectuadas, tanto no âmbito de dois como de três sabores de neutrinos. Uma vez que no âmbito de neutrinos solares nenhuma experiência é capaz de reduzir a região dos parâmetros de oscilação a um único mínimo, a análise de oscilações de neutrinos é efectuada não só para os resultados de SNO, mas também para os dados combinados de todas as experiências de neutrinos solares. São ainda apresentados outros estudos efectuados, tais como o efeito de usar diferentes modelos solares ou assumir que os neutrinos apresentam-se com *hierarquia invertida* de massas. Tendo como objectivo obter os resultados mais precisos dos parâmetros de oscilação, são depois efectuadas análises combinadas usando dados de neutrinos de outras fontes, tais como os dados da experiência de reactor KamLAND e os dados de experiências de acelerador com o objectivo de obter a melhor estimativa do valor do ângulo de mistura θ_{13} . Por fim, é efectuada uma análise de sensibilidade da possível

melhoria dos parâmetros de oscilação, assumindo diferentes cenários numa possível medição do fluxos de neutrinos da reacção de *pep* por parte da experiência SNO+, sucessora de SNO, demonstrando que SNO+ tem todas as condições para aumentar ainda mais a precisão do ângulo de mistura θ_{12} e aumentar a significância estatística de um valor não nulo no ângulo de mistura θ_{13} .

Palavras chave: Neutrinos Solares; Oscilações de Neutrinos; Calibração Óptica.

Acknowledgements

First and foremost I would like to thank my supervisor, José Maneira, who had the patience and the resilience to try to make a physicist out of me. I acknowledge that sometimes I might not have had the patience that you had and I really appreciate that you did. I appreciate the support and the always so many comments, corrections, questions (and more comments). The Portuguese SNO group was small, but we made it through. I also would like to thank my other supervisor, Prof. Amélia Maio, for the interesting comments and the support through the thesis.

A really great thanks to Olivier Simard for tutoring me both in the Optics and in the Neutrino Oscillation Analysis and for being an all around good friend. Even if we didn't agree on everything we could improve and make things better. Thanks for the great steaks in Sudbury, the nice pitchers in Ottawa and all other good moments. We have to go watch another hockey game sometime...

I also would like to thank to my colleagues at LIP for the help, and for providing the conditions for me to get through this work. A very special thanks to Sofia Andringa for the many interesting conversations (most of them with coffee and some of them about Physics), for reviewing my thesis and for all the support. A great thanks also to Nuno Dias, João Martins and Gonçalo Borges in the Computing Centre of LIP for the continuous help with my ever stranger questions and requests.

A very special thanks for the whole SNO collaboration, without whom this thesis would not be. A very grateful thanks to Bernie Nickel for his patience and time to discuss the derivation of the survival probability calculation. I also would like to thank Nikolai Tolich, the great helmsman of the Three-Phase Analysis, without whom everything would have been much harder. Thank you for the interesting comments and suggestions, for the interesting questions that are always necessary to make the

work better and for believing that we could really make this analysis. Thanks to Mark Chen, for the very interesting and instructive comments. I also would like to thank the "PhysInt 3-phase Topic Review Committee" (Christine, Jocelyn, Jason, Alain and Nikolai), whose comments and suggestions made not only the analysis for the paper more robust but also helped immensely in the preparation of my thesis. A great thanks for the Optical Calibration people: Peter Skensved, Christine Kraus, José Maneira and Olivier Simard. So many runs, so much data...and the fastest transitional run ever.

A great thanks to the Carleton SNO group for the fun and productive time spent there, for the support and for making me feel welcome. A great thanks to Alain Bellerive, for his support, for inviting me to spend some time in Carleton where I not only had a great time (even with arctic cold and without public transportation) but I also learned a lot. Thanks to Pierre-Luc for his very interesting comments, both in Physics and Computing. A great thanks also to Etienne Rollin for making me feel welcome at Carleton and for great times watching hockey games in the basement.

A great thanks to Kai Zuber for his comments, suggestions of interesting research topics and for allowing me to use the very fast (and big) computing cluster of the Dresden University of Technology without which the oscillation analysis would have taken much longer. I would also like to thank the neutrino group in Dresden, for the friendship and for helping in the smooth transition to a new country where everything was new while I was still writing the thesis. The thesis was already a hard enough fight without all the difficulties and the troubles of the move.

A very special thanks to Dr. Ayres de Campos, whose talks planted the seed that drove me into research in Physics. I have never forgotten the trip to RAL and the interaction with the Coimbra group. In the end, it all began there.

I also would like to thank all my friends with a special mention to the "Power Rangers". It is done guys. Thank you for your faith in me and for simply being there. A big thanks to Luis Pedro, for being such a great friend and a great support even though we barely see each other. The irony of our lives that each of us should pursue what the other originally was set to study...

Finalmente gostaria de expressar o mais profundo agradecimento à minha família, que sempre esteve comigo desde o primeiro momento e me suportou em todas as

circunstâncias. Muito obrigado à minha mãe Madalena, avós Rosa e Conceição, os meus irmãos Ricardo e Catarina por acreditarem que eu conseguiria chegar ao fim. Gostaria também de deixar um agradecimento muito especial à Teresa, que sempre me apoiou e teve a paciência para me aturar em todas as alturas, e ao Messias, com quem tive o prazer de trabalhar e aprender outras coisas mostrando que há um mundo de coisas interessantes para além da Física. Um obrigado também ao João por às vezes me proporcionar, intencionalmente ou não, a pausa que eu precisava "naquele momento".

Finally my greatest appreciation to Ana Farinha, who was a source of infinite support, patience and kept me sane even in the most insane moments. Thank you for being yourself, for being with me and for accepting me despite everything. I love you girl...this is for you.

Contents

Abstract	iii
Sumário	v
Acknowledgements	ix
1 Introduction	1
1.1 Neutrinos in the Standard Model	2
1.2 Neutrino Oscillations	4
1.2.1 Vacuum oscillations	6
1.2.2 Matter Induced Oscillations	8
1.3 Solar Neutrinos	12
1.3.1 The Standard Solar Model	13
1.4 The Solar Neutrino Problem	16
1.5 Solar Neutrino Experiments	18
1.5.1 Radiochemical Experiments	19
1.5.2 Light Water Čerenkov Experiments	22
1.5.3 Liquid Scintillator Experiments	25
1.5.4 The SNO Experiment	28
1.5.5 Present Status of Solar Neutrino Physics	32
1.6 Motivation and Scope of this Thesis	34
2 The SNO Detector	39
2.1 Structure of the Detector	39
2.2 Principles of operation	43
2.2.1 Heavy Water Phase (Phase I)	45
2.2.2 Salt Phase (Phase II)	45

2.2.3	Neutral Current Detector Phase (Phase III)	46
2.3	The PMT System	47
2.4	The Neutral Current Detectors (NCD)	50
2.5	Backgrounds	53
2.6	Detector Calibrations	56
2.6.1	Electronics calibration	57
2.6.2	Detector Calibrations	58
2.7	Detector Simulation	67
3	Optical Calibration	71
3.1	Introduction	71
3.2	Optical Calibration Analysis	74
3.2.1	Optical Model	77
3.2.2	Laserball Position Fits	79
3.3	Data selection	81
3.4	Optical Calibration Fit	86
3.4.1	Prompt Occupancy-Ratio Method	86
3.4.2	Extraction of the PMT Efficiencies	88
3.4.3	Occupancy-Efficiency Method	91
3.5	Summary	91
4	Optical Calibration Results	93
4.1	Optical Calibration Data	94
4.2	Validation of the Occupancy-Efficiency Method	97
4.3	NCD Optical Effects	99
4.3.1	NCD shadows	99
4.3.2	Geometrical cut	100
4.3.3	Effects on the Optical Parameters	102
4.3.4	NCD Reflections	103
4.3.5	Determination of NCD Reflectivity with Monte Carlo Simulation	114
4.4	Additional Improvements to the Analysis	118
4.4.1	NCD Attachment Anchors	119
4.4.2	Up-Down Asymmetry in the Detector	123
4.5	Results on the Optical Parameters	127
4.5.1	Data Set and Selection	128

4.5.2	Results	131
4.6	Systematic Uncertainties of the Optical Calibration	139
4.7	Conclusions on Optics	144
5	Neutrino Signal Extraction	147
5.1	Introduction	148
5.2	Observables	148
5.3	Backgrounds	151
5.4	Systematic Uncertainties	153
5.5	Outputs from the Signal Extraction	154
5.5.1	Reconstructed energy spectra	154
5.5.2	Polynomial parameterisation of the Electron Neutrino Survival Probability	157
5.6	The 3-phase Combined Analysis	159
5.6.1	Combination of Data Sets	160
5.6.2	Pulse Shape Analysis	162
5.6.3	Choice of the Survival Probability Parameterisation	163
5.6.4	Specific Survival Probability Parameterisation	169
5.7	Results from the Signal Extraction	172
5.7.1	Outputs from Signal Extraction of the 3-Phase Analysis	172
5.7.2	Signal Extraction results of the full 3-Phase data set	173
6	Neutrino Oscillation Analysis	179
6.1	Phenomenology of Neutrino Oscillations	180
6.1.1	Introduction	180
6.1.2	Oscillations in Vacuum	182
6.1.3	Oscillations in Matter	182
6.2	Calculation of the Survival Probability	187
6.2.1	Propagation in the Sun	187
6.2.2	Propagation in the Earth	190
6.2.3	Integration over zenith-angle exposure	193
6.3	Neutrino Oscillation Analysis Method	197
6.3.1	Calculation of Expected Event Rates	199
6.3.2	Analysis of SNO 3-phase Output	204
6.3.3	Combination of SNO with other solar Experiments	207

6.3.4	Solar Models and Propagation of their Uncertainties	214
6.4	Validation of the Method	216
6.5	Oscillation Analysis Results	221
6.5.1	Estimation of the oscillation parameters	221
6.5.2	Results from SNO	223
6.5.3	Results from combining all solar neutrino data	226
6.5.4	Effect of the Solar Model in the Oscillation Analysis	230
6.5.5	Probing the Neutrino Mass Hierarchy	232
6.6	Global Analysis of the Oscillation Parameters	235
6.6.1	Combining Solar Data and KamLAND	235
6.6.2	Further constrains from other neutrino sources	238
6.7	A Look Into the Future: SNO+	240
6.8	Summary	243
7	Conclusion	247
A	Acronyms	251
B	More on Optical Calibration	255
B.1	Optical Calibration Systematics	255
C	Additional Information on Neutrino Oscillation Analysis	259
C.1	Inputs of the combined Solar Neutrino Analysis	259
C.2	Parameters of the Standard Solar Models	264
C.3	KamLAND	266
	Bibliography	268

List of Figures

1.1	Diagrams of coherent forward elastic scattering.	8
1.2	pp-chain reactions.	15
1.3	Solar neutrino spectra.	16
1.4	Solar Neutrino Problem.	18
1.5	Results from SAGE.	21
1.6	Feynman diagrams of neutrino-electron elastic scattering interaction.	24
1.7	Results from the Super-Kamiokande experiment.	25
1.8	Results from Borexino experiment.	26
1.9	Results from KamLAND.	28
1.10	Neutrino interactions in SNO.	30
1.11	Solar neutrino flux measurements of SNO.	32
1.12	The evolution on solar ν mixing parameters.	33
1.13	Constrain on mixing parameters in two flavours.	34
1.14	Global limits on mixing parameters.	35
1.15	Mixing angle predictions from symmetry models.	38
2.1	Schema of the SNO detector.	40
2.2	Schematic of a SNO PMT.	42
2.3	Čerenkov spectrum in SNO.	48
2.4	Schematic of a NCD.	51
2.5	NCD energy spectrum.	52
2.6	NCD array distribution in the SNO detector.	53
2.7	SNO manipulator.	60
2.8	Schema of the <i>laserball</i> source.	62
2.9	SNO optical calibration laser.	63
2.10	Wavelength spectra of the SNO calibration laser system.	64

3.1	Optical Calibration analysis chain.	73
3.2	Light paths in the detector.	76
3.3	Single channel time spectrum.	80
3.4	Diagrams of some optical cuts.	84
3.5	Diagrams of the NCD shadow cut. The blue zone depicts the tolerance around the NCD.	85
3.6	PMT efficiency distribution.	90
3.7	Correlation between PMT efficiencies of two heavy water scans. . . .	90
4.1	Laserball positions in an optical calibration scan.	95
4.2	Relative PMT angular response.	98
4.3	Media attenuation coefficients.	98
4.4	NCD shadow cut.	101
4.5	Effects of the NCD shadow cut in the PMT angular response.	102
4.6	Effect of the NCDs in the time spectra.	104
4.7	Acceptance probability of a NCD reflected photon.	105
4.8	MC generated PMT time integrated spectra.	107
4.9	Occupancy ratio versus D_2O optical path.	109
4.10	Distribution of occupancy ratio as function of various measurable quantities.	110
4.11	Uncertainties in the 2D correction.	112
4.12	NCD reflectivity as a function of wavelength (in nm) as implemented in the Monte Carlo simulation.	114
4.13	MC generated PMT timing spectra with different NCD reflectivities. . . .	116
4.14	Detail of region of interest to study the NCDs reflectivity.	118
4.15	Effect of the NCD anchor optical cut.	120
4.16	NCD anchor cut effect in heavy water attenuation.	121
4.17	Effect of the NCD anchors cut in the PMT efficiencies.	122
4.18	Variation of the PMT efficiencies along the coordinate axes.	123
4.19	Asymmetry along the z axis in the PMT angular response.	125
4.20	Variation in PMT angular response with z coordinate.	126
4.21	Systematic uncertainty in the PMT angular response.	127
4.22	D_2O attenuations in SNO.	132
4.23	H_2O attenuations in SNO.	133
4.24	PMT angular response in the NCD phase.	134

4.25	LB characterisation distributions.	136
4.26	PMT angular response for all re-analysed scans.	137
4.27	Time variation of the D ₂ O attenuation.	138
4.28	Time variation of the H ₂ O attenuation.	139
5.1	Observable distributions for each SNO event class.	152
5.2	LETA signal extraction results.	156
5.3	Latest SNO measurement of the total ⁸ B solar neutrino flux.	157
5.4	Example of a survival probability curve.	159
5.5	Sample NCD pulse shapes.	163
5.6	Survival probability curves for different oscillation parameters.	165
5.7	Fit of polynomial parameterisations to the model survival probability.	166
5.8	Accuracy of the polynomial as a function of the oscillation parameters.	168
5.9	Accuracy of the polynomial as a function of the oscillation parameters weighted by the detector sensitivity.	170
5.10	Latest SNO measurement of the total ⁸ B solar neutrino flux.	176
5.11	Signal Extraction results from the 3-phase combined analysis.	176
6.1	Radial profile of electron density in the Sun.	188
6.2	Radial profiles of the neutrino production regions for each reaction as function of the solar radius for different solar models.	189
6.3	Effect of the solar model parameters in the survival probability.	190
6.4	Radial profiles of matter density in the Earth.	192
6.5	Effect of the survival probability calculated at the horizon.	193
6.6	Live time distributions of SNO.	194
6.7	Aliasing effects from finite sampling of Earth paths.	196
6.8	Day, Night and Sun only survival probability at SNO.	198
6.9	Reaction cross sections in SNO.	201
6.10	SNO sensitivity in neutrino energy.	205
6.11	Accuracy of the survival probability calculated using the adiabatic approximation.	212
6.12	Distribution of the fitted oscillation parameters.	218
6.13	Bias and Pulls from oscillation analysis.	220
6.14	SNO-only oscillation analysis results.	225
6.15	Two flavour solar neutrino results.	228

6.16	Three flavour confidence regions from solar data.	229
6.17	Three flavour confidence regions from solar data for different solar models.	232
6.18	Effect of Δm_{31}^2 in the survival probability.	233
6.19	Three flavour confidence regions under different neutrino mass hierarchy assumptions.	234
6.20	Two flavour analysis of Solar and KamLAND data.	236
6.21	Three flavour confidence regions from a combined analysis of solar and KamLAND data.	237
6.22	1D confidence regions from a solar+KamLAND analysis.	238
6.23	Enhanced constrain on θ_{13} from all available neutrino data.	240
6.24	Confidence regions from a neutrino oscillation analysis of solar data with an expectation from SNO+ <i>pep</i> measurement.	242

List of Tables

1.1	Fundamental properties of the Sun-Earth system.	14
1.2	Solar neutrino fluxes.	14
1.3	Current limits on the neutrino oscillation parameters.	35
2.1	^{238}U and ^{232}Th concentrations in SNO.	57
2.2	Properties of the SNO calibration laser.	64
4.1	OCA scans performed during the whole duration of SNO.	96
4.2	Floating parameters in the optical fit.	130
4.3	Systematic uncertainties in the optical parameters.	140
4.4	Effects of the systematic uncertainties.	143
5.1	List of all output parameters in the signal extraction analysis.	174
5.2	Final results from the SNO 3-Phase analysis.	175
5.3	Correlation matrix from the SNO 3-Phase analysis.	175
6.1	Limits and dimensions of the survival probability storage tables.	210
6.2	Region of interest for the neutrino oscillation analysis.	222
6.3	Definition of the confidence levels.	223
6.4	SNO-only oscillation analysis results.	225
6.5	Numerical results from the analysis of all solar neutrino data.	230
6.6	Numerical results from the solar model comparison.	231
6.7	Numerical results from the neutrino mass hierarchy test.	234
6.8	Numerical results from the analysis of all solar neutrino data combined with KamLAND.	239
6.9	Numerical results from the solar model comparison.	242
6.10	Summary of the results from all oscillation analyses performed.	244

C.1	Inputs for the Solar neutrino analysis in 3-phase paper.	259
C.2	Partial derivatives of BS05(OP) SSM.	264
C.3	Partial derivatives of BPS09(GS) SSM.	265
C.4	Partial derivatives of BPS09(Asplund:2009fu) SSM.	265

Chapter 1

Introduction

Neutrinos are a very interesting probe to study some of the most fundamental questions about the Universe. The same properties that make neutrinos so difficult to detect make them the ideal means for studying subjects that would be otherwise hard, if not impossible to address. Solar neutrinos in particular provide a unique opportunity to study the processes in the interior of the Sun due to the large mean free path which allows neutrinos to stream freely out of the Sun.

The detection of solar neutrinos has been discussed for several decades considering different sources [1, 2]. The first proposal for neutrino detection as a way to verify the hypothesis of solar fusion was carried out in a collaborative effort of Davis and Bahcall [3, 4].

Since the very first results it became clear that neutrinos were not as well understood as it was previously thought and thus solar neutrinos became an invaluable instrument for discovering the nature of neutrinos themselves. Since then much was learned about them, and although the studies continue, neutrinos are now an undoubtedly precious tool to understand the way the stars, and the Sun in particular, work.

1.1 Neutrinos in the Standard Model

The existence of the neutrino was first postulated by Wolfgang Pauli in 1930 to explain the continuous electron energy spectrum observed in nuclear beta decay [5], without violating the principle of energy conservation.

At the time, the nuclear models considered the beta decay simply as an electron being ejected from the nucleus. However, this model implied that the electron would always have a fixed energy. Moreover, experimental studies demonstrated that the electron energy had a continuous distribution up to an endpoint, instead of a discrete distribution at that same energy. In order to be consistent with these observations Wolfgang Pauli suggested that a third particle should participate in the decay, accompanying the electron. This particle should be neutral, very light and have a spin $1/2$, so that it also would respect the Pauli exclusion principle and solve the spin statistic problem in atomic nuclei. This explanation perfectly fitted the observations of a continuous energy spectrum of the ejected electron, and at the time Pauli set the first limit on this particle to be 1% of the proton mass [6] .

Two years later, in 1932, Chadwick discovered the neutron [7] which meant that the previous model of the nucleus was incorrect. Although the existence of the neutron as a component of the nucleus solved the issue of the spin statistics, the problem of the continuous electron energy spectrum resulting from the beta decay persisted, being Pauli's theory the only explanation that fitted the observations.

Later, in 1934, Enrico Fermi formulated the basic model of the beta decay, which is the foundation of the theory of weak interactions [8]. In his model, Fermi included the light neutral particle suggested by Pauli, which he named *neutrino*. In his model, beta decay occurred when a neutron converts into a proton, emitting an electron and an antineutrino. These two particles were not considered part of the nucleus, being spontaneously generated by the decay of the neutron. Along with this explanation, Fermi also suggested a method to detect neutrinos via the inverse beta decay reaction:

$$\bar{\nu} + p \rightarrow n + e^+. \tag{1.1}$$

The cross section of this reaction was soon estimated to be in the order of

10^{-44}cm^2 , which would make it virtually impossible to detect from radioactive sources [9]. Neutrinos are also produced in fusion reactions, but the very high temperatures, pressures and energies involved make it extremely difficult to observe in a laboratory.

The detection of neutrinos took twenty years until neutrino sources capable of producing a high flux of neutrinos were created, such as nuclear reactors. It was in fact through the inverse beta decay reaction that neutrinos were firstly detected in 1956 by Reines and Cowan [10] using antineutrinos produced by a nuclear reactor. Since then, the neutrinos have been exclusively described by the weak interaction, which accounts for the neutrino long penetration length in matter (on the order of half light years through lead for neutrinos at energies typical for beta decays) and the difficulty in its detection. Within the *Standard Model of particle physics (SM)* [11], neutrinos were included as massless particles, being the neutral partner of the charged lepton. Thus, three generations of neutrino are considered ($\nu_e; \nu_\mu; \nu_\tau$), each associated to one of the charged leptons e, μ and τ . These three generation of neutrinos are commonly identified as *neutrino flavours*. Each of these flavours have been directly observed through their interactions with the corresponding leptons.

In the context of the SM, neutrinos have interesting properties that set them aside from the other fundamental particles. Unlike the other fermions, neutrinos only experience the weak interaction - they carry no electric or colour charges - and are assumed to be massless. This latter property is related to the fact that only left handed neutrinos have been observed to participate in weak interactions (and correspondingly, only right handed antineutrinos have been observed). Therefore, the neutrino exists in the Standard Model in a left-handed doublet along with its charged lepton partner and with no right-handed field, so no mass term can be constructed.

The weak interaction is mediated by the massive W^\pm and Z bosons. Measurements of the width of the Z boson at CERN have determined that the number of active neutrino states to be three, which is in agreement with the Standard Model prediction [12].

Subsequent experimental evidence from solar and atmospheric neutrino experiments demonstrated a deficit on the total neutrino flux, where one of the possible explanations was the possibility of a non-zero neutrino mass. Later results from

Super-Kamiokande (SK) [13] and SNO [14] clearly demonstrated that the massless assumption of the Standard Model was incomplete and that it necessitated its inclusion in the theory. The results from SK demonstrated flavour and distance dependent suppression in atmospheric neutrinos, while SNO demonstrated flavour transformation in solar neutrinos. Both results are direct evidence of non-zero neutrino masses.

1.2 Neutrino Oscillations

In the Standard Model the three quark states that participate in the weak interactions are linear combinations of the states that participate in the strong interactions and that have definite (although not well determined) masses. The correspondence between the flavour and mass bases is given by a unitary transformation, commonly called the mixing matrix. In the quark sector the Cabibbo-Kobayashi-Maskawa (CKM) matrix describes the mixing between the quark mass and flavour eigenstates.

Considering the neutrinos as having non-zero masses, one can construct a similar formalism involving mixing between the flavour and mass neutrino states. If the flavour eigenstates of the weak interaction are not exactly the same as the mass eigenstates, then it is possible for neutrinos to change flavour. This effect was first suggested by Bruno Pontecorvo [1] in the framework of neutrino-antineutrino oscillations. Later, Z. Maki, N. Nakagawa and S. Sakata further developed the idea in application to the oscillation of neutrino flavours [15]. From the works of Pontecorvo, Maki, Nakagawa and Sakata a matrix relating the neutrino mass eigenstates and the flavour eigenstates was developed, which is usually known as the *PMNS matrix*¹.

Thus, in general, each of the left-handed components of the neutrino field ν_α , with $\alpha = e, \mu, \tau$ can be expressed as a linear combination of the mass eigenstates ν_i , with $i = 1, 2, 3$ [16]:

$$\nu_\alpha = \sum_{i=1}^{N=3} U_{\alpha i} \nu_i, \quad (1.2)$$

¹There is no consensus concerning the name and acronym of the matrix, being also known as MNS matrix and MNSP matrix. Nonetheless all names identify the same matrix.

where ν_α are the flavour eigenstates, ν_i are the mass eigenstates, and $U_{\alpha i}$ is the *Pontecorvo-Maki-Nakagawa-Sakata (PMNS)* mixing matrix:

$$\mathbf{U} \equiv U^{PMNS} = \begin{pmatrix} U_{e1} & U_{e2} & U_{e3} \\ U_{\mu 1} & U_{\mu 2} & U_{\mu 3} \\ U_{\tau 1} & U_{\tau 2} & U_{\tau 3} \end{pmatrix} \quad (1.3)$$

$$= \begin{pmatrix} c_{12}c_{13} & s_{12}c_{13} & s_{13}e^{-i\delta} \\ -s_{12}c_{23} - c_{12}s_{23}s_{13}e^{i\delta} & c_{12}c_{23} - s_{12}s_{23}s_{13}e^{i\delta} & s_{23}c_{13} \\ s_{12}s_{23} - c_{12}c_{23}s_{13}e^{i\delta} & -c_{12}s_{23} - s_{12}c_{23}s_{13}e^{i\delta} & c_{23}c_{13} \end{pmatrix}. \quad (1.4)$$

For simplicity, $c_{ij} \equiv \cos \theta_{ij}$ and $s_{ij} \equiv \sin \theta_{ij}$. The phase δ is the CP-violating phase, which, in case it is different from zero, breaks the symmetry of interactions involving the mixing matrix.

Being neutral particles, unlike the quarks, it is possible that neutrinos are their own anti-particles. This was originally suggested by Ettore Majorana [17]. It is known that neutrinos behave differently from antineutrinos [1], but this could be due just to their different handedness, rather than to an intrinsic quantum number. Particles that comply with this property are known as *Majorana particles*. Thus, if indeed neutrinos are Majorana particles two additional phases λ_1 and λ_2 must be added to the mixing matrix:

$$\mathbf{U} = U^{Dirac} U^{Majorana} \quad U^{Majorana} = \text{diag} (1, e^{i\lambda_1}, e^{i\lambda_2}), \quad (1.5)$$

and U^{Dirac} has the same form as in Equation 1.4. The Majorana phases contribute to an overall phase shift applied to all neutrino flavours and thus cannot be observed in neutrino oscillation experiments, leaving only the Dirac part of the matrix as the relevant part to model the flavour change of neutrinos.

One common parameterisation of the mixing matrix consists in the separation

into a product of three separate two-neutrino mixing matrices:

$$U = \begin{pmatrix} 1 & 0 & 0 \\ 0 & c_{23} & s_{23} \\ 0 & -s_{23} & c_{23} \end{pmatrix} \times \begin{pmatrix} c_{13} & 0 & s_{13}e^{i\delta} \\ 0 & 1 & 0 \\ -s_{13}e^{-i\delta} & 0 & c_{13} \end{pmatrix} \times \begin{pmatrix} c_{12} & s_{12} & 0 \\ -s_{12} & c_{12} & 0 \\ 0 & 0 & 1 \end{pmatrix}. \quad (1.6)$$

In the following subsections the phenomenology of neutrino oscillations will be explained for two particular cases: vacuum oscillations and induced matter oscillations.

1.2.1 Vacuum oscillations

A specific mass eigenstate is a linear combination of the flavour eigenstates, whose basis transformation is also described by the mixing matrix:

$$|\nu_\alpha\rangle = \sum_{i=1}^{N=3} U_{\alpha i}^* |\nu_i\rangle \quad |\nu_i\rangle = \sum_{\alpha=\{e,\mu,\tau\}} U_{\alpha i} |\nu_\alpha\rangle. \quad (1.7)$$

This is the standard approach in the classical theory of neutrino mixing and oscillations [18]. These massive states are eigenstates of the Hamiltonian of the propagating neutrinos, being produced with definite energies². It follows, by solving the Schrödinger equation, that the time evolution of a neutrino state in vacuum is:

$$|\nu_\alpha(t)\rangle = \sum_{i=1}^3 U_{\alpha i}^* e^{-iE_i t} |\nu_i\rangle = \sum_{\beta} \left(\sum_{i=1}^3 U_{\alpha i}^* e^{-iE_i t} U_{\beta i} \right) |\nu_\beta\rangle. \quad (1.8)$$

Equation 1.8 demonstrates that a neutrino originally produced with a flavour α , will become a superposition of the three flavour eigenstates. Hence, there is a non-zero probability that it can be detected with a different flavour β .

²It can be shown [18] that the assumption of equal momentum implied here is not necessary for the conclusions of the theory.

One can now define a *transition probability* from initial flavour state α to a flavour state β as the square of the transition amplitudes:

$$P_{\nu_\alpha \rightarrow \nu_\beta}(t) = |\langle \nu_\beta | \nu_\alpha(t) \rangle|^2 = \sum_{i,j} U_{\alpha i}^* U_{\beta i} U_{\alpha j} U_{\beta j}^* e^{-i(E_i - E_j)t}. \quad (1.9)$$

As neutrinos are ultra-relativistic particles, the energy eigenvalues can be approximated as $E_i \approx E_\nu + m_i^2/2E_\nu$ with $E_\nu = |\vec{p}^2|$. The difference between two energy eigenvalues can now be described as

$$E_i - E_j = \frac{\Delta m_{ij}^2}{2E_\nu} \quad \text{with} \quad \Delta m_{ij}^2 = m_i^2 - m_j^2. \quad (1.10)$$

The ultra-relativistic nature of the neutrinos also allows the conversion of times t into distances L , which are more convenient for the observation of the oscillation effects given the distance from a detector to the neutrino source. Applying this transformation to Equation 1.9 and combining the equations above one can rewrite the flavour transition probability equation as:

$$P_{\nu_\alpha \rightarrow \nu_\beta}(L, E_\nu) = \sum_{i,j} U_{\alpha i}^* U_{\beta i} U_{\alpha j} U_{\beta j}^* e^{-i \frac{\Delta m_{ij}^2 L}{2E_\nu}}. \quad (1.11)$$

This expression demonstrates that the probability of flavour transition is an oscillating function of the distance L and neutrino energy E_ν , weighted by the elements of the mixing matrix U and the mass-squared differences Δm_{ij}^2 . These elements are commonly referred as the *neutrino oscillation parameters*, as they are independent of the individual experiment, unlike the distance and the energy.

One can also define a *survival probability* of a flavour α as $P_{\nu_\alpha \rightarrow \nu_\alpha}$, being the probability that at a distance L a neutrino of energy E_ν will be detected with the same flavour that it was originally produced. As unitarity enforces the conservation of the total survival probability of all flavours, it means that the survival probability

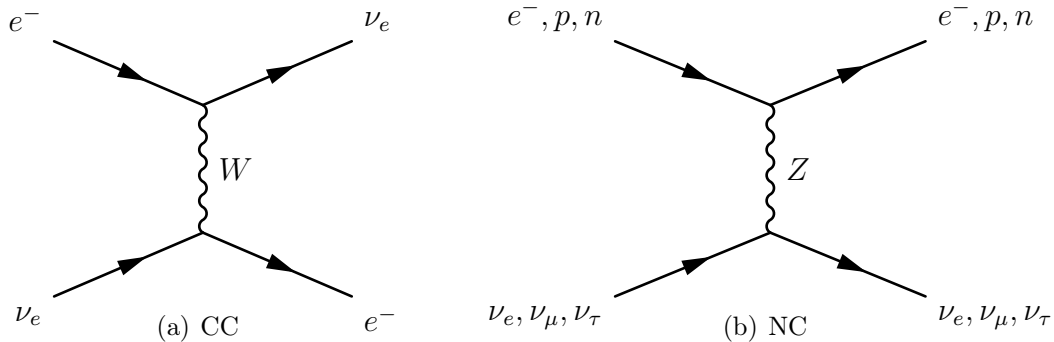


Figure 1.1: Feynman diagrams of the coherent forward elastic scattering interactions that generate effective potentials affecting the neutrino propagation in matter.

can be expressed as:

$$P_{\alpha \rightarrow \alpha} = 1 - \sum_{\beta \neq \alpha} P_{\alpha \rightarrow \beta}. \quad (1.12)$$

1.2.2 Matter Induced Oscillations

In 1978 L. Wolfenstein discovered that while travelling through matter, the neutrinos are affected by a potential due to *coherent* forward elastic scattering with the electrons and nucleons in the medium causing a modification of the vacuum evolution equation [19]. Later, S. Mikheev and Y. Smirnov [20–22] further developed this theory, demonstrating the existence of resonant flavour transitions when neutrinos travel through a medium of varying density. This mechanism became known as the *Mikheev-Smirnov-Wolfenstein (MSW)* effect.

While propagating through matter, the evolution equation of the neutrinos is affected by effective potentials due to weak *charged current (CC)* and *neutral current (NC)* coherent forward elastic scatterings [18]. In this context *coherent* means that the medium isn't affected by the passage of the neutrino. The Feynman diagrams of these scatterings are shown in Figure 1.1. As demonstrated by Mikheev, Smirnov and Wolfenstein, this scattering effect can enhance the flavour conversion. The neutrinos produced in the Sun are initially only in *electron* flavour, and are thus sensitive to both the CC and NC potentials (V_{CC}, V_{NC}). The neutrinos of this flavour are the only ones to experience the effect of the V_{CC} potential.

Furthermore, in astrophysical environments, such as the Sun, electrical neutrality implies an equal number of electrons and protons. In this case, their NC potentials cancel out, leaving only the contribution from neutrons in the V_{NC} potential in the medium.

Thus, the total potential induced by matter to a neutrino of flavour α is [18]:

$$V_\alpha = V_{CC}\delta_{\alpha e} + V_{NC} = \sqrt{2}G_F \left(N_e\delta_{\alpha e} - \frac{1}{2}N_n \right), \quad (1.13)$$

where N_e is the density of electrons and N_n is the density of neutrons. All neutrino flavours are equally affected by the V_{NC} potential. Here $\delta_{\alpha e}$ ensures that only electron neutrinos are sensitive to V_{CC} . In the time evolution equation the V_{NC} potential will translate into a phase, common to all flavours, that can easily be removed by a phase transformation. Therefore, the effect of matter in neutrino oscillations can be accounted by adding only the contribution of V_{CC} to the Hamiltonian.

In order to consider the enhancement caused by matter the flavour basis Hamiltonian has to be re-written in order to accommodate both the vacuum and matter components [18]:

$$H^f = H^0 + H^1, \quad (1.14)$$

where H^0 is the vacuum Hamiltonian and H^1 is the Hamiltonian of the matter component that includes the effective potential V_α affecting the neutrino of flavour α :

$$H^0 |\nu_i\rangle = E_i |\nu_i\rangle \quad (1.15)$$

$$H^1 |\nu_\alpha\rangle = V_\alpha |\nu_\alpha\rangle. \quad (1.16)$$

Following a procedure similar to the one employed for the vacuum oscillations, the time evolution equation for a neutrino produced in an initial flavour state $|\nu_\alpha(0)\rangle =$

$|\nu_\alpha\rangle$ is given by:

$$i\frac{d}{dt}|\nu_\alpha(t)\rangle = H|\nu_\alpha(t)\rangle. \quad (1.17)$$

Developing this equation and performing the approximation for ultra-relativistic neutrinos, and performing a transformation $t \rightarrow x$, one can obtain the following evolution equation in space coordinates:

$$i\frac{d}{dx}A_{\alpha\beta}(x) = \left(E + \frac{m_1^2}{2E} + V_{NC}\right)A_{\alpha\beta}(x) + \sum_\eta \left(\sum_i U_{\beta i} \frac{\Delta m_{i1}^2}{2E} U_{\eta i}^* + \delta_{\beta e} \delta_{\eta e} V_{CC}\right)A_{\alpha\beta}(x). \quad (1.18)$$

As it is easily observed, the first term of Equation 1.18 is common to all flavours and can be eliminated by a phase transformation without producing any effect on the flavour transition probability:

$$A_{\alpha\beta}(x) \rightarrow A_{\alpha\beta}(x) e^{-i\left(E + \frac{m_1^2}{2E}\right)x - i\int_0^x V_{NC}(x')dx'}. \quad (1.19)$$

Further developing Equation 1.18 one can obtain the effective Hamiltonian H^f :

$$H^f = \frac{1}{2E} (\mathbf{U}\mathbf{M}^2\mathbf{U}^\dagger + \mathbf{A}), \quad (1.20)$$

with \mathbf{U} being the PMNS matrix and

$$\mathbf{M}^2 = \begin{pmatrix} 0 & 0 & 0 \\ 0 & \Delta m_{21}^2 & 0 \\ 0 & 0 & \Delta m_{31}^2 \end{pmatrix} \quad \text{and} \quad \mathbf{A} = \begin{pmatrix} A_{CC}(N_e) & 0 & 0 \\ 0 & 0 & 0 \\ 0 & 0 & 0 \end{pmatrix}, \quad (1.21)$$

with $A_{CC} \equiv 2EV_{CC} = 2\sqrt{2}EG_F N_e(x)$, where G_F is the Fermi constant, and N_e is the electron density in the medium. This potential is usually very small (due to the dimension of G_F), unless the electron density grows very large, as in the case of

the Sun. Note that for a non-point like source, this term will vary along the traveling path (hence the representation as a function of the traveled distance x).

One interesting feature of the matter oscillations is that, from Equation 1.20 now there exists a new basis - the matter eigenstate basis - where the Hamiltonian is diagonal. One can now solve the Hamiltonian in this basis and find a transformation leading back to the flavour basis [23]. This procedure leads to the definition of a new set of effective angles and masses - the matter mixing parameters - which can be treated in the same way as in the flavour case. In the case of the oscillation parameters relevant for a solar neutrino analysis, one obtains two effective effective mixing angles in matter [18]

$$\begin{aligned}\tan 2\theta_{12}^M &= \frac{\tan 2\theta_{12}}{1 - \frac{\cos^2 \theta_{13} A_{CC}}{\cos 2\theta_{12} \Delta m_{21}^2}} \\ \sin \theta_{13}^M &= \sin \theta_{13} \left[1 + \frac{A_{CC}}{\Delta m_{31}^2} \cos^2 \theta_{13} \right]\end{aligned}\quad (1.22)$$

and an effective mass squared difference,

$$\Delta m_{M21}^2 = \sqrt{(\Delta m_{21}^2 \cos 2\theta_{12} - \cos^2 \theta_{13} A_{CC})^2 + (\Delta m_{21}^2 \sin 2\theta_{12})^2}. \quad (1.23)$$

Equation 1.22 presents a resonance for

$$\cos^2 \theta_{13} A_{CC} = \cos 2\theta_{12} \Delta m_{21}^2, \quad (1.24)$$

where the mixing in matter can be large, regardless of the vacuum mixing angle. The development of Equations 1.22 was of major importance for the study of solar neutrino oscillations. In order to explain the deficit of electron flavoured solar neutrinos through vacuum neutrino oscillations, it was necessary to fine-tune the input parameters, such as the distance Sun-detector, in order for the oscillations to effectively explain the data. By considering induced oscillations in matter, a good

agreement between data and the oscillations model was easily achieved without need of any fine tuning.

The treatment of matter oscillations in three active flavours is extremely hard to achieve as it requires solving Equation 1.18 and it can lead to interplays of effects from the different Δm^2 terms. Usually a numerical solution is achieved by performing a numerical integration of the time evolution equation over the Solar radius.

Alternatively, it is possible to employ a series of approximations for different oscillation scenarios, deriving analytical solutions to describe the survival probability. One such treatment consists in performing an adiabatic transport of the neutrino states [20]. When the electron density in the medium presents a small variation when compared with the neutrino oscillation length in matter one can consider that there is no transition between the mass eigenstates in the neutrino propagation. Therefore, the neutrinos propagate through matter in the same mass eigenstate, with the flavour change being explained by the changing flavour composition of the mass eigenstates in matter. In this case one describes the evolution of the neutrino wave function in terms of stationary eigenstates of the time dependent Hamiltonian evaluated for the instantaneous electron density.

Considering the present knowledge of the neutrino oscillation parameters, this approximation can safely be applied, providing a fast and accurate calculation of the survival probability. More details about this calculation shall be given in Chapter 6.

1.3 Solar Neutrinos

The study of solar neutrinos is a very productive and rich area of neutrino physics. The Sun is a very powerful source of neutrinos in the MeV range, producing neutrinos up to 18 MeV, in thermonuclear reactions in the solar core. As stated previously, by being subject only to the weak interaction, neutrinos interact very weakly and thus the vast majority of the neutrinos produced in the Sun flow undisturbed from its interior into space.

Although the flux of neutrinos produced in the interior of the Sun is approximately $10^{11} \text{cm}^{-2} \text{s}^{-1}$, the small interaction cross sections make them extremely difficult to

detect and therefore large detectors are necessary. These detectors are usually placed underground, in order to reduce the backgrounds, especially cosmic muons whose interactions in the detector would easily outnumber the neutrino interaction rate.

Although neutrino physics is very often considered an area of particle physics, the study of solar neutrinos is strongly tied to the physics of the Sun and its good understanding. These two fields of research are strongly tied as neutrinos present themselves as the best possible means to "look" into the center of the Sun, and only with a correct understanding of the Sun thermonuclear fusion one can hope to correctly understand the properties of the detected solar neutrinos.

There is yet another reason why solar neutrinos are an extremely useful tool to study the properties of neutrinos. The matter enhanced oscillations have a very weak potential, and thus require a very high electron density to become relevant. While the electron density in the Earth is too small to have a significant effect in the neutrino oscillations, the Sun has a very high density, especially in the region where neutrinos are produced. In fact, as it will be discussed later, the neutrino oscillations in the Sun are dominated by this effect, which would be very difficult to observe in any experiment using a neutrino source at the Earth.

1.3.1 The Standard Solar Model

The *Solar Standard Model (SSM)* is a model describing the physical properties of the Sun, such as its luminosity, temperature and radius at the present epoch, while also matching the observed ratio of heavy elements, when compared to hydrogen, at its surface [24].

As is easily understandable, an SSM uses several independent sources of input and depends on many internal parameters which cannot be compared to independent measurements. In recent years, different SSMs were developed, or updated, based on different assumptions on some of the parameters and new updated measurements of some of the Sun properties. In Table 1.1 some of the Sun's fundamental properties that are common to all recent SSMs, are shown.

Multiple SSMs will be considered in the present analysis, as each solar model predicts different neutrino fluxes and different electron densities in the Sun. Thus,

Solar luminosity	$\mathcal{L} = (2.400 \pm 0.005) \times 10^{26} \text{ MeV s}^{-1}$
Solar Radius	$R_{\odot} = (6.9551 \pm 0.0004) \times 10^{10} \text{ cm}$
Solar Mass	$M_{\odot} = (1.9984 \pm 0.0002) \times 10^{30} \text{ kg}$
Astronomical unit	$1 \text{ au} = (149.59787066 \pm 0.00000002) \times 10^6 \text{ km}$
Solar Constant	$K_{\odot} = \mathcal{L}/4\pi 1 \text{ au} \approx 8.534 \times 10^{11} \text{ MeV cm}^{-2} \text{ s}^{-1}$
Year	$1 \text{ yr} = 3.15569252 \times 10^7 \text{ s}$

Table 1.1: Some fundamental properties of the Sun-Earth system. Information from [12].

	BS05(OP)	BPS09(GS)	BPS09(AGSS09)
$\Phi_{pp}(10^{10})$	5.99 (1 ± 0.01)	5.97 (1 ± 0.006)	6.03 (1 ± 0.005)
$\Phi_{pep}(10^8)$	1.42 (1 ± 0.017)	1.41 (1 ± 0.011)	1.44 (1 ± 0.01)
$\Phi_{hep}(10^3)$	7.93 (1 ± 0.155)	7.91 (1 ± 0.15)	8.18 (1 ± 0.15)
$\Phi_{7\text{Be}}(10^9)$	4.84 (1 ± 0.105)	5.08 (1 ± 0.06)	4.64 (1 ± 0.06)
$\Phi_{8\text{B}}(10^6)$	5.69 (1 ± 0.163)	5.88 (1 ± 0.11)	4.85 (1 ± 0.12)
$\Phi_{13\text{N}}(10^8)$	3.07 ($1_{-0.281}^{+0.312}$)	2.82 (1 ± 0.14)	2.07 ($1_{-0.13}^{+0.14}$)
$\Phi_{15\text{O}}(10^8)$	2.33 ($1_{-0.288}^{+0.332}$)	2.09 ($1_{-0.15}^{+0.16}$)	1.47 ($1_{-0.15}^{+0.16}$)
$\Phi_{17\text{F}}(10^6)$	5.84 (1 ± 0.522)	5.65 ($1_{-0.16}^{+0.17}$)	3.48 ($1_{-0.16}^{+0.17}$)

Table 1.2: Solar neutrino fluxes predicted by the BS05(OP) [25], BPS09(GS) [26] and BPS09(Asplund:2009fu) [26] SSMs. Fluxes are given in units of $\text{cm}^{-2} \text{ s}^{-1}$. The scale of the fluxes are given in the first column.

in order to aim for a precise measurement of the neutrino oscillation parameters, one has to consider multiple SSMs. In this thesis, three SSMs are used, which are henceforward named as BS05(OP) [25], BPS09(GS) [26, 27] and BPS09(AGSS09) [26, 28]. All these models predicted observables in good agreement with the *helioseismological* measurements, such as the helium concentration in the surface of the Sun and the depth of the convective zone. The latter models make use of updated measurements, and most up to date simulations of the Sun’s interior. The major difference between these models comes from the abundances of heavy elements in the Sun that affect not only the rates of the fusion reactions, but also the density of electrons along the solar radius, which are the most important parameters in determination of the neutrino survival probability. The fluxes predicted by these SSMs are listed in Table 1.2, together with the respective uncertainties.

Figure 1.2 summarises the fusion chain of reactions that occur in the Sun, responsible for producing the solar neutrinos. There are two independent chains responsible for the solar neutrino flux: the so called *pp* chain, which is the major contributor for

energy and neutrino production yielding neutrinos up to 18 MeV; and the *Carbon-Nitrogen-Oxygen cycle (CNO)*, which produces low energy neutrinos from reactions involving heavier elements. Neutrinos from this latter chain have not yet been observed, as the flux is strongly suppressed by the more intense pp chain and its detection made harder by the higher background levels from radioactive sources and cosmogenic activations. Figure 1.2 shows a diagram of the pp chain.

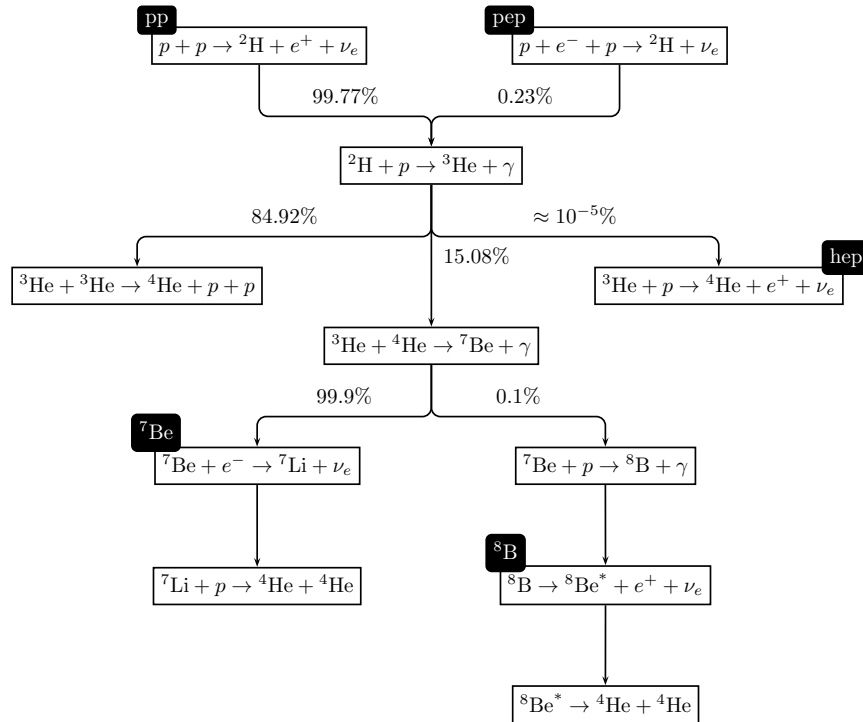


Figure 1.2: Nuclear reactions involved in the proton-proton (*pp*) fusion chain.

Since the elements are heavier in the CNO cycle, the model prediction of its reaction rates is not as precise as rates resulting from the pp chain. Also as it can be observed in Table 1.2 that the uncertainties on the neutrino fluxes from the pp chain have been dramatically reduced in the most recent SSMs. Figure 1.3 shows the energy spectra of the neutrino fluxes from the *pp* chain and CNO cycle in the BS05(OP) SSM [25].

Considering the logarithmic scale, it becomes clear that the *pp* reaction³ produces the most part of the solar neutrinos. Unfortunately, most of the current experiments

³Not to be confused with the *pp* chain, which encloses the whole reaction cycle shown in Figure 1.2, and which starts precisely with the *pp* reaction.

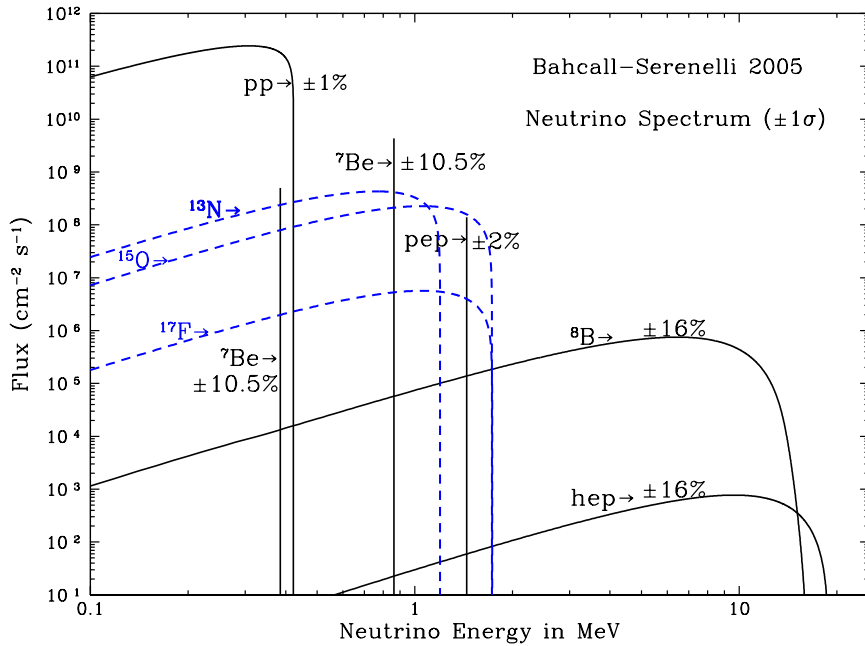


Figure 1.3: Neutrino flux spectra with model uncertainties. Image taken from [25]. Neutrinos produced through the pp chain are shown as continuous lines; those produced by the CNO cycle are shown as dashed lines.

are not sensitive to their low energy ($E_\nu < 0.43\text{MeV}$), but rather to the less intense high-energy ${}^8\text{B}$ and hep fluxes.

1.4 The Solar Neutrino Problem

In 1964, John Bahcall and Raymond Davis, Jr. planned an experiment to detect solar neutrinos through the capture on ${}^{37}\text{Cl}$ (see Section 1.5.1) [3, 4] following a study of Luiz Alvarez [29] developed from the original proposal for neutrino detection suggested by Pontecorvo [30]. The primary purpose of the experiment was to test the hypothesis of fusion reactions in the Sun and thus testing the solar model that had been proposed [31].

As explained in their proposal, neutrinos were a natural test candidate, as their low interaction cross sections would permit them to quickly exit the Sun retaining their original energy.

The experiment was built in the Homestake mine, in South Dakota and in 1970

the first results were published [32]. These measurements clearly demonstrated that something was wrong either with the model of the Sun, or with Standard Model description of neutrinos, as they only measured one third of the predicted flux. This discrepancy became known as the "Solar Neutrino Problem". However, no independent verification of the Homestake measurements existed and thus it was possible that the problem was in the experiment itself. However, further experiments were set up (which will be described below), also demonstrating a clear deficit in the detected solar neutrino flux. The results of Homestake, and other solar neutrino experiments, together with the theoretical predictions, are shown in Figure 1.4.

In the following decades a series of experiments were built aiming to uncover the "Solar Neutrino Problem". In particular, the Kamiokande experiment [33], besides detecting solar neutrinos, was also able to detect atmospheric neutrinos coming from cosmic ray showers. In this case the neutrinos were produced from the decays of secondary and tertiary particles, which would result in a well predicted ratio of ν_μ and ν_e . However, the results, which were confirmed by the IMB experiment [34], showed a clear deficit of ν_μ .

The first unambiguous evidence of neutrino flavour disappearance was reported by Super-Kamiokande in 1998 through the observation of atmospheric neutrinos [35]. Having a much larger active volume (50 kt of H_2O), this experiment was able to gather high statistics while mapping the zenith angle distribution of the neutrino flux, which was dependent of the ratio of L/E . The results showed that the ratio of ν_μ and ν_e depended on the distance traveled by neutrinos. The neutrinos produced right above the detector have a considerably lower distance to travel than the neutrinos produced on the other side of the Earth. The results could be explained by the neutrino oscillation hypothesis (c.f. Section 1.2).

The resolution of the Solar Neutrino Problem came finally in 2001 and 2002 with the measurements of the *Sudbury Neutrino Observatory (SNO)* [14, 36]. Like Super-Kamiokande, SNO was also a water Čerenkov detector, but using D_2O instead of *light water* (H_2O). As a result SNO was able to measure not only the flux of ν_e , but also the flux in all active flavours ν_e, ν_μ and ν_τ . While the measurement of the ν_e flux was consistent with the solar neutrino flux measurement of Super-Kamiokande, the total neutrino flux measurement was consistent with the solar model predictions. This milestone marked the first detection of neutrino flavour appearance and the

solution to the Solar Neutrino Problem.

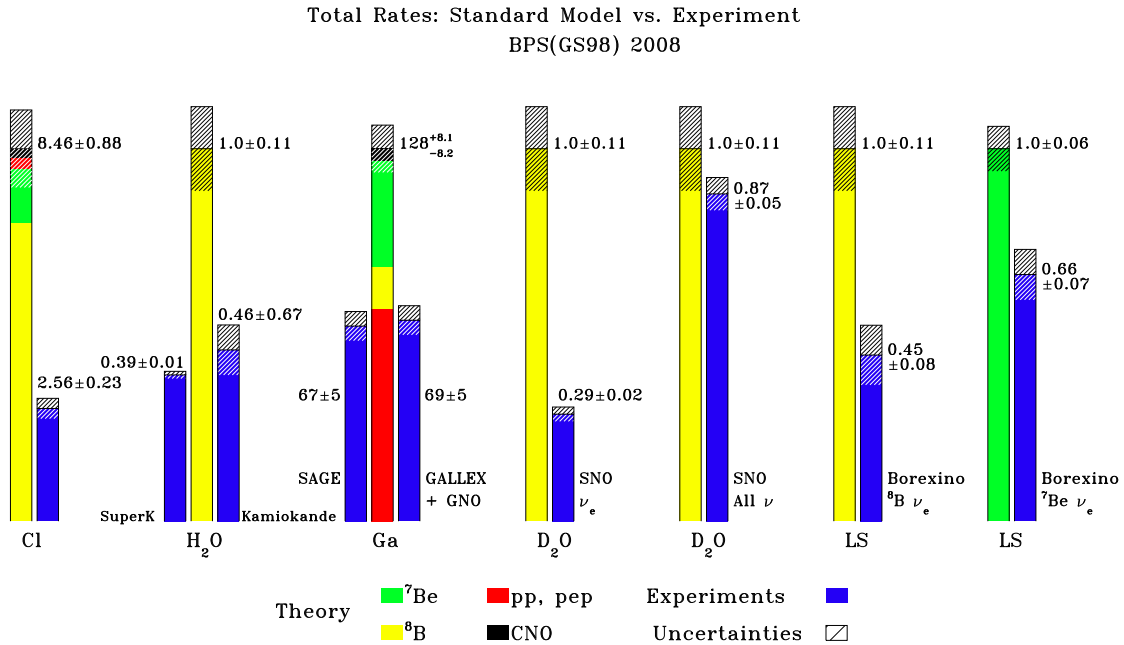


Figure 1.4: Comparison of solar neutrino results from seven experiments with the corresponding predictions from the SSM. The experiments have different thresholds, making them sensitive to solar neutrinos from different reactions, which are shown in different colours. The results from the radiochemical experiments are given in units of SNU, while the results from the other experiments are given as a fraction of the SSM prediction. Figure from [37].

In the following section a more detailed description of the different solar neutrino experiments will be presented.

1.5 Solar Neutrino Experiments

As described in the previous section, the detection of solar neutrinos, and the subsequent resolution of the Solar Neutrino Problem, was a process that involved several decades. Several experiments have tested SSM neutrino flux predictions by directly sampling various energy regions of the spectra shown in Figure 1.3.

In this section a summary of solar neutrino experiments will be presented along with its results and different technologies applied. Additionally, a description of the KamLAND reactor experiment will also be given. Despite being a reactor anti-neutrino experiment, their results are important in the context of neutrino oscillations, being strongly related with the solar neutrino experiments due to its sensitivity to the same oscillation parameters. The SNO experiment itself is also briefly discussed here and a more thorough description is given in Chapter 2.

1.5.1 Radiochemical Experiments

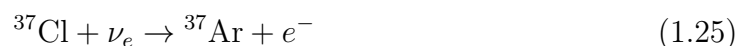
The first solar neutrino observations came from a radiochemical experiment (Homestake). The principle of operation of this type of experiment consists in having large volumes of a material containing a target nuclei that can be changed into some other nuclei by electron neutrino charged current interactions. The changed nuclei are later collected and counted through their radioactive decay and the number of neutrino-induced reactions is inferred from the extracted number of nuclei.

This type of experiments cannot retain any directional or time information, and the only information comes from the energy threshold of the nuclear capture reaction.

The Homestake Chlorine Experiment

The first detection of solar neutrinos was performed by Ray Davis Jr. in the ^{37}Cl radiochemical experiment [38]. This experiment consisted in a tank of 650 tons of C_2Cl_4 , located inside the Homestake gold mine in Lead, South Dakota.

Located 1870 m below the surface, with 4200 *meter water equivalent* (*m.w.e.*) of shielding from cosmic rays, the Homestake experiment could detect solar neutrinos through the *inverse β -decay* Cl-Ar reaction



which has a threshold of 814keV . Therefore, this experiment was only sensitive to ${}^7\text{Be}$, pep , ${}^8\text{B}$, and hep neutrinos. As the detection cross section increases with energy, the majority of the observed neutrinos came from the ${}^8\text{B}$ reaction.

The Ar daughter nuclei were extracted through chemical methods [38] with 90% efficiency, and the radioactive ${}^{37}\text{Ar}$ were then counted using small proportional counters which detected the Auger electron produced in the electron-capture of ${}^{37}\text{Ar}$.

The average solar neutrino rate measured was [38]:

$$R_{37\text{Cl}}^{exp} = 2.56 \pm 0.16(\text{stat.}) \pm 0.16(\text{syst.})\text{SNU} \quad (1.26)$$

while the theoretically predicted rate by the BS05(OP) solar model was of $R_{37\text{Cl}}^{exp} = 8.5 \pm 1.8\text{SNU}$, which is approximately three times the measured rate. The units are in *Solar Neutrino Unit (SNU)*, which correspond to 10^{-36} neutrino captures per target atom per second.

The Gallium Experiments

After the results of Homestake, a series of similar experiments were deployed using Gallium as the active medium.

There were three Gallium based solar neutrino experiments: GALLEX [39], GNO [40]⁴ and SAGE [41]. These experiments detected solar neutrinos in a similar way to Homestake through the reaction



which has a much lower energy threshold of 0.233MeV , permitting to detect neutrinos produced by all reactions. In these experiments the Germanium atoms produced by solar neutrino interactions are extracted through chemical processes and counted using proportional counters by observing the decay back to ${}^{71}\text{Ga}$.

⁴It is common to consider GALLEX and GNO as a single experiment, as GNO was a follow-up of GALLEX. Originally GALLEX ran from 1991 to 1997, being followed by GNO, which used the same detector, but improved extraction equipment.

Unlike Homestake, the low threshold makes pp neutrinos the major contribution to the observed rate. Thus these experiments were extremely important to the study of the solar models since the pp reaction is the first in the pp chain, being directly tied to the luminosity of the Sun.

The results reported by these experiments were [40–42]:

$$\begin{aligned} 77.5 \pm 6.2(\text{stat})_{-4.7}^{+4.3}(\text{syst}) \text{ SNU} & \quad (\text{GALLEX}) \\ 62.9_{-5.3}^{+5.5}(\text{stat}) \pm 2.5(\text{syst}) \text{ SNU} & \quad (\text{GNO}) \\ 69.1_{-4.2}^{+4.3} \text{ SNU.} & \quad (\text{SAGE}) \end{aligned}$$

The Standard Solar Model at the time (BP2000 [24]) predicted 128 ± 8 SNU, clearly in disagreement with the experiments.

A more recent combined measurement for the neutrino flux of all three Gallium experiments is 66.1 ± 3.1 SNU, where all statistical and systematic uncertainties have been combined [43]. In Figure 1.5 the results of the SAGE experiment, over the whole experiment run time from 1990 to 2007 are shown.

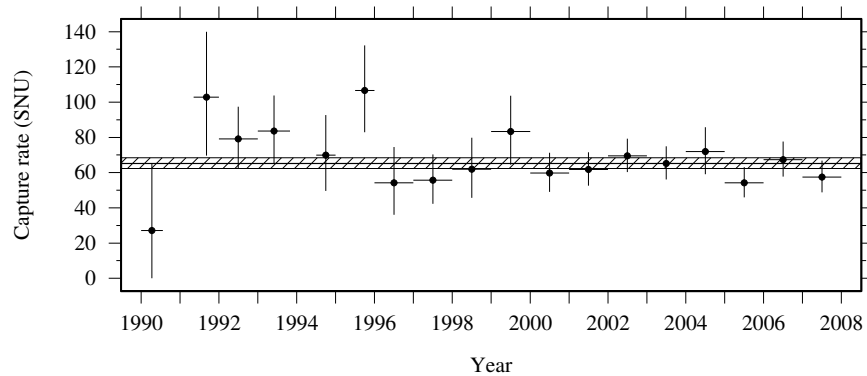


Figure 1.5: Results from the SAGE radiochemical experiment from 1990 to 2007. Figure from [41].

1.5.2 Light Water Čerenkov Experiments

Water Čerenkov experiments use large volumes of water surrounded by *photomultiplier tubes (PMTs)* light detectors to detect neutrino interactions in real time. When the ultra-relativistic leptons generated by the neutrino interactions pass with a velocity $v > c/n$ through a medium with a refractive index n , the lepton generates a cone of Čerenkov light around the direction of motion.

Water has a refractive index of $n \approx 1.33$, which means that the relativistic electrons will generate a cone of light with a half-opening angle of $\theta \approx 41^\circ$ [12]. For each cm of track, approximately 340 photons are generated, whose wavelengths range from 300 nm to 600 nm, and are collected by the PMTs. With a good discrimination of the arrival time of the photons at each PMT, it is possible to determine the origin of the interaction, the direction of the electron and its energy.

It is also important to note that these experiments operate at significantly higher energy thresholds than the radiochemical experiments because of backgrounds at low energy from naturally occurring radioactivity in the detector and its surroundings. This limits water Čerenkov experimental sensitivity to ^8B and *hep* neutrinos.

Super-Kamiokande

The Super-Kamiokande experiment was a much larger version of its predecessor KamiokaNDE, which was originally planned to observe proton decays, and later upgraded to observe solar neutrinos, being the first experiment to successfully detect ^8B solar neutrinos in real time [44].

Following the success of the Kamiokande experiment, the much larger Super-Kamiokande was built and continues to collect neutrino data from different sources [45]. Although Super-KamiokaNDE's first major result was regarding atmospheric neutrinos [35, 46], the detector also has substantial sensitivity to solar neutrinos, being also used as the far detector for accelerator neutrinos in the *KEK to Kamioka (K2K)* experiment [47, 48] and, more recently, in the *Tokai to Kamioka (T2K)* experiment [49].

SK is a 50 kton water Čerenkov detector located in the Kamioka mine. The water volume is surrounded by 11 146 inward facing 50 cm diameter PMTs, which provided a coverage of 40%.

The experiment measured the solar neutrino flux through the elastic scattering reaction

$$\nu_x + e^- \rightarrow \nu_x + e^-, \quad (1.28)$$

which is mostly sensitive to electron neutrinos, due to available channels for the interaction. In the case of electron neutrinos, this reaction can occur both through W and Z exchanges, while for neutrinos of any other flavour this reaction can only occur through the Z exchange. The Feynman diagrams of the different channels of neutrino-electron elastic scattering are shown in Figure 1.6. The different interaction channels give the elastic scattering experiments some sensitivity to all neutrino flavours in the proportion $\phi_{\nu_e} + \frac{1}{6}(\phi_{\nu_\mu} + \phi_{\nu_\tau})$. However, in the presence of neutrino oscillations an experiment detecting events only through elastic scattering alone cannot perform a measurement of neither the total electron neutrino flux nor the total active neutrino flux (all flavours), as both the oscillation parameters and the fluxes are unknown.

The direction of the recoil electron of the *elastic scattering (ES)* interaction is strongly correlated with the direction of the incoming neutrino. This allows to distinguish solar neutrino events from the isotropic background by measuring the directional correlation of the recoil electron with the Sun.

The first phase of the experiment (SK-I), started in 1996 and ended in 2001. The data from the first 280 days of the experiment were analysed with an energy threshold of $E_e^{th} = 6.5 MeV$ and the remaining 1216 days were analysed with an energy threshold of $E_e^{th} = 5.0 MeV$ [50].

An accident in 2001 destroyed approximately half of the PMTs. The experiment redistributed the remaining PMTs and started their second phase (SK-II), which ran from December 2002 to October 2005. However, even after the redistribution of the PMTs, the coverage was reduced to 19% [51]. Due to the low coverage, the uncertainties were considerably higher, resulting in an analysis with a higher energy threshold ($E_e^{th} = 7.0 MeV$).

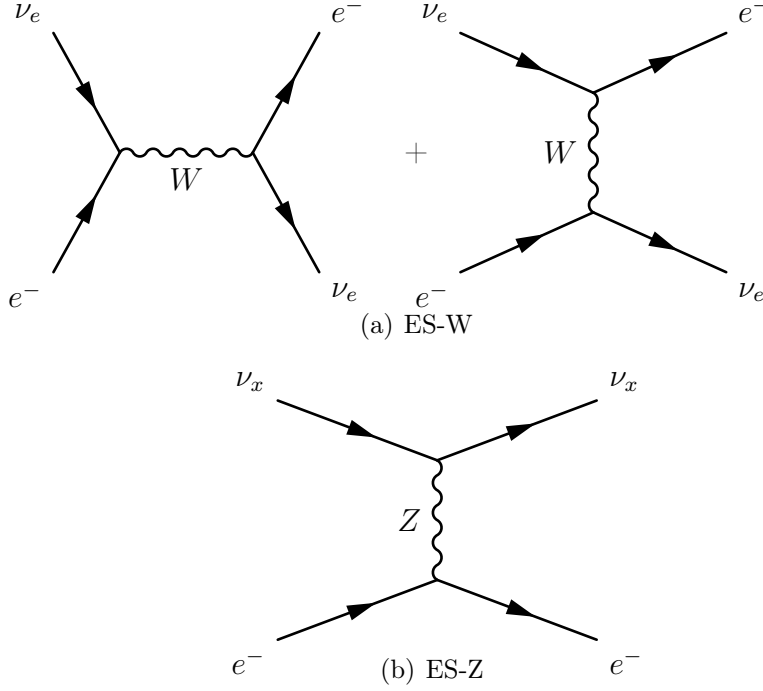
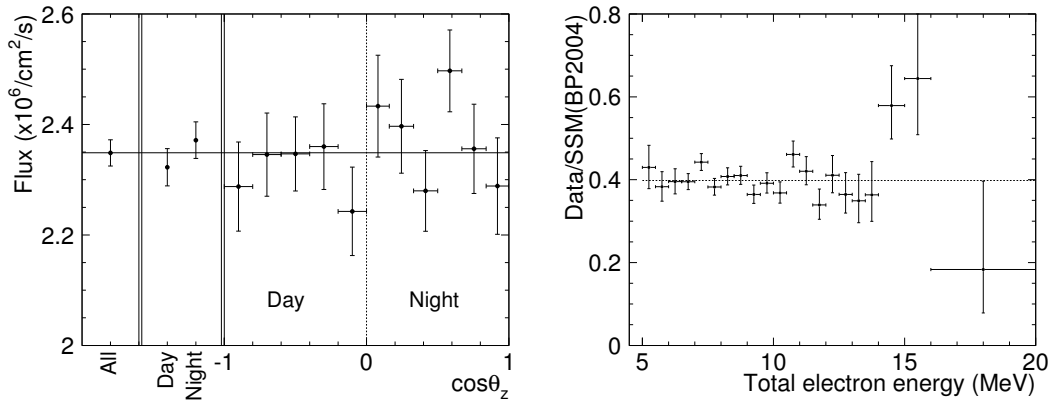


Figure 1.6: Feynman diagrams of the neutrino-electron elastic scattering interactions. While being the only detection method of the Super-Kamiokande experiment, SNO also detects events through these interactions, but with low statistics due to the considerably smaller size of its volume.

At the end of SK-II, the lost PMTs were replaced, restoring the total coverage to 40%, and starting the third phase of the experiment (SK-III), which ran from October 2006 until August 2008. The analysis methods were also improved in this phase, with better simulations and calibrations that allowed to achieve more accurate results than any of the previous phases with an energy threshold of $E_e^{th} = 5.0 \text{ MeV}$, even though the running period was smaller.

The results released by the SK Collaboration from the three phases, SK-I and SK-II and SK-III, with measured solar neutrino fluxes of [51–53]:

$$\begin{aligned} \Phi_{ES} &= 2.35 \pm 0.02(\text{stat}) \pm 0.08(\text{syst}) \times 10^6 \text{ cm}^{-2} \text{ s}^{-1} && \text{(SK-I)} \\ \Phi_{ES} &= 2.38 \pm 0.05(\text{stat})_{-0.15}^{+0.16}(\text{syst}) \times 10^6 \text{ cm}^{-2} \text{ s}^{-1} && \text{(SK-II)} \\ \Phi_{ES} &= 2.32 \pm 0.04(\text{stat}) \pm 0.05(\text{syst}) \times 10^6 \text{ cm}^{-2} \text{ s}^{-1} && \text{(SK-III)} \end{aligned}$$



(a) SK-I flux measurement as according to different orientations towards the Sun. (b) SK-III energy spectrum as a fraction of the solar model prediction.

Figure 1.7: Results from the Super-Kamiokande experiment. Figure 1.7(a) shows the result of the measured flux and its separation in components taking into account different intervals of zenith angle. Figure 1.7(b) shows the flux result as a fraction of the solar model prediction and as a function of total electron energy. Figures from [52, 53].

which are far below the predictions of the solar models [26]. Figure 1.7 shows the results from two phases of SK. The experiment is now in its fourth phase (SK-IV), after upgrading the electronics, expecting to further improve their neutrino measurements, both on atmospheric, accelerator and solar neutrinos.

1.5.3 Liquid Scintillator Experiments

Liquid Scintillator (LS) experiments are also designed to detect solar neutrinos in real time, but, unlike Čerenkov detectors, their event detection is based on the scintillation light generated by the ionisation of the active medium, allowing to reach lower energies than what is possible with Čerenkov detection. This opens the possibility to reach low enough energies to probe in the regions dominated by the much more intense ${}^7\text{Be}$ neutrino fluxes. However, to reach these low energies, some tradeoffs had to be made.

The LS experiments observe solar neutrinos through the ES of electrons by incoming neutrinos. However, unlike Čerenkov light, the scintillator does not provide any directional information, which makes background rejection much more difficult.

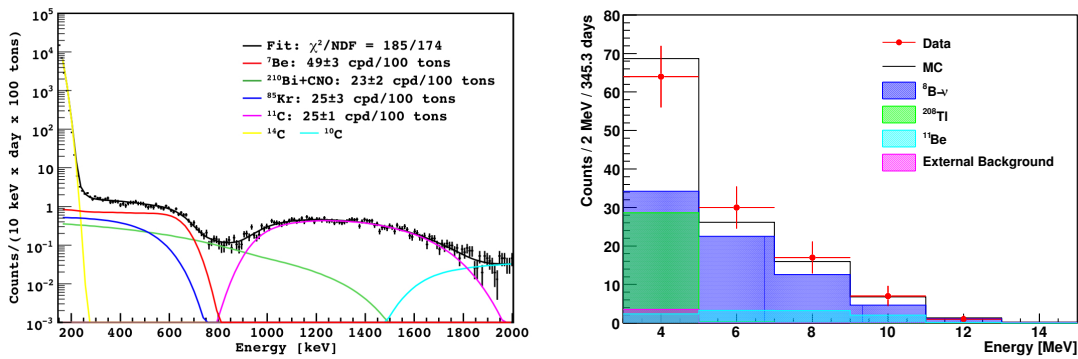
In order to reach low energy ranges of ~ 1 MeV, it is necessary to achieve extremely high levels of radio-purity of the order of 10^{-16} g(U,Th)/g(medium) .

Borexino

The Borexino experiment is currently the only solar neutrino experiment of this type in operation [54] being designed primarily to observe ${}^7\text{Be}$ neutrinos.

The detector is composed by a spherical inner target volume of 300 tons of pseudocumene with 1.5 g/L of PPO mixed in as a fluor. Encased in a thin nylon vessel, the scintillator is suspended in a larger sphere of buffer liquid (pseudocumene with a scintillation quencher), surrounded by 2212 PMTs in a spherical, inward looking configuration. Of these, 1828 have light concentrators to increase the effective photocathode coverage.

In Figure 1.8 the latest results of the experiment are shown. The Borexino collaboration successfully achieved to observe ${}^7\text{Be}$ neutrinos (Figure 1.8(a)) [55, 56], and also reported the observation of the higher energy ${}^8\text{B}$ neutrinos (Figure 1.8(b)) [57]. The latter observation, however, has very large uncertainties due to the low statistics.



(a) Energy spectrum in the ${}^7\text{Be}$ energy range. (b) Energy spectrum in the ${}^8\text{B}$ energy range.

Figure 1.8: Reconstructed energy spectra from the Borexino experiment in the energy ranges of ${}^7\text{Be}$ and ${}^8\text{B}$ energy ranges. Figures from [56, 57].

The 192 day result of Borexino shows an interaction rate of ${}^7\text{Be}$ neutrinos of $49 \pm 3(\text{stat}) \pm 4(\text{syst})$ counts per day per 100 tons which again is far below the unoscillated SSM prediction of 74 ± 4 counts per day per 100 tons.

KamLAND

The KamLAND experiment [58] is another liquid scintillator detector, but designed for a completely different purpose. Instead of searching for solar neutrinos, KamLAND detects antineutrinos produced by nuclear reactors in Japan and neighbouring areas, with an average baseline of 180 km. The L/E ratio for reactor antineutrinos over this baseline gives KamLAND sensitivity to the same range of mixing parameters observed in the solar experiments. This provides a valuable crosscheck, and complementary measurements to the solar results, as this experiment is looking into a completely independent source of neutrinos, its measurements being independent of the solar model.

The detector is located in the original Kamiokande detector hall, and is comprised of 1 kton of liquid scintillator (80% dodecane, 20% pseudocumene, and 1.52 g/L of PPO). Antineutrinos interact with hydrogen in the detector through the inverse beta decay process



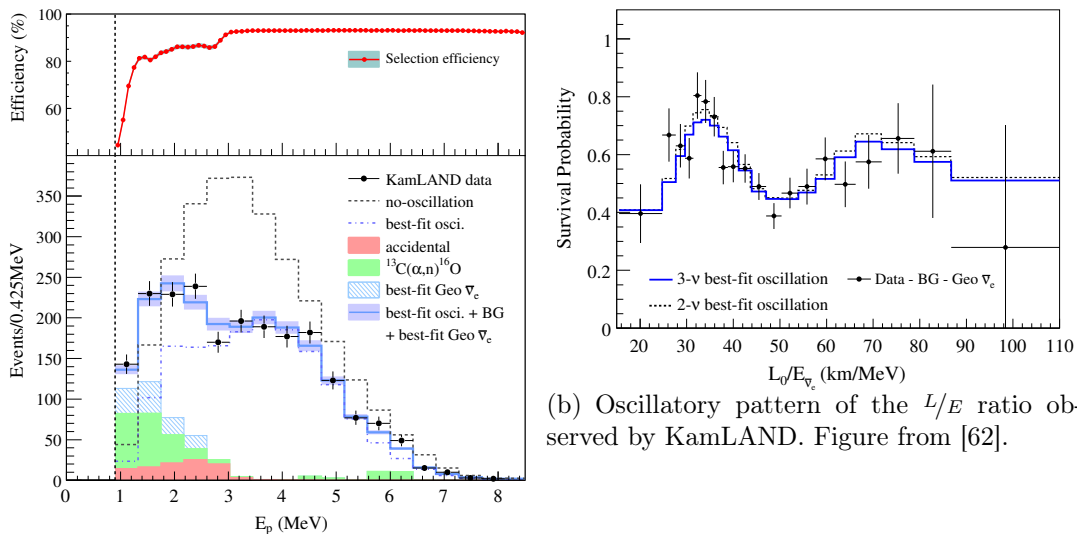
the same reaction used to first discover neutrinos. The prompt positron annihilation followed by a delayed neutron capture provides a coincidence signal with high background rejection. Both signals are observed in the scintillator by a total of 1879 PMTs.

The outgoing positron energy is strongly correlated with the incoming neutrino energy. Unlike the solar neutrino experiments, where the sensitivity lies, as we will see, mostly in the θ_{12} mixing angle, the KamLAND experiment is mostly sensitive to the Δm_{21}^2 parameter due to its much better known ratio of L/E . In fact, the KamLAND experiment was able to observe the oscillation pattern of this ratio [59], which is shown in Figure 1.9(b).

Combining the observations with the solar neutrino experimental results is a straightforward operation as both types of experiments are independent of each other, providing nearly orthogonal constraints on the mixing parameters. This allows to

combine the good sensitivity of the solar neutrino experiments on the parameter $\tan^2 \theta_{12}$ to the high sensitivity of KamLAND on the parameter Δm_{21}^2 .

In Figure 1.9 two major results from this experiment are shown [59–62]. Figure 1.9(b) shows the oscillatory pattern observed by the KamLAND experiment, while Figure 1.9(a) shows the observed energy spectrum of antineutrino events, together with the non-oscillated prediction.



(a) Reconstructed energy spectrum of events observed by KamLAND. Figure from [62].

(b) Oscillatory pattern of the L/E ratio observed by KamLAND. Figure from [62].

Figure 1.9: Latest results from the KamLAND experiment [62].

1.5.4 The SNO Experiment

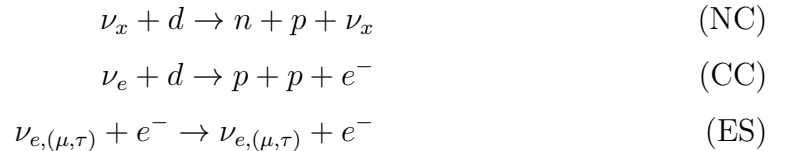
The experiments discussed previously, while providing valuable information to the solar neutrino picture, always incorporated an uncertainty that limited the physical interpretation of the results: the solar model itself. Although the consistent neutrino flux deficit observed by all experiments, none of those could actually make a statement about the actual neutrino flux coming from the Sun.

It was strongly suggested that an explanation of this deficit lies in physics beyond the standard electroweak model (*e.g.* oscillations) rather than new solar models or systematic problems with the experiments. In order to undoubtedly solve the

Solar Neutrino Problem, and confirm the hypothesis of new physics, an independent measurement of the total neutrino flux was necessary.

The radiochemical experiments mentioned above were sensitive only to electron neutrinos. The light water Čerenkov experiments (Kamiokande and Super-Kamiokande) had additional sensitivity to other active neutrino flavours (ν_μ, ν_τ) through the neutral current component to neutrino-electron elastic scattering. However, this sensitivity was weak, as the cross section for the Z channel is weaker in the order of ν_e ($\sigma_{\nu_e} \sim 6\sigma_{\nu_\mu, \nu_\tau}$). Furthermore, the NC interactions could not be separated by the dominant CC interactions. Without additional information on flavour content of solar neutrinos, a direct determination of whether the neutrino deficit was due to a simple suppression (fewer ν_e 's produced in the Sun or $\nu_e \rightarrow \nu_e$ oscillations) or active flavour neutrino oscillations ($\nu_e \rightarrow \nu_\mu, \nu_\tau$) remained inconclusive.

In 1985, Herb Chen further stressed this point and also provided a possible solution [63]⁵. Chen pointed out that a *heavy water* (D₂O) Čerenkov detector would be able to detect neutrinos through CC and NC reactions independently, besides the ES interaction:



with $\nu_x \equiv (\nu_e, \nu_\mu, \nu_\tau)$. The Feynman diagrams of the CC and NC interactions are shown in Figure 1.10.

SNO is a water Čerenkov detector which uses 1 kt of D₂O as the interaction and detection medium. The detector is located near Sudbury, Ontario, Canada at the 6800 ft level (2072 m) of an active nickel mine operated by Vale Canada Limited. SNO is the deepest solar neutrino experiment, with more than 6000 m.w.e. of overburden limiting the rate of cosmic ray components to less than 80 muons per day. More details about the detector will be given in Chapter 2.

⁵The paper by Herb Chen already includes contributions obtained through collaborative discussions with the newly founded Sudbury Neutrino Observatory collaboration.

As originally suggested by H. Chen, SNO could detect neutrinos through three types of interactions:

The NC breakup of the deuteron is independent of neutrino flavour, producing a neutron that then thermalises and is subsequently detected. This means that the observed NC rate would give a measurement of the total solar neutrino flux that was unaffected by oscillations.

On the other hand, at solar neutrino energies the CC interaction of neutrinos on deuterium results in an electron that would be detected through its Čerenkov light. This interaction would be only sensitive to ν_e , meaning that in the same detector it would be possible to measure simultaneously the flux of electron flavoured neutrinos and the flux of all types of neutrinos.

This idea was further developed in the following years, resulting in the construction of the *Sudbury Neutrino Observatory (SNO)*.

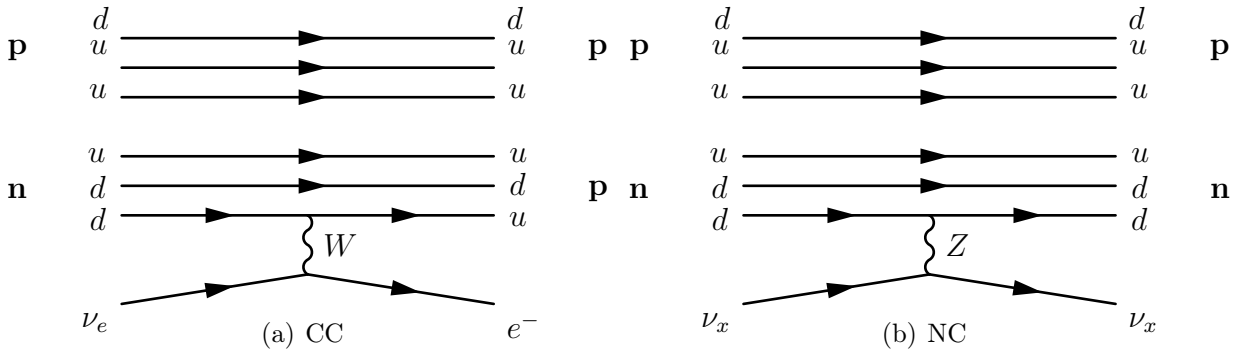


Figure 1.10: Feynman diagrams of the CC and NC interactions that occur in SNO. The ES interactions shown in Figure 1.6 also occur in SNO, but with a much lower probability.

In the ES reaction, neutrinos scatter with electrons in the water volume producing relativistic electrons that are detected through Čerenkov light. This reaction corresponds to the same method of detection used by SK, which allows for a direct comparison of the results. However, due to the smaller fiducial volume of SNO, this detection method suffers from low statistics.

In addition to the ES interaction with electrons, neutrinos interact with deuterons through two different reactions. As explained before, the CC reaction only occurs for electron neutrinos with energy greater than 1.44 MeV. The electron direction is slightly forward/backward asymmetric having a $1 - 0.340 \cos \theta_{e\nu}$ angular distribution,

where $\theta_{e\nu}$ is the angle between the incident neutrino direction and the initial direction of the electron. The energy of CC electrons is much more closely related to the neutrino energy than the ES reaction that has an almost flat distribution in energy up to the kinematic limit.

Also, neutrinos can also break up the deuteron through the neutral current reaction which occurs at the same rate independent of neutrino flavour. The threshold for the NC reaction is 2.2 MeV. In contrast to the ES and CC reactions, the NC reaction results in a free neutron and the subsequent signal does not provide any angular or energy information (aside from the production threshold).

The SNO experiment took data in three phases, distinguished by the method used to detect the neutrons from the NC reactions: pure D₂O, D₂O loaded with two tonnes of NaCl and a set of ³He proportional counters (NCDs). More details about the three phases and further details about the SNO detector are given in Chapter 2.

The SNO Collaboration has already confirmed the hypothesis of neutrino oscillation with the simultaneous measurement of the CC and NC fluxes, in the form of the $^{CC}/^{NC}$ ratio [14, 36, 64]:

$$\frac{\Phi(\nu_e)}{\Phi(\nu_x)} \approx \frac{\Phi(CC)}{\Phi(NC)} = 0.34 \pm 0.023(\text{stat})_{-0.031}^{+0.029}(\text{syst}), \quad (1.30)$$

which proves the conversion of ν_e 's into $\nu_{\mu,\tau}$'s as solar neutrinos travel from different regions of the Sun to the various detectors on Earth, while the NC flux agrees with the SSM predicted flux:

$$\Phi(NC) = 5.54_{-0.31}^{+0.33}(\text{stat})_{-0.34}^{+0.36}(\text{syst}) \times 10^6 \text{ cm}^{-2} \text{ s}^{-1}. \quad (1.31)$$

Figure 1.11 shows the relation between the different fluxes observed by SNO as well as the solar model prediction (dashed lines), which can be confirmed to agree quite well with the total flux measurement of SNO.

After providing a major contribution to the resolution of the Solar Neutrino Problem, the SNO experiment proceeded to re-analyse their data, entering a period of precision physics.

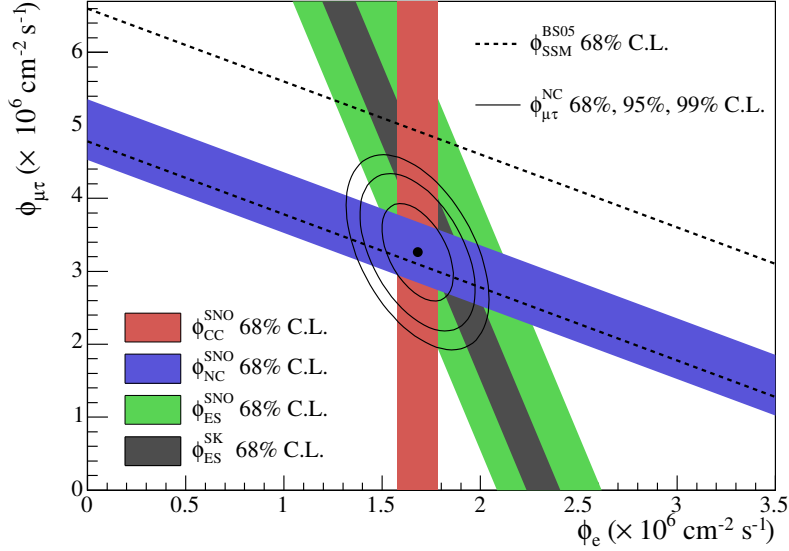


Figure 1.11: Solar neutrino flux measurements of SNO. The CC, NC and ES measurements are shown in the filled bands. The total ^8B solar model prediction is also shown as dashed lines. The point represents the measurement of SNO of ϕ_e , through the CC flux, and $\phi_{\mu,\tau}$ from the difference of NC-CC. Figure from [65].

1.5.5 Present Status of Solar Neutrino Physics

The considerable diversity of solar neutrino experiments is a fundamental tool to understand the underlying physics of neutrinos. All these experiments can be combined to produce a best estimate of the solar neutrino mixing parameters. The independent measurement of the total ^8B solar neutrino flux performed by SNO, allowed a deeper study of neutrino oscillations. This led to the observation that, unlike in the *Cabibbo-Kobayashi-Maskawa (CKM)* matrix, the PMNS matrix is not characterised by small mixing angles, but rather by large mixing angles contradicting, once again, the best bet of many theories. Figure 1.12 shows how the knowledge of the neutrino oscillations evolved in the solar sector until the results from SNO.

Furthermore, the excellent agreement between the oscillation parameters obtained with solar and terrestrial neutrinos [59, 65, 67–69] reflects the great success of the neutrino oscillation experiments. This agreement is shown in Figure 1.13, where contours of the allowed values of neutrino oscillation parameters relevant in the context

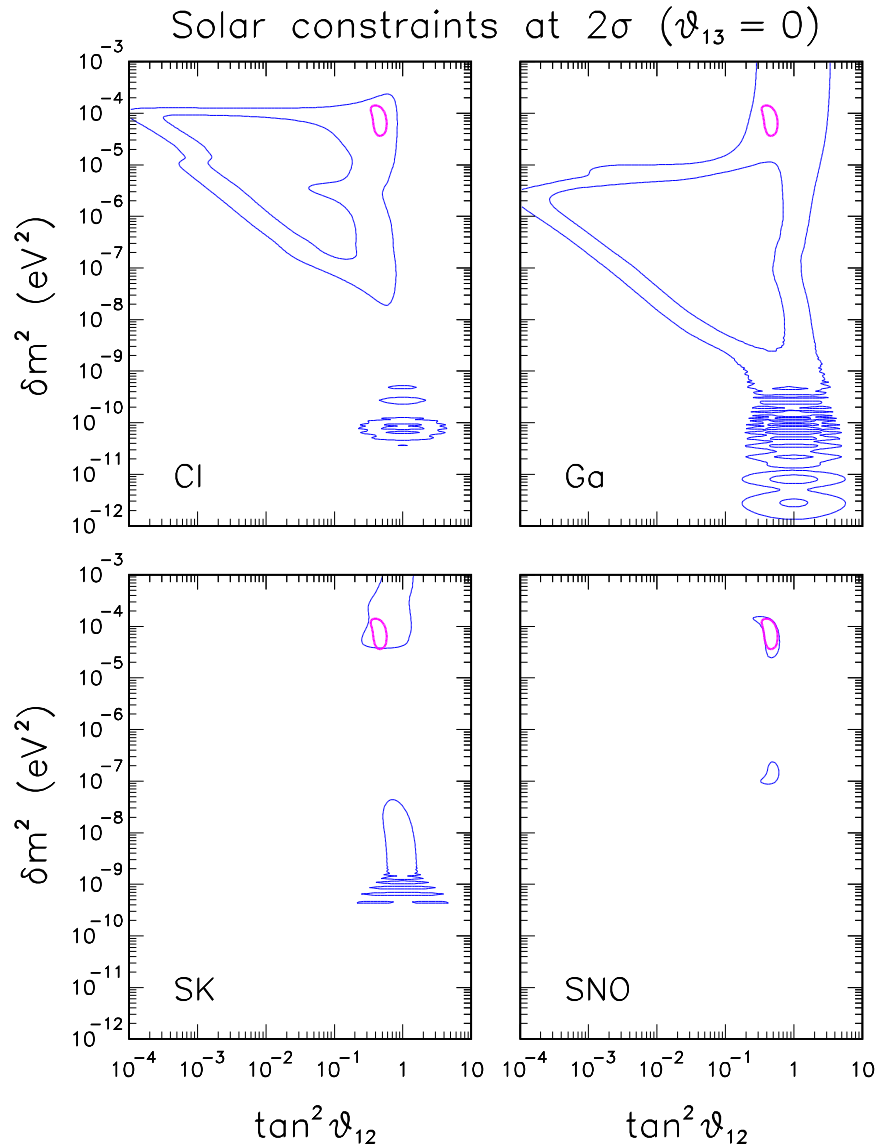


Figure 1.12: The evolution of the constrain on solar neutrino oscillation parameters as of 2006. Since then, more experiments have contributed to the knowledge, entering a phase of precision measurements. Figure from [66].

of solar neutrinos are shown from a combined analysis from all solar neutrino experiments, and compared to the corresponding contours obtained by the KamLAND experiment. This analysis was performed with an effective 2ν oscillation model (two-flavour), where the effects from θ_{13} , Δm_{31}^2 and the CP violating phase δ are ignored (2ν analysis). As it is possible to observe, the agreement is good with an overlap of the 68.30% confidence regions. The figure shows the only allowed region, which is

called the *Large Mixing Angle (LMA)* region.

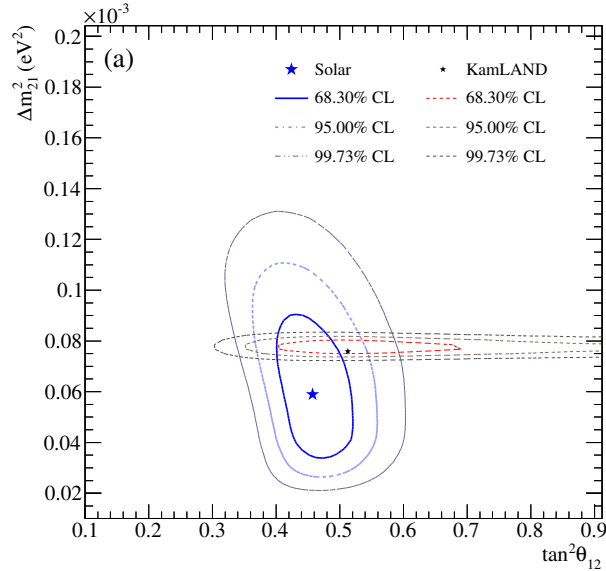


Figure 1.13: Global analysis of all solar neutrino experimental results as of 2009 in a two-flavour framework. The result from the KamLAND experiment is also shown. Figure from [70].

Figure 1.13 is depicting that by introducing the θ_{13} parameter to the fit for a 3ν oscillation model (three-flavour), the agreement between the solar neutrino experiments and the reactor experiment KamLAND improved, which could imply a non-vanishing θ_{13} mixing angle. However the uncertainties are yet very large [67, 68, 70].

In Table 1.3 the present knowledge on the neutrino oscillations is compiled in terms of the values and uncertainties of all neutrino mixing parameters. The Majorana phases are not shown since there is no data to constrain those phases at the moment.

1.6 Motivation and Scope of this Thesis

At this point, considering the numerous results from solar neutrino experiments, there is little doubt that neutrinos do experience flavour oscillations. However, like in many fields, the solution to a problem opens several doors to new challenges.

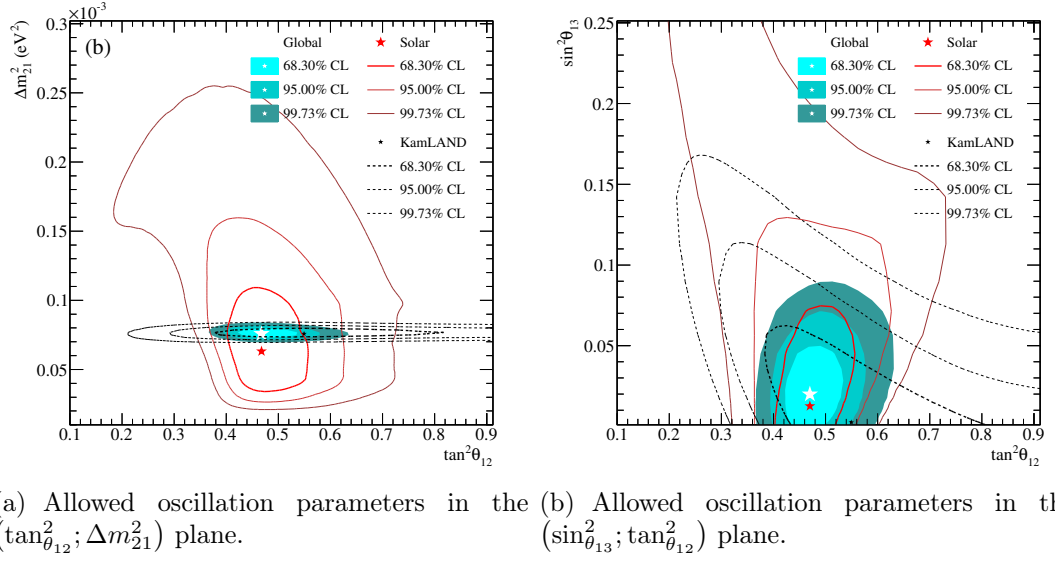


Figure 1.14: Allowed values of the oscillation parameters from a global three-flavour analysis combining all solar neutrino experiments and the KamLAND results. Figure from [70].

$$\begin{aligned} \Delta m_{21}^2 &= 7.59 \pm 0.20 \left(\begin{smallmatrix} +0.61 \\ -0.69 \end{smallmatrix} \right) \times 10^{-5} eV^2 \\ \Delta m_{31}^2 &= \begin{cases} -2.36 \pm 0.11 (\pm 0.37) \times 10^{-3} eV^2 & \text{(Inverted Hierarchy)} \\ +2.46 \pm 0.12 (\pm 0.37) \times 10^{-3} eV^2 & \text{(Normal Hierarchy)} \end{cases} \\ \theta_{12} &= 34.4 \pm 1.0 \left(\begin{smallmatrix} +3.2 \\ -2.9 \end{smallmatrix} \right)^\circ \\ \theta_{23} &= 42.8 \begin{smallmatrix} +4.7 \\ -2.9 \end{smallmatrix} \left(\begin{smallmatrix} +10.7 \\ -7.3 \end{smallmatrix} \right)^\circ \\ \theta_{13} &= 5.6 \begin{smallmatrix} +3.0 \\ -2.7 \end{smallmatrix} (\leq 12.5)^\circ \\ \delta_{CP} &\in [0, 360]^\circ \end{aligned}$$

Table 1.3: Present limits on the neutrino oscillation parameters from analysing all available neutrino data. Values from [67].

The anticorrelation (or "tension") observed in the allowed values of the mixing angles when comparing the results from solar neutrino experiments and the KamLAND experiment lead to a hint that the presently unknown mixing angle θ_{13} might be non-minimal [67, 68, 71]. This is indeed a very interesting prospect as any chance

of measuring the CP violating phase is dependent on the scale of the θ_{13} mixing parameter⁶. At present, attempts of measuring this parameter haven't been able to set strong constraints to it [67, 72, 73]. In order to validate the *tension* suggested from this combined analysis, it is necessary to ensure that the details of each experiment are correctly combined with the data from all other experiments. Furthermore, in both cases the effect of θ_{13} is a second-order effect, strongly dependent on the mixing angle θ_{12} . Thus, a precision measurement of θ_{12} would allow to further constrain the θ_{13} mixing angle, and to further test the statistical significance of the results presented in Figure 1.14.

Besides this immediate benefit from a precise measurement of the solar neutrino oscillation parameters there is another, more fundamental, motivation. SNO terminated its data taking by the end of 2006, after six successful years of operation. The current precision in the determination of the θ_{12} mixing angle is due mostly to SNO, as shown in Figure 1.12, and there is only one experiment that has the potential to further improve this precision: its successor experiment SNO+ [74]. However it is not yet clear that SNO+, looking into solar neutrinos from the *pep* reaction, will be able to improve significantly over the current precision⁷. It is thus very important that the SNO data should be analysed to extract the most information for neutrino physics.

Besides the most immediate motivations concerning the solar neutrino picture, there is also a more general reason to reach the most precise measurements of the solar neutrino mixing parameters.

The neutrino mixing angles are fundamental parameters in the SM, and their precise determination can provide new light into fundamental new physics. One of the peculiarities of the PMNS mixing matrix is how different it is from its analog CKM matrix in the quark sector. The quark flavour number is only weakly broken, resulting into an almost diagonal matrix. In the neutrino sector, however, the mixing is maximal for one angle (θ_{23}) and almost maximal for another (θ_{12}), while the third is known to be small, albeit not exactly how much (θ_{13}); resulting in large non-diagonal

⁶In the expression for the survival probability all terms with δ_{CP} appear with a $\sin^2 2\theta_{13}$ factor.

⁷It should be noted that SNO+, by probing the neutrino energy region where the transition between matter enhanced oscillations takes over the pure vacuum oscillations, opens the possibility for new physics searches.

matrix terms.

This effect has been pointed out to be very close to the product of a $\pi/4$ rotation matrix with a $\pi/5$ rotation matrix [75]. This mixing matrix is known as *Tri-Bimaximal Mixing (TBM)* matrix and has the form

$$|U^{TBM}| = \begin{pmatrix} \sqrt{\frac{2}{3}} & \sqrt{\frac{1}{3}} & 0 \\ \sqrt{\frac{1}{6}} & \sqrt{\frac{1}{3}} & \sqrt{\frac{1}{2}} \\ \sqrt{\frac{1}{6}} & \sqrt{\frac{1}{3}} & \sqrt{\frac{1}{2}} \end{pmatrix}. \quad (1.32)$$

These values are consistent at the 90% C.L. with the present values of the PMNS mixing matrix.

While there is some scepticism concerning these symmetry models, their specific form may provide some information about the underlying physics of neutrinos. The TBM model has been found to have relations to group theory [76], explaining the small mixing observed in quarks. Furthermore, working upon this model, it has been shown that if the PMNS and the CKM matrices are equal at the *Grand Unified Theory (GUT)* scales, it is possible that these matrices diverge at low energy under the assumption that neutrinos have Majorana masses and are quasi-degenerate [77, 78]. In this framework, the CKM matrix can be used to estimate the value of the mixing angles. In particular, following the previous assumptions, it is estimated the neutrino mixing angle θ_{13} to be in the range $\approx 3.5^\circ$ to 10° .

Besides this particular model, a plethora of variations have been developed, each one providing predictions for the exact values of the mixing angles. Figure 1.15 shows a list of the predicted θ_{12} and θ_{13} , as well as the current limits from experimental data [79].

It is clear that from the increasing amount of models, new experimental input is necessary. In particular, it is interesting to note that these models predict very specific values for the mixing parameters, which means that by improving the precision on the current experimental data, it would be possible to directly test them.

This thesis was developed in the context of the very final analysis of the SNO data. In this analysis, all neutrino data taken by the SNO experiment will be analysed

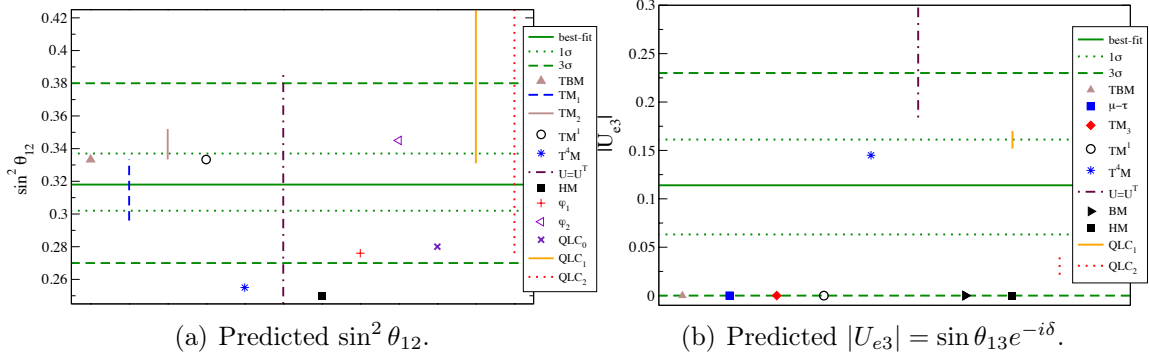


Figure 1.15: Predicted values for the mixing parameters $\sin^2 \theta_{12}$ and $|U_{e3}|$. For some models, the mixing parameters depend on each other, for which the allowed 3σ region is shown. Figures from [79].

as a single data set, which spans over six years of operation of the experiment and accounts for more than three years of live-time. As it will be explained in Chapter 2, combining the considerably different phases of the SNO experiment won't be an easy feat, and analysing the data in the context of neutrino oscillations together with the input from all other solar neutrino experiments will pose a major challenge, as there are a large amount of particularities that have to be correctly addressed in order to deal with the correlations between all experiments and particularly between all the systematic uncertainties of all the phases of SNO.

Chapter 2

The SNO Detector

The *Sudbury Neutrino Observatory (SNO)* experiment consisted of a one kiloton D₂O Čerenkov detector, located in Vale Canada Limited's Creighton mine near Sudbury, Ontario, Canada.

The detector was constructed after the initial idea of Herb Chen in 1985 [63], aiming to solve the so called Solar Neutrino Problem. Its unique design allowed neutrinos to be detected by three different types of interactions, of which one was insensitive to the neutrino flavour, providing a measurement of the total ⁸B solar neutrino flux independent of neutrino mixing. Conversely, since another reaction measured only the ν_e component, a test of neutrino mixing could be performed independently of the solar models by comparing both SNO measurements.

In this Chapter the structure and principles of operation of the SNO detector will be detailed, providing the necessary background for the work of this thesis discussed in later Chapters.

2.1 Structure of the Detector

The centre of the SNO detector is located at 2092 m underground, corresponding to a rock overburden of 6010 m of water equivalent. With this much amount of shielding,

the detector had less than 80 cosmic ray muons passing every day. A schema of the detector is shown in Figure 2.1.

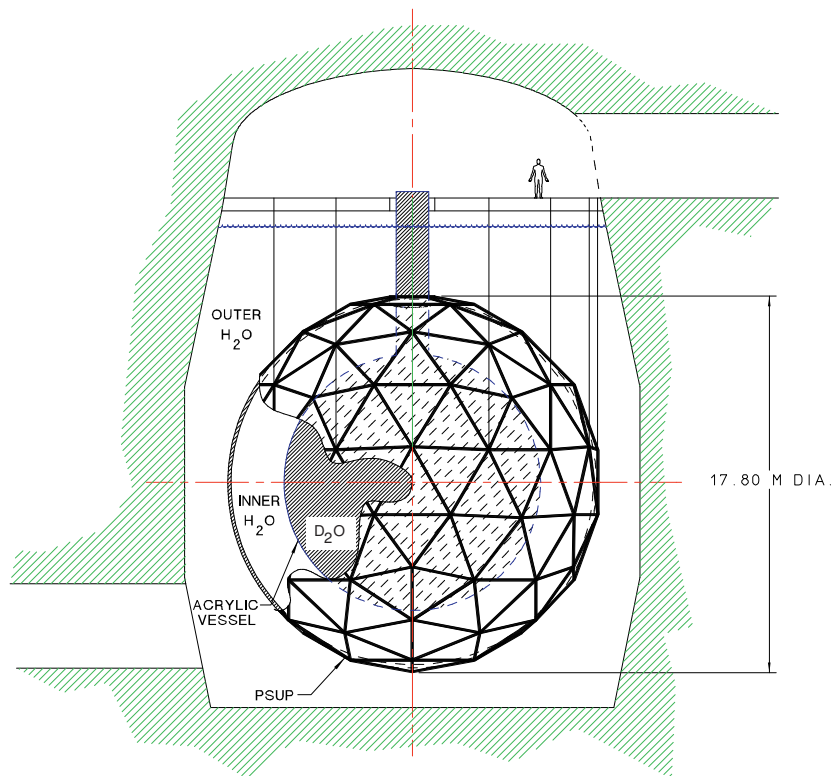


Figure 2.1: Schematic drawing of the SNO detector. Taken from [80].

The detector design consisted of two concentric spheres: the acrylic vessel, containing the *heavy water* (D_2O) volume was the active medium for neutrino interactions, and the geodesic structure to which the *photomultiplier tubes* (*PMTs*) are attached to detect the neutrino interactions in the active medium.

The active medium consists of 1000 tonnes of 99.92% ultra-pure D_2O , which is contained by the *acrylic vessel* (*AV*), an acrylic sphere of 12 m in diameter and 5.5 cm thick. The acrylic used was specifically designed for SNO, to reduce the ultraviolet absorption [80]. The AV is supported by ten loops of rope made of synthetic fibres that are attached to the deck structure on top of the detector. The ropes are attached

to the detector at ten specifically carved acrylic tiles distributed equidistantly around the detector equator.

The access to the D₂O volume is provided by a chimney (also identified as *neck*) of 1.46 m in diameter and 6.8 m height, which is made of the same acrylic as the rest of the vessel. This chimney was needed to fill the AV, to deploy calibration sources and the NCDs. The top of the chimney is attached to an airlock in the *deck clean room (DCR)*, from where the calibration sources are lowered into the D₂O volume. The DCR is the clean room on top of the detector where the instrumentation for the calibration sources is located, such as the optical calibration laser, and is the cleanest area in all the laboratory.

As mentioned before, surrounding the AV, there is a geodesic structure, the *PMT support structure (PSUP)*, where 9456 PMTs are supported, oriented towards the D₂O volume. The structure is composed by triangular panels of PMTs, which surround smaller hexagonal panels at each node of the geodesic structure. In each panel, the central PMT is pointed towards the detector centre.

The region outside the AV is filled with 7000 tonnes of ultra-pure H₂O (1700 tonnes between the AV and PSUP, and an additional 5300 tonnes between the PSUP and the cavity wall), providing a shield against the radioactivity from the instrumentation (PSUP and PMTs) and the surrounding rock.

The PMTs are the active detectors for the Čerenkov light produced by the neutrino interactions in the D₂O volume. These phototubes are Hamamatsu R1408, designed to provide high photon detection efficiency, high timing resolution ($RMS = 1.7ns$) and to minimise the intrinsic radioactivity. Each PMT was mounted in the PSUP with a light-concentrator of 26.9 cm in diameter to increase the photocathode coverage from 31% to a total 54% solid angle coverage. A schema of a PMT from SNO is shown in Figure 2.2.

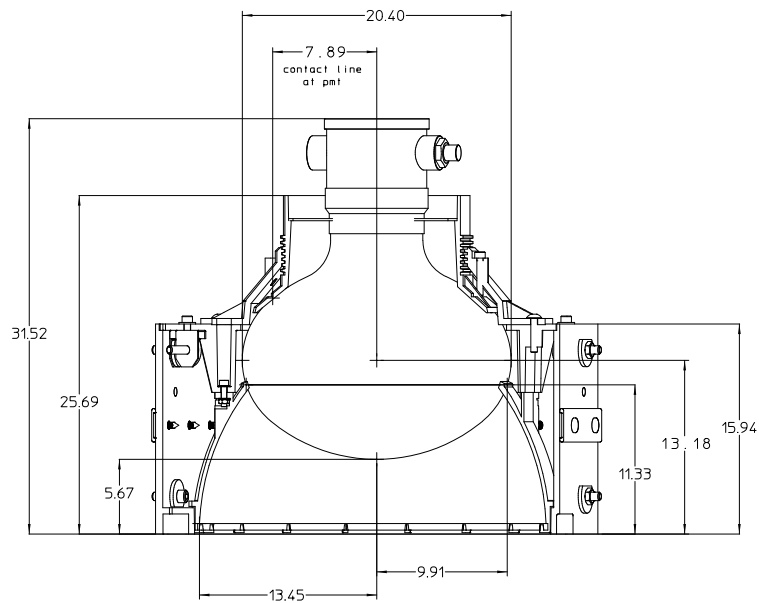


Figure 2.2: PMT schematic with dimensions (in cm). The light-concentrator housing is also shown. Figure from [80].

Besides the inward looking PMTs, an additional 91 outward looking PMTs are mounted on nodes of the geodesic structure of the PSUP acting as background vetoes. Another 23 inward-looking PMTs are arranged in a structure on top of the H₂O volume to detect cosmic rays. In the walls of the detector pit 14 magnetic compensation coils were mounted in order to cancel the vertical component of the Earth's magnetic field in order to increase the PMT detection efficiency by approximately 10% [80].

In the third and last phase of SNO, an array of ³He proportional counters, the *neutral current detectors (NCDs)*, was deployed in the AV to measure the total flux of solar neutrinos from NC events in the D₂O, independently of the PMTs. The NCD array consists of 36 strings filled with ³He to detect neutrons and 4 additional strings filled with ⁴He that, being insensitive to neutrons, were deployed to identify backgrounds, coming primarily from α particles. More details about these counters will be given in the following Sections. The technical details of the experiment are given in [81].

2.2 Principles of operation

Unlike other water Čerenkov detectors, SNO was specifically designed to detect solar neutrinos through different reactions, allowing an independent measurement of the total neutrino flux.

By replacing the hydrogen in the water molecule with deuterium, three reactions with solar neutrinos are possible:

$$\text{CC : } \quad \nu_e + d \rightarrow p + p + e^- \quad (Q = -1.44\text{MeV}) \quad (2.1)$$

$$\text{NC : } \quad \nu_x + d \rightarrow p + n + \nu_x \quad (Q = -2.2\text{MeV}) \quad (2.2)$$

$$\text{ES : } \quad \nu_x + e^- \rightarrow \nu_x + e^- \quad (2.3)$$

The first two interactions are named to correspond with the current carried by the charged W boson and the neutral Z boson, which mediate the processes.

The *charged current (CC)* interaction involves the exchange of a W boson. At the energy range of solar neutrinos, this reaction is exclusive to neutrinos of electron

flavour, since the neutrinos do not have enough energy to produce the other heavier charged leptons. As a result of this interaction, the down quark of a neutron is transformed into an up quark, resulting in the D_2O to break into two protons, while the neutrino is converted into an electron. This interaction has an energy threshold of 1.44 MeV. Only the electron is detected, and its energy is highly correlated with the energy of the incoming neutrino, such that it provides important information concerning the shape of the solar neutrino spectrum. However, the electron does carry some directional information [82] due to the V-A coupling of the W boson. Due to the large amount of low energy backgrounds the SNO analyses have higher energy thresholds, which means that SNO is only sensitive to the 8B neutrinos and the much less intense *hep* neutrinos.

The *neutral current (NC)* interaction is the unique detection signature of SNO. This interaction is mediated by a neutral Z boson, that equally couples with all three neutrino flavours ν_α with $\alpha = e, \mu, \tau$. Through this interaction, the deuteron is dissociated and the resulting free neutron is then detected. This reaction has an energy threshold of 2.224 MeV but, as the neutron is detected upon thermalisation, no information about the incoming neutrino energy and direction is retained. Being equally sensitive to all neutrino flavours, the events provide a direct measurement of the total solar 8B neutrino flux. It was due to this that SNO was able to test and confirm the predictions of the solar model, and infer that the Solar Neutrino Problem is due to neutrino mixing and flavour transitions. Unlike the CC and ES reactions, the NC interaction does not produce a relativistic charged particle and therefore it does not directly generate Čerenkov light. However, the free neutron can be detected in several ways. The experiment ran for a total live-time of 1054.29 ± 0.03 days, and was operated in three different configurations, henceforward called *phases*, each one employing a different neutron detection technique. The characteristics of each SNO phase are detailed below.

The *elastic scattering (ES)* interaction involves the bound electrons in the water molecule, and so is the only one of the three interactions in common with light water Čerenkov detectors. This interaction has a smaller cross-section than the first two, and is weakly sensitive to all neutrino flavours. Being dominated completely by kinematics, the direction of the recoil electron is highly correlated to the direction of the incoming neutrino, and therefore ES events are usually separated from the other

events by verifying the direction of the recoil electron with respect to the direction to the Sun. In SNO this interaction didn't play a special role due to the low event statistics.

The CC, NC and ES events are distinguished by having different distributions of observables, such as event energy, direction, position and isotropy. However, these differences are not enough to perform an event-by-event identification. Therefore, a statistical separation is used to obtain the total number of events in each class. This procedure will be described in more detail in Chapter 5.

2.2.1 Heavy Water Phase (Phase I)

The pure heavy water phase, also called the D₂O phase, is defined as the period of detector operation between November 1999 and May 2001, with a total of 300.4 live-time days. During this period the active volume consisted solely of D₂O, and the NC interactions were observed through the neutron capture on deuterium:



with the event detection being made through the mono-energetic γ of 6.25 MeV, generating Compton scattering electrons which were subsequently reconstructed through their Čerenkov radiation. This reaction has a cross section of 0.5 mb. The details and results of the data analysis in this phase are detailed in [14, 36].

2.2.2 Salt Phase (Phase II)

This phase of operation was from July 2001 to August 2003 for a total of 391.4 live-time days. During this period, 2 tons of NaCl ($\approx 0.2\%$ by mass) were added to the D₂O volume in order to increase the neutron detection efficiency through neutron capture on chlorine via the reaction



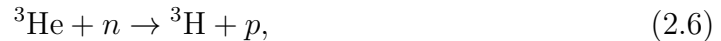
where n represents a cascade of multiple γ 's with a total energy of 8.6 MeV. This reaction has a neutron capture cross section of 44 b, which is much higher than the neutron capture cross section on deuterium.

During this phase, approximately 80% of the NC neutrons were detected. Furthermore, the Compton scattered electrons from the multiple γ rays are distributed more isotropically in the detector, which makes it easier to separate NC from the other neutrino interactions. Furthermore, the higher total energy released in the reaction permitted to make a precise measurement of the NC signal, well above the region of low energy backgrounds. The details of this phase are described in [64, 65].

2.2.3 Neutral Current Detector Phase (Phase III)

The *neutral current detector (NCD)* phase was the final operation phase of SNO as it spanned from December 2004 to November 2006 with a total of 385.2 live-time days. This phase was the most distinguishable from the other phases.

For this phase 36 ^3He proportional counters (NCDs) were installed inside the AV, after the removal of the salt. Four additional counters were installed, filled with ^4He , to provide background control. The neutrons produced by the NC interaction were captured through the reaction



producing a ^3H -proton pair that originated an electrical pulse in the anode wire of the NCD proportional chambers. This reaction has an even higher cross section (5330 b), having a very high neutron capture efficiency. Furthermore, by detecting the NC neutrons in the NCDs, the correlations with the other reactions are strongly reduced, providing a virtually independent detection method of NC events. Besides this obvious advantage, the NCDs also provided a neutron event count, something that was not possible in previous phases. More details about the NCDs are provided in Section 2.4.

2.3 The PMT System

The PMT system in SNO was the primary method for event detection, being used in all the three phases of the experiment. In this section a brief description of this detection system will be provided, as well as the associated electronics.

As explained previously, except for the NCD phase, the signals detected by SNO consisted of Čerenkov photons. The photons detected by the PMTs had a wavelength ranging from 300 to 620 nm, which means that the wavelength ranged from the visible to the ultraviolet. When a photon is produced in the D₂O volume, it also has to cross at least 5.5 cm of acrylic from the AV. Figure 2.3 shows the media transmissions, PMT quantum efficiency¹ and the emitted and observed Čerenkov spectra for a source at the centre of the detector [83].

After leaving the vessel, the photons cross the inner *light water* (H₂O) volume of about 3 m, reaching the PSUP. This structure contains 9456 inward looking PMTs with a radius of 20 cm, which would normally produce a photocathode coverage of 31%. However, the PMTs were mounted into a 27 cm reflective light concentrator, designed in the shape of a Winston cone [84] to provide optimal collection efficiency for light generated inside the D₂O volume, increasing the coverage to 54% [80]. An example of a SNO PMT/concentrator assembly is shown in Figure 2.2.

The PMTs are Hamamatsu R1408, which have a good charge amplification with a gain $> 10^7$. In terms of charge resolution the PMTs are characterised by a reasonable resolution with a peak-to-valley ratio of > 1.25 . Besides the charge, the PMT pulse timing is also one of the characteristics of interest having a short *photo-electron (PE)* transit time of 30 ns with a resolution of 1.7 ns.

The electronics were responsible for the measurement and storage of the charge and time information from the PMTs. In SNO electronics each PMT was connected to a channel by a coaxial cable which was responsible simultaneously for transmitting the signals and providing the high voltage supply. The channels are handled by *front end cards*, which are responsible for signal processing and digitisation.

¹In the context of SNO the term "quantum efficiency" is used to refer to the wavelength-dependent probability of registering a hit in a PMT.

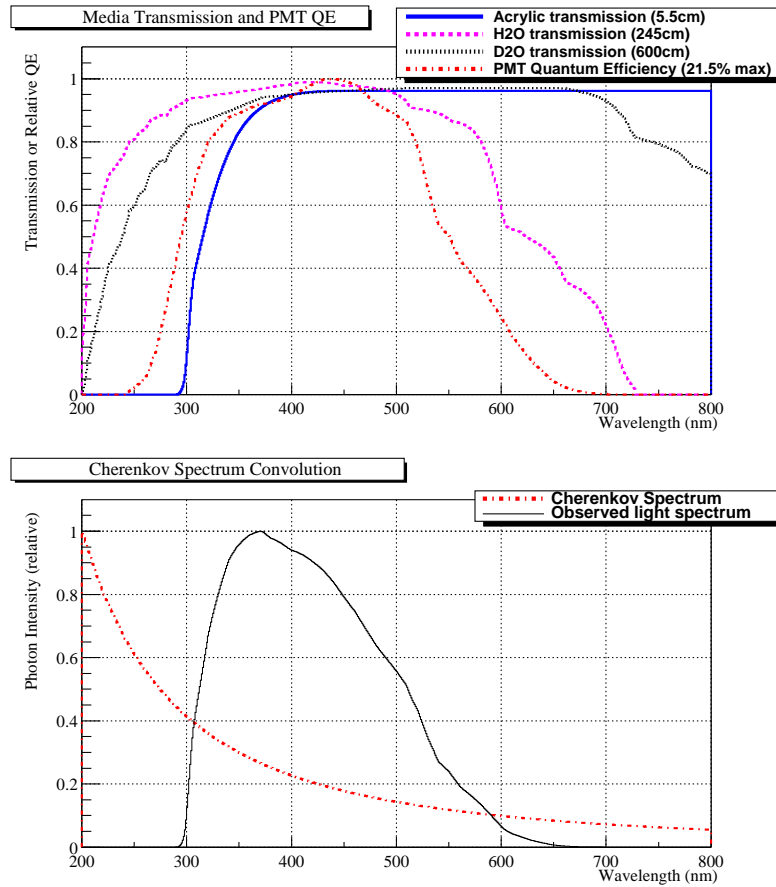


Figure 2.3: Čerenkov spectrum convolved with PMT quantum efficiency and media extinctions. Figure from [83].

Each time a signal was detected, individual discriminators determined if it crossed a given threshold. In case the discriminator fired, multiple types of trigger signals were generated. Based on these signals, the trigger system classified the event and determined if it should be stored on disk.

Several types of triggers existed for a wide variety of purposes [85]. For example, the *ESumHi* trigger recorded an analogue copy of the pulse from each PMT, summing the pulses gave the total charge deposited in the detector and served as an important diagnostic tool for non-physics backgrounds. For the physics analysis, the most important trigger was the *NHIT100* which identified events based on the number of channels that gave signal within a set time window. When a discriminator fired, a square pulse of 30 mV was generated, 93 ns wide and 2.5 ns rise time. These pulses were continuously summed over all channels and when 16 hits were detected within

the 93 ns window a global trigger was initiated. The *pulsed global trigger* was a fixed interval trigger, firing at a rate of 5 Hz providing a good measurement of the ambient noise in the detector. There were also external triggers which could be activated when using calibration sources, providing a good way to discriminate particular events.

The trigger pulses were summed separately over each crate (and each card). The summed signals were sent to a series of master trigger cards which performed a detector wide sum of the signals and verified if the trigger was flagged to be stored, initiating a *global trigger*. Once a global trigger was initiated, the integrated charge and time information for each hit PMT was read out by the *data acquisition system (DAQ)* system and stored on disk.

The time at which each PMT was fired was determined by a *time-to-amplitude converter*. Basically, a capacitor started ramping when a discriminator fired and stopped when the global trigger was received. If no global trigger was received after a fixed time interval, the time-to-amplitude converter was reset. This information was stored along with the integrated charge (digitised by the *analog-to-digital converters*), a *global trigger identification* and was used to assemble the individual hits from PMTs into events.

The trigger system had a very high efficiency. Using a threshold of 16 hits within a 100 ns time window, the NHIT100 trigger was 100% efficient at total energies of 4 MeV [86].

In principle the SNO detector could operate almost continuously, storing all the PMT data into a single data set. However, the events were grouped into time periods classified as *runs* and were typically adjusted to the type of data being acquired (calibration or neutrino data) and other constraints such as detector operation shifts. During the NCD phase each physics run had a duration of about 7 hours. Calibration runs, however, usually had shorter time periods. For example, an optical calibration run had an average duration of 15 minutes as the high intensity laser source allowed to collect enough statistics in a short time period.

2.4 The Neutral Current Detectors (NCD)

The *neutral current detectors (NCDs)* consisted of thirty-six strings of ^3He proportional counters aimed at an independent measurement of the ^8B solar neutrino flux. In addition to the ^3He counters, four additional strings were deployed, filled with ^4He to act as control counters. These were not sensitive to neutrons and were therefore used to characterise the non-neutron backgrounds in the array.

The NCDs were cylindrical in shape, having a radius of $R_{ncd} = 2.579$ cm and a length ranging from 9 to 11 m, depending on their specific location making up a total of 398 m of counter length. Figure 2.4 shows a diagram of a NCD string.

The NCD strings were composed of three or four individual gaseous proportional counters made of ultra-pure nickel welded together. The gas in the counters was a mixture of 85% ^3He (or ^4He for the control strings) and 15% of CF_4 , which generated a pressure of 2.5 atm.

The proportional counters that made up the NCD array operated by measuring the current pulse created on the anode wire by ionisation of the counter gas. A charged particle passing through with sufficient energy would ionise the gas. The anode wire was kept at a high voltage (1950 V) relative to the cathode wall forcing the ionisation electrons to drift towards the wire.

The NCDs detect neutrons by its capture on ^3He :



which has a Q-value of 764 KeV, and the resulting proton and ^3H have kinetic energies of, respectively, 573 keV and 191 keV. Furthermore, both products have electrical charge, which means that both cause ionisation of the counter gas producing an identifiable signal.

Each particle has a characteristic energy deposition profile that gives the basic shape of a neutron-capture NCD pulse. Figure 2.5 shows the energy spectrum of the NCD events detected in the third phase [69], along with the spectrum obtained from a ^{24}Na calibration run. In Figure 2.5(a) the shape of alpha and instrumental backgrounds have a shape almost flat in energy and are represented with the dashed

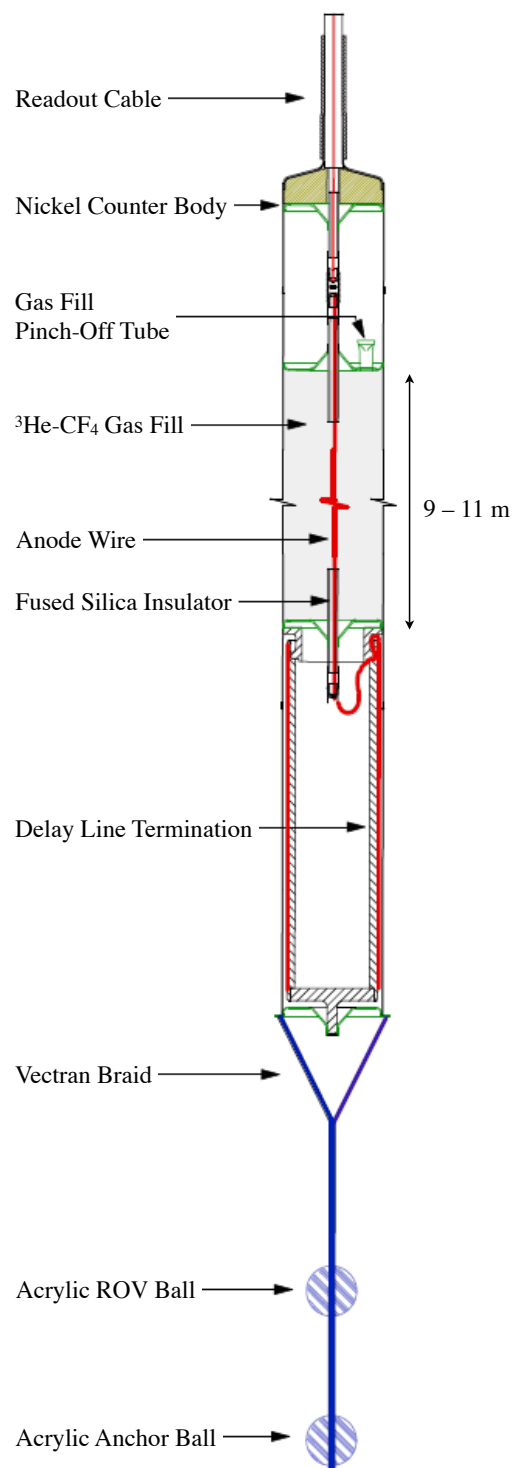
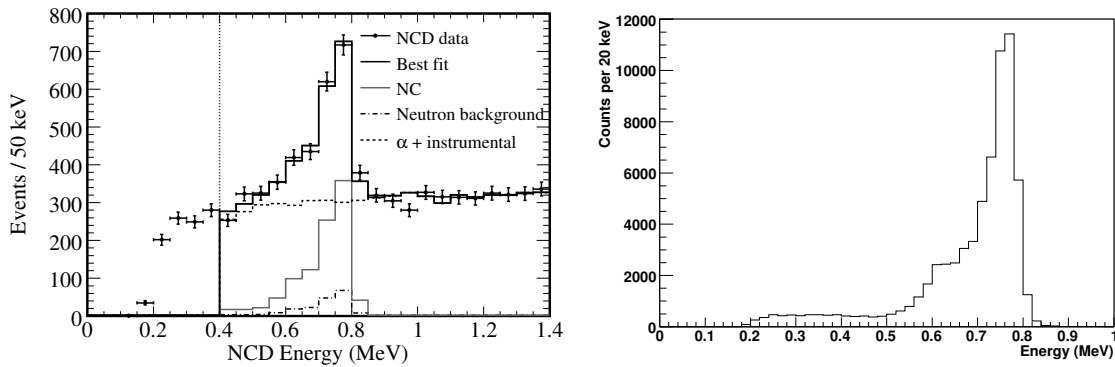


Figure 2.4: Schematic of a NCD string with readout cable, active region, delay line, and anchor system. Figure from [69].

line. The background neutrons are also shown, having a shape identical to the signal (dash-dotted line). The neutron signal has a series of distinctive features that can be better observed in Figure 2.5(b) as a result of the detection of the produced proton-triton pair. The neutron peak is clearly visible at 764 keV, and corresponds to deposition of the full kinetic energy of the proton and triton in the active volume of the NCD counter. The 573 keV shoulder is due to events where the triton energy is fully absorbed by the wall of the counter and the 191 keV shoulder is caused by total absorption of the proton energy in the wall.



(a) NCD energy spectrum from neutrino data. (b) NCD energy spectrum from calibration data.

Figure 2.5: NCD energy spectrum obtained in the NCD phase and corresponding calibration spectrum obtained with a uniformly-distributed ^{24}Na calibration. Figures from [69, 87].

The strings were deployed in a grid, each string 1-m apart from its closest neighbours. Figure 2.6 shows the NCD array configuration in the detector's (x, y) -plane. Although the total volume of the NCD array is small, this is sufficient as the neutron capture cross section of ^3He is very large (5330 b). For neutrons generated uniformly over the detector volume, the NCD array had a neutron capture efficiency of 21%. The main reason for making the grid so sparse was to avoid a drastic reduction of the PMT signal due to shadow effects. In the configuration used the reduction due to shadows was of about 9% [88]. More details on the NCD installation procedure and operation can be found in [69, 81].

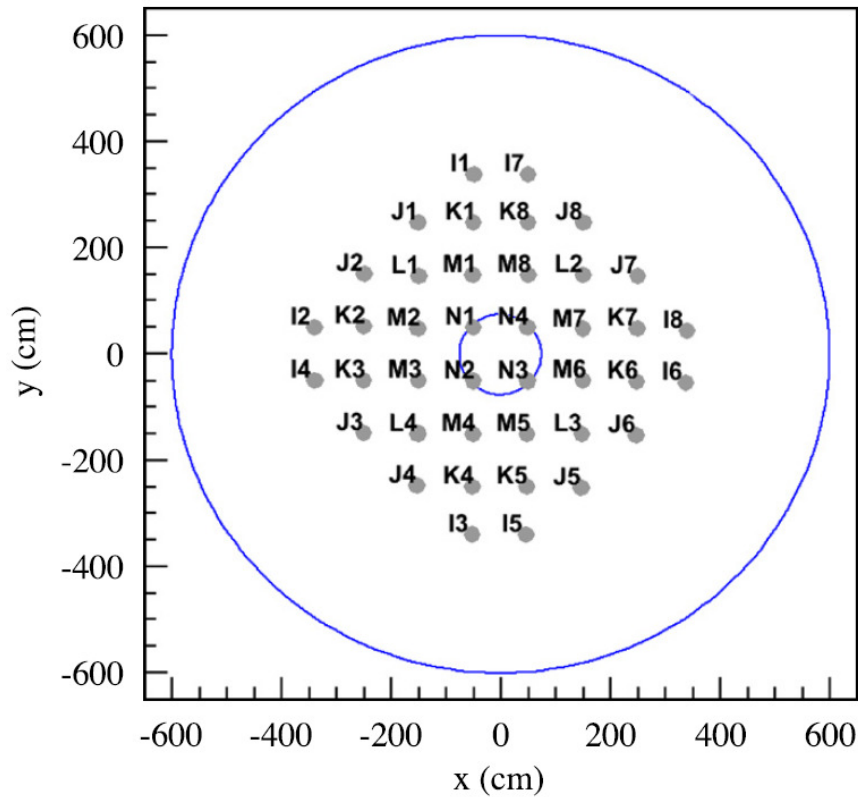


Figure 2.6: The SNO geometry during the NCD phase, viewed from the top of the detector, including the locations of the 40 parallel NCD counters deployed in the AV volume.

2.5 Backgrounds

As in any experiment, the control of backgrounds was a major concern in the design of SNO. In particular a proper knowledge of the neutron backgrounds was necessary as these events could not be distinguished from the NC signals.

In the initial data analyses, SNO dealt with most of the low energy backgrounds by increasing the energy threshold. The background events appear mostly at low energy and thus a substantial part of the problem just disappeared (with the exception of the neutron backgrounds). When preparing the combined analysis of the first two phases of SNO, since the past results were limited by statistics, an effort was made in reducing the low energy backgrounds so that one could reach the lowest possible energy threshold, thus dramatically increasing the available statistics [70].

Cosmic rays are an important background to low signal rate experiments, and one

of the main reasons why underground locations are chosen to host them. These can produce spallation neutrons and short-lived isotopes (muon followers). By having 6000 m.w.e. of rock shielding, SNO has only approximately 80 muons entering the detector per day. The muon followers can be easily removed by cutting all the data collected for 20 seconds after the initial muon, ensuring that no muon induced signal contaminates the neutrino data set.

The dominant physics background in the SNO data arises from radioactive contamination. In order to cope with this limitation, the materials used in the construction of the detector were specially selected for radiopurity, but naturally occurring radioisotopes such as ^{238}U and ^{232}Th were still present in trace quantities in all components of the detector. As these elements decay, particles can be released that are energetic enough to mimic both electron and neutron-like neutrino signals.

- Decays releasing electrons from β -decays above the Čerenkov threshold generate events that are almost indistinguishable from low energy CC events.
- Decay branches including gamma photons (γ s) above an energy of 2.224 MeV could cause photo-disintegration of a deuteron, producing a free neutron that could be confused with those from NC neutrino interactions.
- α particles produced in the U and Th decay chain could interact with nuclei present in the detector, such as ^2H , ^{13}C , ^{17}O and ^{18}O , producing further neutron background events. However, the cross section for these reactions is very small. Although they occurred in the water volumes, their major contribution come from events occurring in the acrylic vessel itself.

The decay chain of ^{238}U leads to the ^{214}Bi which decays by β -emission with an endpoint energy of 3.27 MeV. It also decays 2.8% of the time to an excited state of ^{214}Po that emits a γ -ray of 2.445 MeV. This energy can initiate the deuteron photo-disintegration and produce at most one background neutron per decay chain.

The decay chain of ^{232}Th produces the ^{208}Tl daughter that decays to an excited state of ^{208}Pb through several β branches. The de-excitation of ^{208}Pb always emits 2.614 MeV γ 's which can also photo-disintegrate the deuteron and produce a background neutron. Both ^{214}Bi and ^{208}Tl can at most generate one neutron each per decay chain.

It is important to distinguish two types of backgrounds in the SNO experiment: the external and the internal backgrounds. The external backgrounds come from radioactivity in the AV, light water, PSUP and the PMTs themselves. In this case the orientation of the PMT reflectors cause low geometrical acceptance for events in the light water, but many events are still detected between 3.5 and 4 MeV. The proportion of these events dominate the total number of events at the analysis threshold of 3.5 MeV.

Internal backgrounds have their origin in residual radioactivity in the D₂O and cannot be differentiated from the neutrino events other than by measuring their concentration and estimating the resulting rate of background events.

Due to the impossibility to tag several of the background event types, background control had to be put into place. The strategies for managing these backgrounds depended on the type of material in question. For example, in the case of the solid instrumentation, the AV and the glass in the PMTs were the major concern, for which specific manufacturing processes were employed to achieve low levels of radioactive contamination.

The water volumes were also a source of backgrounds. In particular the D₂O volume was a critical component as the backgrounds described above could generate events completely indistinguishable from NC events. Contaminants coming from Radon present in the mine air and leaching of Uranium and Thorium from the solid instrumentation were sources of background very hard to control. The background control in this case was performed through re-circulation and purification of both D₂O and H₂O.

Both light and heavy water water was circulated out of the detector, filtered, de-ionised, de-gassed (to remove Radon), then re-gassed with pure nitrogen before being reintroduced to the detector. In order to improve the radiopurity of the light water region, a plastic barrier was installed on the back side of the PSUP, dividing the light water into two volumes: 1.7 kilotons between the acrylic vessel and the PMTs, and 5.7 kilotons between the PMTs and the walls of the cavity. The water inside the PSUP could be made much cleaner, which helped reduce backgrounds in the region where they could cause the most problems. During the light water purification process, the water was reintroduced into the inner volume, in order to

avoid the water from the outer volume to move in. A barrier of pure nitrogen gas was also maintained in the neck between the D₂O and the air of the laboratory to reduce radon contamination.

Along with the purification process, the water was also assayed to determine the amount of uranium and thorium still present in the water. There were two different processes to do this: the HTiO [89, 90], and the MnOx [91] assays.

The HTiO is deposited in the filtration instrumentation and is used as an ion exchanger to collect the radioactive components present in the water. These components are then stripped from the filter with acid, concentrated and then mixed with a scintillator and observed for β and α decays, typical of the decay chains from U and Th. Essentially, the activity from the Thorium chain is obtained from the activity levels of ²²⁸Th, ²²⁴Ra, ²¹²Pb and ²¹²Bi. Analogously, the activity of the Uranium chain is obtained from the activity levels of ²²⁶Th, ²²²Ra, ²¹⁴Pb and ²¹⁴Bi.

The MnOx process uses columns of acrylic beads covered with MnO_x , where x stands for different amounts of oxygen atoms in the molecule. The water flows along the column, depositing the contaminants, predominantly Radon, in the process. The Radon is then removed and placed in a decay chamber, where the Po daughter is detected using an α counter.

The results from both techniques were then compared and combined to produce an estimate of the radioactivity in the water in terms of ²³⁸U- and ²³²Th-equivalent grams per gram of D₂O (or H₂O). Table 2.1 contains a summary of the concentration measurements of U and Th performed in all phases of SNO that were used in the analysis.

Besides the measurements described in this section, in the latest analyses the background levels are also fitted alongside the neutrino signals, using the background estimates as constraints in the fit.

2.6 Detector Calibrations

In order to understand the data taken by the SNO detector, it is necessary to have an accurate knowledge of the detector response. Thus, an intensive calibration program

Phase	Type	Medium	Measurement (g per g of medium)
D_2O	^{238}U	D_2O	$(1.01^{+0.34}_{-0.20}) \times 10^{-14}$
	^{232}Th		$[2.09 \pm 0.21(stat.)^{+0.96}_{-0.91}(syst.)] \times 10^{-14}$
	^{238}U	H_2O	$(29.5 \pm 5.1) \times 10^{-14}$
	^{232}Th		$(8.1^{+2.7}_{-2.3}) \times 10^{-14}$
Salt	^{238}U	D_2O	Upper Limit: 2.0×10^{-14}
	^{232}Th		Lower Limit: $(1.41 \pm 0.46) \times 10^{-16}$
	^{238}U	H_2O	$[1.76 \pm 0.44(stat.)^{+0.70}_{-0.94}(syst.)] \times 10^{-15}$
	^{232}Th		$20.6 \pm 5.0) \times 10^{-14}$
NCD	^{238}U	D_2O	$5.2 \pm 1.6) \times 10^{-14}$
	^{232}Th		$(6.14 \pm 1.01) \times 10^{-15}$
	^{238}U	H_2O	$(7.7 \pm 2.1) \times 10^{-16}$
	^{232}Th		$(35.5^{+9.9}_{-5.4}) \times 10^{-14}$
			$(2.77 \pm 1.04) \times 10^{-14}$

Table 2.1: Summary of ^{238}U and ^{232}Th concentrations at SNO measured through radio-assays in both the heavy and light water volumes.

was put in place. Of the total running period of the experiment, approximately 30% of the operational live-time was spent in calibrations.

The calibration programme in SNO can be separated into two different groups: the electronics calibrations and the source calibrations. Details about each of these types will be given below.

2.6.1 Electronics calibration

The electronics calibrations were used to determine the parameters determining the charge and time response of each PMT and the front-end electronics.

Two sets of calibrations were performed on a regular basis, in order to measure the stability of the detector instrumentation:

Electronic Calibration (ECA)

The *Electronic Calibration (ECA)* was performed every two weeks in order to measure the variation of channel properties over time. Two measurements were performed:

the pedestal value of the charge analog-to-digital conversion and the time slope of the time-to-amplitude conversion. The pedestal value was calibrated by firing the individual discriminators with no incoming pulse, by having the DAQ sending a pulse to the discriminators, and the charge was recorded and digitised, providing a definition of the *zero charge* in each channel. In order to calibrate the time slope, the DAQ sent a pulse to fire the individual discriminators and then a global trigger was forced at a fixed time delay. The time slope was then measured by varying the delay between the input pulse sent by the DAQ and the global trigger.

PMT Calibration (PCA)

The *PMT Calibration (PCA)* was performed monthly to measure the time response of each PMT². This calibration mimicked the data taking sequence in order to ensure a proper measurement of the timing of the PMT system. Individual discriminators fired when the leading edge of a pulse crossed a fixed voltage threshold. The time recorded thus depended on the pulse amplitude, with a larger amplitude to cause the discriminator to fire earlier. This was affected by variations in the pulse height recorded by a single PMT, causing variations in the PMT firing time as large as 2 ns. Therefore, to correct for PMT-to-PMT timing differences caused by this effect, an approximately isotropic laser source, the *laserball (LB)*, was deployed in the centre of the detector to measure the relation between the deposited charge and firing time, producing a charge dependent channel-by-channel correction.

2.6.2 Detector Calibrations

During operation, a variety of calibration sources were deployed in SNO in order to measure the detector response to signal and background events. Several properties of the detector had to be measured, including the PMT collection efficiency, the angular response of the PMTs, the optical attenuation lengths, the position dependent energy response to both electrons and neutrons, and also the acceptance of background

²A calibration of fundamental channel properties such as the discriminator thresholds was also performed whenever an electronics component, such as the *Front End Card (FEC)*, was replaced.

events. In order to perform all these measurements, a wide range of calibration sources were used.

Source deployment

The sources could be deployed both in the D₂O volume, through the neck, or outside the AV, in the H₂O volume between the AV and the PMTs, through guiding tubes that ran parallel to the z -axis in six different positions. The sources were deployed in the D₂O volume using a manipulator system where sources of different types and geometries could be attached. Inside the D₂O volume, the calibration system could be ran on two modes: single-axis and dual-axis mode. Figure 2.7 shows a schematic of the calibration system responsible for deploying the sources in the detector.

In the single axis mode, the source could be deployed along the z -axis (the vertical axis), using ropes fixed at a well known position $(-16.03, 23.5)$ cm in the (x, y) plane. The single-axis mode provided a very accurate mode of deployment, allowing the source position to be known to 2 cm.

In order to deploy sources off the central axis of the detector, the dual-axis mode was used. This mode uses two ropes in opposite sides to move the sources in the (x, z) or the (y, z) plane. A total of four side ropes exist, one in each quadrant of the (x, y) plane, which were commonly identified according to the cardinal orientations (N,S,E,W). The ropes run down the AV neck, through pulleys on the manipulator and then terminated at fixed locations on the AV, as shown in Figure 2.7. By controlling the length and the tension at each rope, it is possible to place the source in approximately 65% of the possible positions in each plane. In this mode, the position accuracy is of the order of 5 cm for central positions, and of the order of 10 cm for positions close to the AV, where most strain was put on the ropes and pulleys of the deployment system [92].

In the following subsections the most relevant calibration sources are described, with particular emphasis on the optical calibration source called the *laserball* (*LB*).

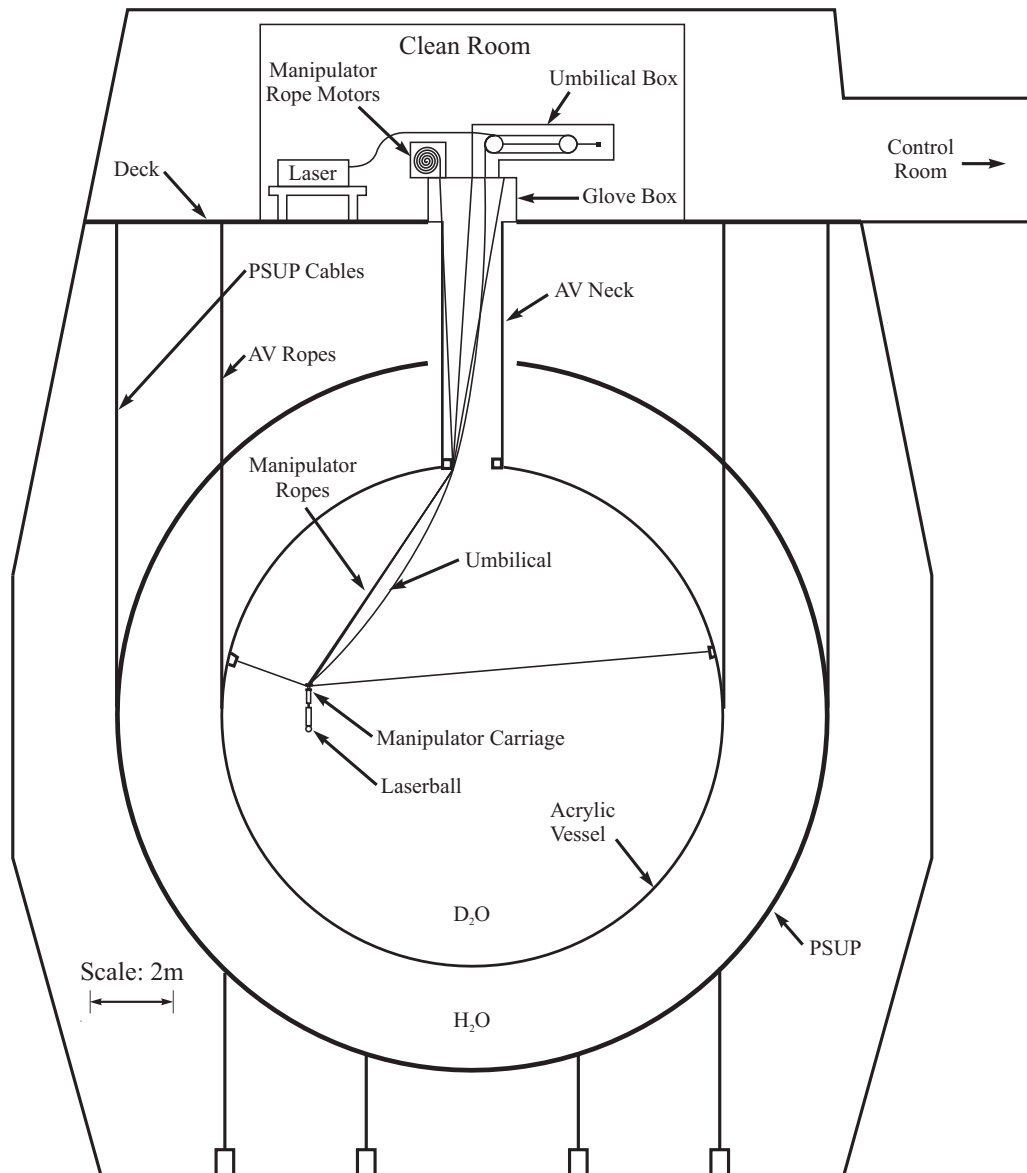


Figure 2.7: Schematics of the SNO source manipulator system. Figure from [92].

Laserball

The *laserball* (*LB*) is a triggered, multi-wavelength and virtually isotropic laser source, used in both the PCA and the *optical calibration* (*OCA*). It was used to measure the detector optical properties such as the media attenuation lengths, and the PMT angular response, but also the PMT relative efficiencies and timing. A schematic of the LB is shown in Figure 2.8.

The LB consists in a quartz spherical container filled with a mix of silicone gel and small hollow glass bubbles [92]. The scattering length of light inside the source is of order of 1 cm, which is a good compromise between having a good isotropy (which requires a short scattering length) and reducing the intensity losses due to dispersion and absorption (for which we want a larger scattering length). An optical fibre, carrying the laser pulses, terminates at the centre of the ball.

The body of the LB is encased in a stainless steel light shield to prevent refracted light going upwards from reaching the PMTs. However, this considerably reduced the intensity of the source upward, where the whole support structure is located.

The LB itself is just a diffuser. The light pulses are generated by an external short pulse-length N₂ laser ($\lambda = 337.1$ nm) which could be coupled to a series of laser dyes to produce pulses with longer wavelengths [93]. The layout of the laser, with its dye system is shown in Figure 2.9. From the laser system, the light is injected into a fibre-optic that is part of a specially designed cable used for SNO calibrations, the *umbilical*, which connected the laser source to the LB diffuser. The umbilical is shown in Figures 2.7 and 2.9.

In order to cover most of the Čerenkov spectrum of interest for SNO, the laser has five dyes being able to produce pulses in a total of six wavelengths. The properties of the laser system are described in Table 2.2 and the spectra of the dyes are shown in Figure 2.10. The laser system allows the selection of filters of different neutral densities from two wheels, shown in Figure 2.9 as "Attenuator Wheels", to reduce the intensity of the laser light. This is particularly important for optical calibrations, where the intensity of the light is adjusted to very low values so that each hit PMT has seen essentially a single *photo-electron (PE)*, which will correspond to 300 – 400 hit PMTs per event [92].

The ¹⁶N Source

The ¹⁶N triggered source [94] was a high rate, mono energetic γ source. The β decay of ¹⁶N produced an excited state of ¹⁶O which produced a single γ of 6.13 MeV upon de-excitation. The 6.13 MeV γ then Compton scattered an electron that consequently generated Čerenkov light. The source was encased in a steel container to absorb the

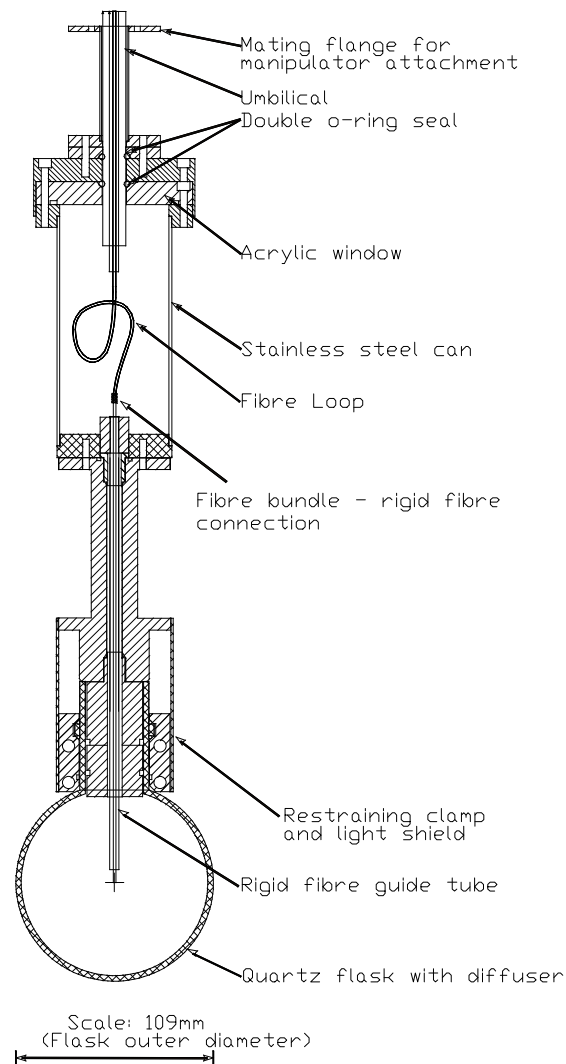


Figure 2.8: Laserball schema. Figure from [80].

emitted β . Furthermore, this source had a small PMT in its interior that triggered on the β , which permitted the tagging of events from the source. Thus, this source produced a very clean data sample.

This was the main calibration source used for energy calibration (scale and resolution) within the detector, as the γ produced tended to scatter an electron with an energy close to the peak of the CC spectrum. It was thus deployed in several locations in the detector, being used to determine energy systematic uncertainties such as position-to-position uncertainties, time variations in energy and accuracy of vertex fitter.

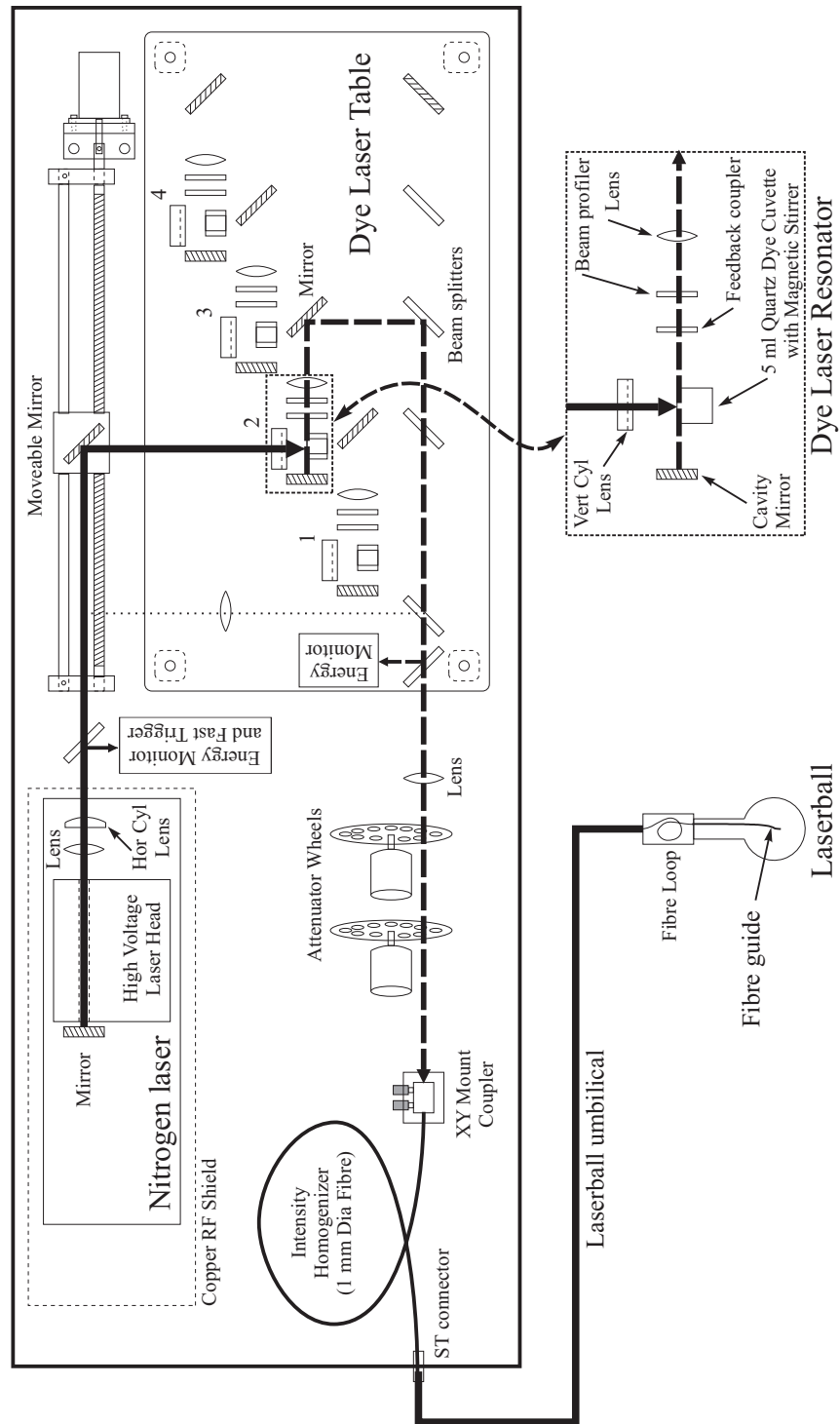


Figure 2.9: Schematics of the optical calibration laser. Figure from [80].

Pulse width	$t_{N_2} \sim 0.6$ ns
	$t_{dyes} \sim 0.3$ to 0.5 ns
Pulse energy	$E_{N_2} \sim 100 \mu J/\text{pulse}$
	$E_{dyes} \sim 10$ to $30 \mu J/\text{pulse}$
Pulse rate	1 to 45 Hz
Available wavelengths	
Central value (nm)	σ_λ (nm)
337.1	0.1
369	10
385	8
420	8
505	14
619	10

Table 2.2: Properties of the laser system, as well as available wavelengths. $\lambda = 337.1$ nm corresponds to the laser fundamental wavelength. Data from [80].

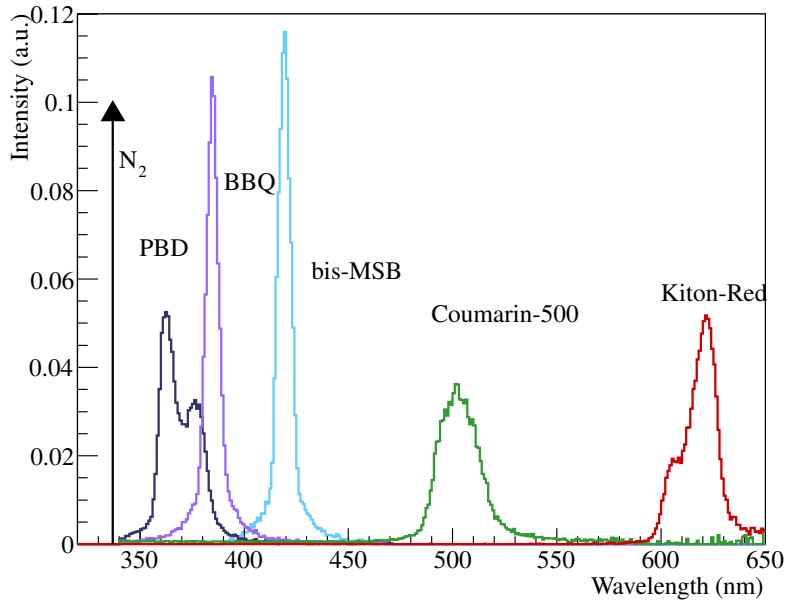


Figure 2.10: Wavelength spectra of the N_2 laser, as well as the dyes.

The ^8Li Source

The ^8Li source [95] was also a triggered source that produced a β spectrum with an endpoint of $\sim 14\text{MeV}$. Using a *deuterium-tritium* ($D-T$) generator with a ^{11}B target,

^8Li was produced, which was transported through the umbilical into a spherical decay chamber that had been lowered into the detector. The chamber has very thin walls (0.6 mm) so that the β can escape. This source produced a spectrum very similar to the one from the ^8B CC reaction, both in shape and in endpoint, as both isotopes decay to the same excited state of ^8Be . The events were tagged by scintillation of the Helium gas that was used to transport the ^8Li and filled the chamber. The scintillation was produced by α 's resulting from the prompt decay of the daughter making a coincidence with the β . The scintillation light was then detected by a PMT located in the container.

The proton- ^3H Source

The proton- ^3H (pT) source [96] consisted in a small accelerator that collided protons with ^3H to produce ^4He and 19.8 MeV γ 's. It was mostly used to measure the response of the detector at high energies. This source was not deployed during the Salt phase as it also generates large amounts of neutrons as a by-product, which would activate the sodium into a ^{24}Na radioactive source.

The ^{252}Cf Neutron Source

The ^{252}Cf decays by spontaneous fission, producing one or more neutrons. It was used primarily to measure the neutron capture efficiency. This source was enclosed in a plastic container to absorb the β 's that were generated by fission fragments. However, this source also produces fission γ 's, which could be reconstructed as neutron captures. Therefore, large efforts were taken to properly analyse its calibration data, in order to properly account for the γ contamination.

Acrylic Radioactive Sources

These sources were also called *canned sources* [97], as they consisted of radioactive isotopes encased in acrylic to produce daughters belonging to either the ^{238}U or ^{232}Th chain. As stated in Section 2.5, these radioactive chains were the origin of most of the dominant physics backgrounds in the detector. Due to the large half-lives of ^{238}U

and ^{232}Th , short-lived isotopes from each of the chains (^{226}Rn and ^{232}U) were used, producing, respectively, ^{214}Bi and ^{208}Tl events, the major low energy background in SNO. These sources were not tagged, *i.e.*, did not provide a simultaneous trigger signal to the DAQ.

The $^{241}\text{Am-Be}$ (AmBe) Neutron Source

The ^{241}Am emits an α , which interacted with Beryllium ejecting a free neutron and a 4.14 MeV γ in coincidence. This source was not tagged, but one could impose a requirement for the coincidence, which resulted in considerably lower levels of contamination. This source was only used in the last two phases of SNO (Salt and NCD), and was particularly relevant to verify the measurements of neutron capture efficiency in the Salt phase.

Radon Spike

This source consisted of a controlled injection of Radon into the water volumes. This allowed to obtain a measurement of the detector's response to uniform, isotropic low energy backgrounds events. This source generated a high rate of events which made the contamination from any other source of events negligible.

The ^{24}Na Source

This source was only employed in the NCD phase [98]. Its principle is similar to the Radon Spike. A sample of neutron activated salt was dissolved in the D_2O volume. The activated ^{24}Na produces a 2.6 MeV γ , which is strong enough to induce the deuterium photo-disintegration, producing a free neutron, indistinguishable from the NC events. By being a distributed source, it was possible to calibrate the whole detector volume, which was not possible with the other calibration sources.

This source was used in SNO mostly to calibrate the NCD system, where the other neutron sources couldn't be positioned close to some of the NCDs due to the limitations of the source deployment system. However, this calibration required a long time as the ^{24}Na , with a half-life of $T_{1/2} = 14.959$ hours, required at least

two weeks before its activity was negligible compared to the typical backgrounds. However, it was a key element in the calibration of the NCD array. Usually, after a ^{24}Na calibration, an optical calibration followed, as the background from the ^{24}Na was completely suppressed by the much more intense laser source.

2.7 Detector Simulation

The processing of PMT and NCD information from the SNO electronics and the Monte Carlo (MC) simulation are handled by the *SNO Monte Carlo and ANalysis software (SNOMAN)* [99], a FORTRAN package developed by the SNO collaboration to simulate the response of the detector to various kinds of events, but also for the first stage of data processing and reconstruction.

The Monte Carlo component is a full photon-tracking simulation which starts with seed particles, such as electrons, gammas, neutrons and muons, and propagates them through the detector. Electron and gamma physics are calculated using code from EGS4 [100] which has been embedded into the simulation framework. EGS4 computes energy loss due to ionisation, Compton scattering of electrons by gammas, pair production, electron multiple scattering and photo-electric effect.

The production of Cherenkov light has been added to the simulation by seeding photon vertices along each segment of the electron track. Neutron propagation and capture are calculated with MCNP [101]. Higher energy particles like muons and electrons above 2 GeV are simulated with LEPTO [102], and hadrons with FLUKA [103] and GCALOR [104], all from the CERNLIB software library.

Particle tracking through the detector geometry is handled by custom SNOMAN code that reads the dimensions, materials and optical properties of each element of the SNO detector from a database on startup. Calibration source geometries were also included when simulating runs in which they were deployed. The particle tracking code was also used when propagating optical photons through the detector, with reflection and refraction happening at media boundaries, and Rayleigh scattering and absorption in the bulk. Once photons cross into the PMT concentrator region, one of two simulations could be used. There was a phenomenological simulation of PMT response derived from laserball calibrations (called “greydisk”), and there was

also a full 3D photon tracking model that traced the photon through all parts of the PMT/Concentrator unit.

If the photon produced a photoelectron in the PMT, a full simulation of the data acquisition hardware integrated the pulse, and simulated the operation of the trigger system. At the end, a data structure very similar to that produced by the real detector was generated for the event. The Monte Carlo event differed only from real data in that the quantisation error of the ADCs and the charge pedestals were not simulated. As a result, the simulation and the real data were only comparable after the electronics calibration had been applied to the real data, converting charges back into hit times in nanoseconds. After this point, processing for data or Monte Carlo was identical. A user supplied command file pipelined the events through a series of analysis tasks which could include position reconstruction, energy estimation, application of cuts, and finally generation of output files in either HBOOK or ROOT format.

Most of the detector configuration in SNOMAN was set *a priori*. That is, parameters like dimensions, materials, and locations of detector elements were input based on design documents. Measurements of PMT charge and timing distributions, and photocathode efficiencies were also included. Other parameters were measured using the calibration sources and inputted to the simulation to provide realistic looking Monte Carlo events.

A run in SNO ranged from 30 minutes to 4 days, with most runs lasting 7 hours. At the start of each run, the detector state was recorded. After the run ended, additional information was computed and loaded into the SNOMAN database. These data included

- Start and stop time of the run
- Trigger thresholds and list of enabled triggers
- Channel discriminator thresholds
- Channel status (online, offline)
- Average PMT noise rate
- Source type and location (if deployed)

All of these values were used by SNOMAN when deciding whether PMTs could register hits, how many noise hits to add to the event, and whether to enable a particular source geometry.

Chapter 3

Optical Calibration

3.1 Introduction

In a Čerenkov detector such as SNO, the accurate knowledge of its optical properties was a key component to effectively understand the signals detected and correctly associate them to the underlying physical processes. The SNO detector was essentially a large transparent volume surrounded by PMTs, with the physics events of interest to occur inside the PSUP and producing Čerenkov light. Therefore, in order to make a precise measurement of the energy and direction of each event, it was necessary to keep a tight control over the conditions of light propagation. This was accomplished by ensuring that the detector media were as clean as possible and by measuring the optical properties of the PMTs, acrylic and water.

The first question that should be answered when discussing the optical calibration is: "Why?". In principle, without the optical calibration the whole experiment could run. The detector was calibrated in energy using a different source, and with that the analysis could in principle be carried out. However, there were a few reasons why a good optical calibration of the detector was essential for the accuracy of the physics measurements.

In order to perform an accurate measurement of the neutrino interactions, a good energy resolution was a mandatory requirement. For instance, the distortions imposed in the solar neutrino energy spectrum are very small in the energy region

where SNO was sensitive. In order to detect these variations, the energy scale of the detector must be known to better than $\pm 1\%$ [105]. SNO employed a series of techniques, by using several calibration sources covering different energy ranges, in order to better understand the energy response of the detector. The energy of the events were determined by the spacial and temporal distribution of the PMT hits, as well as the total number of hits. For an electron produced in the detector, its track length would be proportional to its energy. So, as the energy of the electron increased, more Čerenkov light would be produced, yielding a larger number of hits in the PMTs. The number of PMT hits, on the other hand, would be affected by the optical properties of the media, such as the media attenuations. Therefore, by having an accurate estimation of the detector optical properties a more accurate conversion from the number of hit PMTs into event energy was achieved. Furthermore, the analysis threshold was determined by the contributions of radioactive backgrounds at the low energy end of the energy spectrum. The isolation of the background relied also on a good calibration of the detector volume.

The present chapter will describe the *optical calibration (OCA)* process carried out in SNO, explaining the optical model and its parameters, and detailing the analysis of the optical data, including a description of the improvements implemented and the results obtained. The optical calibration data taken in SNO passes through a series of steps until the optical parameters can be extracted.

In Figure 3.1 a diagram of the data processing and analysis chain is shown. In the following sections each step of this chain will be addressed with results obtained and the relevant improvements added by the author of this thesis.

This work follows up the studies previously done for the initial SNO analyses [83, 106–108]. The work described here was applied in the analysis of the SNO NCD phase and the analysis of the combination of the D₂O and Salt phases (LETA). For the combined 3-phase analysis no reprocessing was carried out, meaning that some of the improvements described were not applied in the final analysis of SNO. Despite the neutrino data not being reprocessed for the *three phase combined analysis (3-phase)*, these improvements were nonetheless important to demonstrate that the previous reprocessing was valid and no major differences arose from the tests performed.

As the SNO experiment progressed with the data taking, so the optical calibration

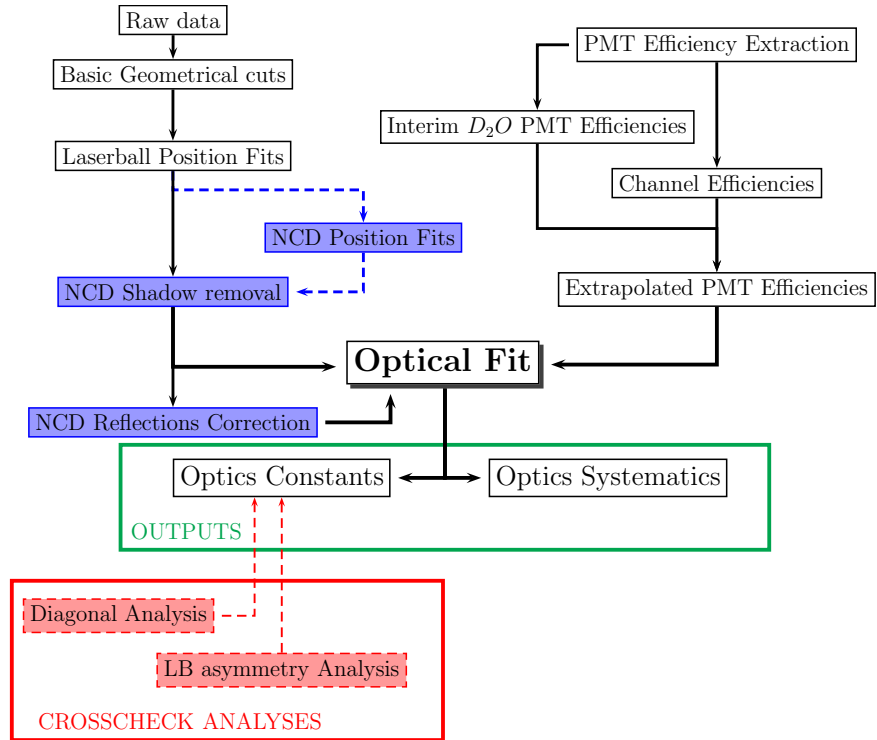


Figure 3.1: Optical Calibration analysis chain.

evolved, getting continuously improved in order to better accurately describe the optical properties of the detector. The work described in this thesis relates mostly to the third and last phase of the experiment (NCD phase), and the combined analyses that followed (LETA and 3-phase).

By the end of the SNO Salt phase, a NCD commissioning phase took place, consisting in the installation of the NCDs into the SNO detector after desalination of the D_2O . This period started in October of 2003 and ended in August 2004. During this period two OCA *scans* were performed by positioning the *laserball* (*LB*) in several positions in the detector and taking data at six different wavelengths, which are detailed in Table 2.2. An OCA *scan* consists of a series of data taking *runs*, which are characterised by a LB position and orientation and a laser wavelength (see Section 4.1).

In the October 2003 scan (before the NCDs deployment) the main goal was to verify that the optical properties of the detector remained consistent with salt phase properties, and more similar to the first (D_2O) phase properties, where in principle

only ageing effects would change the detector optical properties. As this was confirmed, this scan became the benchmark calibration data set for comparisons in the following scans. A second OCA scan was performed in July 2004 with the NCDs already in place, but due to a poor isotropy of the LB source its data was not used in any OCA analysis to extract the detector optical properties.

As described in Section 2.6.2, the optical calibration was performed with a *laser-ball* source that can be tuned to six wavelengths. However, the Čerenkov radiation spectrum is continuous (see Figure 2.3). The data from the optical calibration simply aimed to obtain a measurement at six sampled wavelengths. The extracted optical properties of the detector were later extrapolated to other wavelengths in the simulation and reconstruction algorithms.

A note about the spacial coordinates should also be made. In most cases, the cartesian coordinate system is used to describe most of the positions and directions. In the case of SNO, the top of the detector was oriented along the z axis, while the x -axis pointed from the centre of the AV towards north and y -axis pointed towards west. However, due to the symmetry of the detector, the specific choice of the latter two were not particularly important. Although this coordinate description can easily be used to characterise any position or direction in the detector, in some cases, due to the spherical symmetry of the detector, it is convenient to use spherical coordinates.

3.2 Optical Calibration Analysis

The optical model of the SNO detector describes the light propagation through the optical elements of the detector until it is detected by the PMTs. This model relies on the assumption that the detector can be well characterised by average properties, implying that the water is homogeneous and the PMTs have similar angular response [83, 92].

The major effects that are considered in the optical model are:

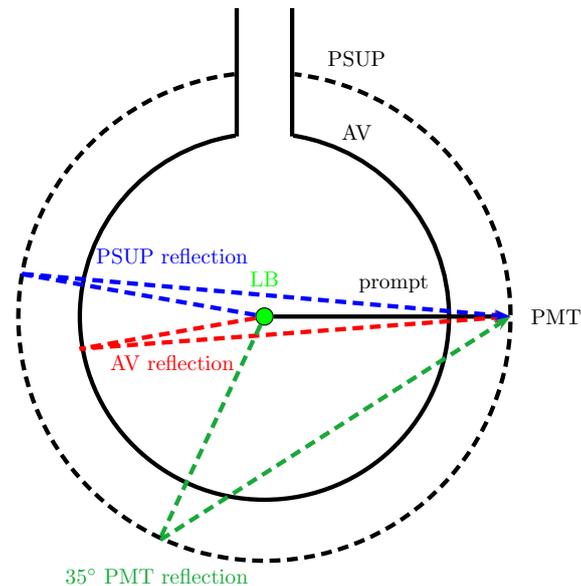
- Attenuation in the media crossed by the signals: D_2O , H_2O and acrylic.
- Bulk scattering in the water media.

- Reflections from the detector elements (AV, PSUP and PMTs).
- PMT efficiencies.

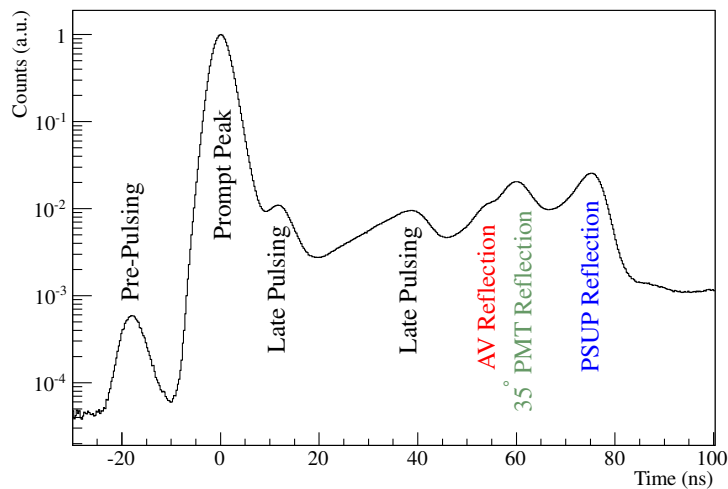
Here one has to consider that the PMT efficiencies have several components that should be understood, such as its dependence with the direction of the incident light, wavelength and location in the detector. It was verified that from the effects cited previously the dominant ones are the media attenuations and the PMT angular response [83, 108].

Reflections on detector elements need to be considered in the optical calibration. For instance, the selection of the prompt peak needs to take under consideration the position of the source, in order to minimise the inclusion of the reflected photons. Figure 3.2(a) shows a diagram of different contributions from reflections on detector elements in the particular, and simple, case of a source positioned in the centre of the detector. Prompt light reach the PMTs directly from the source, while reflections cause extra PMT signals at delayed times. Figure 3.2(b) shows the corresponding timing histogram, integrating the light collected over all PMTs. The reflection peaks are indicated in the figure, together with the prompt peak and the peaks due to pre- and late-pulsing. These signals occur at well defined time offsets relative to the prompt peak signals. When an incident photon strikes directly a dynode, there is no production of a photo-electron at the cathode. A pre-pulsing signal then occurs at approximately 15 ns before the prompt peak, which corresponds to the transit time of the photo-electron between the cathode and the first dynode. On the other hand, photons escaping the dynode stack are a likely cause for the late-pulsing. In this case the photons go back to the photocathode and start another photo-electron down the dynode chain . The two peaks shown in the figure are likely to be caused by photons escaping from different regions in the dynode stack. While the first peak would probably be generated by a photon coming from the top of the dynode stack, the second pulse would probably correspond to photons coming from dynodes further down the stack [83].

In the NCD phase, it was also necessary to account for additional optical effects caused by the introduction of the NCDs. In the previous phases of the experiment, the detector maintained a geometrical symmetry that allowed the average properties of the detector to be obtained in a straightforward manner. With the introduction of



(a) Optical reflection paths.



(b) Integrated PMT time histogram

Figure 3.2: Examples of light paths from the centre of the detector and corresponding integrated time spectrum. The time spectrum was obtained from a central laserball run at 500 nm taken in October 2003.

the NCDs it was still valid to consider that the optical properties were well described by average quantities, but it was now necessary to account for the variations induced by the NCDs. Here, two major optical effects had to be considered: the reflections

on the NCDs, which affected the totality of the PMTs, but not exactly all in the same manner; and the NCD shadows cast, which caused a reduction of the detected signal in some of the PMTs.

The optical calibration was performed by using the LB source discussed in Section 2.6.2. The relevant properties of this source have already been introduced there. The optical calibration model also includes a series of properties that describe the LB:

- Intensity distribution as function of angle.
- Total intensity over a run.
- LB position.
- LB orientation.

The reason for including these parameters in the optical calibration model is because the LB itself is not totally isotropic, and the source manipulator system has an associated uncertainty in the position that is dependent in the tension in the holding ropes, which varies with the specific absolute position in the detector.

3.2.1 Optical Model

Considering the source deployment instrumentation, the optical calibration was performed by placing the LB in several different positions of the detector and taking data with different wavelengths. Therefore, each source position and wavelength of the laser define a *run*. The set of calibration runs taken at a certain period defined a *scan*. These two concepts will be widely referred in the following sections.

In the optical model of SNO, we identified the prompt intensity with the measured occupancy O_{ij} , observed for a run i and a PMT j as the number of hits detected by the PMT in the *prompt time window* of ± 4 ns:

$$O_{ij} = N_i \Omega_{ij} R_{ij} T_{ij} L_{ij} \epsilon_j e^{-(d_{ij}^d \alpha_d + d_{ij}^a \alpha_a + d_{ij}^h \alpha_h)}, \quad (3.1)$$

where the terms are described as follows:

- \mathbf{N}_i Number of photons emitted per pulse by the laserball in run i , and detected within a prompt timing window of ± 4 ns at each PMT. This term is the intensity normalisation for each run and cannot be precisely measured¹.
- $\mathbf{\Omega}_{ij}$ Solid angle from LB in run i for PMT j . This term is calculated analytically based on the detector geometry.
- \mathbf{R}_{ij} Phototube and reflector assembly angular response beyond the solid angle Ω_{ij} . This factor is parameterised as a function of the photon incident angle on the PMT surface and is extracted from the data, as 45 independent bins (1° wide).
- \mathbf{L}_{ij} LB light distribution expressed as a function of the angles relative to LB position $L_{ij}(\theta_{LB}, \phi_{LB})$. It is extracted from the data and described as a combination of polynomial functions of the angles and discrete binned distributions.
- \mathbf{T}_{ij} Fresnel transmission coefficients for the media interfaces (D₂O/Acrylic and Acrylic/H₂O). Calculated analytically, based on the LB and PMT positions.
- ϵ_j Absolute quantum efficiency of PMT j combining the overall PMT efficiency and electronic threshold. Also referred to as *quantum efficiency (QE)*, which refers to the wavelength-dependent probability of registering a hit. This term is independently extracted from the data.
- $\mathbf{d}_{ij}^{d,a,h}$ Light path lengths through the media (D₂O, Acrylic and H₂O, respectively). Calculated analytically based on the detector geometry.
- $\alpha_{d,a,h}$ Attenuation coefficients for the optical media (D₂O, Acrylic and H₂O, respectively). α_s and α_h can be extracted from the data².

Several of these terms can be calculated precisely, such as the solid angle (Ω_{ij}) and the Fresnel transmission coefficient (T_{ij}), which are calculated by the model along with the direct optical path from the LB to each PMT ($d_{ij}^{d,a,h}$).

The remaining terms can be extracted from the LB data through an optical calibration fit. Although Equation 3.1 shows only a few multiplicative factors, in

¹That is not needed since the other parameters are overconstrained.

²Due to the high correlation between d_{ij}^a and d_{ij}^h the calibration method usually obtains a combination of α_a and α_h . For that reason α_a is usually fixed to *ex-situ* measurements reported in [83].

fact the number of parameters is much larger, as some of the terms hide dependence on geometric variables, such as angles of incidence in the case of the phototube and reflector angular response (also called *PMT angular response (PMTR)*).

In the occupancy described in Equation 3.1 no corrections are included. In fact several corrections have to be applied in order to make the occupancy a better light intensity estimator. Amongst others, the main correction consists in the *multi photoelectron correction (MPE)*, which corrects for the PMT signals from multiple photoelectrons that were fired as a single event.

Other optical effects such as diffusion, reflection and absorption are not considered in the optical model. Thus, PMTs whose optical path crosses detector components such as ropes, tubes and NCD attachment anchors, are labeled as *bad* and are rejected from the OCA fit. Only a PMT that is labeled as *good* in multiple runs (the number can be customised) is used in the fit. In Section 3.3 an explanation of the different cuts is presented.

The media attenuations ($\alpha_{d,a,h}$), and the PMTR are the main detector parameters of the optical model and are extracted for each wavelength.

The PMT efficiencies are not extracted in the optical fit as it would introduce approximately 9000 new independent parameters to the fit. The efficiencies are thus extracted separately after the remaining optical parameters are fitted. This procedure is explained in more detail in Section 3.4.2.

3.2.2 Laserball Position Fits

The precise determination of the laserball positions is a key aspect of the optical calibration analysis. Variations of occupancy due to solid angle are larger than those due to the optical parameters and thus a special effort had to be made in order to ensure a high level of accuracy for the determination of the LB position. Although the source positioning system can provide an estimate of the LB position, its positioning algorithm was based in the tension and length of the ropes that supported the source, which were not precise enough. Typically the precision of the source positioning system could vary from ~ 2 cm for a central position up to ~ 5 cm at high radius positions.

The position of the LB was even more important in the NCD phase, where the shadow patterns caused by the NCDs were strongly dependent on the source position. The LB and NCD position extraction is thoroughly documented in [108]. The method used to determine the LB position was not changed since the D₂O phase and is described in more detail in [83].

After the standard correction of the measured data with the PMT Calibration constants, the calibration data was analysed in the form of a summary histogram with individual PMT counts as a function of time.

For each channel j , a constant time offset (t_0) was subtracted to the raw PMT time, as well as an estimate of the time of flight (t_{tof}^{MANIP}) between the source and the PMT, considering the position given by the source manipulator system. The time stored in the histogram for a channel was then:

$$t_j = t_{j,RAW} - t_0 - t_{j,tof}^{MANIP} \quad (3.2)$$

Figure 3.3, presents an example of a time distribution with the identification of the prompt time window and respective mean time.

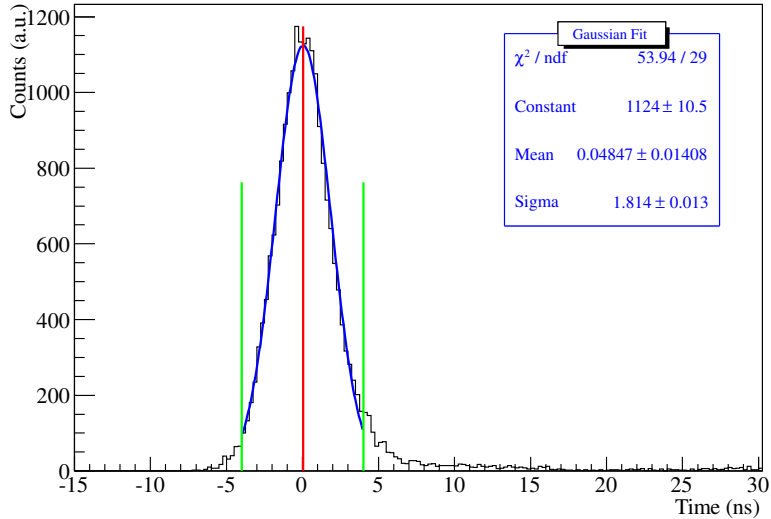


Figure 3.3: Single channel time spectrum. The red line indicates the maximum obtained from a Gaussian fit. The green lines show the limits of the 4 ns prompt time window.

This mean and width were determined from a timing histogram with 0.25 ns bin width, and sliding a time window 8 ns wide, so that the counts were maximised. The Gaussian mean μ_j was thus identified as the PMT mean time and its uncertainty was the uncertainty in the mean $\sigma_{j,\mu} = \sigma_t/\sqrt{N_{bins}}$.

After applying the PCA corrections and determining each channel time the LB position was determined by minimising the time residuals of all PMTs that passed the cuts for a given run:

$$\chi^2 = \sum_j^{N_{PMT}} \frac{(\mu_j + t_{j,tof}^{MANIP} - t_{tof})^2}{\sigma_{j,\mu}^2}, \quad (3.3)$$

where μ_j and $\sigma_{j,\mu}$ were the channel time and uncertainty discussed earlier, and t_{tof} was the model calculated time-of-flight from the source at each fit trial position.

In order to ensure the quality of the fit, a run averaged mean time μ_{run} and spread σ_{run} were also calculated and all channels whose time uncertainty was $\sigma_{j,\mu} > 3\sigma_{run}$ were removed from the fit. Additionally, all PMTs whose occupancies were below a chosen threshold were also removed. These cuts affected the statistics differently depending on the position of the source, but an average of 5% of the tubes were removed.

This fit resulted in a source position resolution well below 1 cm. An additional systematic uncertainty of 2 cm was also associated with this fit, due to the typical differences observed between the fit positions and the manipulator position recorded.

Therefore a final LB position uncertainty of $\Delta r_{LB} = 2cm$ was assigned from the average of all fits.

3.3 Data selection

Before the optical data were fit, a quality check on the data from the PMTs was performed. As the optical model assumes averaged properties, it was essential that the conditions of data taking were as similar as possible for all runs and therefore a series of data quality cuts were applied in order to remove data points that sampled

the detector in special situations, like PMTs that were affected by shadows or lensing effects. Although in the NCD phase, these cuts affected a large portion of the available PMT for each run (reducing the amount of PMT not affected by cuts in a run by approximately 65% with respect to the previous phases), the overall quantity and quality of the optical data in the NCD phase improved due to the optimised scan scheme. For each run i and PMT j , a series of checks were performed to decide whether the PMT should be considered for the optical fit of that particular run.

A series of geometrical cuts were implemented to discard PMT data whose estimated optical paths crossed detector components were not considered in the optical fit model. The cuts identified in both D₂O and Salt phases are [83]:

Belly plate There are 10 acrylic plates, equally distributed around the equator of the AV, where the support ropes are attached. These plates have a larger thickness than the remaining of the AV and a series of grooves, which makes the optical paths difficult to model. Furthermore, these plates are bevelled at the edges, which causes the light to refract and concentrate in a projected square of PMTs behind the plates, causing an increase of its occupancy. This cut removed 8.3% of the data points. Figure 3.4(a) shows a diagram explaining how this cut is applied.

AV rope There are 10 loops of ropes supporting the AV, which means that a total of 20 rope cuts are applied. Any PMT whose light path crosses at a distance of $d_{min} < 15$ cm of a rope is removed from the fit. This cut affect 4.8% of the PMTs in a run.

Recirculation pipes A series of pipes used to recirculate the heavy water were attached along the AV down to the bottom. These pipes, close to the $\phi = 90^\circ$ meridian, can cause light to be both refracted and absorbed. A wide cut is applied for any light ray crossing the AV in that vicinity.

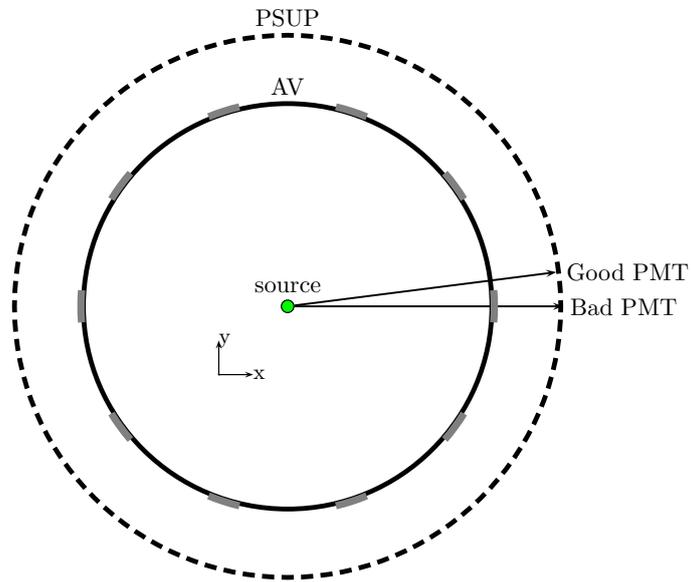
AV neck and connection ring The AV neck and the ring attaching it to the AV sphere affect the occupancy of the PMTs located behind it in the optical path. Thus an optical cut was implemented so that the PMTs whose light rays pass at less than 30 cm of the neck ring or go through the AV neck are flagged as bad and are not included in the optical fit. This cut affects 1.2% of the data points.

Prompt AV reflection This cut was implemented to account for PMT hits from reflected photons that are not removed by the prompt time window cut alone. For runs where the LB is in the most external positions, the PMTs on the opposite side of the detector are contaminated by light that reflects on the AV and arrives at the PMT inside the prompt window. This effect varies with the position of the LB, and thus a more dynamic cut was implemented. For runs with source radii $R > 450$ cm, only the PMTs satisfying the condition $\hat{p} \cdot \hat{s} \geq 0.1$ pass this cut, where \hat{p} is the PMT position unit vector and \hat{s} is the source position unit vector. The effect of this cut depends on the source position. An average of 3.5% of the statistics reduction is caused by this cut. Figure 3.4(b) shows a diagram of this effect.

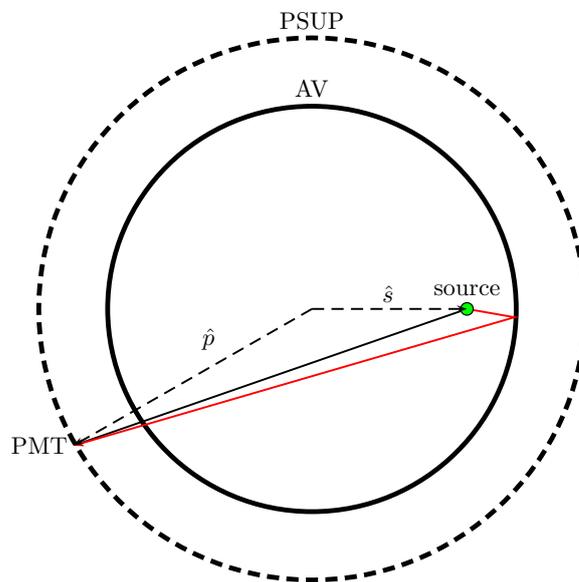
NCD attachment anchors During the construction of the detector 96 acrylic cylinders were placed in a grid pattern in the bottom of the AV, to be used in the third phase as anchors for the NCDs. For each run, PMTs whose light paths pass at less than 10 cm of any anchor are removed from the fit. This cut affects 1% of the points and is described in more detail in Chapter 4.

Most of these cuts are due to light propagation in the detector, which correspond to an approximate 27% reduction in statistics in D₂O and Salt phases, and an approximate 55% reduction in the NCD phase. An additional 3% reduction in statistics is caused by PMTs which have a large contribution to the χ^2 and that removed from the fit after a first pass.

In the NCD phase an additional geometrical cut had to be implemented, to deal with the NCD shadows. Although this effect could be dealt with in a form of an occupancy correction for a point like source [109], the LB has a non-negligible radius and thus it would be necessary to account for the uncertainties in the positions of both the source and the NCDs. Thus an optical cut was implemented, removing the PMTs affected by the NCD shadows from the fit. To deal with the uncertainty on the positions a tolerance parameter ΔL was introduced, which adds a radial distance to the effective radius of the NCDs. For each run and PMT, the minimum distance of the corresponding light ray to all NCDs was calculated. Any PMT for which the distance of the light ray to one of the NCDs was smaller than the tolerance parameter was removed from the fit. In Figure 3.5 a diagram of the NCD shadow cut is shown.



(a) Diagram of optical cut due to AV belly plates.



(b) Diagram of prompt AV reflection cut.

Figure 3.4: Diagrams of some optical cuts.

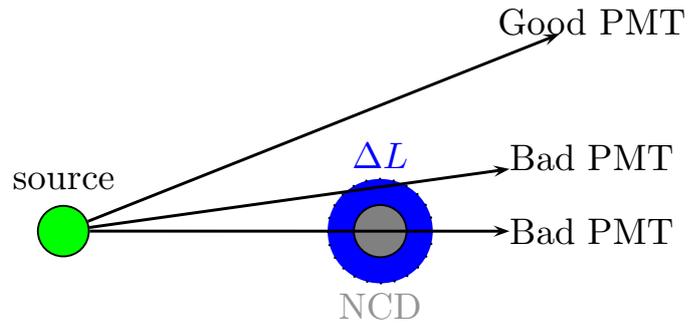


Figure 3.5: Diagrams of the NCD shadow cut. The blue zone depicts the tolerance around the NCD.

The statistical effect of this cut depended on the source position and the tolerance assumed. For example, for a central run, this cut can affect between 55% and 71% of the data points.

After applying the geometrical cuts, additional quality checks were performed while running the fit procedure. The fit was implemented to be ran through 5 iterations, after which a series of data quality cuts are applied based on the statistical contribution of the channel to χ^2 . These cuts depended on the particular method of analysis that are described in Sections 3.4.1 and 3.4.3.

3.4 Optical Calibration Fit

Along with the different phases of SNO, different fit methods were developed to better adjust to the characteristics of each phase. Two methods were implemented to perform the extraction of the optical model parameters. Section 3.4.1 describes the Occupancy-Ratio method which was used to analyse the optical calibration data in the first two phases of SNO, using central runs to normalise the measured occupancies and cancel the ϵ_j efficiencies from the occupancy ratio model prediction. Section 3.4.3 describes a new method implemented to extract the optical parameters in the NCD phase (Occupancy-Efficiency) by using a set of measured PMT efficiencies to obtain the same parameters.

The main figure of merit of the optical fit consisted in χ^2 obtained by minimisation using a custom implementation of the Levenberg-Marquadt minimiser [110]. Due to the typically large number of parameters in the fit, the fit algorithm was modified to speed up the process of building the covariance matrix, which otherwise scaled with the product of the fit statistics (on the order of 5×10^5 data points, after cuts) and the square of model parameters (~ 500). Further details about the fit procedure are described in [83].

3.4.1 Prompt Occupancy-Ratio Method

The *Occupancy-Ratio* (*OccRatio*) method uses the ratio between the intensities in two runs to eliminate the unknown PMT efficiencies ϵ_j . In this method, a central run with high statistics ($\sim 10^4$ hit PMTs) was used as denominator in the intensity ratio, so that the optical parameters can be obtained relative to the centre of the detector. In the equations presented in this section the central run is defined with the index $i = 0$.

Thus, in order to cope with this method some optical model properties had to be rearranged. The terms that can be precisely calculated from the source-PMT geometry, solid angle Ω_{ij} and Fresnel transmission coefficients (T_{ij}) were directly calculated for both runs. The ratio of these properties account for the geometrical

effects in the occupancy for both runs and are applied to the occupancy ratio as a geometrical correction:

$$\text{OR}_{ij}^{data} = \frac{N_{ij}}{N_{0j}} \left(\frac{\Omega_{0j} T_{0j}}{\Omega_{ij} T_{ij}} \right). \quad (3.4)$$

The model occupancy ratio is then:

$$\text{OR}_{ij}^{model} = \frac{N_i}{N_0} \left(\frac{R_{ij} L_{ij}}{R_{0j} L_{0j}} \right) e^{-(\delta d_{ij}^d \alpha_d + \delta d_{ij}^a \alpha_a + \delta d_{ij}^h \alpha_h)}, \quad (3.5)$$

where δd^d , δd^a and δd^h are the path differences in the light propagation in each media. From Equations 3.4 and 3.5 one can now extract all the optical model parameters by minimising the χ^2 goodness-of-fit estimator:

$$\chi^2 = \sum_i^{N_{runs}} \sum_j^{N_{PMT}} \frac{(\text{OR}_{ij}^{data} - \text{OR}_{ij}^{model})^2}{\sigma_{ij}^2 + \sigma_{PMT}^2(\theta_{ij}, \text{PMT})}, \quad (3.6)$$

where $\sigma_{ij} = \Delta \text{OR}_{ij}$ is the statistical uncertainty in the occupancy ratio due to counting statistics in N_{ij} . The term $\sigma_{PMT}(\theta_{ij}, \text{PMT})$ is an additional systematic uncertainty that is included to account for the variability in the PMT response with incident angle θ_{PMT} ³.

In the third phase of SNO (NCD phase), the introduction of the NCDs brought additional optical effects that had to be considered, such as NCD induced shadows and light reflections. The former was dealt with by creating an additional data selection cut, described in Section 3.3, while the latter was addressed by implementing an occupancy correction, described in Section 4.3.4.

The implementation of the optical cut to account for the NCD shadows led to a 70% decrease in the statistics of the optical fit. This cut affected the central runs even more than any other runs, which led to not only to the removal of a

³The PMT variability has an effect of the order of 10% in the χ^2 and allows to properly take into account the spread of the PMT efficiency that is larger for higher incidence angles. That is not simply due to counting statistics, but also due to systematic differences in response as a function of incidence angle.

significant amount of PMTs from both pairs of runs, but also to the problem that the occupancy ratio depended on the convolution of two different shadow patterns, since the NCD shadows depend on the position of the source. For this reason the precision in the extraction of the optical parameters became compromised, such as the water attenuations ($\alpha_{d,h}$) and the PMTR [111].

In order to minimise the statistics loss an optical fit was developed that uses the PMT occupancies directly, as opposed to the occupancy ratios. This required that the PMT efficiencies (ϵ_j) were used as input to the optical fit.

3.4.2 Extraction of the PMT Efficiencies

The extraction of the PMT efficiencies were originally a separate step of the optical calibration, due to the large number of parameters (≈ 9000) that it would introduce in the fit. It's extraction method was originally implemented in [106] and became a critical parameter in the optical analysis of the NCD phase.

After extracting the other optical parameters using the OccRatio method, one could use them in Equation 3.1, along with the run information, to estimate the model occupancy of a PMT. The ratio of the data/model occupancies

$$\epsilon_{ij} = \frac{O_{ij}}{N_{ij}} \quad (3.7)$$

could then be used as the efficiency estimator of a PMT. Assuming that the PMT efficiencies remain approximately unchanged in an OCA scan, these efficiencies were then averaged for each PMT over all runs, extracting then an average PMT efficiency (ϵ_j) that is quoted in Equation 3.1.

Thus, for a run i and PMT j , a *raw* efficiency (ϵ_{ij}) is calculated using Equation 3.7. However, this efficiency incorporates a residual dependency on the source position. In order to obtain a normalised PMT efficiency let's consider a *run-averaged* PMT efficiency (ϵ_i^{run}):

$$\epsilon_i^{run} = \frac{1}{N_{PMT}^i} \sum_j^{N_{PMT}^i} \epsilon_{ij}, \quad (3.8)$$

where N_{PMT}^i is the number of PMTs that contributed to the optical fit in run i . Then, for each PMT j , we could average its *raw* efficiency over all runs where it contributed to the optical fit N_{run}^j , by dividing each run efficiency by the run average,

$$\langle \epsilon_j \rangle = \frac{1}{N_{run}^j} \sum_i^{N_{run}^j} \frac{\epsilon_{ij}}{\epsilon_i^{run}}. \quad (3.9)$$

Finally, since the model is sensitive only to relative, and not absolute efficiencies (N_i is an arbitrary normalisation), the efficiency obtained in Equation 3.9 is normalised to unity by dividing the average efficiency of the individual PMTs that contributed for the optical fit (N_{PMT}), for the overall average efficiency. Figure 3.6 shows the distribution of the PMT efficiencies obtained using this method for one of the first OCA scans (September 2000) and for the interim D₂O scan (October 2003). The last one was used as MC input and in the *Occupancy-Efficiency (Occupancy)* optical calibration method. It should also be noted that this procedure was performed independently for each wavelength, resulting in six separate efficiency distributions. Although the PMT efficiencies were propagated into the MC simulation as a PMT by PMT correction, the Occupancy method also used the spread of this distribution as the PMT variability, in the $\sigma_{PMT}^2(\theta_{ij}, \text{PMT})$ term of Equation 3.10. The statistical uncertainties of the PMT efficiencies vary with the amount of runs in which a PMT was considered good. The mean statistical uncertainty in the extraction was of the order of 5%.

This extraction was performed in all D₂O and Salt phase scans, in order to verify the stability of the PMT efficiencies over time. This was essential to validate the use of the Occupancy method in the NCD phase. In Figure 3.7 one can see the distributions of the PMT efficiencies for two D₂O scans (September 2000 and October 2003). A strong correlation is observed, as well as a very small change, which means that the PMT efficiencies have not changed significantly over the SNO data taking period until the NCD phase.

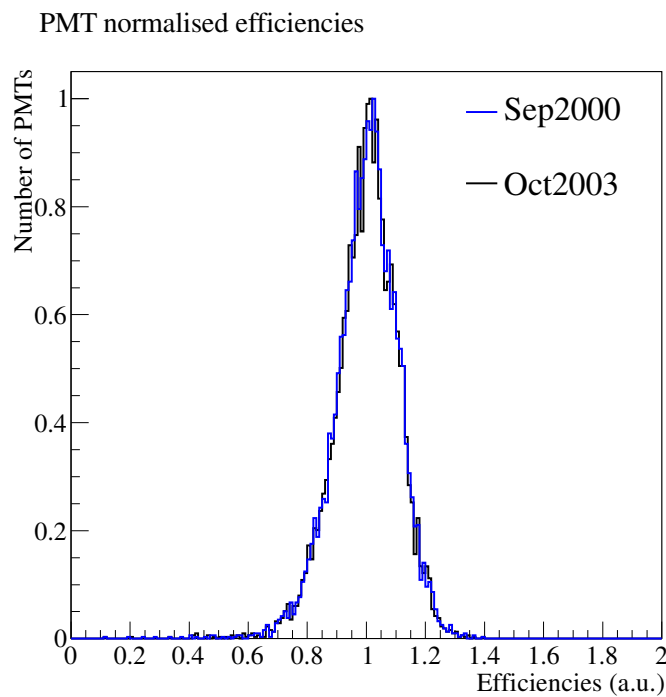


Figure 3.6: PMT normalised efficiencies for a first phase scan and for the interim heavy water scan at 500 nm.

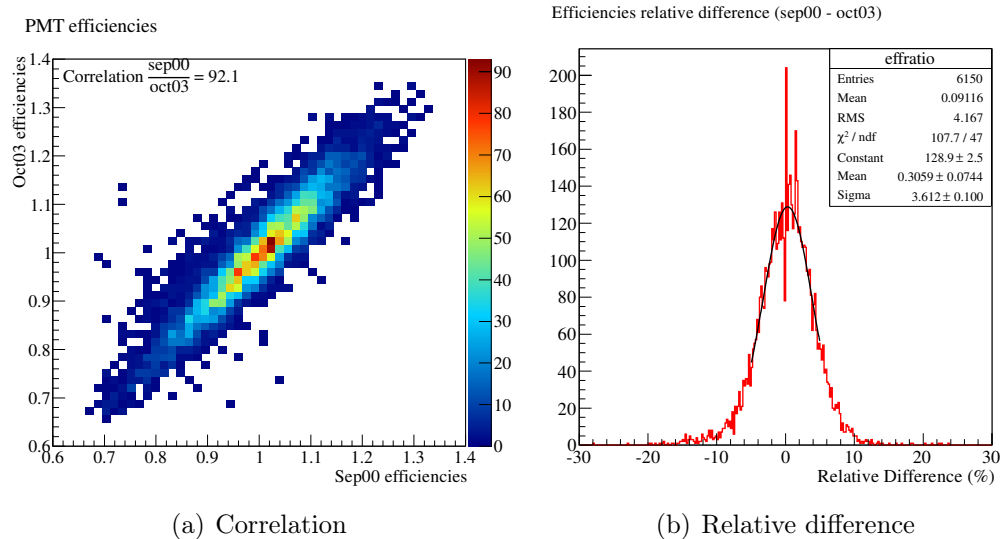


Figure 3.7: PMT efficiencies for the September 2000 and October 2003, and correlation between the scans for a source wavelength of 500 nm.

3.4.3 Occupancy-Efficiency Method

The Occupancy method uses PMT occupancies directly as observables in the optical model. The problem of statistics loss caused by the optical cuts is thus reduced by using the PMT efficiencies (ϵ_{ij}) as an input in Equation 3.1.

Assuming that the PMT efficiencies for a PMT j remain unchanged for all runs in a scan, one can directly compare the measured occupancy O_{ij} with the efficiency-weighted model occupancy N_{ij} and the fit becomes the minimisation of the χ^2 goodness-of-fit:

$$\chi^2 = \sum_i^{N_{run}} \sum_j^{N_{PMT}} \frac{(O_{ij} - N_{ij})^2}{\sigma_{ij}^2 + \sigma_{PMT}^2(\theta_{ij}, \text{PMT})}, \quad (3.10)$$

where the term $\sigma_{PMT}^2(\theta_{ij}, \text{PMT})$ represents the error associated with the efficiency measurements as a function of θ_{PMT} .

3.5 Summary

In this chapter the optical calibration concepts were introduced, providing a basis to understand the optical calibration model in SNO.

The OCA methods were significantly changed with the introduction of the NCDs into the detector, mostly due to its effect in the detector geometry and response. In Chapter 4 we will continue to describe the optical calibration with more emphasis on the work developed by the author of this thesis and the results obtained.

Chapter 4

Optical Calibration Results

In Chapter 3 a description of the *optical calibration (OCA)* model and principles of the analysis were presented. This chapter will have a particular emphasis on the work carried out this thesis and the results obtained in the optical calibration of the NCD phase.

The work described in this chapter covers mostly the effort of the optical calibration in the NCD phase, where the introduction of the NCDs led to a different detector geometry and response and posed many challenges to extract the optical parameters of the detector. In the NCD phase a new optical calibration fit was developed to use the PMT efficiencies as a base to predict the PMT occupancies. For all the analyses of the OCA data in the NCD phase, the PMT efficiencies extracted in the interim D₂O scan (October 2003) were used as a baseline. A description of the improvements implemented will be performed. Some studies, related to the detector response asymmetry, while not conclusive enough to lead to a change in the response model, have identified sources of inconsistency in the detector response explaining an identified energy response bias correction that was applied to the LETA data processing.

A more detailed description of the analysis method will be presented, as well as a description of the systematic uncertainties associated with the OCA analysis. Finally, a description of the importance of the optical calibration in the neutrino analysis of SNO will be presented, with a description of the effect of the OCA parameters in the position and energy estimation.

4.1 Optical Calibration Data

An OCA scan consists in a series of runs of data taking with the LB deployed in different positions, and the laser tuned for different wavelengths. Each run is defined by the position of the LB and the source wavelength. The data taking plan was the same for the first two phases of SNO. However in the third phase the different detector geometry lead to a re-planning of the scan scheme.

OCA method in D₂O and Salt phases

In the first and second phases of SNO, the optical calibration consisted in a series of runs with the LB placed in different locations in order to sample most of the detector. In Figure 4.1, is shown the LB positions sampled in the first of the D₂O phase OCA scans (February 2000), in the $y - z$ plane¹.

The LB positions are represented by black circles and the shaded area in the outer part of the acrylic vessel represents the areas not accessible by the LB due to limitations in its support mechanism. In the figure the ropes (two side ropes and one vertical rope) responsible for the source positioning are also shown. A typical scan in these phases consisted in a series of runs taken along both the $y - z$ and $x - z$ planes, with all 6 wavelengths.

A series of special runs taken in the centre of the detector, the *central runs*, usually had more statistics, to avoid increasing the statistical errors of the relative occupancy with respect to the simple occupancy. Additional central runs were usually taken with the LB facing each of the four orthogonal orientations in order to sample the source anisotropy independently of the detector optical parameters.

During this period the OCA scans started with a high statistics PCA calibration run. This is a central run taken with very high statistics to perform the time calibration of the PMTs, as described in Section 2.6.2 [112].

¹As mentioned in Section 2.6.2, the source manipulator system contains four side ropes attached to the interior of the detector, allowing the calibration sources to be positioned in a wide range of positions along the $y - z$ and $x - z$ planes.

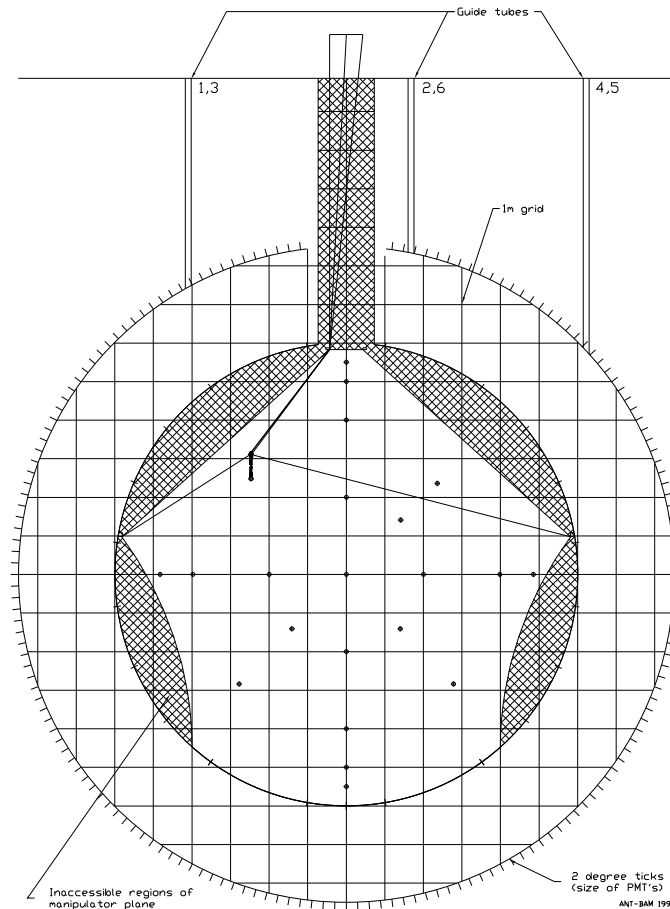


Figure 4.1: Laserball positions in optical calibration scan of February 2000. Figure taken from [83].

In Table 4.1 is a list of the most relevant OCA scans taken during the running time of SNO. The October 2003 scan was taken during the NCD commissioning phase, when the heavy water was desalinated and thus worked as an assessment of the detector changes since the D₂O phase. This scan was also used later as a basis for the OCA analysis of the NCD phase scans.

OCA method in NCD phase

In the NCD phase, due to the additional optical effects introduced by the NCDs, the scheme of the OCA scans was changed. A series of *horizontal runs* were added to the scan plan, where the LB was placed in the equator region ($z_{LB} = 0$) and outside the NCD array, in order to take data without NCD shadowing effects. Additionally,

Scan	Characteristics	Re-analysed in this thesis
February 2000	First D ₂ O scan. Only sampled 365nm and 500nm	No.
September 2000	Full D ₂ O scan (all wavelengths sampled)	Yes.
January 2001	Last D ₂ O scan.	No.
September 2001	First Salt scan.	Yes.
November 2001	Stability check.	No.
February 2002	Stability check.	No.
May 2002	LB positions optimised.	No.
October 2002	Diagonal scan.	Yes.
January 2003	Stability check.	Yes.
April 2003	Stability check.	Yes.
August 2003	Last Salt scan.	Yes.
October 2003	Interim D ₂ O scan.	Yes.
July 2004	First NCD scan. Evaluate changes.	No.
October 2004	New laserball.	Yes.
February 2005	Optimised LB positions.	Yes.
May 2005	Stability check.	Yes.
October 2005	Stability check. H ₂ O data taken.	No.
February 2006	Improve NCD position fits.	Yes.
August 2006	Last OCA scan.	Yes.

Table 4.1: OCA scans performed during the whole duration of SNO.

the duration of both these and the central runs was longer, in order to increase the statistics. Another change implemented was a re-planning of the LB positions, in order to minimise the number of shadowed PMTs.

Besides these changes, that were applied for all NCD phase scans, some scans also suffered some modifications to their run plan in order to address specific purposes. An example of such changes is the February 2006 scan where the calibration plan included more LB positions in order to be able to fit the NCD positions from the OCA data. In the lower section of Table 4.1 a list of the NCD phase OCA scans is given.

Additionally, the higher statistics of the OCA runs in the NCD phase led to a similar statistics, after cuts, with respect with the previous phases, despite the new detector geometry and acceptance.

4.2 Validation of the Occupancy-Efficiency Method

After the optical cuts and corrections are applied and both the LB and NCD positions are extracted, all conditions necessary to extract the optical parameters are met. In this section, the main goal is to show the typical values for these parameters using as reference the optical data taken in a D₂O scan. Additionally, a comparison that both methods of fit (OccRatio and Occupancy) will be shown to yield similar results, which demonstrates that the application of the Occupancy fitting method is a valid choice to overcome the difficulties imposed by the NCD phase.

As previously stated the primary results of the optical fitting procedure are the determination of:

- heavy water attenuation,
- light water attenuation,
- PMT/reflector assembly angular response.

Additionally the fit also produces a set of parameters describing the laserball light distribution. Although the fit model also accounts for the acrylic attenuation α_a , there are very strong correlations with the light water attenuations, and thus this parameter is fixed to values from prior measurements of light transmission through the acrylic panels that make up the AV [83].

Figure 4.2 shows the extracted PMTR from the October 2003 scan with both fitting methods (OccRatio and Occupancy) at 500 nm, showing also the results obtained with the OccRatio method in the September 2000 scan. For the Occupancy method, the fit used the PMT efficiencies extracted in the first optical scan in the D₂O phase (September 2000). The results are shown with total uncertainties, which include a set of systematic uncertainties. The results for all other wavelengths were consistent with the ones presented.

Figure 4.3 shows the extracted water attenuations (D₂O and H₂O) at all six wavelengths. Again, the results are consistent in both methods. The error bars in the October 2003 scan fitted with the OccRatio method are total uncertainties. All other results shown display only statistical uncertainties.

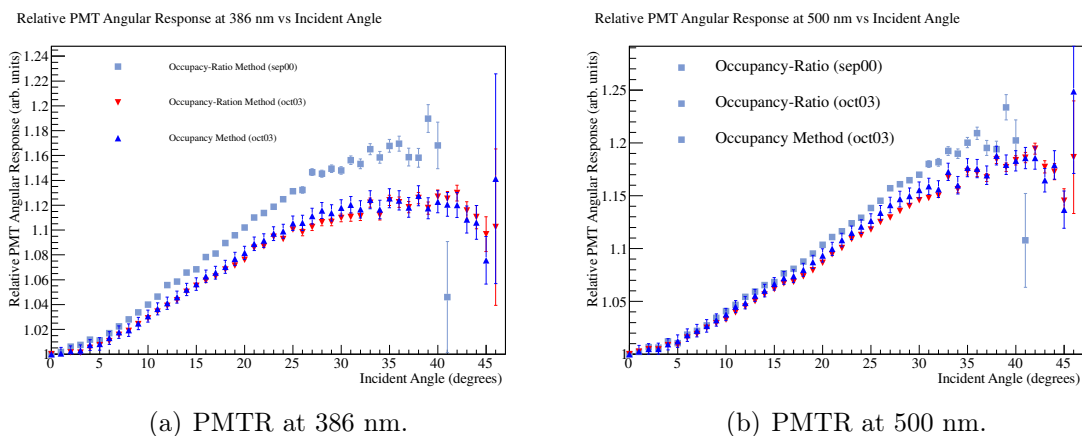


Figure 4.2: Relative PMT angular response at 386 and 500 nm in October 2003 optical scan extracted with different optical fitting methods. For comparison, the results obtained with the Occupancy-Ratio method in the September 2000 scan are also shown.

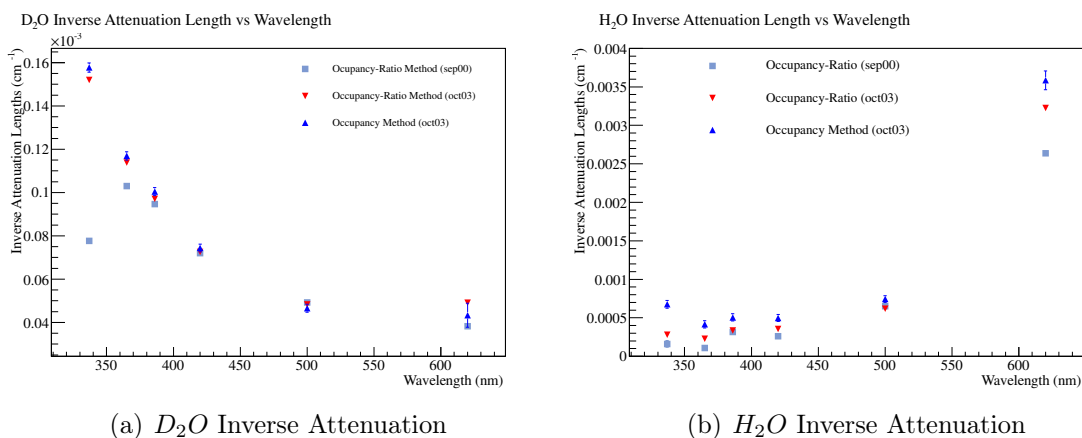


Figure 4.3: Media attenuation coefficients extracted in the October 2003 scan for both OccRatio and Occupancy methods for all six sampled wavelengths. The results extracted in the September 2000 scan are also shown.

A detailed list of systematic uncertainties is explained in Section B.1. The effect of the systematic uncertainties was observed to affect mostly the media attenuations, while the PMTR seemed to be very robust to the systematic effects.

The overall conclusion on the comparison between the OccRatio and Occupancy methods is that the results agree within the total uncertainties. Furthermore, by comparing the results obtained between two heavy water scans with data taken two years apart it is noticeable a steady decrease in the PMT angular response, which

most likely account for differences in ageing effects of the detector².

4.3 NCD Optical Effects

The new effects brought by the NCDs in the PMT occupancy data had to be properly considered in the optical calibration. These effects were the shadow patterns caused by the NCDs, which decreased the occupancy of the affected PMTs, and the reflections of the PMTs, which increased the occupancy of all PMTs. This section will cover both effects and how they were dealt with.

4.3.1 NCD shadows

The NCD shadows were particularly relevant in the OCA analysis in the sense that it decreased the occupancies of the affected PMTs. Furthermore, by having 40 NCDs in the D₂O volume, a large number of PMTs were affected, which led to the implementation of a different fitting method for the optical calibration.

If we considered a point source of light, it would be possible to correct the PMT occupancies with the ratio of NCD-shadowed solid angle [109]. However, the LB diameter is twice the size of an NCD, so the accuracy of the correction would vary with the source light distribution. Since the available data statistics were still enough, it was simpler to deal with the NCD shadows by means of a simple cut, thus removing the affected PMTs from the optical fit.

The NCD shadow cut is a purely geometrical cut, depending on the positions and sizes of the LB, NCD and PMT. Additionally, a tolerance parameter was also added to control the acceptance of the cut. The tolerance parameter, ΔL , consists in the physical radius of the NCDs plus an additional radial distance to account for the position uncertainties. Therefore it cannot be lower than 2.579 cm, which is the physical radius of the NCDs.

²The apparent difference in the D₂O attenuation at the 337 nm between Sep00 and Oct03 scans is not real and is caused by a problem in the optics fibres in Sep00.

For each NCD phase scan, the NCD positions were fitted from the OCA data. From the extracted uncertainties in the positions, a NCD radial uncertainty was defined as $\Delta r = \sqrt{\Delta\mu_x^2 + \Delta\mu_y^2}$, where $\Delta\mu_{x,y}$ are the NCD coordinate uncertainties. The tolerance parameter ΔL was then defined as

$$\Delta L = \Delta r + 3\sigma_{\Delta r} + \Delta r_{LB}, \quad (4.1)$$

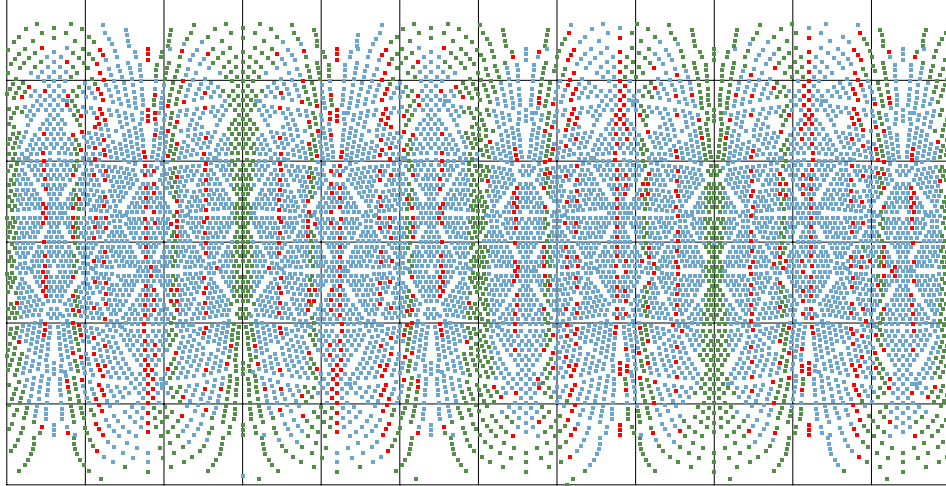
where Δr was the average NCD radial position uncertainty ($\Delta r = 2.2\text{cm}$), $\sigma_{\Delta r}$ was the spread of the radial uncertainty for all 40 NCDs ($\sigma_{\Delta r} = 0.3\text{cm}$), in order to account the fact that not all NCD positions had the same accuracy, and Δr_{LB} was the uncertainty in the LB source position ($\Delta r_{LB} = 2\text{cm}$) [113]. Applying these values in Equation 4.1 yielded a tolerance parameter of $\Delta L = 5.1\text{cm}$, which could be used for all NCD scans [108]. Nonetheless, in order to ensure the most accurate information, the tolerance parameter was calculated for each individual NCD scan.

4.3.2 Geometrical cut

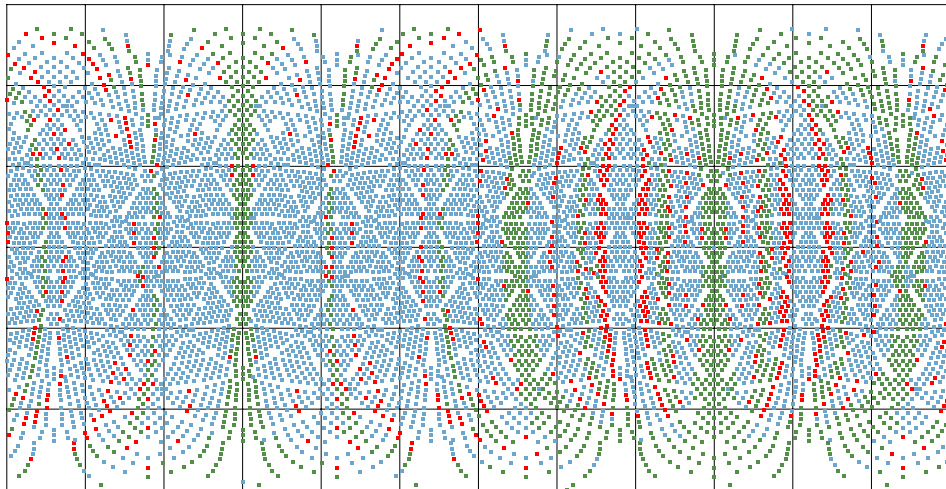
Using the shadow cut described in the previous subsection, a geometrical cut was implemented into the analysis algorithms. The cut removed the photons entering regions in a radius ΔL around the central axis of any NCD. For each set consisting of a LB position and a PMT, determination of the full optical path was performed (D_2O , acrylic, H_2O) and the minimum distance of the photon path to the surface of each of the 40 NCDs was calculated (δL). If the minimum distance was smaller than the tolerance parameter ($\delta L < \Delta L$), the corresponding PMT was flagged as being shadowed and was consequently removed from the optical fit for that run.

Figure 4.4 shows the effect of the NCD shadow cut for a central (source located in the centre of the detector) run and for a high radius run (source outside the NCD array). The different colours show the effect of using different tolerance values. Both red and green marks represent tubes that pass a geometrical cut of $\Delta L = 0\text{ cm}$ (only the NCD radius is considered in the geometrical cut), while the green markers represent the tubes that pass the cut when using a tolerance parameter of $\Delta L = 5.1\text{ cm}$. This cut affected mostly the runs inside the NCD array, due to overlapping shadow patterns. In a typical central run with a tolerance parameter of $\Delta L = 5$

cm, approximately 71% of the PMTs were removed, while in a run outside the NCD array the cut typically removed 41% of the PMTs, for the same tolerance parameter.



(a) Source at centre (0,0,0)



(b) Source inside the NCD array (0,200,0)

Figure 4.4: NCD shadow cut considering sources at different positions. The different colours represent the difference in affected PMTs by using different tolerance parameters. The figure shows the location of the PMTs on a plane of the two spherical coordinate angles, where the X axis represents the azimuth angle ϕ and the Y axis represents the inclination angle θ . The radius is fixed to the PSUPs distance to the centre of the detector.

4.3.3 Effects on the Optical Parameters

Due to the large amount of PMTs removed by this cut, concerns were raised due to possible biases in the analysis caused by such a drastic reduction of statistics. A good way to verify the effects of this cut in the extraction of the optical parameters was to analyse a pre-NCD phase scan. As shown in Section 4.2, the Occupancy fitting method yielded consistent results when compared with the OccRatio method. Therefore, in order to effectively compare if this cut would affect significantly the results in the NCD phase scans, two analyses were performed over the interim D₂O scan (October 2003): one with and other without the NCD shadow cut.

The results obtained for the PMTR are shown in Figure 4.5 for two selected wavelengths (420 and 500 nm). The error bars shown in the figures only contain the statistical uncertainties. Nonetheless a very good agreement is clearly visible, with the results being consistent within their statistical uncertainties. Similar results were obtained for the water attenuations.

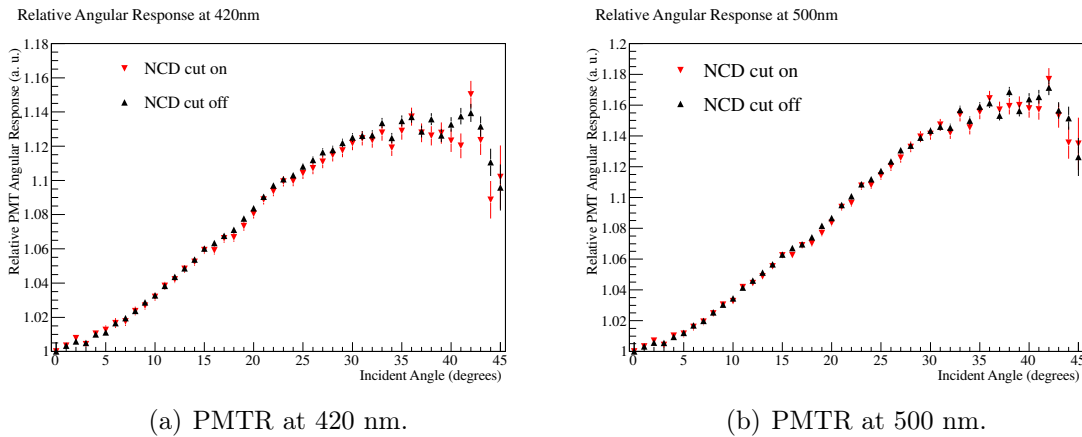


Figure 4.5: PMT angular response extracted at 420 and 500 nm on the October 2003 scan with and without applying the NCD shadow cut. Both analysis were performed with the Occupancy-Efficiency method.

The results show that by using the Occupancy method with the NCD shadow cut, the statistics reduction does not impose any bias in the optical parameters, despite an effect in their uncertainties. This is expected as the statistics reduction is significant. However, it is important to remark that in the NCD phase, by using the Occupancy

method it is possible to minimise the statistics loss by avoiding the convolution of shadow effects from two scans.

4.3.4 NCD Reflections

After accounting for the NCD shadows, the NCD reflections are the major component affecting the PMT occupancies that is caused by the NCDs. The main reason to implement a NCD reflection correction was to ensure an unbiased measurement of the media attenuations.

There are other sources of reflections in the detector, however most of them were dealt with by setting the prompt time window to a full width of ± 4 ns. The effect of the NCD reflections can be clearly seen from the timing histogram from two identical central runs in which one has the NCDs and the other does not. Figure 4.6 shows this effect, where an increase in the number of hits due to reflections in the NCD phase run is clearly visible. It is interesting to note, however, that the NCD phase run shows a decrease in the number of hits in the PSUP reflection peak (≈ 75 ns). This is caused by the fact that the NCDs, despite being reflective, cast a large shadow pattern that blocks the reflections coming from the PSUP.

Although the prompt time window cut would remove most of the reflections, in the case of the NCD reflections this is not enough, as the NCDs are inside the D₂O volume and a non-negligible fraction of the reflected photons hit the PMT inside the prompt time window. Furthermore, the diffuse nature of the NCD reflections makes it impossible to correct by means of an optical cut, as all the PMTs are affected. It is also very difficult to model all the reflection paths from the LB to the NCDs and then to the PMTs, as each position has an associated uncertainty.

Therefore, a more sophisticated method to deal with the NCD reflections was implemented, by performing an occupancy correction. Two methods were followed, one purely analytical and a second one based on Monte Carlo simulation. These will be addressed in the following sections.

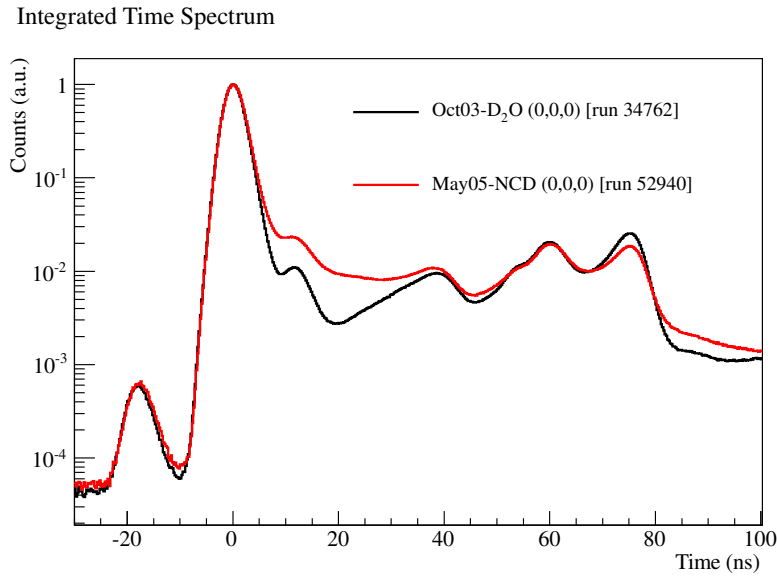


Figure 4.6: Time spectra of two central runs, integrated over all PMTs. Run 34762 was taken in the interim D_2O phase and does not contain NCDs. Run 52940 was taken during the NCD phase and contains NCDs. Both distributions are normalised at the prompt peak.

Analytical PMT occupancy correction

This method assumed that the PMT hits from NCD reflections were mixed with the direct light prompt signal and thus could not be separated from it. This method consists in evaluating the acceptance probability, w_{ij} , of a photon leaving the source i , reflecting on an NCD, and hitting a PMT j within the prompt time window. This probability is based on solid angle acceptances weighted by the NCD reflectivity, to account for the dependence in the photon wavelength [108]. As there is no information about the direction of the incident photon, the reflections are assumed to be diffuse, and thus, untraceable.

Figure 4.7 show the acceptance probability evaluated for a series of NCD phase scans. As it can be observed, the reflection probabilities range from 0.5% to 1.5%, mostly due to the narrow prompt time window.

The probability w_{ij} was then used to correct the observed occupancy O_{ij} , being combined with the MPE correction, which corrects for the effect of registering a single PMT hit caused by multiple photoelectrons, by effectively increasing the occupancy. In fact, the NCD reflection correction worked in a way similar to the MPE correction,

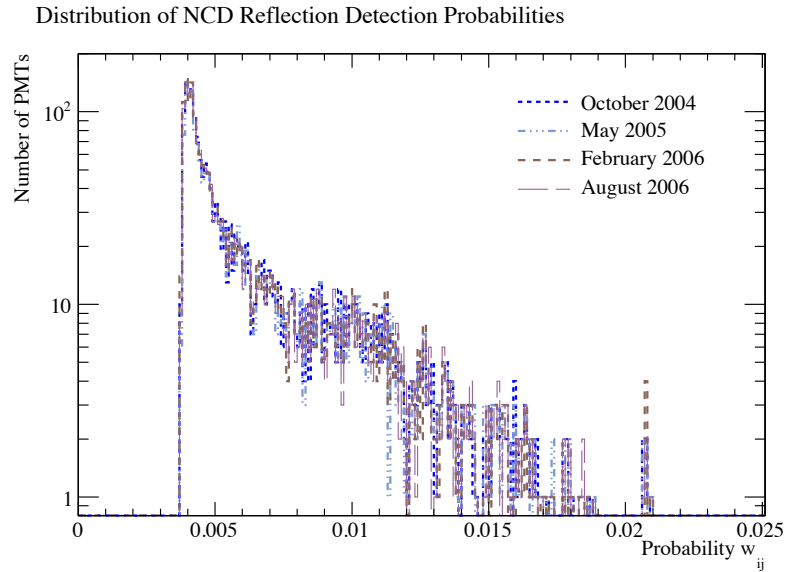


Figure 4.7: Acceptance probability of a NCD reflected photon hitting a PMT in the prompt time window. Figure from [108].

but instead it decreased the observed occupancy O_{ij} .

The resulting corrected occupancy μ_{ij} was then obtained from [108]:

$$O_{ij} = 1 + (w_{ij}\mu_{ij}) e^{-\mu_{ij}} \quad (4.2)$$

These combined corrections in general resulted in an approximated increase of the order of 1 – 2% in the occupancies, depending on the location of the source and the PMT. This total increase resulted from the fact that while the reflection correction caused a decrease in the occupancy to compensate the amount of reflected light within the prompt time window, the MPE correction increased the occupancy to compensate the multiple PMT hits counted as single hits. As the latter correction dominated over the whole prompt time window, the total net change in the occupancy was an increase, albeit smaller than in the previous phases ($\approx 5\%$) [83].

PMT Occupancy Correction using Monte Carlo

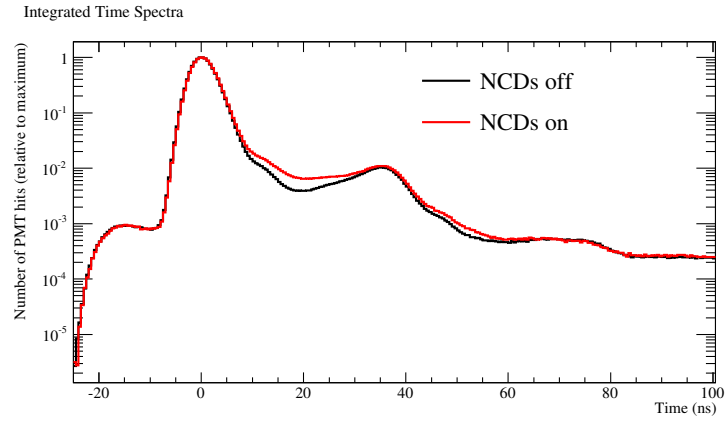
An alternative method, relying in the generation of Monte Carlo simulations of the NCD scans was also developed to correct the NCD reflections. As the previous

method, the aim was to build a correction to the occupancy to remove the portion of signal due to NCD reflections that affected the prompt peak. As it was shown in Section 4.3.4, this effect accounted for a relatively small amount of signal in the prompt peak, due to its narrow time window (± 4 ns).

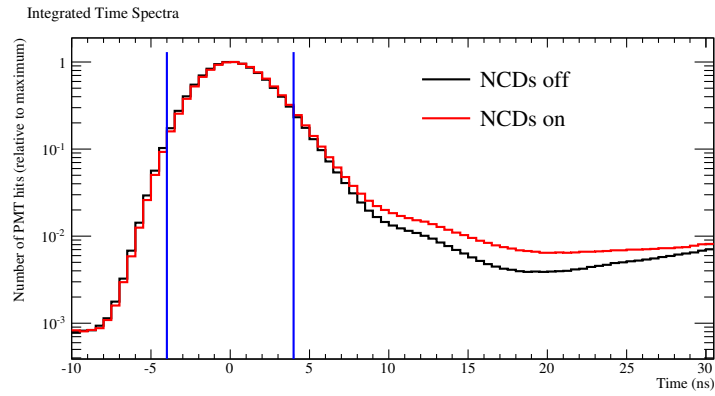
In order to obtain a correction two sets of *Monte Carlo (MC)* simulation runs were produced with fixed conditions. The only difference between the sets was that one included the NCD array geometry, while the other did not include the NCDs. The goal was to compare the PMT occupancies between the runs generated in the same position with and without the NCDs in the geometry. Each pair of runs used the same seeds and random numbers, to ensure that the only effect in the observed occupancies was caused by the NCD reflections. Figure 4.8 show the time distribution of the signal obtained for a central run generated by MC. Figure 4.8(b) shows a detail in the region around the prompt peak. Due to the different statistics caused mostly by the NCD shadows, both spectra are normalised at the peak. The difference between the curves in the prompt peak is very small and only noticeable towards its upper edge.

In order to isolate the effects from the NCD reflections, the simulations were configured to discard other effects that would compete with the correction, such as Rayleigh scattering and the MPE correction. Additionally a very large amount of positions were simulated in order to avoid effects from statistical fluctuations in the correction. A total of 875 positions were simulated in the detector distributed along the planes where the calibration sources could be deployed. Although several of these positions were never or seldom used in an optical calibration scan, by sampling a larger amount of positions it was possible to account for the uncertainty in the source position. Furthermore, the two data sets were generated in the most similar fashion as possible, using the same source positions, random seeds and PMT and laser properties. The data was later analysed where patterns were searched, such that could be used to create an occupancy correction that could be robust for the uncertainties in the optical fit.

The NCD reflections cause an increase in the PMT occupancy, which in the optical fit will translate into a shift in the fitted optical parameters, with particular incidence in the D_2O attenuation length, which is decreased as a result of the NCD reflections. This effect is clearly illustrated in Figure 4.9(b) where the ratio of the



(a) Integrated Time Spectrum



(b) Integrated Time Spectrum

Figure 4.8: PMT hit time distribution for a central run generated with Monte Carlo events with and without the NCDs. Both distributions are normalised at the prompt peak.

PMT occupancies are shown for all simulated scans as a function of the light rays path length in D_2O . The ratio was obtained according to:

$$w_{ij} = \frac{O_{ij}^{NCD}}{O_{ij}^{no-NCD}}, \quad (4.3)$$

where O_{ij}^{NCD} is the occupancy obtained from the MC run i in PMT j with the NCD reflections turned on and O_{ij}^{no-NCD} is the corresponding pair NCD-PMT with NCD reflections turned off.

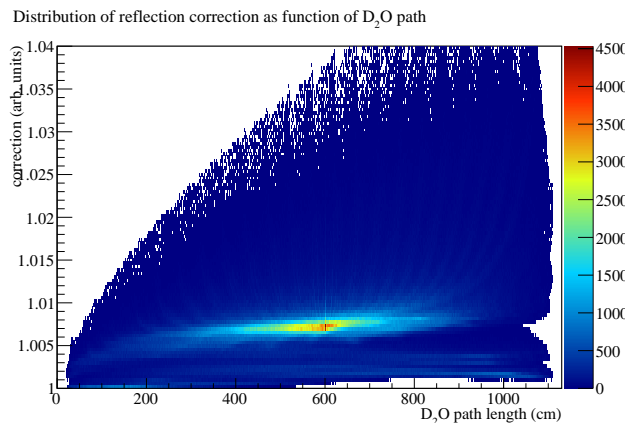
Figure 4.9(a) shows the distribution obtained when considering a dependence in the D_2O path length (d_{D_2O}), while Figure 4.9(b) shows the corresponding profile

of the distribution. The points in the profile correspond to the mean ratio in the occupancies - the occupancy correction - for a given distance traveled in the D₂O and the error bars represent the uncertainty in the correction defined as the *root mean square (RMS)* in the occupancy ratio. From Figure 4.9(a) it is possible to notice that there is a significant spread on the occupancy ratio. It is also clear an increase of the ratio in the occupancies with the D₂O path length. Obviously, as the distance traveled by the light rays in heavy water increases, the amount of reflected photons reaching the prompt time window increases as well, mimicking the effect of a smaller attenuation length. There is also a regular pattern observable in the average ratio, especially for distances above 600 cm. This pattern is caused by the regular positioning of the NCDs between the source and the detector, combined with the fact that as the distance increases, so do the amount of PMTs that are discarded due to shadows, resulting in a larger contribution from secondary reflections.

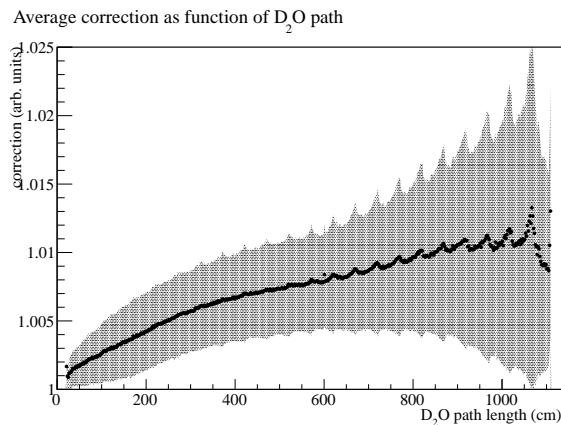
The results shown in Figure 4.9(b) could be used as a correction by themselves. However, as the large error bars indicate, this correction would have a large uncertainty as it would apply the same correction to PMTs with different occupancy ratios but with the same D₂O path lengths. This spread (error bars in Figure 4.9(b)) reflects particular cases that are not taken into account by using an unidimensional correction. To illustrate this, let's consider the following two situations: let's consider a run whose source is located close to the AV along the X or Y axes and a PMT on the opposite side of the detector; and a second run whose source is located close to the detector neck (along the Z axis) and a PMT at the bottom of the detector. In both cases, the D₂O path length is roughly the same, but due to the alignment of the NCDs along the Z axis, the amount of reflected photons arriving at the PMTs inside the prompt time window is different.

Several other observables were tested to build an unidimensional correction. Some of the most relevant examples are shown in Figure 4.10. However, similar spreads were observed, indicating that a correction based on a single measurable quantity would not be as accurate as necessary.

It is hard to define what would be the accuracy of this correction, as one of objectives is to test the analytical correction itself and it is not trivial to estimate the effect of the convolution of the reflections with the different elements and physical processes in the detector. Therefore, it was set as a goal that the correction should



(a) Distribution of occupancy ratio versus D₂O path length.

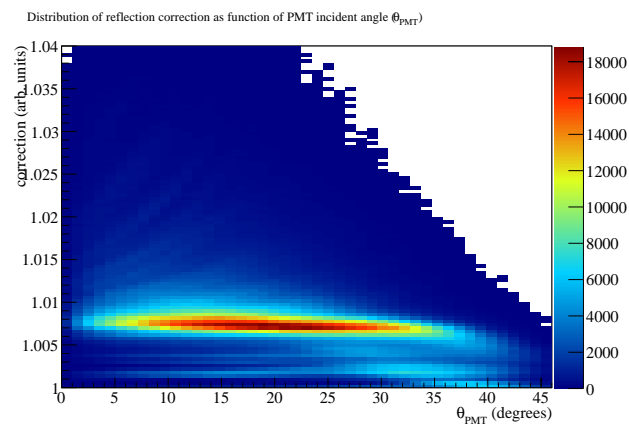


(b) Profile of occupancy ratio versus D₂O path length (RMS).

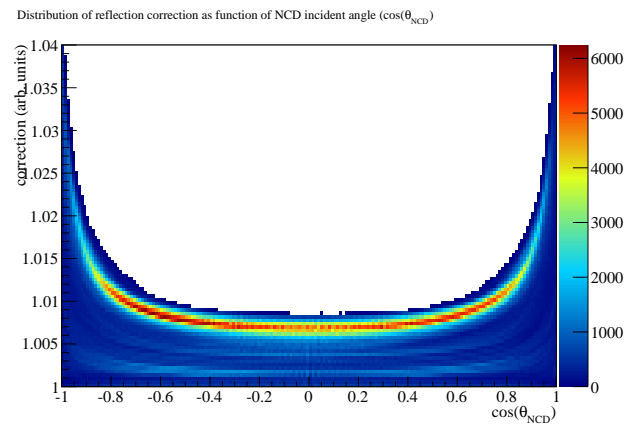
Figure 4.9: Distribution of the ratio of occupancies (with and without NCD reflections) as a function of the photon path length in D₂O. The profile of the distribution is also shown. The colour code represents the number of PMT hits for each pair (occupancy; D₂O path length).

not have a spread larger than 1% of the occupancy ratio. This uncertainty in the correction would mean that the correction itself would be more accurate than the typical statistical uncertainty in the occupancy.

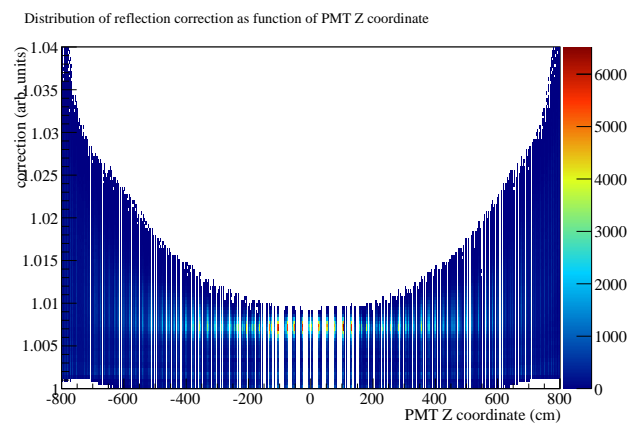
In order to achieve this precision in the correction, an alternative approach was followed by combining the observations discussed previously into the production of a single 2D correction. The aim was to obtain a distribution of occupancy ratios that could be accurately defined by a combination of two measured quantities. However, although the uncertainty was successfully reduced through this method, it still didn't



(a) Distribution of occupancy ratio versus PMT incidence angle.



(b) Distribution of occupancy ratio versus NCD reflection angle along Z.



(c) Distribution of occupancy ratio versus PMT z position.

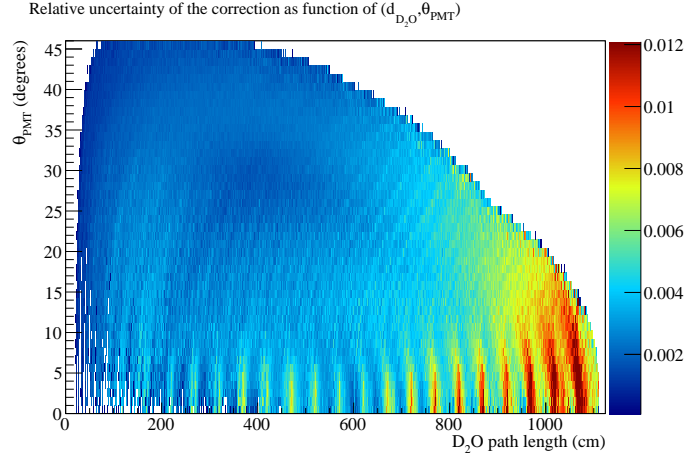
Figure 4.10: Distribution of the ratio of occupancies (with and without NCD reflections) as a function of different tested measurable quantities. The colour scheme represents the number of PMT hits.

produce a correction accurate enough. In Figure 4.11 the relative spread obtained for the two best results. In both cases the path length in D₂O was used, as this was found to be the property where the uncertainty in the correction was smaller. In both cases significant improvement was found in the uncertainty of the correction. In Figure 4.11(a) it is clear that by using both the PMT incident angle (θ_{PMT}) and the path length in D₂O the correction becomes very accurate for the large majority of the situations. However it loses precision for large D₂O path lengths, as most of the hits on the PMTs have a low incident angle and therefore this observable does not contribute to the correction. In this case, the example illustrated previously is still applicable in this case and the correction cannot distinguish between both situations. In order to account for this, a different observable was tested which took under consideration the alignment of the NCDs with respect to the optical path between a source and a PMT, which consisted into considering the angle between the light ray and the alignment of the NCD ($\vec{p}_{NCD} = (0, 0, 1)$) through a factor $\cos \theta_{NCD}$. The uncertainty in the correction obtained using this observable and the path in heavy water is shown in Figure 4.11(b). In this case the correction satisfies the required precision in all cases but for the situation where the optical path connecting the source to a PMT is parallel to the NCDs.

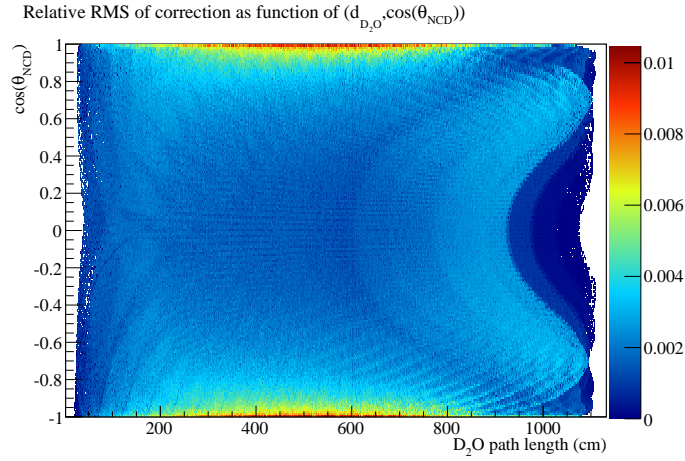
Therefore, a third dimension was introduced into this correction which consisted in the incident angle of the optical path in the PMT (θ_{PMT}). Due to the spherical distribution of the PMTs around the AV, optical paths parallel to the NCDs would have different incident angles in the PMTs. This correction was found to have an uncertainty smaller than 0.1%, which was well below the required accuracy.

This correction was implemented into the optical fit as a 3D lookup table of occupancy ratios. The correction was applied in the initial stages of the fit. For each pair consisting of a LB position i and a PMT j , the full photon optical path was calculated d_{ij} , which was decomposed into three components: each being the distance traveled in each media (d_{D_2O} , d_a and d_{H_2O}).

At the same time, the pair was tested for the optical cuts previously described, removing the ones that were flagged as bad. For the remaining PMTs, the PMT incidence angle and the angle of the optical trace against the z axis was then calculated. Using the 3D map previously produced and the calculated quantities the ratio of occupancies was then obtained w_{ij} , which represents the increased occupancy due



(a) Relative uncertainty in the correction as a function of $(d_{D_2O}; \theta_{PMT})$.



(b) Relative uncertainty in the correction as a function of $(d_{D_2O}; \cos \theta_{NCD})$.

Figure 4.11: Uncertainties in the occupancy reflection correction as a function of two selected measurable quantities. The colour scheme represents the RMS in the correction for the displayed parameters.

to NCD reflections.

This value was then used to rescale the measured occupancy O_{ij} into a corrected occupancy O_{ij}^{corr} :

$$O_{ij}^{corr} = \frac{O_{ij}^{raw}}{w_{ij}(\theta_{PMT}, \cos \theta_{NCD}, d_{D_2O})}. \quad (4.4)$$

Unlike the analytical method explained in Section 4.3.4, the MPE correction is applied separately to this correction, after the reflection correction was applied. The reason for this is to reduce the amount of parameters in the Monte Carlo simulation prone to cause random variations in the PMT occupancies.

For a typical value of observed occupancy O_{ij}^{raw} , the MPE correction alone increased the occupancy by 1.53% [83], while the NCD reflection correction causes a decrease in the occupancy of approximately 0.5%. These results are in very good agreement with the analytical correction.

By simulating a large amount of source positions (within the possibilities of the manipulator system) and high source intensity (leading to high statistics), it was possible to build a map that could be used for all NCD phase scans. This decision was further validated by the verification that the geometry of the detector was very stable through the whole NCD phase [108]. Thus, considering the large amount of MC runs generated, the map accounted for almost all run positions in the NCD phase scans, even though not all scans had the same run plan.

One advantage of using this method is that its systematic uncertainty is already included when calculating the other systematics. For instance, the propagation of the uncertainty in the LB and NCD positions is performed by means of a shift, which results into potentially different values of d_{D_2O} and θ_{PMT} , leading to a different reflection correction. For this reason, the grid size of the correction map was set to be of the same order as the uncertainties in each of the parameters.

Associated with this method an additional systematic uncertainty was also calculated, which accounted for the error in the correction. However, as the RMS was typically very small (less than 0.1%), this calculation didn't show any effective change in the optical parameters.

In the process of development of this correction, different alternatives were also tested. For instance, another correction was implemented consisting in generating MC runs, again with and without NCD geometry, for all the runs in the NCD phase scans and implementing a PMT-by-PMT correction. Thus, while performing an optical fit, besides the *real* OCA data for each run in the scan, the simulated data was also loaded and a occupancy correction was applied by considering the ratio of the simulated occupancies for that specific run and PMT. However, this method

was much more dependent on the precision to which we knew both the LB and the NCD positions for each specific run and could not match the precision of neither the analytical correction nor the more generic method described previously.

Due to schedule constraints in the SNO data reprocessing and analysis, it was not possible to propagate the results of this correction into the final neutrino data. Nonetheless it was important to determine if there was a relevant difference from using the analytical correction. The results shown in Section 4.5 use the MC-based correction instead of the default analytical correction.

4.3.5 Determination of NCD Reflectivity with Monte Carlo Simulation

All the corrections to the PMT occupancies due to NCD reflections described in Section 4.3.4 relied in the NCD reflectivity, which is defined in the Monte Carlo as [88]:

$$R(\lambda) = -0.01387 + 4.5357 \times 10^{-4}\lambda - 2.3154 \times 10^{-7}\lambda^2 \quad (4.5)$$

and is shown graphically in Figure 4.12 (λ is in nm).

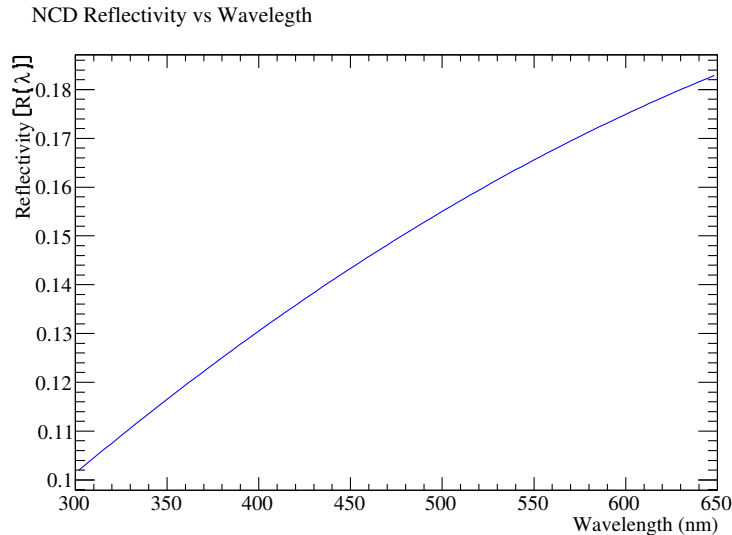


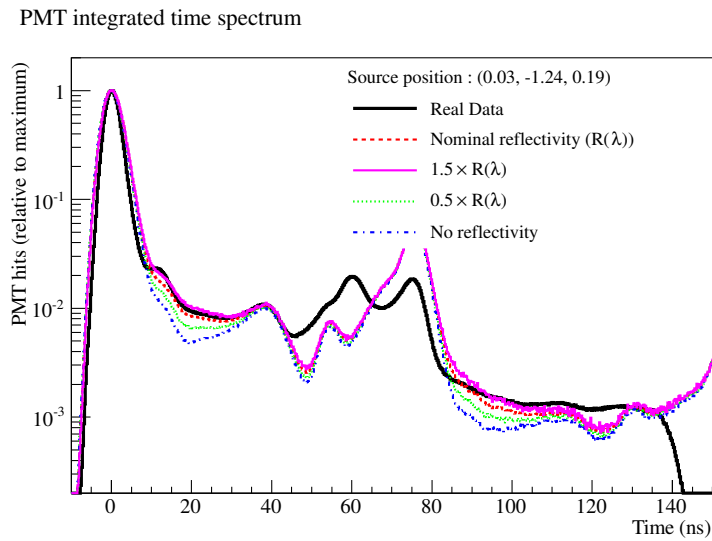
Figure 4.12: NCD reflectivity as a function of wavelength (in nm) as implemented in the Monte Carlo simulation.

It should be noted that the parameters in the reflectivity parametrisation in Equation 4.5 have unknown errors. A study to evaluate the NCD reflectivity by using MC was then performed [114] to estimate the reflectivity from the match between real data and MC. The technique consisted in generating a series of MC runs at each of the six wavelengths using different NCD reflectivities and use this information to verify which MC data set best described the real data.

From the studies performed while implementing the occupancy correction for the NCD reflections, it was known that it wouldn't be possible to accurately perform this study by looking just at the prompt light of the PMTs. This is illustrated in Figure 4.8(b) where the difference inside the prompt time window is shown to be extremely small. In this case, the study would inherently have a large uncertainty due to the low reflection statistics in this region.

Thus, the best option would be to look at the PMT late light, where it was guaranteed that a more considerable portion of the collected light would be due to NCD reflections. This is illustrated in Figure 4.8(b), where there is a clear increase in the integrated PMT hits in several regions outside the prompt time window. However, this method imposed other difficulties, such as overlapping reflection patterns from other elements of the detector. For example, in Figure 3.2(b), several peaks caused by different types of signals are identified, including the prompt AV reflections and the PSUP reflections. Potentially, any of the identified peaks could affect this analysis as all of them scale with the event statistics. It was therefore necessary to first identify a suitable region in the timing spectrum. Figure 4.13 shows the timing spectra from MC generated data using different values of reflectivity for two runs where the source was located in different positions. In Figure 4.13(a) the source is located in the centre of the detector and the features shown in Figure 3.2(b) can be identified. On the other hand Figure 4.13(b) shows the time spectrum, integrated over all PMTs, for a run whose source is located on the edge of the NCD array. In this case the reflection peaks are not visible, eliminating a large region of the timing spectrum as a candidate for this study.

In the figure the time spectrum obtained with real data is also shown. It should be noted that, unlike in the Monte Carlo based NCD reflection correction discussed in Section 4.3.4, in this study the Monte Carlo simulation was configured to perform an exact simulation of the real data, including all physical effects that could change



(a) Source at centre of detector.

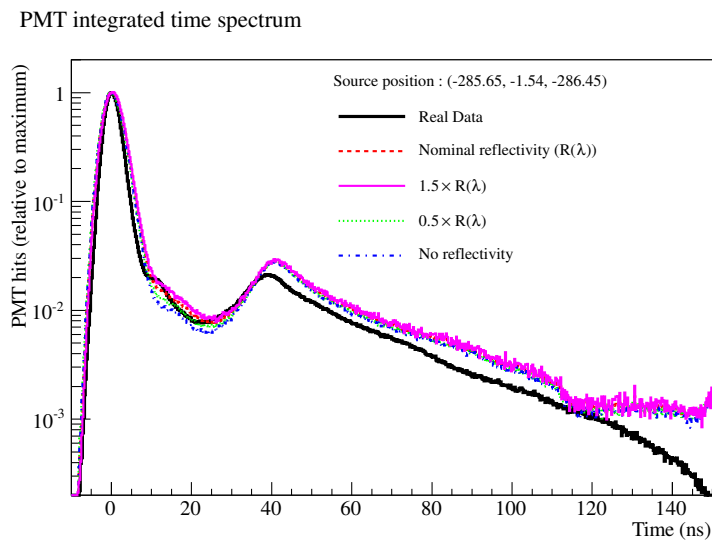
(b) Source at $(-285, 0, -285)$.

Figure 4.13: Integrated timing spectra for MC generated runs with 500 nm laser at different positions in the detector. The corresponding real data run obtained at the same location is also shown for comparison.

the number of hits in the PMTs, such as laserball intensity distribution, Rayleigh scattering, and a more advanced model of the PMT geometry.

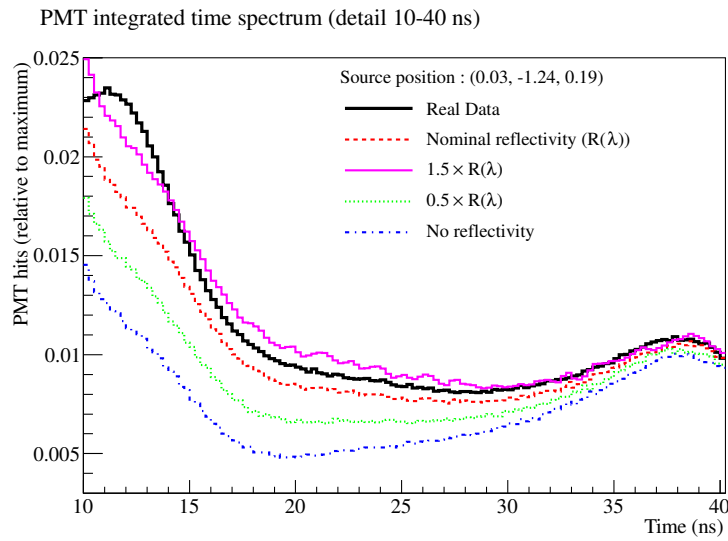
From Figure 4.13, two conclusions could be drawn right away. Firstly, the late light was not being correctly modelled by the Monte Carlo simulation. Taking as an

example the central run of Figure 4.13(a), it is visible that the first late pulsing peak ($t \approx 10$ ns) shows more hits in the real data than in it does in the simulations, while the second late pulsing peak ($t \approx 40$ ns) seems to be a good match between MC and real data. However, the most striking differences seem to concern the reflection peaks: the prompt AV reflection peak ($t \approx 50$ ns) shows a considerably lower number of hits in the MC simulation, the PSUP reflection peak ($t \approx 75$ ns) shows a much higher number of hits in the simulation and the 35° PMT reflection peak seems to have completely vanished in the MC simulation. It should also be noted that these features were observed for all wavelengths [114].

Since in the NCD phase the energy estimator algorithm only uses the prompt time window [115], there was never a great concern with the accuracy of the late light timing spectrum. Nonetheless, this analysis was still carried out by choosing a region of the time spectrum where none of these effects dominate. From Figure 4.13, the chosen candidate was the region between 15 – 30 ns. A detail of this region is shown in Figure 4.14 for the same runs shown in Figure 4.13.

From Figure 4.14 another difficulty to this analysis became clear. The simulated runs show a variation according to the source position. By looking at Figure 4.14(a), and using an interpolation of the integral counts in the interval 20 – 25 ns, the NCD reflectivity was estimated to be approximately 20% higher than the nominal value implemented in the Monte Carlo. However, as the source position moved towards the outer region of the detector, the spectrum shapes became more distinct from the real data. In particular, for Figure 4.14(b) by using the same time interval the NCD reflectivity was estimated to be approximately 25% lower than the nominal value. This suggests that the problem lies not only in the value for the reflectivity, but likely also in the model for its angular distribution.

Therefore, even though the spectra suggest that the model has a potential to be applicable, the discrepancies between Monte Carlo and real data in the late light portion of the spectrum raised questions to its accuracy, as the discrepancy in the structures of the late timing spectra suggest that the MC was not tuned to accurately reproduce the optics at late timing. In order to further develop this method it would be necessary to tune the MC to accurately match the real data. Due to schedule constraints in the SNO experiment, this was not possible and therefore the analysis was not pursued any further.



(a) Source at centre of detector.

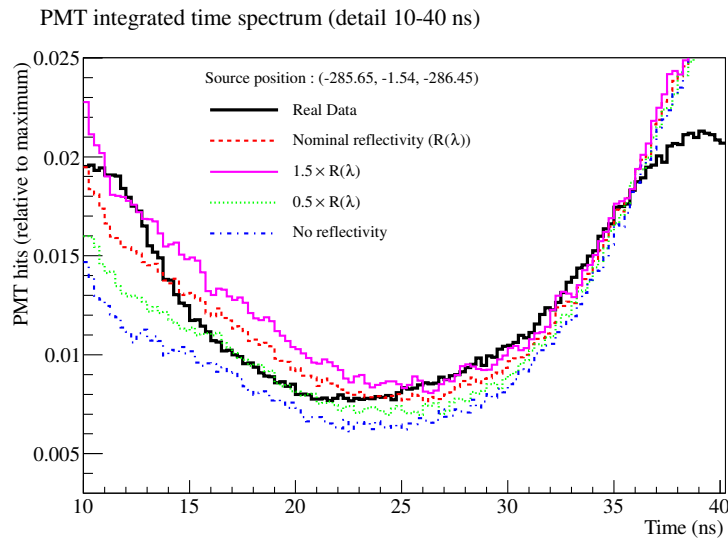
(b) Source at $(-285, 0, -285)$.

Figure 4.14: Detail of time spectra in the region of interest to study the NCD reflectivity, integrated over all PMTs.

4.4 Additional Improvements to the Analysis

Although the introduction of the NCDs brought major changes to the optical calibration, further improvements were sought that were not directly related with the NCDs. In this section two major improvements to the analysis affecting all the optical

calibration data since the beginning of SNO will be described.

4.4.1 NCD Attachment Anchors

In the detector design, 96 NCDs were planned to be deployed³. In order to fix the NCDs in the desired position an acrylic anchor was attached, for each planned NCD, on the bottom of the AV during the detector building phase. Each anchor was shaped as a cylinder with a diameter of 7.62 cm (3 in), and a height of 5.72 cm (2.25 in). These anchors were made of standard commercial acrylic [116], having different optical properties than the acrylic in the AV, resulting in an unknown effect in the optical parameters.

Geometrical Cut

An optical cut was then implemented to identify, for each LB position, which PMTs were shadowed by the NCD anchors. A similar cut to the one used to mask the NCD shadows was employed, with a slight modification to adapt to a 3D reference frame.

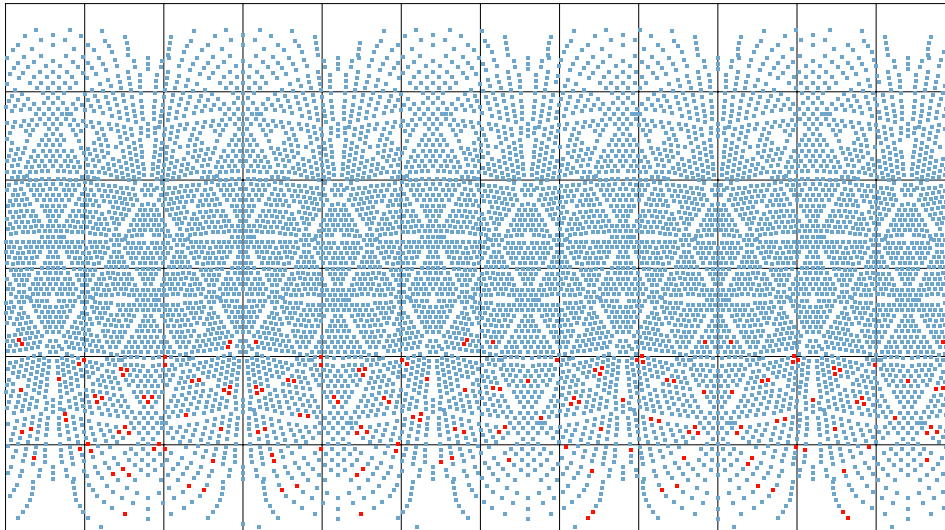
For each set of a LB position, a NCD anchor and a PMT, the full optical path between the source and the PMT was found. This path was then tested against all the NCD anchor positions, in order to determine the minimal distance between the optical path and the anchors d_{min} . This distance included a correction to account for both the LB and the PMT solid angles.

This distance was later checked against a tolerance value (ΔL), like in the NCD shadow cut, which was typically 5 cm, measured from the centre of the anchor. If, for a pair of PMT-LB, there was an anchor for which $d_{min} < \Delta L$, that PMT was flagged as bad and removed from the optical fit.

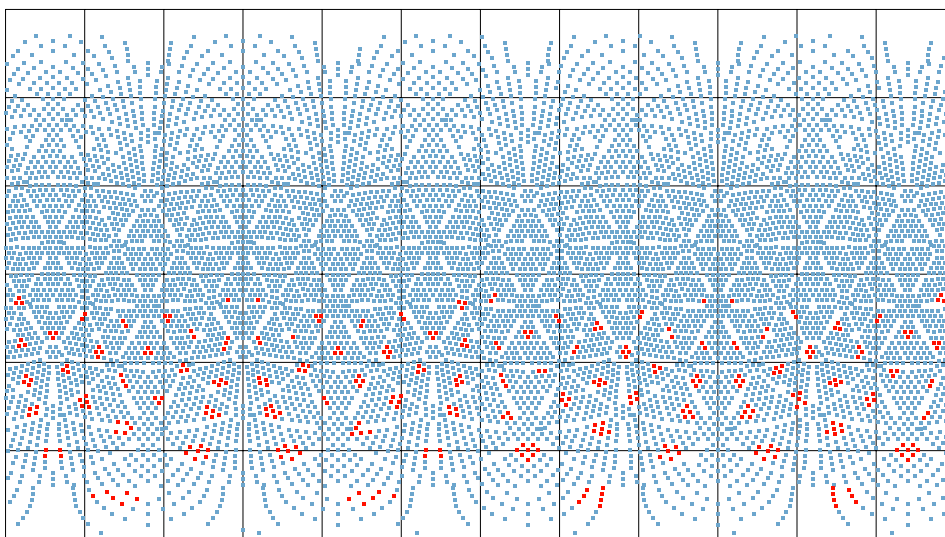
Figure 4.15 shows the amount of PMTs affected by this cut for two different source positions. For a central run this cut typically affected 5% of the PMTs, while a run with the source in the bottom of the AV affected approximately 11% of the

³Only 40 NCDs were effectively deployed as it was later concluded that by deploying all the 96 NCDs the signal degradation from the D₂O events would be too large.

PMTs. In a full optical calibration scan, this cut would affect a total of 5% of the data points.



(a) Source at center of the detector $(0, 0, 0)$.



(b) Source at bottom of the detector $(0, 0, -490)$.

Figure 4.15: Affected PMTs in a flat projection of the detector, with the source at the centre and at the bottom of the AV. The blue marks represent unaffected PMTs and the red marks represent PMTs discarded from the optical fit due to this cut.

Effect on the Optical Parameters

After implementing this cut a series of optical calibration scans were reprocessed, in order to evaluate the effect of this cut at different stages of the experiment live-time. The results showed that the cut didn't produce any effect in the PMTR. However, a non negligible difference was observed in the media attenuations, especially in the D₂O and Salt phases. Figure 4.16 shows the difference observed in the D₂O attenuations for a series of D₂O (oct03) and Salt phase scans (sep01, may02, apr03). A similar difference was observed for the H₂O attenuation, but this parameter has a large statistical uncertainty and thus the difference is covered by the uncertainties.

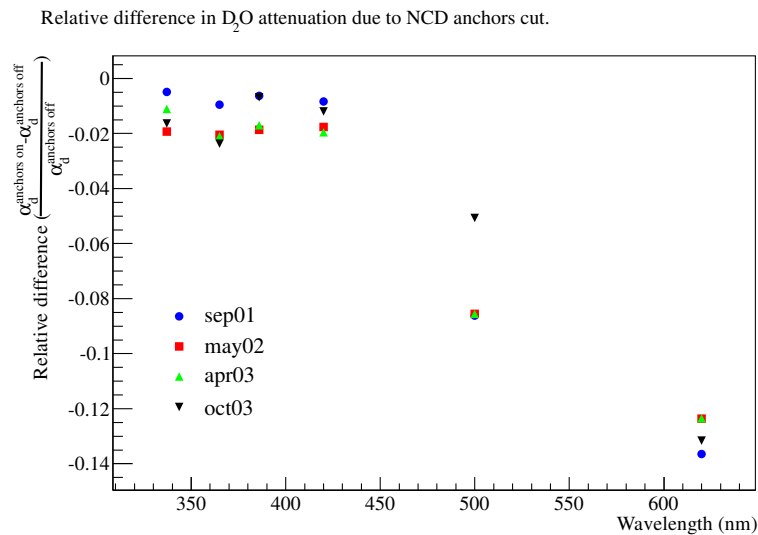


Figure 4.16: Difference in heavy water attenuations due to the NCD anchor cut in D₂O and Salt scans.

This study was also performed on the NCD phase scans, but as most of the PMTs affected by this cut were also affected by the NCD shadow cut, there was no visible effect in the results caused directly by this cut [88, 117].

Effect in the PMT Efficiencies

The results obtained after applying the NCD anchor cut provided a good basis to suggest that the PMT efficiencies might be affected as well. Since the optical fit in the NCD phase relies in the PMT efficiencies of the interim D₂O scan taken in

October 2003, a new set of PMT efficiencies were then extracted applying the new optical cut [88, 117]. The distribution of the extracted PMT efficiencies before and after the implementation of the optical cut are shown in Figure 4.17(a).

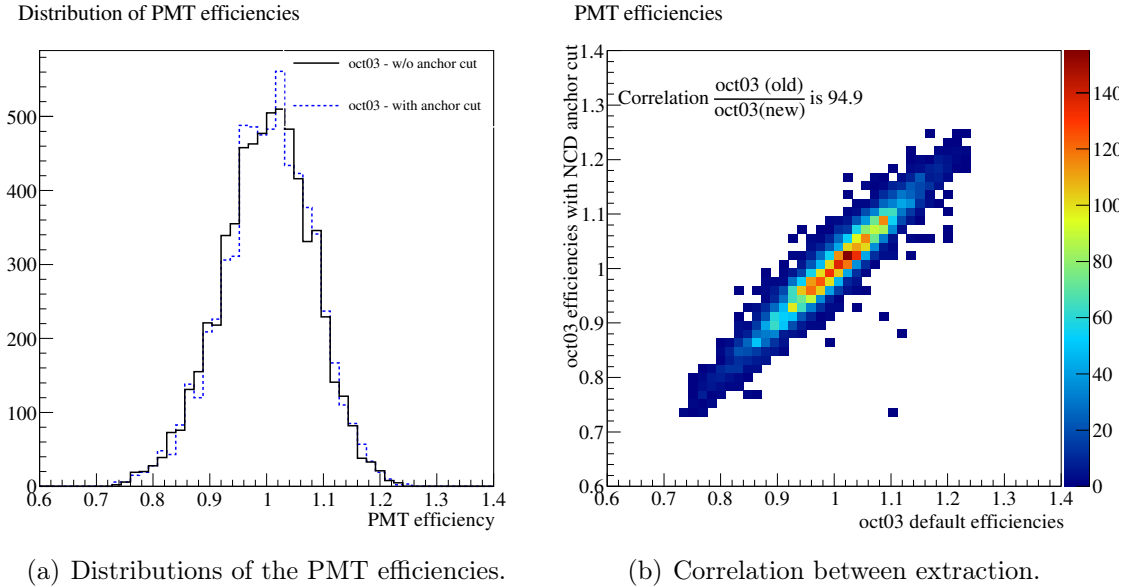


Figure 4.17: Effect of the NCD anchors optical in the extracted PMT efficiencies at 420 nm of the October 2003 scan.

Figure 4.17(b) shows the correlation between the extracted PMT efficiencies, which was approximately 94.9%. This was expected as the optical parameters extraction only shows a difference in the heavy water attenuation. Nonetheless, as there was a decrease of up to 10% at larger wavelengths, a difference was still expected.

Albeit the strong correlation between the PMT efficiencies obtained from both extractions, a more interesting result was observed when looking at the spacial distribution of the PMT efficiencies in the detector. Figure 4.18 shows the distribution of the PMT efficiencies as a function of one spacial coordinate. While the results are perfectly consistent along the y axis (Figure 4.18(a)), the same was not observed in the case of the distribution along the z axis. In fact, from Figure 4.18(b), a difference can be clearly observed a difference in the PMT efficiencies at the bottom of the detector ($Z \approx 600$ cm). This difference grows as one goes towards the bottom of the detector, which is where the NCD anchors are attached. In fact, this difference is clearly understood by considering the fact that, being *Ultra-Violet (UV)* absorbent, the NCD anchors were causing a reduction in the PMT occupancies at the bottom of

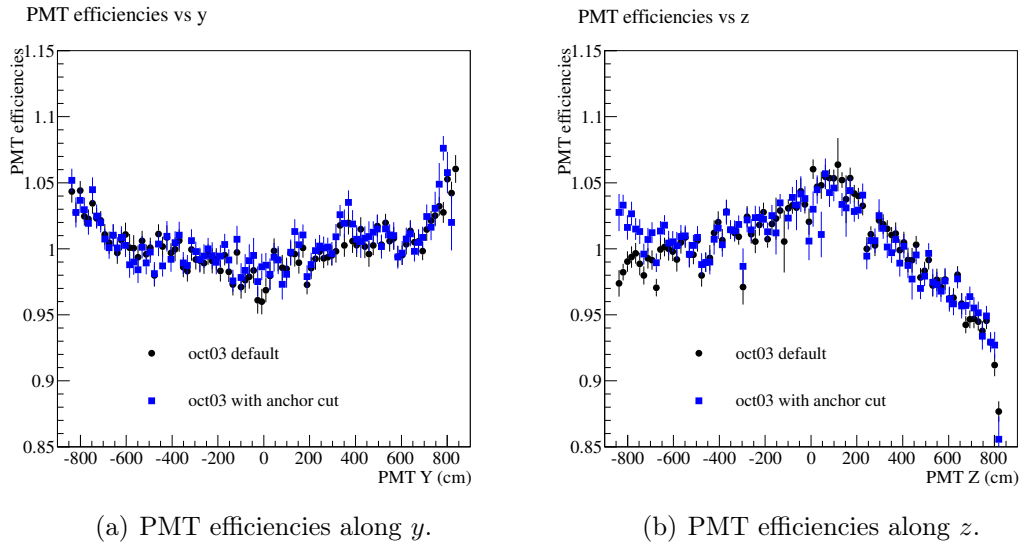


Figure 4.18: Profile of PMT efficiency distribution along two coordinate axes. Results from the 420 nm runs in the oct03 scan. Similar results were observed for all wavelengths.

the detector. In the extraction of the optical calibration parameters this translated into a shorter heavy water attenuation length, which was observed in Figure 4.16, and lower PMT efficiencies at the bottom of the detector.

As the optical calibration method in the NCD phase (Occupancy) relied in the PMT efficiencies, these results suggested that the NCD anchors could play a role in the optical analysis of the NCD phase. Therefore, the newly extracted PMT efficiencies were used to re-analyse the NCD phase scans to obtain an updated estimation of the optical parameters. The results from this re-analysis showed that the new efficiencies only caused a small change in the H_2O attenuations, which was irrelevant due to the large uncertainties in this parameter [117].

Nonetheless, the new efficiencies were used in further reprocessing of the neutrino data of the NCD phase, in order to use the best knowledge of the optical properties of the SNO detector.

4.4.2 Up-Down Asymmetry in the Detector

During the combined analysis of the neutrino data of phase I and II with a lower threshold (*low energy threshold analysis (LETA)*), a difference of up to 5% in the

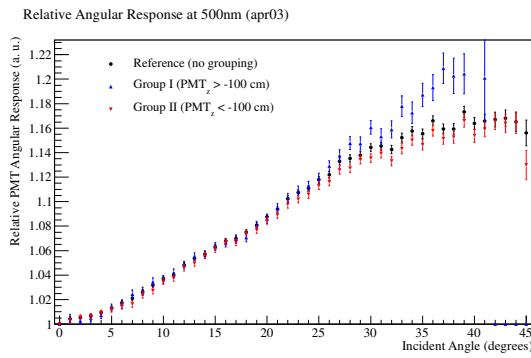
reconstructed energy of the events occurring in the top and bottom hemispheres of the detector [118]. While this effect was independently studied in the context of the energy reconstruction [118, 119], a similar study was also performed in the context of the optical calibration [120–122]. As stated in Section 3.2, the optical model of SNO measures average quantities, assuming an homogeneous detector response. However, this was thought to be an oversimplification in the case of the PMT and reflector assembly.

In order to search for an asymmetry in the detector, the OCA algorithms were modified to fit simultaneously for two separate PMT angular responses. The PMTs could then be separated into two groups, according to their location, and two different PMTRs were fitted in the same optical scan, allowing to search for different PMT angular responses in the detector [121].

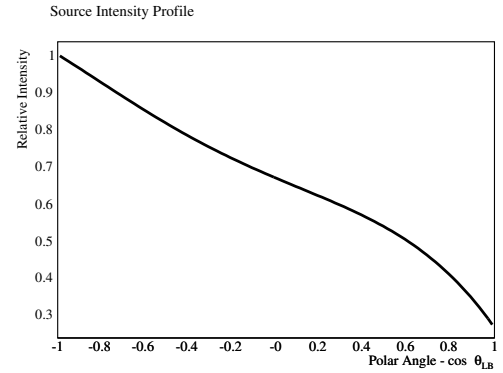
Figure 4.19 shows the results obtained for a selected Salt phase scan (April 2003) and the interim D₂O scan (October 2003). The figures show the results obtained by grouping the PMTs by its z coordinate. In the particular case of Figure 4.19, the separation is performed by the plane $z = -100$ cm. The reason for this particular separation plane is because upon several tests over a large amount of the Salt phase scans, the separation by this plane resulted in the largest asymmetry. Similar tests were performed using other coordinates as the separation plane, but no asymmetry was observed in those cases.

The results show a clear asymmetry between the two groups of PMTs, with the PMTs on the top part of the detector showing a larger PMTR at higher incidence angles. It is also possible to observe that there is an effect due to uneven detector coverage in this analysis: the PMTR on the top of the detector has consistently larger statistical uncertainties. As shown in Figure 4.1, a portion of the upper part of the detector is not reachable by the calibration source and therefore fewer calibration runs exist in the upper hemisphere, especially at high radius which are the major statistics contributors to the PMTR at higher incidence angles. By grouping the PMT on the upper part of the detector and fitting their angular response separately, the reduced statistics in each PMTR are reflected.

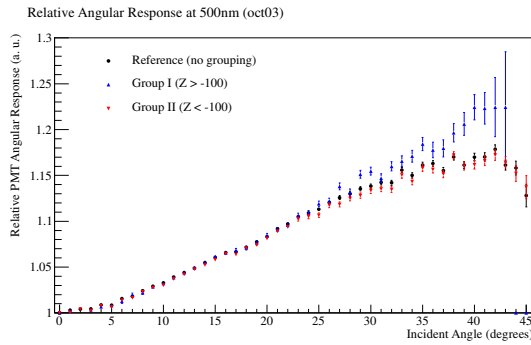
This effect was thought as being a result of the degradation of the PMT reflectors, and thus an asymmetry increasing with time was sought. However, this was hard to



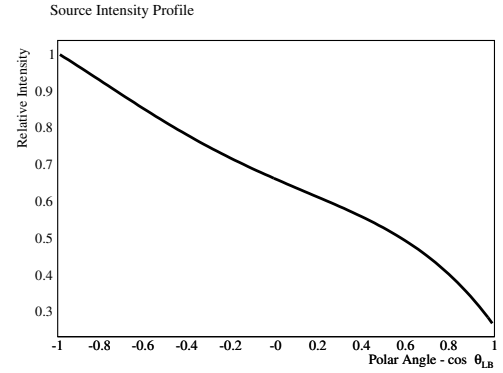
(a) Apr03 PMTR



(b) Apr03 LB distribution profile



(c) Oct03 PMTR



(d) Oct03 LB distribution profile

Figure 4.19: PMT angular response of two scans demonstrating the asymmetry along the z axis by separating the PMTs into two groups according to their position. The corresponding functional profiles of the laserball distribution are also shown.

verify as the asymmetry was found to depend strongly with other optical parameters, such as the source isotropy, and therefore it was hard to attribute a single conclusive reason to the asymmetry.

Therefore, by looking at a wide range of scans it was not possible to determine any relation of the asymmetry with time, nor with any specific optical parameter. The asymmetry was shown to be weakly dependent on the particular *separation plane* z coordinate used. This is shown in Figure 4.20 where the PMTR is shown for the same scan and wavelength, but applying different *groupings*. The reference value obtained considering all PMTs as having the same angular response is shown in black, together with a shaded area which corresponds to its statistical uncertainty. All other results were grouped by performing the separation of the PMTs at different

z coordinates. Each pair of groups from a individual fit have the same colour and a different symbol. The results show that the PMTR in the lower part of the detector completely dominates the values obtained when no separation is made and that the response in the upper part of the detector varies considerably.

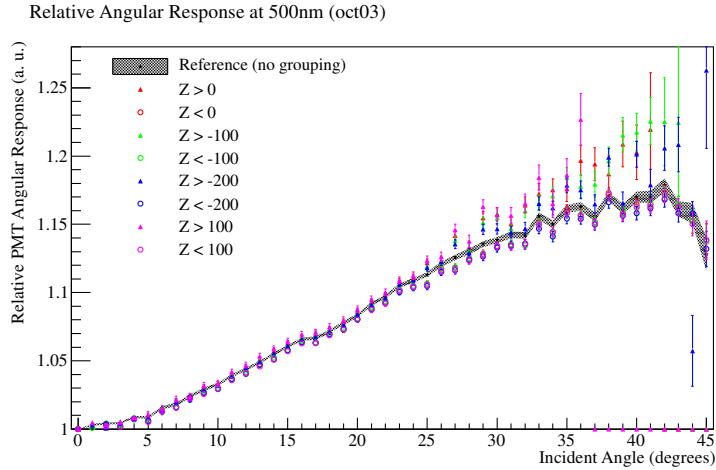


Figure 4.20: PMT angular responses obtained by grouping the PMTs by different regions in z .

Similar tests were performed grouping the PMTs by a series of different criteria, such as their position along the x and y axes, but the asymmetry was only observed along the z axis, with a maximal asymmetry when one group of PMTs contained all PMTs whose z coordinate was below the plane $z = -100\text{cm}$.

Despite confirming the existence of an up-down asymmetry in the detector, it was not possible to find out the source of such effect. Several hypotheses were considered, being the most accepted one that the effect was caused by debris deposited in the bottom of the detector, both in the AV and the PMTs, such as the degradation of the PMT reflector petals (different production batches were distributed in the top and bottom part of the detector).

Not being able to correct the asymmetry observed in the optical calibration, an additional systematic uncertainty was then implemented on the PMTR that would account for the asymmetry observed. For this, the difference at each incident angle obtained from the two groups of PMTRs was used, each one separated by the plane $z = -100\text{ cm}$.

It should be noted that this systematic uncertainty varies from scan to scan and from wavelength to wavelength. The specific implementation of this systematic consisted in effectively adding an additional iteration to the optical fit where two PMTRs were extracted. The difference between the PMTR of each group was then calculated and stored as a systematic uncertainty. Figure 4.21 shows the correction for all wavelengths of the interim D₂O scan (October 2003).

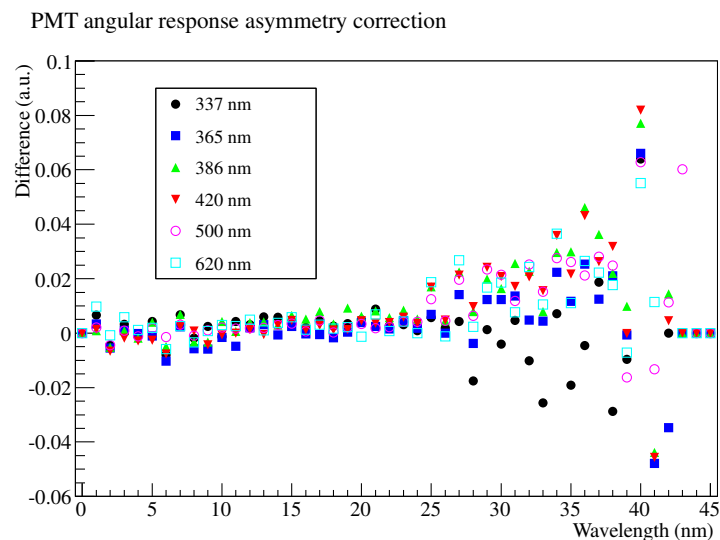


Figure 4.21: Systematic uncertainty applied to the PMT angular response due to the PMTR asymmetry along z .

It should be noted that although the image shows negative and positive values, the associated uncertainty is implemented as an additional symmetric uncertainty to the PMTR. From Figure 4.21 it is possible to notice that the uncertainty varies with the wavelength. This uncertainty represents at most an additional 5% systematic uncertainty in the PMTR.

4.5 Results on the Optical Parameters

This section presents the optical constants extracted from the optical fit after implementing all the improvements described in this chapter. The results focus mostly on the NCD phase, although the extraction of the optical parameters for individual D₂O and Salt scans were also performed, in order to check the time evolution of

the parameters. Furthermore, some of the improvements discussed before also affect these phases.

The D₂O and Salt phase scans were analysed using the OccRatio method, for maximum consistency with the official extraction at the time of the analysis of each phase. The NCD phase scans were analysed using the Occupancy method, applying the PMT efficiencies from the October 2003 scan (NCD commissioning phase).

The comparison of the results of the NCD commissioning phase scan using the OccRatio method are already shown in Section 4.2. The errors quoted in the parameters include the contribution of the systematic uncertainties that are pertinent for that specific phase, which are explained in more detail in Section 4.6.

4.5.1 Data Set and Selection.

The results are presented for the marked optical scans in Table 4.1. Of these, only one scan is from the D₂O phase (September 2000). There are also four scans from the Salt phase and another five scans in the NCD phase. Although there were other optical calibrations scans, not all of them were included as some of them presented technical difficulties, such as bad runs and low statistics. This selection however is sufficient to demonstrate the time dependence of the optical parameters and their evolution through the whole time of operation of SNO.

The analysis of the data occurred in the way already described in the previous sections. In particular cases some runs were removed from the data sets due to various reasons such as corrupted occupancies, failure in calculating the optical paths between the source and the PMTs, or the fitted positions of the source were not compatible with the recorded position by the calibration instrumentation. Then, for each chosen run the PMT data was selected following two types of cuts. The first type was based in the geometry of the detector and the light paths, and was described in Sections 3.3, 4.3.1 and 4.4.1. This type of cuts removed from the fit PMTs whose optical paths were difficult to model, for a specific run, and therefore would introduce variations that were not compatible with the characterisation of the detector by average quantities that is the base of the optical calibration.

A second type of cut was also implemented as an implicit χ^2 cut. This cut aimed to remove outlier PMT data, whose individual contribution to the χ^2 was too large. As mentioned in Section 3.3, the optical calibration fit, after applying the quality cuts and reconstructing the source positions and optical paths, ran through five iterations. At the end of each iteration, the individual PMTs whose data had a contribution to the global χ^2 above a certain threshold was removed from the fit and a new iteration of the optical calibration fit started. This procedure allowed to identify outlier PMTs, and ensure that the data in the fit was consistent with the homogeneous detector optical response model. The χ^2 threshold for the last iteration was $\chi^2 < 25$. This χ^2 cut affected approximately 3 – 5% of the PMT data in a scan.

The geometrical cuts affected a much larger portion of PMTs, being dependent on the source positions in a scan. In the D₂O and Salt phase they affected approximately 40% of the PMTs statistics, while in the NCD phase the geometrical cuts affected approximately 75%, where the NCD shadow cut was the largest contribution.

The number of floating parameters in the optical fit varies for each combination of scan-wavelength, due to the quality cuts and options of the fit. Table 4.2 lists the different contributions to the total number of floating parameters. Some of these contributions are exclusive, i.e., only one of the options can be active. Such an example is the LB intensity distribution, where only one of the options (histogram or functional form), or none at all, can be active. In the case that none of the LB distribution models is floating, the LB distribution profile in θ (mask function) is also deactivated from the floating parameters. The same happens in the case of the PMTR, where the number of floating parameters depends on the configuration of the fit (whether the PMTs are separated into two groups or not).

OCA parameter	Total possible parameters	Notes	Typical free parameters	
			D_2O , Salt	NCD
PMTR	2×90	1 bin per incidence angle (total of 90). Two possible PMTR being fitted. Dynamically adjusted by PMT statistics.	45	45
Source characterisation (LB)		Only one model can be used		
Histogram distribution	12×36	12 bins in $\cos \theta_{LB}$ 36 bins in ϕ_{LB} Dynamically adjusted by PMT statistics.	432	432
Functional distribution	2×24	Amplitude and phase of sinusoidal wave 24 angles in $\cos \theta_{LB}$	48	48
Source profile in θ (LB mask function)	6	Exact value dependeds on source characterisation model used	6	4
Media attenuations	3	acrylic attenuation was usually fixed	2	2
Rayleigh scattering	3	Usually fixed to pre-determined values	0	0
Run Occupancy normalisations	N_{runs}	Depended on the total number of runs in the fit	20 – 30	40 – 50

Table 4.2: List of possible configurations of the optical fit and corresponding number of floating parameters. The typical values for each type of scan are also shown.

Besides these adjustments to the number of floating parameters there are also dynamic adjustments that are based in the quality of the data. This dynamic adjustment is also applied to both the PMTR parameters and the LB distribution. In both cases, if the number of data points contributing to a particular parameter is smaller than a pre-set threshold, that parameter is fixed. For example, in the D₂O and Salt phase scans, any PMTR parameter (incidence angle bin) containing less than 100 PMTs contributing to it was fixed to one. In the case of the LB distribution, the threshold to fix a particular parameter was 25 PMTs. Due to the different statistics of the NCD phase scans, these thresholds were decreased, respectively, to 50 and 15.

In the NCD phase analysis the use of the functional parameterisation of the laserball distribution was used since the results were shown to not be significantly affected by the change in model and the new parameterisation largely reduced the number of floating parameters, improving the statistical uncertainties. An extensive description of each model and respective comparison is performed in [123].

More details about the individual OCA parameter characterisation are given below.

4.5.2 Results

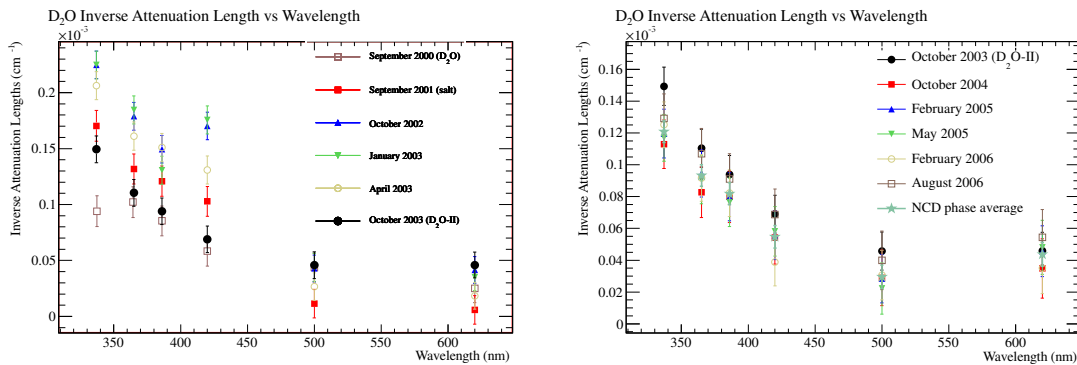
In this section the results of the optical parameters are shown. The figure of merit of the fit is the χ^2 of Equation 3.6 for the case of the D₂O and Salt scans, or the χ^2 of Equation 3.10 in the case of the NCD scans. As demonstrated in Section 4.2 both methods yield similar results meaning that a direct comparison of the extracted parameters is valid.

In the following sections we will cover the results of each optical parameter in more detail. The errors in the plots correspond to the total uncertainties, which are composed of a statistical component, and a systematic component, which is discussed in more detail in Section 4.6. The analysis of the time variation of the optical parameters is provided in more detail in Section 4.5.2.

Media Attenuations

The media attenuations are fitted, and extracted, as the inverse of the of the attenuation length in the medium. The values obtained in the fit correspond to the total media attenuations. However, a fraction of the photons experience forward Rayleigh scattering and arrive to the PMTs outside the prompt time window. The results shown account for the pure media extinctions, which are obtained by subtracting a fraction of the theoretical prediction of Rayleigh scattering lengths from the values obtained in the fit. Therefore, the quoted results are all pure absorption lengths, having the Rayleigh component already subtracted.

The results obtained for the D₂O attenuations as a function of the wavelength in the analysed scans are shown in Figure 4.22. Figure 4.22(b) show the results obtained in the NCD phase, while Figure 4.22(a) shows the corresponding results for D₂O and Salt phases. The results of the interim D₂O phase (October 2003) are shown in both figures to allow a better comparison.



(a) D₂O attenuation in D₂O and Salt phases.

(b) D₂O attenuation in NCD phase.

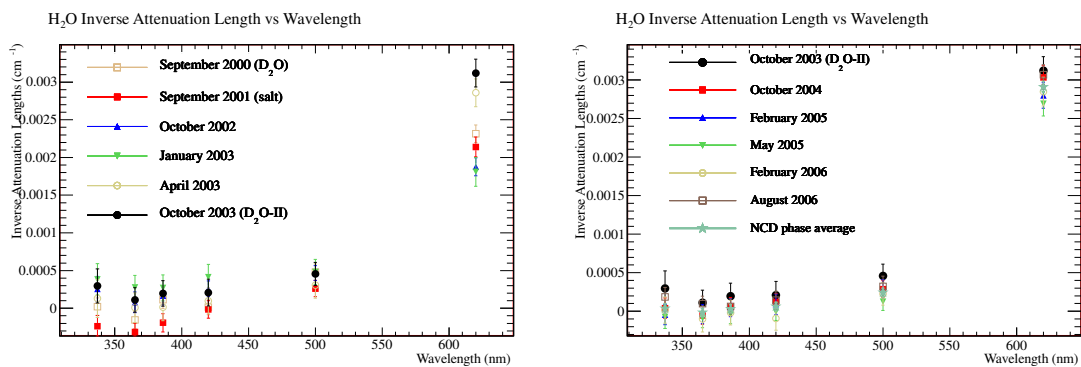
Figure 4.22: D₂O media attenuations as a function of wavelength. The October 2003 results are shown in both figures.

The D₂O attenuations are consistent within the uncertainties. A problem in the optics fibres during data taking at 337 nm in the September 2000 scan gave origin to an artificial lower value in the D₂O attenuation.

It is also possible to verify that although the values are compatible, there is a larger variation between the heavy water attenuations in the Salt phase than in any other phase. This was found to be caused by residual contamination with MnOx

used for radio assays already discussed in Chapter 2. The attenuation showed an increase during this phase and returned to the original values by the end of the Salt phase, when the heavy water was desalinated and re-purified [124, 125]. The media attenuations in the NCD phase are more compatible with the ones from the D₂O phase, showing a larger uncertainty due to the additional systematic uncertainties.

The results for the H₂O attenuations are shown in Figure 4.23. The layout of the plots is the same as for the D₂O. The H₂O attenuations show a similar behaviour as the D₂O attenuations. The results are consistent across all scans, within uncertainties. In this case no discrepancy is observed in the Salt phase.



(a) H₂O attenuation in D₂O and Salt phases.

(b) H₂O attenuation in NCD phase.

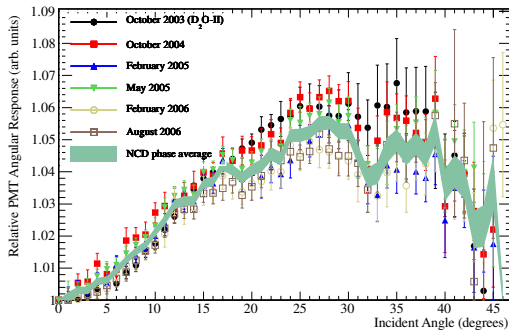
Figure 4.23: H₂O media attenuations as a function of wavelength. The October 2003 results are shown in both figures.

PMT Angular Response

The results obtained for the PMT angular response are shown in Figure 4.24 for all six wavelengths. Similarly, the results obtained for all analysed scans, including D₂O and Salt phases, are shown in Figure 4.26.

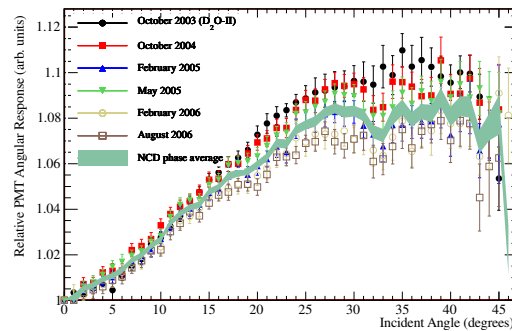
The results are consistent at low incidence angles, but a larger variation between scans is observed for higher angles, where the NCD phase scans show consistently a lower response. The cause for the lower response is most likely to be due to PMT reflector degradation which causes the light collection at higher incidence angles to be less efficient [126].

Relative PMT Angular Response at 337 nm vs Incident Angle



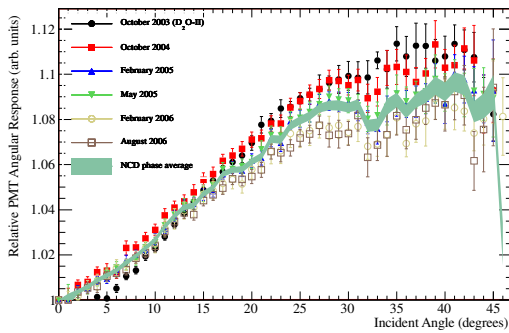
(a) 337 nm.

Relative PMT Angular Response at 365 nm vs Incident Angle



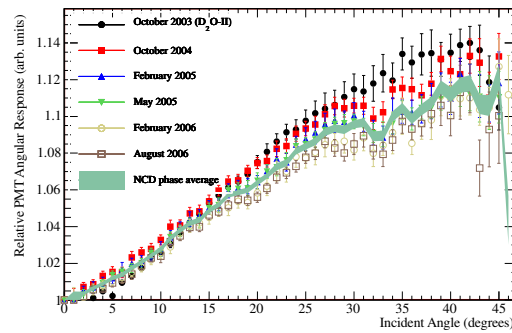
(b) 365 nm.

Relative PMT Angular Response at 386 nm vs Incident Angle



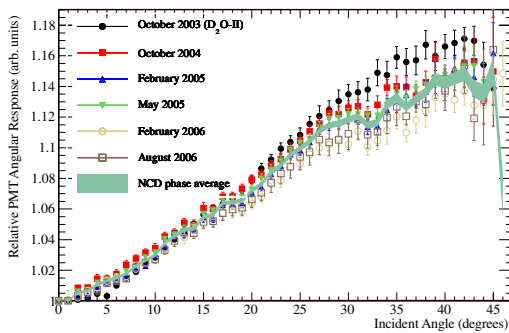
(c) 386 nm.

Relative PMT Angular Response at 420 nm vs Incident Angle



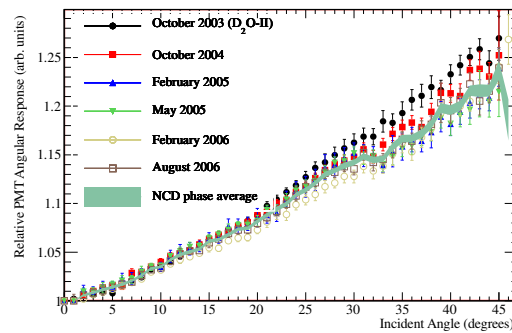
(d) 420 nm.

Relative PMT Angular Response at 500 nm vs Incident Angle



(e) 500 nm.

Relative PMT Angular Response at 620 nm vs Incident Angle



(f) 620 nm.

Figure 4.24: PMT angular response as a function of the incidence angle in the NCD phase for all six tested wavelengths.

Laserball Characterisation

The LB intensity is also fitted and is modelled as a source with intensity distributed in terms of the polar angles ($\cos \theta_{LB}, \phi_{LB}$). The angle θ_{LB} describes the angle of

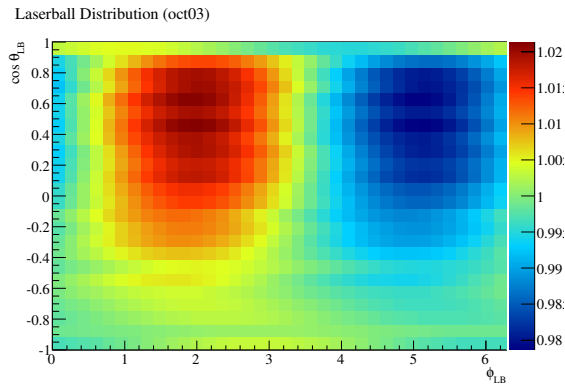
emission with respect to the z axis and the ϕ_{LB} describes the angle of emission with respect to the x axis. The source intensity is also weighted by a function, known as the *laserball mask function*, which depends on $\cos\theta_{LB}$ and describes the variation caused by the source support body.

The LB characterisation takes the most part of the variable parameters in the optical fit. Two parameterisations of the intensity distribution were implemented in the fit. The simplest model assumes that the LB distribution is smooth, being the LB characterisation modelled by sinusoidal functions for a total of 54 parameters (six parameters for the LB mask function and 48 parameters for the LB intensity of which 24 are bins in $\cos\theta_{LB}$ and two are coefficients of the sinusoidal azimuthal intensity distribution function ($A\sin\phi_{LB}$), where A is the amplitude and ϕ_{LB} is a phase). The second model does not make any assumption about the LB distribution and thus introduces 438 parameters in the fit, describing a grid of 12 bins in $\cos\theta_{LB}$ and 36 bins in ϕ_{LB} (plus the six parameters of the LB mask function).

The LB characterisation was also one of the parameters that most varied in the optical calibration, being considerably different in a scan-by-scan basis, as improvements in the LB distribution were attempted. However, in the NCD commissioning phase, one last intervention in the LB resulted in a very uniform source, which was kept stable through the whole phase.

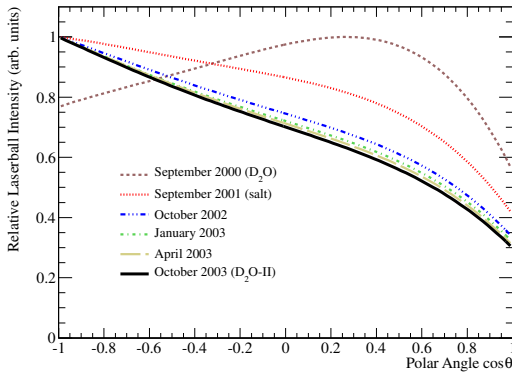
Figure 4.25(a) shows the result obtained for the LB characterisation obtained with the functional form for a 500 nm run in the October 2003 scan.

Figures 4.25(b) and 4.25(c) show the profile of the LB intensity as a function of the polar angle θ_{LB} . The shadowing effect of the source support structure is clearly visible in the region close to $\cos\theta_{LB} \approx 1$. The profiles for several scans is shown, which demonstrates how the isotropy of the source varied along the whole live-time of SNO. The NCD phase scans show a large stability, which is not verified in the other phases. Although only the intensity profiles for 500 nm are shown, similar results were observed for all wavelengths.

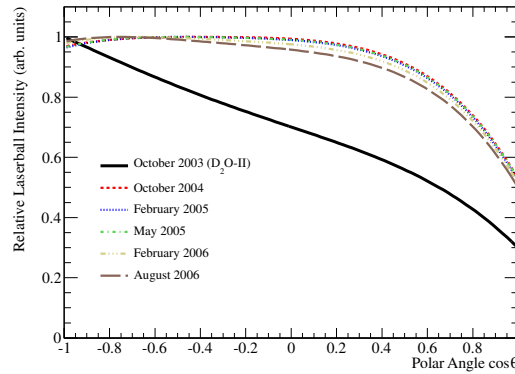


(a) Functional parameterisation.

Laserball Mask function at 500 nm

(b) LB mask function in D₂O and Salt phases.

Laserball Mask function at 500 nm



(c) LB mask in NCD phase.

Figure 4.25: Distributions of the laserball characterisation at 500 nm in the october 2003 scan. Figure 4.25(a) shows the functional parameterisation that implicitly assumes an uniform laserball. The intensity profiles in the different phases are shown in Figures 4.25(b) (D₂O and Salt phase scans) and 4.25(c) (NCD phase scans).

Time Variation of the Optical Parameters

The frequent OCA scans permitted the study of the time variation of the optical parameters, especially the media attenuations and the PMTR. This analysis was of particular importance to study the stability of the optical properties in the detector. Furthermore, if the stability of the the detector was confirmed by this analysis it would be possible to use the average optical properties in the Monte Carlo simulation and energy reconstruction algorithms, greatly simplifying the neutrino data analysis.

In Figure 4.26, the PMTR for all re-analysed scans is shown, sampling the whole SNO data taking period. Except for the September 2000 scan, all other results

are consistent taking into account the uncertainties. However, a decreasing trend of approximately 2% was observed between scans in each phase at high angles. Nonetheless, this drift is smaller than the total uncertainties in the PMTR meaning that, for each phase, the average PMTR of the OCA scans of that phase could be used.

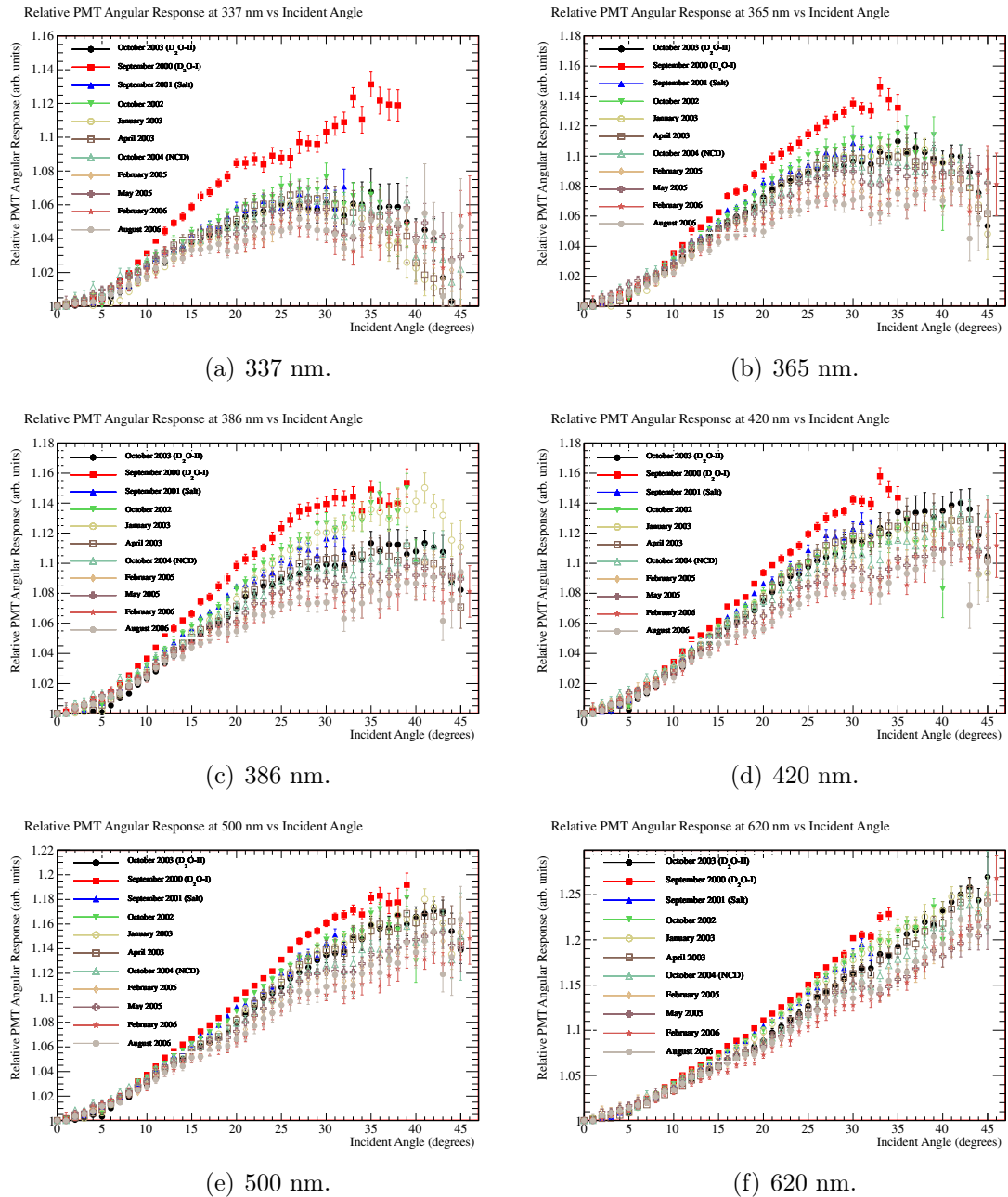


Figure 4.26: PMT angular response as a function of the incidence angle for all re-analysed scans.

Figure 4.27(a) shows the variation of the D₂O attenuations for all six wavelengths for all re-analysed scans. It should be noted the consistency in the attenuation between the D₂O scans (including the NCD commissioning phase) and the NCD phase results. In the Salt phase a drift was observed which was caused by the contamination due to *MnOx* calibrations mentioned before [124, 125]. In fact for this reason the propagation of the optical constants into the simulation and reconstruction was propagated differently, with a drift function being used to model the variation of the optical properties over time.

Figure 4.27(b) shows a more detailed comparison for a single wavelength (500 nm) comparing only the D₂O and NCD phase scans, together with a linear function estimating the drift in the attenuations. A consistent result is clear, with the slope of the function, which characterises the drift in the attenuations, being consistent with zero when the uncertainties are taken into account, with a slope of $(-1.4 \pm 3.5) \times 10^{-4}$. The same figure shows the results obtained by averaging the D₂O attenuation in the NCD phase. As the results were consistent over the whole NCD phase, one could use a weighted average of all NCD phase results, which were later used in the Monte Carlo and energy reconstruction.

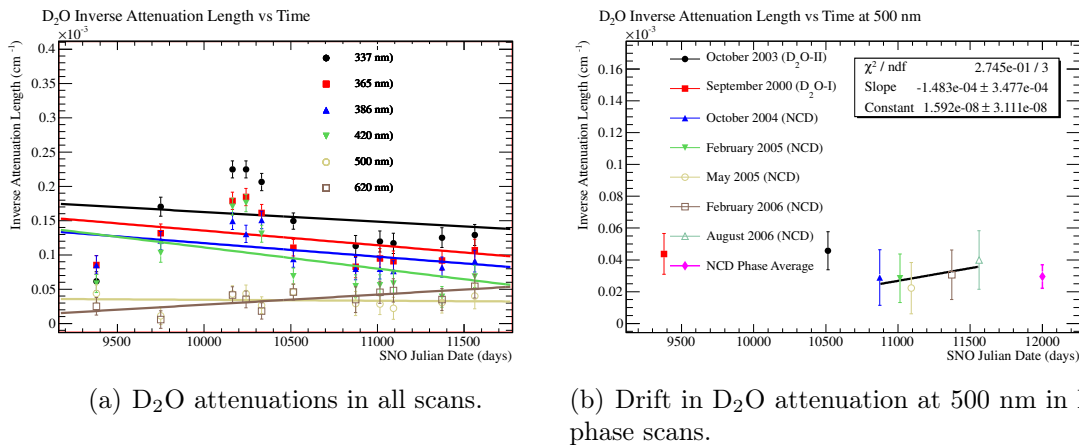


Figure 4.27: D₂O attenuations for all six wavelengths for all re-analysed scans.

Figure 4.28 shows a similar comparison performed for the H₂O attenuation. In this case there is no drift observable in the Salt phase. As in the case of the D₂O attenuation, the slope is consistent with zero (slope = $(-3.2 \pm 25.1) \times 10^{-4}$).

For this reason it was safe to assume that the detector was stable and therefore

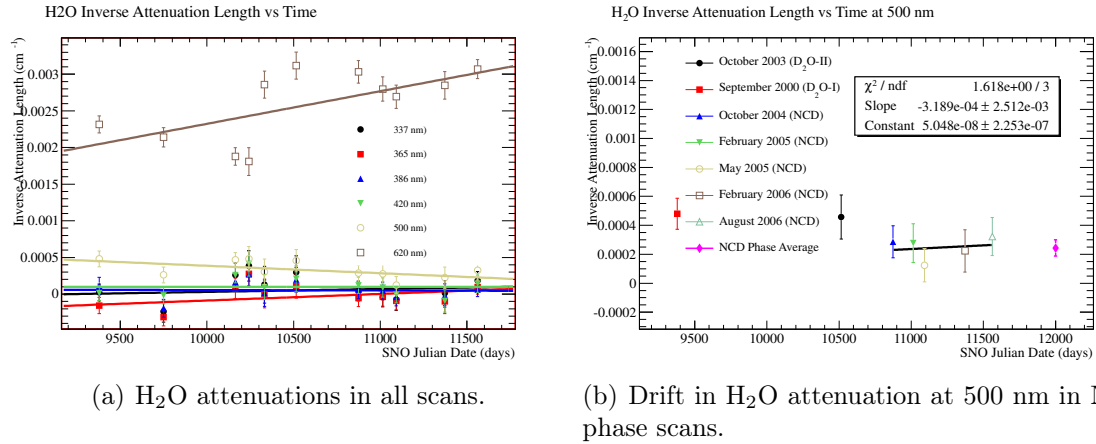


Figure 4.28: H₂O attenuations for all six wavelengths for all re-analysed scans.

in the Monte Carlo simulation and energy reconstruction the average quantities for the media attenuations were used.

4.6 Systematic Uncertainties of the Optical Calibration

Along with the extraction of the optical parameters, a series of systematic uncertainties were implemented to estimate the effect of the different cuts and assumptions employed in the extraction. These systematic uncertainties can be grouped into classes, depending on the origin of the systematic uncertainty. Table 4.3 shows a list of the systematic uncertainties for the optical parameters, along with the different classes they belong to.

The total systematic uncertainties that are common to all phases and deal with errors related with the distance between the source and the PMTs, as changes to the way the fit is executed (statistical cuts) were first defined in [83]. The NCD phase systematic uncertainties were first defined in [108]. The systematic errors were evaluated by either smearing the data points or by fixing a parameter of the optical fit and refit the data to extract a new set of optical parameters. The systematic error was then obtained by quantifying the differences between the nominal and the *shifted* fits.

Origin	Systematic	Effect	Weight factor (f_i)
Systematics Common to all phases			
Source position	Radial position scale	$R'_{PMT} = R_{PMT} \times 1.01$	0.20
	Radial position shift	$R'_{PMT} = R_{PMT} + 5cm$	0.20
	Radial position smear	$R'_{PMT} = R_{PMT} + Gauss(0, 5)cm$	0.20
	Source z position	$Z'_{LB} = Z_{LB} + 5cm$	0.40
	Source x position	$X'_{LB} = X_{LB} + 5cm$	0.20
	Source size	$d'_{PMT} = d_{PMT} - 3cm$	0.50
Source Distribution	Source intensity	$L'_{ij} = L_{ij}^2$	0.05
	Source uniformity	$L'_{ij} = 1$	0.05
PMT-PMT variability	–	$\sigma_{PMT} = 0$	0.2
Statistics	$\chi^2 cut(3\sigma)$	$\chi^2 < 9$	1.0
	$\chi^2 cut(4\sigma)$	$\chi^2 < 16$	1.0
PMT Response	PMT Efficiencies	$\epsilon'_j = \epsilon_j + Gauss(0, 0.001)$	0.50
	z asymmetry	Separate fit of PMTR(Section 4.4.2)	0.5
NCD phase systematics			
NCD effects	NCD tolerance parameter	$\Delta L' = 0.5 \times \Delta L$	0.5
	NCD reflections	$R(\lambda) = 0$	1.0
	NCD reflection probability	$w'_{ij} = w_{ij} \times 10$	0.2
	NCD reflectivity	$R(\lambda)' = 2 \times R(\lambda)$ (in MC)	1.0

Table 4.3: Systematic uncertainties in the optical parameters.

In most cases the systematic variations employed are larger than expected for actual running conditions in the detector in order to exaggerate the possible effect on the final oscillation analysis. In order to account for this, each systematic effect is weighted by a factor f_i , which estimates the fraction of the systematic change that actually applies to the data. These factors are shown in the last column of Table 4.3.

A brief description of the uncertainties considered, as well as the weights applied, are given in Appendix B.1. Two particular systematics are strongly related to the work of this thesis.

The z asymmetry systematic is only applied to the PMTR and was previously discussed in Section 4.4.2. This systematic affects all optical calibration scans and accounts for observed asymmetry in the PMTR, as it was not possible to find a definite reason for this asymmetry in a way that would be possible to produce a correction. This systematic is calculated by adding an additional iteration to the optical fit, after the final results were obtained, in which the optical parameters are re-extracted using two PMT angular responses. As it was observed in Section 4.4.2, this procedure causes a reduction of statistics in each PMTR, especially in the group of PMTs that are located in the upper part the detector ($z > -100$ cm). For this reason a weight of $f_{zasy} = 0.5$ is applied to the difference in the PMTR of the two groups. This results into an overall effect of 2% in the PMTR.

The *NCD reflectivity* systematic is only applied in the case the MC based NCD reflection correction is used (Section 4.3.4). Therefore, this systematic supersedes the *NCD reflection probability*, which is specific for the analytical correction (Section 4.3.4). Although this systematic is partly propagated together with other systematics such as the source position and size systematics and the NCD tolerance parameter, a second correction map using a NCD reflectivity that is twice as large as the nominal value was generated and is used in the correction. In order to fully evaluate the extent of this correction, and also accounting for the fact that the NCD reflectivity used is taken from a model and thus has no uncertainties, a factor $f_{NCDref} = 1.0$ is applied.

It is also important to note that the PMT efficiencies systematic was not effectively applied in the D₂O and Salt phase scans, as in this case the PMT efficiencies were not used in the fit, since in these phases the OccRatio fitting method was used.

Table 4.4 summarises the effect of each systematic in the optical parameters for all phases. It should be noted that the effect of each systematic was observed to vary with the wavelength in the same scan, due to the available statistics. This was particularly important in the earliest scans, with a larger incidence in the September 2000 scan [83]. In the D₂O and Salt phases the dominant systematics were related with the source position, which affected mostly the media attenuations. In the NCD phase, although these systematics were also dominant, the contribution from the NCD related systematics, such as the shadow cut and the NCD reflection correction, were also considerable. In both cases the most affected optical parameters were the media uncertainties.

However it is hard to perform a proper comparison of the systematics from phase to phase. As the experiment progressed, the optical calibration method also evolved by improved algorithms and better planning of the source positions and statistics collected. Therefore the results in Table 4.4 should be understood as an evaluation of the contribution of each systematic in the optical parameters and not as an evaluation of the variation of the systematic uncertainties from phase to phase.

It should also be noted that although the results of the D₂O phase include the results from the October 2003 scan, the uncertainties are dominated by the fit results in the September 2000 scan which has typically much larger systematic uncertainties than the results from October 2003. Again, this is due to the different planning on the source positions and the statistics accumulated. While the September 2000 consisted of data taken in 19 different positions, the October 2003 scan uses data taken in 30 different positions and considerably more statistics.

In both cases, the dominant uncertainty in the PMTR was the PMTR asymmetry systematic that could induce an effect of up to 3%.

Index	Systematic Error	Affected Parameters		
		D ₂ O	Salt	NCD
1	Radial Position Scale	$\alpha_d(\leq 15\%), \alpha_h(\leq 35\%)$	$\alpha_d(\leq 10\%), \alpha_h(\leq 30\%)$	$\alpha_d(\leq 10\%), \alpha_h(\leq 20\%)$
2	Radial Position Shift	$\alpha_d(\leq 10\%), \alpha_h(\leq 35\%)$	$\alpha_d(\leq 10\%), \alpha_h(\leq 25\%)$	$\alpha_d(\leq 15\%), \alpha_h(\leq 25\%)$
3	Radial Position Smear	$\alpha_d(\leq 5\%), \alpha_h(\leq 5\%)$	$\alpha_d(\leq 8\%), \alpha_h(\leq 10\%)$	$\alpha_d(\leq 5\%), \alpha_h(\leq 10\%)$
4	Source z Position	$\alpha_d(\leq 10\%), \alpha_h(\leq 20\%)$	$\alpha_d(\leq 10\%), \alpha_h(\leq 15\%)$	$\alpha_h(\leq 5\%)$
5	Source x Position	$\alpha_d(\leq 2\%), \alpha_h(\leq 5\%)$	negligible	$\alpha_h(\leq 1\%)$
6	Source Size	$\alpha_d(\leq 10\%), \alpha_h(\leq 15\%)$	$\alpha_d(\leq 7\%), \alpha_h(\leq 10\%)$	$\alpha_d(\leq 5\%), \alpha_h(\leq 10\%)$
7	Source Intensity	negligible	negligible	negligible
8	Source Uniformity	negligible	negligible	negligible
9	PMT-PMT variability		$\alpha_d(\leq 1\%), PMTR(\leq 1\%)$	
10	$3\sigma\chi^2 cut$	$\alpha_d(\leq 3\%), \alpha_h(\leq 40\%)$	$\alpha_d(\leq 3\%), \alpha_h(\leq 30\%)$	$\alpha_d(\leq 2\%), \alpha_h(\leq 10\%)$
11	$4\sigma\chi^2 cut$	$\alpha_d(\leq 5\%), \alpha_h(\leq 20\%)$	$\alpha_d(\leq 4\%), \alpha_h(\leq 35\%)$	$\alpha_d(\leq 3\%), \alpha_h(\leq 5\%)$
12	PMTR z asymmetry		PMTR ($\leq 3\%$)	
NCD Phase Systematics				
13	PMT Efficiencies			$\alpha_d(\leq 5\%), PMTR (\leq 1\%)$
14	NCD Tolerance			$\alpha_d(\leq 1\%)$
15	NCD Reflections			$\alpha_d(\leq 2\%)$
16	NCD Reflection Probability			$\alpha_d(\leq 5\%)$
17	NCD Reflectivity			$\alpha_d(\leq 3\%)$

Table 4.4: Effects of the systematic uncertainties.

4.7 Conclusions on Optics

Chapters 3 and 4 describe the optical calibration improvements implemented to address the challenges of an experiment composed of different phases of operation. In particular the introduction of the NCDs in the third phase required a reimplementation of the OCA analysis, in order to address the physical detector changes and the new physics phenomena resulting therein.

The work described in these chapters led to a better understanding of the detector response, which was then used in the reprocessing of the SNO data for the LETA analysis and for the NCD phase.

In particular, the implementation of the Occupancy method allowed to obtain a precision in the optical parameters that was comparable to the D₂O and Salt phases, despite the large statistics reduction of photon detection by the PMTs caused by the NCD shadows. Along with this improvement, the extraction of the PMT efficiencies allowed a more accurate simulation of the detector response.

The implementation of an optical cut to address the previously ignored NCD attachment anchors, led to an improvement in the PMT efficiencies that helped understanding the existing asymmetries in the detector [119], and thus led to an improvement in the detector response. Along with this change, the implementation of a simultaneous fit of two PMT angular responses led to the characterisation of the detector asymmetry in the optical calibration, observable in the PMT angular response.

A Monte Carlo based correction to address the NCD reflections was implemented, even though it was not used in the final reprocessing of SNO data, which was done before the work was completed. However, this analysis yielded results consistent with the analytical correction in place at the time, validating the analytical correction. In fact as the NCD reflections are one of the dominant systematics specific of the NCD phase, this correction demonstrated a slight reduction of the systematic uncertainty.

A study to determine the NCD reflectivity based on late light from Monte Carlo generated data was also carried out. This study showed a considerable discrepancy in the timing spectrum between real data and the Monte Carlo, which was only visible

in the late light. Although this did not affect the physics analysis, it questioned the validity of the NCD reflectivity study. Nonetheless, by choosing a region where there were no secondary contributions expected, such as other detector element reflections, the study suggested that the average NCD reflectivity might be approximately 20% higher than indicated by the initial ex-situ measurements.

Although in a scan-by-scan basis, the optical parameters in the NCD phase had larger uncertainties than in previous phases, the number of good calibration scans and the detector stability over time in the NCD phase allowed to decrease the uncertainties by performing a weighted average of the optical parameters.

The media attenuations were stable in the NCD phase, and consistent with the results obtained in the D₂O phase. A decrease was observed in the PMT angular response at large incidence angles which was consistent with the drift also seen through the Salt phase, which is most likely caused by the degradation of the PMT reflectors. Nonetheless, this variation is negligible considering the uncertainties in the PMT angular response.

Unlike the previous SNO analyses, the last analysis of SNO started after the detector was already shutdown and thus some of the analyses discussed in these chapters did not make it into the last data reprocessing. Nonetheless these analyses were important to validate the detector description used in the last data reprocessing and to assess the need for the extra effort in an additional data reprocessing. The results showed that the latter was not necessary. Furthermore, some of the results discussed were important to validate assumptions made in the calibration analysis, in particular the MC based NCD reflection correction validated the previously analytical correction that was used in the data analysis. The study of the up-down asymmetry in the detector demonstrated that the asymmetry observed also in the energy reconstruction was also visible in the optical calibration data therefore validating a data correction applied directly in the energy reconstruction level [118].

In addition to the validation and confirmation of observed results, this work will also be important in the future as the SNO detector will be re-used by the SNO+ collaboration.

Chapter 5

Neutrino Signal Extraction

The *signal extraction* (*SigEx*) in SNO is one of the most important steps of the analysis chain, providing the link between the *raw* data and the physics interpretation. In the combined 3-phase analysis the whole SNO data is analysed together, leading to additional difficulties due to the differences between each phase.

In this Chapter a brief description of the analysis formalism and methods will be presented, with emphasis on the solar neutrino flux and survival probability parametrisation. Although the work developed in this thesis did not cover directly the signal extraction, it is nonetheless important to understand the analysis chain leading to the measurement of the solar neutrino oscillation parameters. However, a contribution to this part of the analysis was also performed: a study to determine the best polynomial parameterisation to describe the electron neutrino survival probability was performed and is described in Section 5.6.3.

A detailed description of the SigEx analysis can be found in [127–131]. A general description of the SigEx observables will be given in Section 5.2. Sections 5.3 and 5.4 will then provide a reference for the backgrounds and systematic uncertainties. The output of SigEx will then be provided in Section 5.5, with a reference to previous SNO analyses. Finally, Sections 5.6 and 5.7.1 will describe the strategy of the 3-phase combined SigEx and the outputs that shall be used in the neutrino oscillation analysis described in Chapter 6.

5.1 Introduction

SigEx is responsible for separating the neutrino events into different classes in a way that can later be used in physics analyses. As the objectives of the different SNO analyses changed with time, so the SigEx methods and outputs have evolved:

- In the individual analyses of phases I and III, the objective of the SigEx consisted in the separation of the neutrino data into different classes of events, providing the output in the form of a number of events for CC, ES, NC and backgrounds integrated over the energy window of the analysis.
- The analysis of phase II provided the output in the form of a spectrum of reconstructed electron kinetic energy of CC and ES events, as well as an integrated number of events detected through the NC reaction, which directly translated into a ^8B Solar neutrino flux measurement.
- Later, the first combined analysis of the two first phases of SNO (LETA) also followed the method of phase II, as well as a measurement of the Solar electron neutrino spectral distortion, which will be the only SigEx method employed in the 3-phase analysis, where a new analysis of the proportional counter data from the NCD phase is also carried out, performing *pulse shape analysis (PSA)* of NCD events (Section 5.6.2).

5.2 Observables

In phases I and II, and also for the PMT data of phase III, it was not possible to make a distinction of the event types in an event-by-event basis. Therefore, the main goal of SigEx was to attribute a probability of belonging to a certain class (CC, ES NC or background) for each event based on their observables signature, and to perform a statistical separation of the CC, ES, NC and background event classes.

In the following subsections each observable shall be described, as well as the cuts applied through each observable to the data. Figure 5.1 shows the Monte-Carlo distribution *probability density functions (PDFs)* of the observables discussed below for the D₂O, Salt and NCD phases.

Event Position

The event position is characterised by a volume weighted radius, the parameter ρ , which is defined as

$$\rho = \left(\frac{r_{ev}}{R_{AV}} \right)^3. \quad (5.1)$$

where r_{ev} is the distance of the event vertex to the centre of the detector and R_{AV} is the radius of the acrylic vessel (600 cm). Two position estimators were used in the analysis of SNO data: the position of the events from the D₂O and Salt phases were assigned by using the FTP estimator [132], while the data in the NCD phase were assigned the position by using FTU/FTN [109, 133]. Both estimators are similar in concept, using the residual between the transit time for each PMT, but the FTN/FTU fitter was optimised to deal with the additional challenges imposed by the NCDs, such as shadows and reflections.

This observable has a critical role in the event reconstruction, as it is used as an input to determine two other observables: the event energy and isotropy, both of which are described below. Furthermore, the reconstructed position was also important to apply a fiducial cut in order to separate the events that originated inside from those from outside the AV, such as backgrounds. Finally, this observable is used to separate CC and NC events and to identify tails from external backgrounds inside the fiducial volume.

Event Direction

The direction of the events is another of the fundamental observables, along with the event position, being used in the determination of other observables, such as the event energy. This observable is obtained by fitting the PMT hit pattern to the Čerenkov ring distribution. In the context of the SigEx it is usually characterised as $\cos \theta_{\odot}$, where θ_{\odot} is the angle between the event direction and the Sun-Detector axis.

This observable is crucial to separate the ES events from the other classes of events, as the direction of ES events is strongly correlated with the direction of the incoming neutrino, due to the kinematic distribution of the electron from the ES reaction.

Isotropy (β_{14})

The isotropy parameter of an event is evaluated by using the distribution of hit PMTs from the event position and is defined as [134]:

$$\beta_{14} = \beta_1 + 4\beta_4, \quad (5.2)$$

$$\beta_l = \frac{2}{n(n-1)} \sum_{i=1}^{n-1} \sum_{j=i+1}^n P_l(\cos \theta_{ij}), \quad (5.3)$$

where n is the number of hit PMTs, θ_{ij} is the angle between PMTs i and j from the vertex and P_l is a Legendre polynomial [135]. This observable was crucial in the separation of CC and NC events in the Salt phase [65, 70]. In the NCD and D₂O phases this observable is not relevant, as the NC reaction in the D₂O produces a single γ , nonetheless it was used for D₂O phase data in the LETA analysis.

Effective Electron Kinetic Energy (T_{eff})

The effective electron kinetic energy (T_{eff}) is reconstructed for each event based on the number of hit PMTs. Each detected event was assigned an observed energy by an energy estimator algorithm. Different estimators were used in SNO, namely the FTK [118] and the RSP [115].

The difference between these energy estimators lie mostly in the hit PMT time window used for the energy estimation. While RSP only uses the data in the prompt peak to assign the energy of the event, FTK uses virtually the full time window (150 ms), including reflected photons, resulting in an improvement in the energy resolution of about 6%. This translates in a considerably more efficient separation of signal and backgrounds, and consequently into an improvement in the background reduction of approximately 60% [118]. The LETA analysis (combination of phases I+II) used the FTK estimator, while the NCD phase used the older RSP estimator, as there was no reprocessing of the NCD data for the 3-phase analysis.

The analysis window for this observable is also different for each phase. The data from D₂O and Salt phases have a threshold of 3.5 MeV in T_{eff} , while the NCD phase data are selected with an energy threshold of 6 MeV. The higher energy threshold of the NCD phase data is due to the larger low energy backgrounds introduced by the NCDs and to the worse energy resolution.

The results of the SigEx procedure were usually presented as a function of only one of the observables that was left free to float: the effective energy T_{eff} . However, this is not compulsory, as it would be equally valid to represent the results as a function of any other observable. The reason for this choice lies in the fact that the observed energy is the observable that retains more features about physical meaning of the results, since neutrino oscillations are energy dependent.

5.3 Backgrounds

The backgrounds represent a large fraction of data at low energies. In the early SNO analyses of the individual phases the energy thresholds were set high enough to avoid them, especially to avoid low energy *tails* that were difficult to characterise [36, 65, 69]. The main sources of backgrounds were already described in Section 2.5, and are explained in detail in [69, 70]. Like in the LETA analysis, in the 3-phase analysis the backgrounds are treated as another class of events, for which a series of MC simulations were generated in order to build background PDFs, the same way as for the signal classes of events. These simulations were validated through extensive source calibrations and analysis in the 3.5 to 16 MeV energy range.

Some particular backgrounds, due to having shapes very similar between them, have their scale (measured independently) constrained in the fit [131]. Thus, in the SigEx analysis, some backgrounds have their scales *floating*, *i.e.* free to vary in the fit, while others are fixed and have their uncertainty propagated by shifting the scale to the extremes of the uncertainty range and refitting. This last method is usually called *shift and refit*, and it essentially propagates the maximum effect that the uncertainty in their scales causes in the separation of the event classes. Obviously, it is of utmost interest to minimise the number of background types that are treated this way, as it leads to larger uncertainties in the final results.

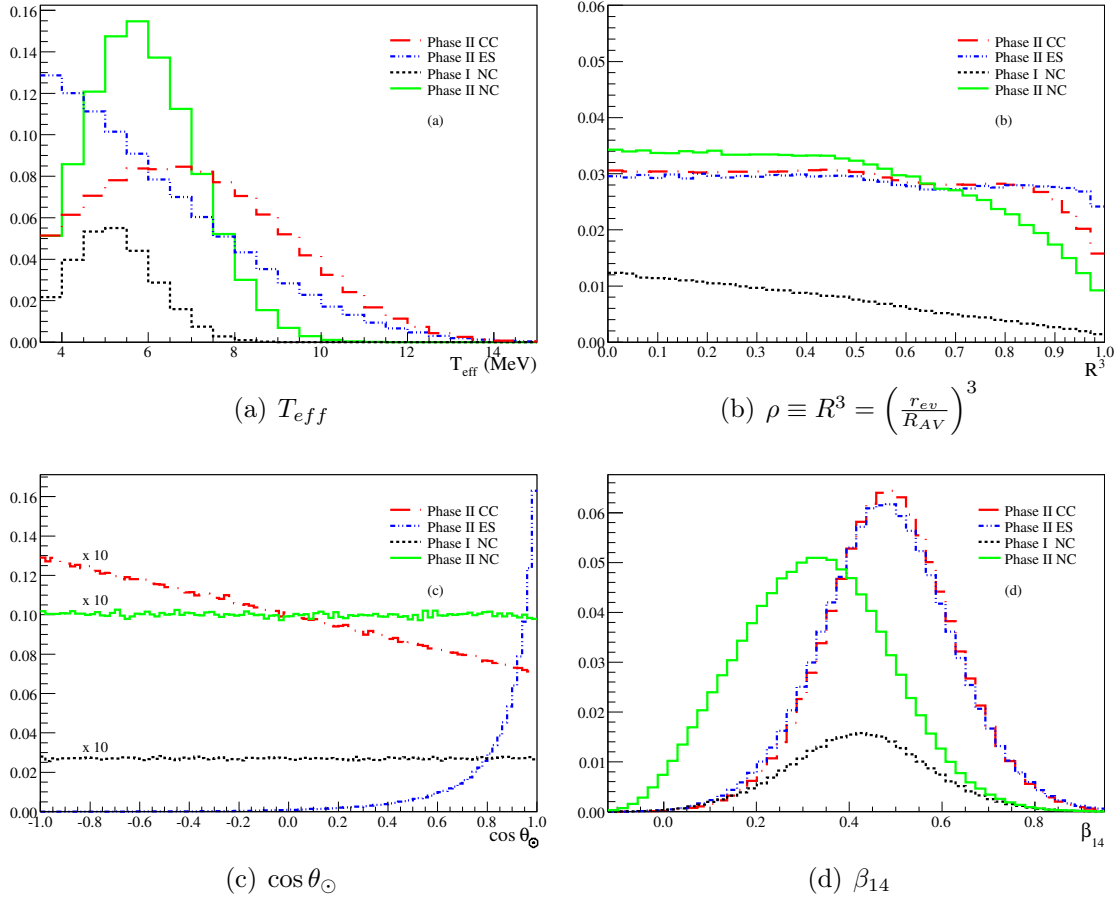


Figure 5.1: Monte-Carlo distributions of the different signals as a function of the observables. Only the D₂O and Salt phase data are shown. Having the same detection medium, the NCD phase distributions are similar to the ones from the D₂O phase, except for the T_{eff} distribution due to the different energy threshold and worse resolution. Figures from [70].

For the neutrino oscillation analysis that is the subject of this thesis, the background levels are of no direct consequence. Only the uncertainty in the physics outputs is used in the neutrino oscillation analysis. Therefore, it is important that the SigEx analysis propagates the effect of the background levels to the uncertainty in the output parameters, but the background levels themselves are not used in the oscillation analysis.

5.4 Systematic Uncertainties

As discussed in Chapter 2, the SNO experiment dedicated a large portion of its live-time to calibrations. This, along with a strong effort in tuning the Monte Carlo simulation to describe the data, led to an improvement of the systematic uncertainties, which are most of the time derived from the comparison of the calibration and simulation data.

In the SigEx analysis most of the systematic uncertainties are described by a central value and a spread of a given parameter and are propagated in two ways: virtual shifts in their central values (within their spreads), or by allowing the central values of the uncertainty parameters to be constrained by the data itself. The latter are integrated into the fit algorithm as floating parameters, along with the remaining observables and some of the backgrounds, so that their value can vary to better fit the data, within a pre-determined allowed range.

This procedure has a number of advantages: by allowing the systematic uncertainty parameters to vary, or float, the data itself helps to constrain these uncertainties, effectively choosing the value of each uncertainty parameter that better agrees with the data itself; a similar advantage is that by constraining the floating range of the systematic parameter by means of penalty terms, the problem of overestimated systematics is minimised.

Being a computationally intensive operation, as one is effectively increasing the number of parameters in the model, the floating procedure is only implemented for the dominant systematics. Two of the most relevant ones being the energy scale and resolution. These systematic parameters are allowed to vary in order to change the acceptance of the detector to low energy background events close to the analysis threshold.

The list of uncertainty parameters results from a combination of the systematic uncertainties of the 3-Phase analysis are described in detail in [131].

In the context of this thesis, as the output consists of a parameterisation of the electron neutrino survival probability, the individual systematics do not have any direct effect in the neutrino oscillation analysis. Thus, the total systematic

uncertainty is summed in quadrature with the statistical uncertainty. More details will be given below.

5.5 Outputs from the Signal Extraction

In this Section, a brief summary of the outputs from the SigEx is given. As stated previously, the SigEx procedure aims at not only separating signal events from backgrounds, but also separate between different types of signal events.

The analysis consists basically of an Extended Maximum Likelihood fit, where the different types of events present in the data set are modelled by means of a *probability density function (PDF)* and a scale, with uncertainties. Usually the PDFs were multi-dimensional, representing the distribution of the event class (including some backgrounds) as a function of each of the observables.

This basis has remained unchanged for all analyses, even though the technical details of the implementation have changed. Similarly, the output of the SigEx has also evolved with the different analyses. Two different models of outputs have been implemented in the different SNO analyses: Reconstructed energy spectrum and polynomial parameterisation of the spectral distortion. In the following subsections the description of these types of output will be clarified.

5.5.1 Reconstructed energy spectra

In the analysis of the three individual phases, and also in the combined analysis of phases I+II, the output of the SigEx analysis focused in a statistical separation of the neutrino events into different types. To avoid a long description of this SigEx method for each analysis, we will focus on outputs of the LETA SigEx analysis through this method. However, detailed descriptions of each individual analysis can be found in [14, 36, 64, 65, 69, 70].

Despite being able to detect events through three different reactions, SNO wasn't able to perform an event-by-event separation of the signals detected by the PMTs. Thus a statistical separation of the event classes by means of an Extended Maximum

Likelihood fit was performed for each dataset. This constraint also influenced the output of the SigEx analysis as, by not being able to tag individual events, the output was either a distribution of each event type in terms of the reconstructed energy (T_{eff}) or a total number of each event class integrated over the whole energy range of the analysis.

In order to perform the SigEx analysis, 4-dimensional PDFs were built from simulated MC events, describing the signature of each class of event as a function of the four observables described in Section 5.2 and taking into account the response of the detector in each phase¹.

A negative extended Log-Likelihood fit was then performed on the data. The results of the fit were the fractions of each class of events, per bin of the PDFs, in the data set. Additionally, the NC events were integrated, as these are detected by capture of the thermalised neutron from the NC reaction, and thus do not have information about the incoming neutrino. The total number of neutrons (statistically) identified as originating from the NC reaction was then an almost direct measurement of the solar flux of ^8B neutrinos².

By letting the relative amplitude of individual T_{eff} bins vary, an *unconstrained fit* was performed, losing the last model dependence, the ^8B spectrum shape. As the number of NC events, after correcting for the neutron backgrounds, was a direct measurement of the total ^8B solar neutrino flux, this allowed to perform a virtually model independent analysis.

The output for the CC and ES signals was presented in terms of a binned reconstructed electron energy spectrum. Alternatively, these spectra were shown in terms of the fraction of the SSM that should be detected in that reconstructed energy bin, in case no neutrino oscillations were present. This last method essentially allows to show an *effective* flux of solar neutrinos detected through CC (or ES) for each bin in reconstructed energy. In Figure 5.2, the reconstructed energy spectra of CC and ES events obtained from two independent SigEx methods used in the LETA analysis is shown as a fraction of the SSM prediction. The large uncertainty on the CC events

¹In case of LETA analysis, the *unconstrained fit* result was obtained by using two separate detector response functions, each one describing one of the analysed phases.

²As described in Chapter 2, there were a series of backgrounds that could fake a NC event. These had to be subtracted in order to obtain the number of NC events from ^8B solar neutrinos.

at the low energy range ($3.5\text{MeV} \leq T_{eff} \leq 4.5\text{MeV}$) in Figure 5.2(a) is due to the large number of low energy background events at these energies.

The corresponding electron energy spectrum for ES events is also shown in Figure 5.2(b), where the large error bars make clear the effect of the low statistics for this reaction in SNO.

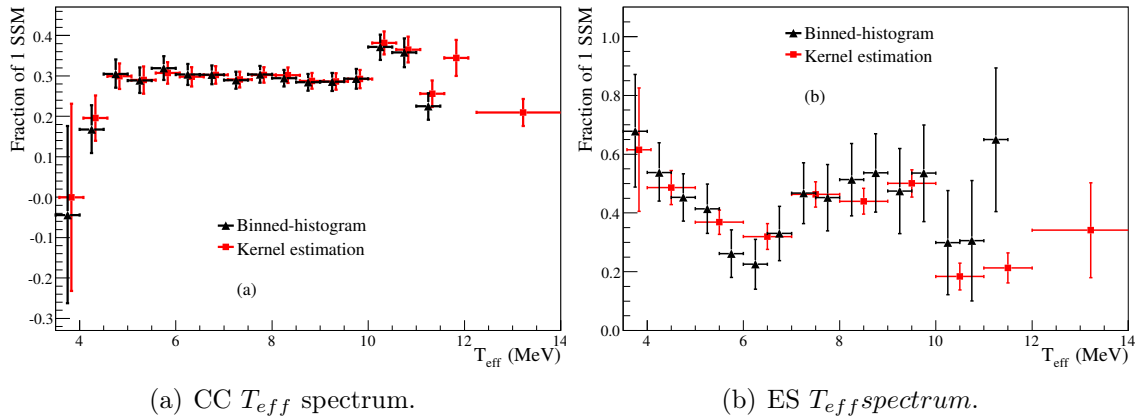


Figure 5.2: SigEx output from the LETA analysis for CC and ES events. The red and black marks represent results from different SigEx methods. Figures from [70].

As the neutron events do not carry any information about the incoming neutrino the total number of NC events was then converted into a flux of ^8B solar neutrinos. Figure 5.3 shows the result obtained in the SigEx in the LETA analysis, compared with two SSMs with different metallicity models .

This method, however, has a few shortcomings when applied in the simultaneous analysis of data from different phases [136].

- Unphysical large number of degrees of freedom: The width of the differential cross section (dE_ν/dE_e), combined with the detector response, spreads a single neutrino energy over nearly 4 reconstructed electron energy bins.
- Interpreting the output spectrum is a non-trivial task: The very broad resolution in mapping neutrino energy to reconstructed electron energy makes individual CC bins to have large correlations which are not captured directly in the covariance matrix in the fit. These correlations come from the assumption that CC events come from a smooth neutrino spectrum which is smeared

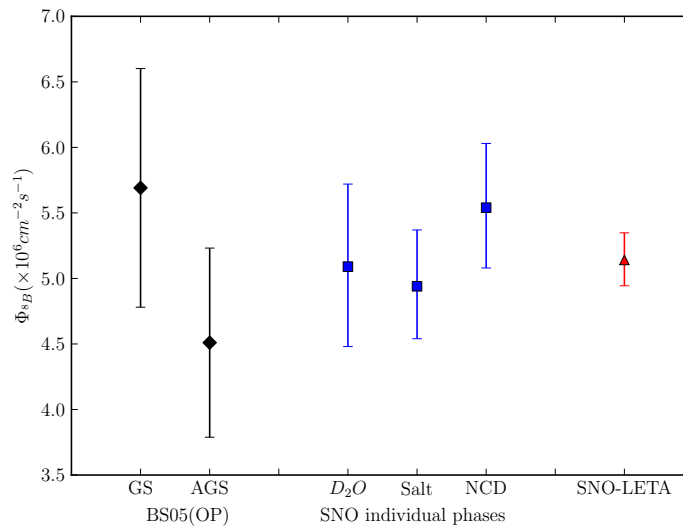


Figure 5.3: Measurement of the total ^8B Solar neutrino flux in LETA analysis, as well as predictions from two SSMs (BS05(OP,GS)) and BS05(OP,AGS) [26]).

out by the CC interaction and the detector response. In order to properly treat these correlations when performing a physics analysis, one needs a full analytic form for all these terms.

- Difficulty in combining phases with very different energy resolutions: By having different energy resolutions, the reconstructed energy of events from each phase may not have a direct correspondence, which strongly limits the number of bins in T_{eff} , and weakens the physics analysis potential of the results.

For these reasons, with most relevance to the last, a different approach for the SigEx was implemented, which is described below.

5.5.2 Polynomial parameterisation of the Electron Neutrino Survival Probability

In the combined analyses of the different phases of SNO, a new method of SigEx was developed, in which the results are now described as a function of the total ^8B solar neutrino flux and a parameterisation of the spectral distortion observed. This method was created in order to deal with a series of shortcomings in the previous method

that are associated with the combination of different phases of SNO. By measuring the distortion of the neutrino ${}^8\text{B}$ energy spectrum, this SigEx method is virtually performing a direct determination of the electron neutrino survival probability (P_{ee}).

The observables are the same as the reconstructed energy method, but now the PDFs have an additional dimension: the MC generated neutrino spectrum (E_ν) for each bin of the reconstructed energy. As there is no direct information from the detector concerning the neutrino energy of each event, the signal PDFs are no longer static as in the previous method. They now have to be re-weighted for each event, as the neutrino energy PDF will have a different shape depending on the reconstructed energy of the event.

Furthermore, this SigEx method attempts to evaluate the distortion of the energy spectrum of the ${}^8\text{B}$ electron neutrinos, and thus its output is a function of E_ν . In lack of a better generic functional form, as the electron neutrino survival probability results from the solution of a system of coupled differential equations (see Chapter 1), the survival probability is expanded in a form of a polynomial around $E_\nu = 10\text{MeV}$, which corresponds to the best energy response of the SNO detector:

$$P_{\nu_e \rightarrow \nu_e} = c_0 + c_1 (E_\nu - 10 [\text{MeV}]) + c_2 (E_\nu - 10 [\text{MeV}])^2. \quad (5.4)$$

Additionally, the asymmetry of the signal events detected by day and night is also parameterised as a linear function:

$$A_{ee} (E_\nu) = a_0 + a_1 (E_\nu - 10 [\text{MeV}]). \quad (5.5)$$

More details about the exact implementation of these functions in the SigEx analysis are presented in Section 5.6. In this context, the centre of the energy response of SNO detector corresponds to the peak of the neutrino spectrum sensitivity, after taking into account all detection effects such as cross sections, efficiencies and detector response in electron reconstructed kinetic energy. This is basically the ${}^8\text{B}$ neutrino spectrum convoluted with the cross sections and detector energy response for electrons, taking into account the analysis cuts and is henceforward referred to as the *detector sensitivity function* (or spectrum). In Figure 5.4 the sensitivity function of

SNO is shown, along with two examples of the electron neutrino survival probability.

The outputs of this analysis method are the polynomial coefficients c_i, a_i and the scale of the ${}^8\text{B}$ flux determined by the NC events in comparison with the SSM used in the MC. Together with the central values, the output also consists of the parameter uncertainties, both statistical and systematic. Additionally, the correlation matrix is also necessary to carry out the physics analysis, as the correlations between the coefficients are stronger than the ones obtained in a reconstructed energy fit.

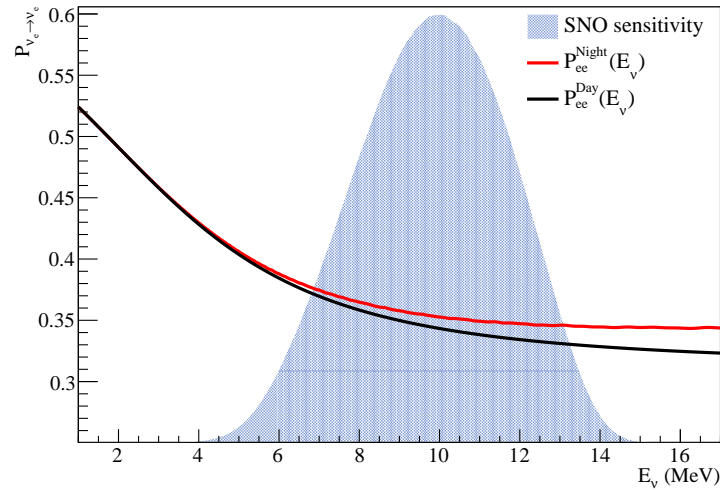


Figure 5.4: Sample survival probability curve of ${}^8\text{B}$ neutrinos as a function of neutrino energy for the energy range relevant for SNO. Both day and night survival probabilities at the SNO location are represented. The SNO sensitivity in neutrino energy is also shown. The sensitivity spectrum is not to scale.

For the neutrino oscillation analysis the detector sensitivity function is also necessary. More information about the usage of this spectrum will be given in Section 6.3.2. This sensitivity spectrum is obtained from the SigEx fit, by projecting the signal PDFs used to obtain the SigEx outputs into neutrino energy.

5.6 The 3-phase Combined Analysis

The *three phase combined analysis (3-phase)* is the latest and probably the last solar neutrino analysis of SNO data sets. It uses the data sets of the *low energy threshold*

analysis (LETA), where the D₂O and Salt phases were combined and reanalysed in a single analysis with a lower reconstructed energy (T_{eff}) threshold of 3.5 MeV [70], with the NCD phase data, both PMT and NCD, and perform a single analysis of all three phases as a single data set. This means that the same cuts, estimates of backgrounds, and systematic errors of each original analysis will be used, where possible. This shall lead to a single result, that will describe the whole data set of SNO covering the three phases of data taking.

A new analysis of the data from the NCD array is also performed, the *pulse shape analysis (PSA)*, which is included in the general signal extraction [137, 138]. The ionisation waveform produced by neutron capture on the ³He proportional counters is distinguishable from other waveforms, making it possible to be used together with the total energy to distinguish neutron captures from other backgrounds. This analysis will produce a constraint in the Neutral Current flux measurement of SigEx. Some more details will be given below.

5.6.1 Combination of Data Sets

The combination of the D₂O and Salt phase is extensively documented in [70, 136, 139, 140]. By aiming to use the most of the previous LETA [70] and NCD phase analysis [69], the systematic uncertainties defined for each analysis were also inherited and used for the 3-phase fit. In this context, the only correlating systematic uncertainty will be the energy scale.

In the previous analysis (LETA), the primary SigEx method consisted in the statistical separation of events using the observables described in subsection 5.2 and the output was obtained as a function of the reconstructed electron energy, as described in 5.5.1. Later, using only the CC part of the events, a measurement of the electron neutrino survival probability was performed providing the output described in subsection 5.5.2. In this case the ES portion of the events was not considered, as the statistics are very low and it was considered that it wouldn't significantly affect the final result [136].

One of the major challenges of combining different phases is dealing with the different energy responses of the detector in each phase. While D₂O and Salt phases

have energy responses similar enough that could be properly dealt with a sensible choice of the bin widths in reconstructed energy; it is not the case in the 3-phase analysis. By introducing the proportional counters in the NCD phase, the PMT energy response was significantly changed and thus a SigEx analysis in reconstructed electron energy was seriously compromised [141] as the width of the reconstructed energy bins would have to be considerably larger (at least 1 MeV, as opposing to the 0.5 MeV used in the past analyses) and thus the physics analyses would be substantially limited.

Thus, in the case of the 3-phase analysis, there isn't a SigEx separation in reconstructed energy, and thus the only SigEx method used is the interpretation of the solar neutrino spectral distortion as described in subsection 5.5.2. The reconstructed energy (T_{eff}) will still be one of the input observables but now, together with the additional dimension in the PDFs (the distribution of neutrino energies as a function of the detector reconstructed energy) the detector response going from neutrino energy to electron energy is included in the MC used to generate the PDFs.

It is important to note that by aiming to extract a survival probability from the whole data set, the ES class of events should be separated into the electronic component (ES_e) and the remaining active component ($ES_{\mu\tau}$), as they contribute differently to the survival probability. The $ES_{\mu\tau}$ component contributes to the survival probability as $\propto 1 - P_{ee}(E_\nu)$, while its electronic component has a direct $P_{ee}(E_\nu)$ contribution. This also means that although improvements such as background estimations and energy resolution will be inherited from the previous analyses, a completely new SigEx will be performed.

Besides the signal extraction of the ^8B flux and survival probability, there is also an attempt to measure the solar neutrino flux from the *hep* neutrino reaction, which up to now has never been experimentally measured. Only theoretical predictions and an experimental upper limit exist [129].

In the following subsections a brief description of the most relevant improvements to the analysis will be given.

5.6.2 Pulse Shape Analysis

In the initial analysis of the data from the NCD phase [69], the data from the proportional counters was analysed by studying only its energy spectrum, originating from the integrated charge of the shaped electrical signal. This was produced by the electron-ion pairs generated by the proton and triton produced in the counter, as described in Section 2.4. This consists in a statistical separation of the neutron events from the other NCD backgrounds, of which α particles are the most common.

For the 3-phase analysis, a new method of counting the detected neutron events was implemented, by use of the digitised NCD pulse shapes: the *pulse shape analysis (PSA)*.

When a particle ionises the gas inside the proportional counter, an ionisation waveform is produced. This waveform has a series of features, that depend on the dE/dx and can be used to distinguish the particle that originated from the pulse. In the case of the NCDs the large majority of the events come from neutrons (signal and background) and from α particles (background). Examples of the corresponding waveforms obtained both from data and MC are shown in Figure 5.5. Figure 5.5(a) shows an α waveform obtained from a NCD counter filled with ^4He and the corresponding best fit from the PSA analysis for the α hypothesis. Figure 5.5(b) shows a neutron waveform obtained from ^{24}Na calibration data and the corresponding PSA best fit for a neutron signal.

Although this technique is very promising for event-by-event discrimination, there are some inherent difficulties. For instance, the exact shape of the current pulse depends on the radius at which the primary ionisation occurred. Therefore the shape of the pulse also depends strongly on the location of the ionisation track in the counter and in what direction the proton and triton or alpha were traveling. This leads to a wide variety of possible pulse shapes.

Due to the large variety of possible pulse shapes, different methods of analysis were implemented using different principles. The details of those methods are thoroughly described in [131, 137, 138]. The final number of NC events is obtained by combining the event-by-event selection of the three PSA methods, and then feeding their background constraint to an energy fit of the NCD data, thus reducing the

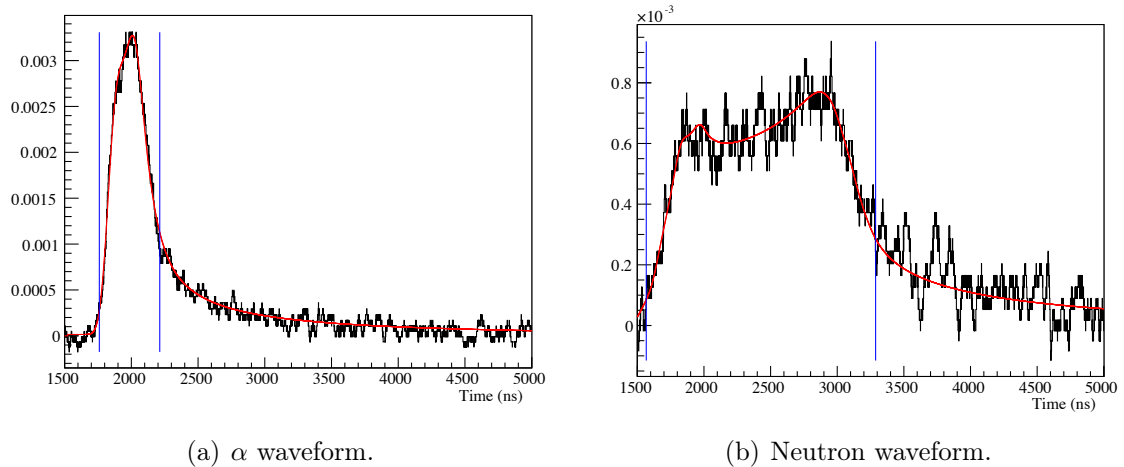


Figure 5.5: Examples of waveforms obtained from real data with the corresponding Monte-Carlo generated pulses. The blue lines represent the boundaries of the time windows used to fit the data to the MC. Figures from [127].

statistical uncertainties [131]. The number of NC neutrons obtained from this fit is then joined in the final SigEx fit as a constraint of the total NC events.

5.6.3 Choice of the Survival Probability Parameterisation

In Section 5.5.2, a description of the new output parameterisation was presented. In this context, the choice of the specific parameterisation is an important step. In order to decide upon the best spectral distortion parameterisation, there are two aspects that need to be taken under consideration. Firstly, since there is no simple theoretically-motivated parameterisation of the electron neutrino survival probability, it was decided to use the most general empirical approach that could describe the distortion. Second, one has to make a compromise in the number of degrees of freedom of the parameterisation in order to optimise the sensitivity to the widest range of oscillation parameters, but still be able to have reasonable uncertainties in the output parameters. In the context of this thesis, a verification of the former consideration was performed and will be explained below [142].

As the electron neutrino survival probability in the presently allowed region of oscillation parameters (quoted in Table 1.3) behaves like a continuous, slowly varying

function, and by lacking a more accurate analytical expression, a high order polynomial was considered to be the best choice. In general, a choice of a polynomial function is a dangerous choice as the regularity of the function can hide effects that otherwise could be visible. In fact, different alternative parameterisations were tried, with particular emphasis on a binned parameterisation [131]. However, this was later verified to yield biased results, coming from the fact that event statistics constrained the number of bins in neutrino energy to be small. Inside a bin the survival probability was thereafter averaged, losing the distinctive features of a slowly varying function [131, 143].

In Figure 5.4, an example curve of *electron neutrino survival probability* (P_{ee}) is shown for a random set of oscillation parameters inside the current allowed region. The SNO sensitivity is also shown in terms of neutrino energy.

Definition of a *goodness of fit* condition

Given the generality of a polynomial parameterisation, one should use the highest polynomial degree possible, keeping under consideration that the higher the degree, the longer the fit would take to converge, and the neutrino event statistics might not be enough to constrain reasonably each of the parameters.

In order to verify which polynomial degree could better describe the model survival probabilities, it was necessary to define a figure of merit that would evaluate the accuracy of the fit over a wide range of survival probability parameters. In Figure 5.6, different examples of survival probability curves are shown for different regions characterised by two oscillation parameters ($\tan^2 \theta_{12}$ and Δm_{21}^2) that were once considered as the best fit solution for the values of these parameters. For instance, the current allowed region of oscillation parameters (quoted in Table 1.3) is located in a region commonly denominated *Large Mixing Angle (LMA)*, characterised by a large (albeit non-maximal) mixing angle of $\approx 35^\circ$ and a value of Δm_{21}^2 on the order of $1 \times 10^{-5} eV^2$. In this region the survival probability has a shape similar to the one shown in the upper left plot of Figure 5.6. However, it should be noted that the current parameter limits are obtained by joining the data from all neutrino experiments. The allowed regions of oscillation parameters for each experiment taken alone are in fact much wider, as their sensitivity is not enough to rule out the other regions.

Figure 5.6 illustrates clearly the problem of defining a reasonable *goodness of fit* in the evaluation of how well a polynomial function describes the survival probabilities. For instance, the survival probability in the LMA region shows a small, slowly decreasing variation of the survival probability around $P_{ee} \approx 0.30$ (for neutrino energies above 4 MeV, which is the region of interest for SNO), while for instance the survival probability in the *small mixing angle* (SMA) or *vacuum* (VAC) shows a different behaviour, not only in shape, but also in the scale. In the figure, the blue shaded area is the sensitivity of SNO in neutrino energy, the same that was shown in Figure 5.4.

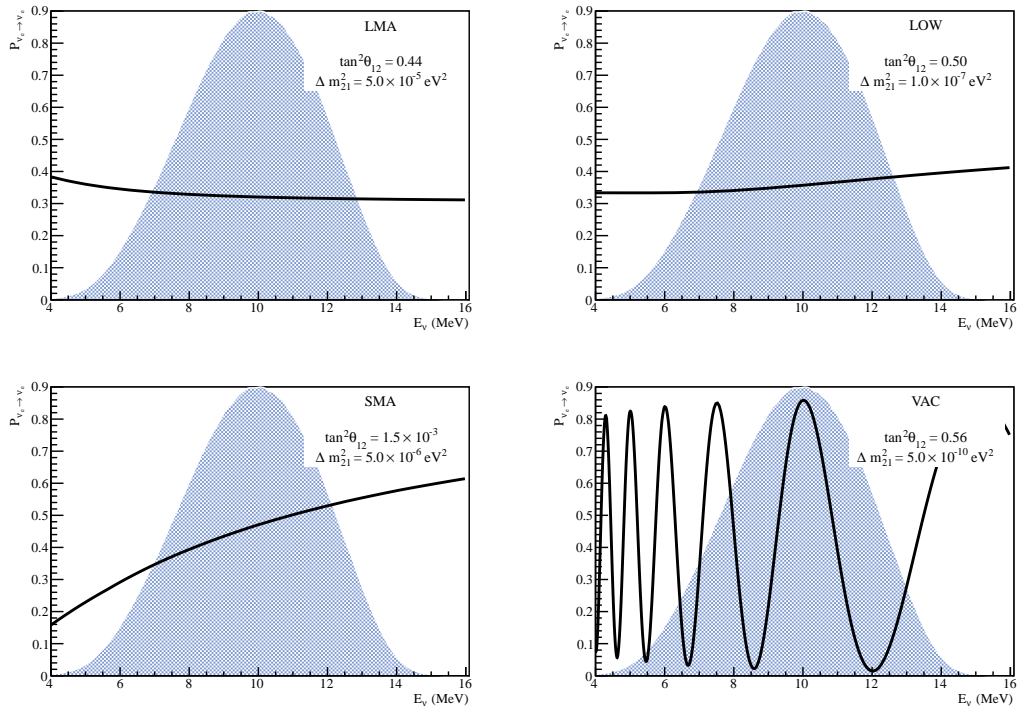


Figure 5.6: Examples of survival probability curves in different solutions, identified by the oscillation parameters. The solutions are: large mixing angle (LMA), low mass (LOW), small mixing angle (SMA) and vacuum (VAC). The oscillation parameters considered for each curve are given in the figure.

In order to estimate how much the polynomial parameterisation is similar to the full numerical calculation of the survival probability $P_{ee}^{theo}(E_\nu)$ the relative difference between the two is used for a discrete, but large, number of points sampled

equidistantly in neutrino energy in the range from 4 to 16 MeV;

$$G^n = \frac{1}{N} \sum_{i=0}^N \frac{|P^n(E_\nu^i) - P_{ee}^{theo}(E_\nu^i)|}{P_{ee}^{theo}(E_\nu^i)}. \quad (5.6)$$

The choice of using the modulus was taken in order to always get a positive value and avoid cancelations in the residual between the polynomial and the full numerical calculation. Furthermore, although the survival probability is a continuous function, in the analysis algorithm there is a well defined number of sampled neutrino energies. By determining the relative difference one does not have to worry about the scale of the survival probability for a particular subgroup of the oscillation parameters. The closer the sum in Equation 5.6 is to zero, the better is the agreement between the theoretical survival probability and the polynomial parameterisation.

As an example, in Figure 5.7, an example of the fit using five polynomial functions of different orders. The results of the agreement between the polynomials and the functions are shown in the figure.

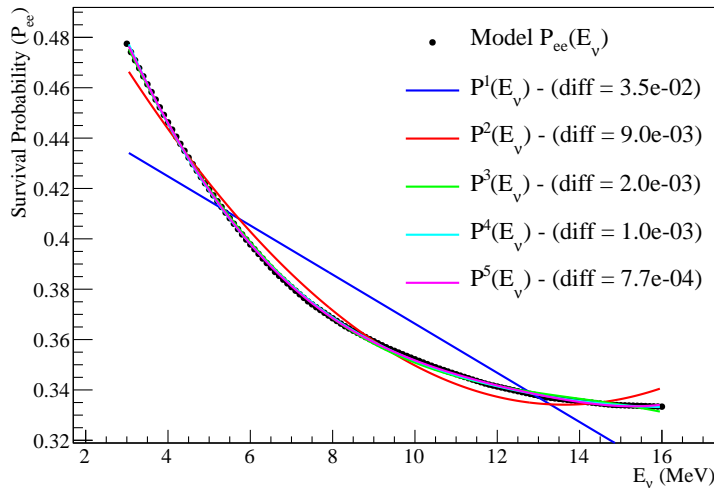


Figure 5.7: Fit of five polynomial functions of different orders, centered at 10 MeV, to the model survival probability a selection of oscillation parameters compatible with the LMA solution. The oscillation parameters used were $\tan^2 \theta_{12} = 0.447$ and $\Delta m_{21}^2 = 8.5 \times 10^{-5} eV^2$. The results obtained by determining the difference using Equation 5.6 are also shown.

It is important to note that the polynomials are defined as the *day* survival probability centered at 10 MeV.

Results

Using the definition of Equation 5.6, the range of the oscillation parameters (henceforward called MSW parameter space) was sampled for the respective day survival probabilities in the region of neutrino energies from 4 to 16 MeV, which is the region where SNO is sensitive. Each survival probability curve was then fitted to five polynomials of different orders following the form described in Equation 5.7:

$$P^n(E_\nu) = \sum_{i=0}^n c_i (E_\nu - 10\text{MeV})^i \quad (5.7)$$

and the term G^n was obtained, for $n = 1, \dots, 5$.

Figure 5.8 shows the results obtained for each of the polynomials considered. The range of oscillation parameter values sampled is much larger than the current allowed region to evaluate how accurate this procedure would be without prior information about the oscillation parameters. As expected the results show an increasing accuracy of the fit with higher orders of the polynomials. From the results it was verified that, for polynomials above third order, the benefit was marginal although a second order polynomial already yields very good results with a relative integrated difference of less than 2%, which is less than the theoretical uncertainties in the ${}^8\text{B}$ neutrino spectrum, showing only a small disagreement in the more peripheral regions of the currently allowed parameter space.

Similar tests performed on the SigEx analysis side demonstrated that the number of events in the data set wouldn't allow the fit to go beyond a second order polynomial [136]. Therefore the final choice was settled as performing a second order polynomial fit.

It is important to recall that this verification aimed solely to verify how well polynomial functions of different orders agreed with the model survival probability. In this sense it would be better to use a third or higher order polynomial. However, there is an important factor that has to be taken under consideration. The expression used to evaluate the accuracy of the polynomial parameterisation weighs equally the survival probability at all neutrino energies, which is not true in the case of a real experiment. A more accurate verification should also account for the sensitivity of

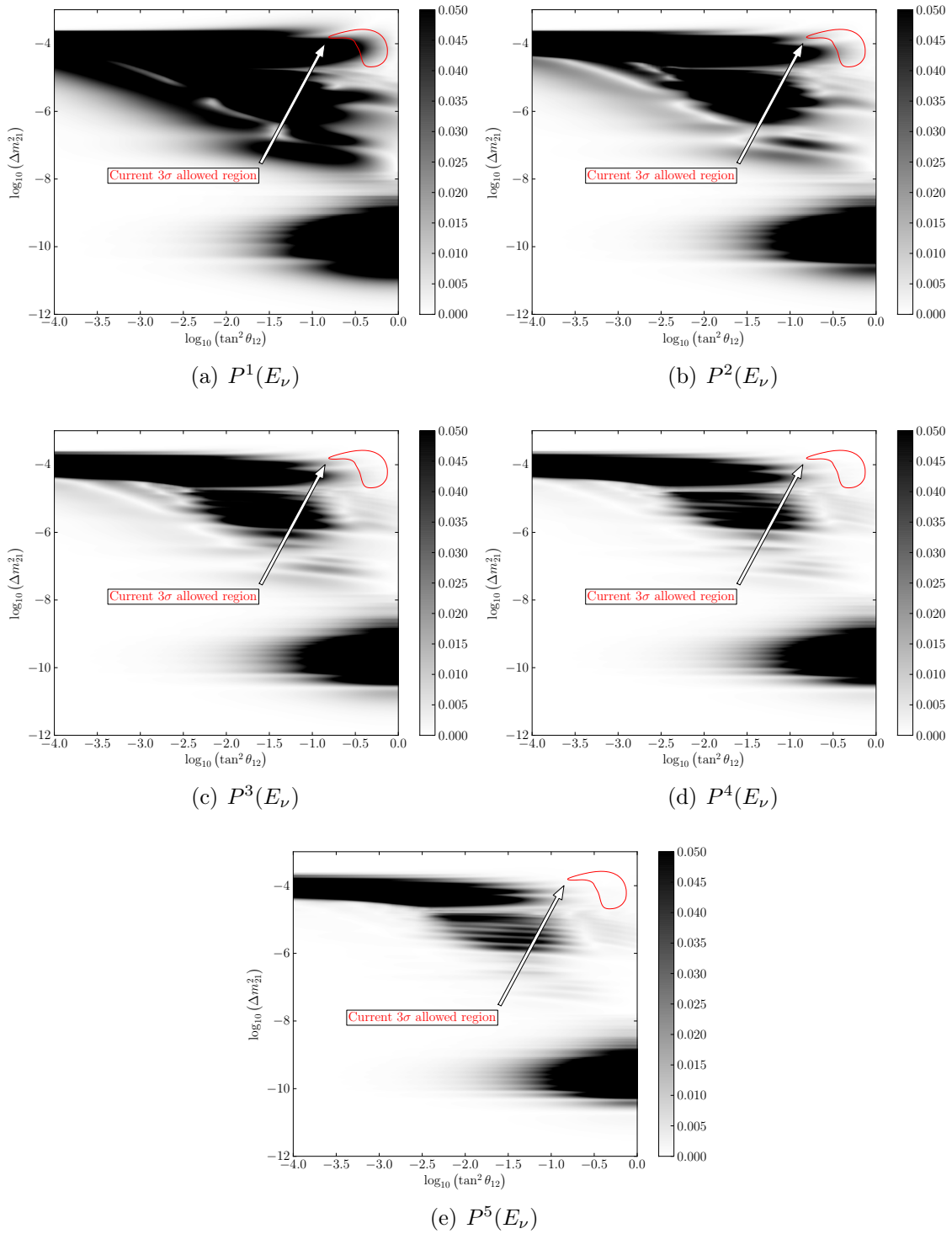


Figure 5.8: Accuracy of the fitted polynomials as a function of the oscillation parameters. The current allowed region for the oscillation parameters obtained from a combined fit of all solar neutrino experiments is also shown. The colours represent the value of the parameter G^m described in Equation 5.6.

the experiment in neutrino energy.

Therefore Equation 5.6 was changed to weigh in the differences according to the sensitivity distribution $w(E_\nu)$ that is shown in Figure 5.6. The new expression to evaluate the accuracy of the fit then became

$$G_{weighted}^n = \frac{1}{N} \sum_{i=0}^N \frac{w(E_\nu) |P^n(E_\nu^i) - P_{ee}^{theo}(E_\nu^i)|}{P_{ee}^{theo}(E_\nu^i)}. \quad (5.8)$$

Repeating the analysis and using the sensitivity distribution, scaled to have the maximum at one (where the sensitivity is higher), the results shown in Figure 5.9 were obtained.

The results show a much better accuracy in the polynomial representations, which now show a discrepancy well below 1%. As the sensitivity decreases steeply from its maximum at 10 MeV, it becomes less relevant if the polynomial function is not so accurate at the edges of the sensitivity range.

Furthermore, taking into account the detector sensitivity it is shown that the second order polynomial agrees with the model survival probability to less than 2% over a wider range of the oscillation parameters. It should be noted that the region of the current limits on the oscillation parameters are at 3σ level, making the regions where the polynomial function does not represent well the model curves strongly disfavoured.

As mentioned before, a similar verification was performed in the SigEx side of the analysis by constructing distorted Monte Carlo data sets distorted by the model survival probabilities and using a polynomial parameterisation to recover the distortion applied. Those tests yielded results consistent with the ones described here [136].

5.6.4 Specific Survival Probability Parameterisation

Following the results discussed in the previous section and the results obtained from the SigEx analysis, it was planned to extract a second order polynomial parameterisation of the day survival probability with an additional first order polynomial to parameterise the asymmetry between day and night.

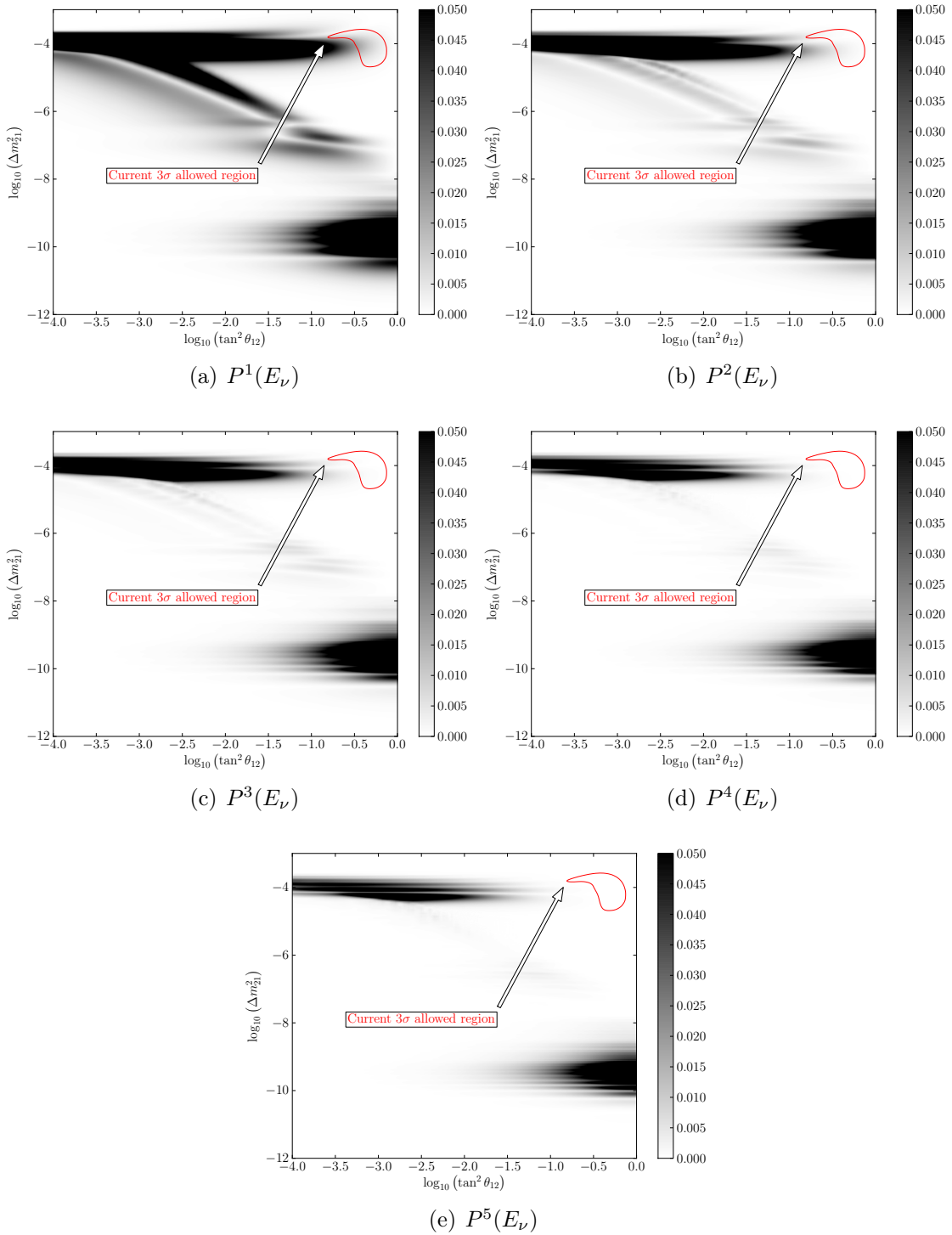


Figure 5.9: Accuracy of the fitted polynomials weighing the residuals by the sensitivity of SNO. The colours represent the value of the parameter G^m described in Equation 5.8.

The polynomial fit employed in the analysis has six free parameters: c_0, c_1, c_2, a_0, a_1 and f_{8B} , which are the output that later is used in the neutrino oscillation analysis (Chapter 6). The c_i terms are the coefficients of the polynomial that describes the survival probability during the *day*, where there are no Earth matter effects:

$$P_{ee}^D \equiv P_{\nu_e \rightarrow \nu_e^D}(E_\nu) = \sum_{i=0}^2 c_i (E_\nu - 10 [MeV])^i. \quad (5.9)$$

The a_i parameters describe the asymmetry between day and night neutrino survival probabilities,

$$A_{ee}(E_\nu) = \frac{2(P_{ee}^N - P_{ee}^D)}{P_{ee}^N + P_{ee}^D}, \quad (5.10)$$

which is defined in the fit as

$$A_{ee}(E_\nu) = a_0 + a_1 (E_\nu - 10 [MeV]). \quad (5.11)$$

Using these definitions, the day CC and electronic component of the ES fluxes during the day are scaled by P_{ee}^D . The night time equivalents are scaled by

$$P_{ee}^N = P_{ee}^D \frac{1 + A_{ee}/2}{1 - A_{ee}/2}. \quad (5.12)$$

The non-electron components of day and night ES flux are scaled, respectively, by $1 - P_{ee}^D$ and $1 - P_{ee}^N$.

Since the fit now aims to look directly into a possible electron neutrino spectral distortion, the fit is no longer independent of the shape of the 8B neutrino spectrum. Although the detector response to neutrons is well known, and the NC reaction is insensitive to neutrino flavour, the term f_{8B} is a direct comparison of the NC flux with respect to the SSM predicted 8B solar neutrino flux.

5.7 Results from the Signal Extraction

The technical details of the SigEx algorithms are extensively documented [70, 128, 130, 131, 136]. For the purposes of this thesis, these details are not particularly relevant as the output parameterisation is well established. In the following sections the structure of the outputs for the specific case of the 3-phase will be given, as well as the additional information necessary to carry on the neutrino oscillation analysis. Furthermore, the final results obtained in the 3-phase analysis will also be presented, as those outputs will be used in Chapter 6 to perform the neutrino oscillation analysis.

5.7.1 Outputs from Signal Extraction of the 3-Phase Analysis

As described earlier, the outputs of the 3-phase analysis will consist in three coefficients of a second order polynomial function, centred at $E_\nu = 10$ MeV, two additional linear function coefficients that describe the asymmetry between day and night (also centred at 10 MeV) and one parameter that describes the scale of the ^8B flux measured by SNO against the prediction of the solar model used in the MC. Each of these outputs will have an associated total statistical uncertainty and a systematic uncertainty.

Besides these outputs, the correlation matrix is also provided, being coefficients of a function in neutrino energy. There are strong correlations between the coefficients themselves. It is easy to understand why it is so. For instance the night survival probability is not added directly to the fit, but is parameterised by the two parameters a_0 and a_1 that describe the difference between the day and night survival probabilities.

Some systematic uncertainties and background levels are also part of the SigEx fit. Although effectively their values are part of the SigEx output, the neutrino oscillation analysis does not depend on them directly. In the final results a single systematic uncertainty is provided for each polynomial parameter, which is obtained by adding up the contribution of each individual *hidden* floating or scanned parameter.

In Table 5.1 there is a complete list of the outputs of the SigEx analysis. The top part of the table lists the parameters that are relevant for the neutrino oscillation analysis, while the second part of the table lists other parameters that were floated

in the fit, along with the model parameters, but are not passed on to the neutrino oscillation analysis, either because they have no physical meaning in terms of neutrino oscillations (like backgrounds), or because their effect is propagated through the systematic uncertainties on the relevant parameters.

5.7.2 Signal Extraction results of the full 3-Phase data set

In the following section the final results obtained from the analysis of the full 3-phase data set are described, with particular emphasis to the results necessary to carry the neutrino oscillation analysis described in Chapter 6. Some informations about each of the phases was already provided in Section 2.2.

Data set results

In Table 5.2 the outputs relevant for the neutrino oscillation analysis are presented. The systematic uncertainty in each parameter corresponds to a total systematic uncertainty adding up the contributions from all fitted, scanned and shifted parameters.

The correlations between the parameters are also necessary in order to perform the physical interpretation of the data and are quoted in Table 5.3.

The results obtained from this analysis can be separated into two parts. The measurement of the total solar neutrino flux, which is extracted in the form of a fraction of the total solar neutrino flux predicted by the solar model used in the generation of the MC (BS05(OP) : $\Phi_{8\text{B}} = 5.69 \times 10^6 \text{ cm}^{-2}\text{s}^{-1}$) and is identified as $f_{8\text{B}}$. Figure 5.10 shows an updated version of Figure 5.3, now including the result obtained from the 3-phase analysis. The uncertainty in the total ^8B neutrino flux was slightly improved with respect to the previous SNO measurement, reducing the uncertainty of 4% obtained in the LETA analysis down to 3.7%. Despite this improvement in the total flux uncertainty, which is now four times smaller than the solar model uncertainty, it is not possible yet to distinguish between different solar models, as shown in Figure 5.10, since the central value of SNO falls precisely in the intersection of the 1σ ranges of both solar models.

Parameter	Type	Description	
a_0	Model parameter	A^{DN} coefficients	
a_1			
c_0			
c_1			
c_2			
f_{8B}		Scale of NC flux versus SSM	
Outputs not used in the neutrino oscillation analysis			
d2o_bi_d2o_day	Internal Backgrounds	^{214}Bi in D_2O	
d2o_bi_d2o_night			
salt_bi_d2o_day			
salt_bi_d2o_night			
d2o_tl_d2o_day		^{208}Tl in D_2O	
d2o_tl_d2o_night			
salt_tl_d2o_day			
salt_tl_d2o_night			
salt_24na_night			^{24}Na in D_2O
salt_24na_day			
d2o_bi_h2o_night	External Backgrounds	^{214}Bi in H_2O	
d2o_bi_h2o_day			
salt_bi_h2o_day			
salt_bi_h2o_night			
d2o_bi_av_bulk_day		^{214}Bi in the AV	
salt_bi_av_bulk_day			
d2o_tl_h2o_day		^{208}Tl in H_2O	
d2o_tl_h2o_night			
salt_tl_h2o_day			
salt_tl_h2o_night			
d2o_tl_av_bulk_day			^{208}Tl in the AV
salt_tl_av_bulk_day			
d2o_av_surface_n_d		Neutron events on AV surface	
salt_av_surface_n_d			
d2o_pmt_day	^{208}Tl and ^{214}Bi in PMTs		
salt_pmt_day			
ncd_pmt_b8nc_n_cap	Scale parameter	NC flux to PMT NC events factor	
ncd_pmt_ex_dn	Systematic Error	External neutrons DN asymmetry	
ncd_pmt_ex	External Background	External neutrons ($\text{H}_2\text{O}, \text{AV}$)	
ncd_pmt_d2opd	Internal Background	Internal neutrons (D_2O)	
ncd_pmt_d2opd_dn	Systematic Uncertainty	Day/night asymmetry (internal neutrons)	
ncd_pmt_atmos	Background	Atmospheric neutron events	
ncd_pmt_ncdpd	Background	NCD bulk neutron events	
ncd_pmt_k2pd	Background	NCD hotspot	
ncd_pmt_k5pd	Background	NCD hotspot	
ncd_ncd_b8nc_n_cap	Scale parameter	NC flux to NCD NC events factor	

Table 5.1: List of all SigEx outputs separated into outputs used in the oscillation analysis and outputs propagated through systematic uncertainties. Detailed explanation of each parameter in [69, 70, 131, 136].

Parameter	Central value	Statistical Uncertainty	Total Systematics
^8B Scale	0.9235	+0.0283 -0.0280	+0.0189 -0.0220
$P_{ee}^D(E_\nu)$ polynomial coefficients			
c_0	0.3174	+0.0163 -0.0156	+0.0093 -0.0093
c_1	0.0039	+0.0065 -0.0067	+0.0045 -0.0045
c_2	-0.0010	+0.0029 -0.0029	+0.0014 -0.0016
$A^{DN}(E_\nu)$ coefficients			
a_0	0.0464	+0.0307 -0.0306	+0.0141 -0.0131
a_1	-0.0163	+0.0253 -0.0253	+0.0096 -0.0106

Table 5.2: Results of $f_{8\text{B}}$, P_{ee} and A_{ee} from the 3-phase data set.

	^8B Scale	c_0	c_1	c_2	a_0	a_1
^8B Scale	1.000	-0.723	0.302	-0.168	0.028	-0.012
c_0	-0.723	1.000	-0.299	-0.366	-0.376	0.129
c_1	0.302	-0.299	1.000	-0.206	0.219	-0.677
c_2	-0.168	-0.366	-0.206	1.000	0.008	-0.035
a_0	0.028	-0.376	0.219	0.008	1.000	-0.297
a_1	-0.012	0.129	-0.677	-0.035	-0.297	1.000

Table 5.3: Correlation matrix of the output parameters quoted in Table 5.2.

Another important result is the functional parameterisation of the electron neutrino survival probability. Figure 5.11 shows the RMS spread in the survival probabilities, $P_{ee}^D(E_\nu)$, $P_{ee}^N(E_\nu)$ and day/night asymmetry $A^{DN}(E_\nu)$ corresponding to the obtained results of Tables 5.2 and 5.3. The bands were computed by generating 1000 samples of correlated random coefficients through Cholesky decomposition [110] and drawing the corresponding RMS spread.

In this context it is relevant to note the value of the parameter c_0 , which corresponds to the scale term of the polynomial. In other words, this parameter represents roughly the ratio $^C/{}^N$. This is further confirmed by the large anticorrelation with $f_{8\text{B}}$ verified in Table 5.3. Similarly, one can interpret the value of $1-c_0/\sigma_{c_0}$ as the significance of the flavour change hypothesis. From the values in Table 5.2 one can verify that the flavour change hypothesis has a significance of over 30 sigma. Looking at the numerical values and respective uncertainties of the remaining polynomial parameters it is possible to infer that the final results are consistent with a flat distribution (*i.e.* no spectral distortion). The same conclusion can be drawn from the asymmetry parameters, whose values are consistent with zero. In this context it is

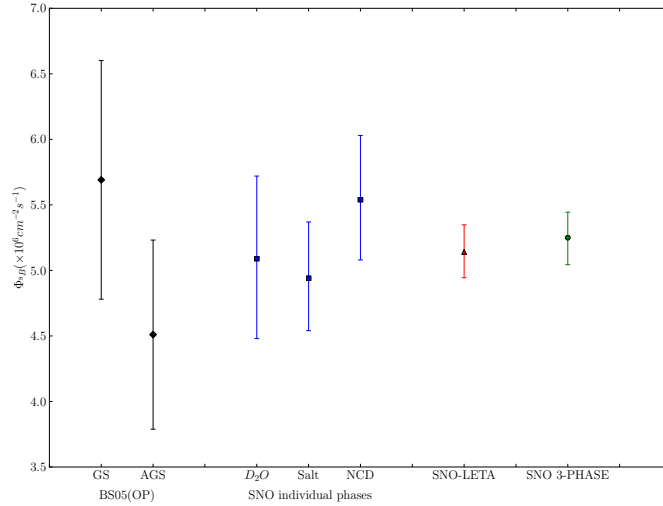
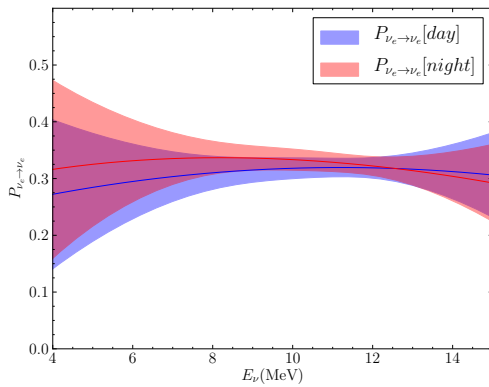
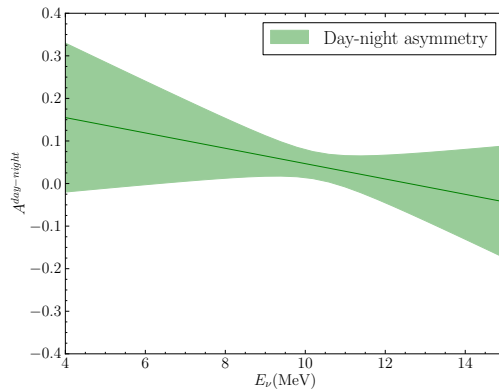


Figure 5.10: Comparison of the total ^8B Solar neutrino flux measured by the different analyses of SNO with the predictions from two solar models using different heavy element abundance models (BS05(OP,GS) and BS05(OP,AGS) [26]). The final results from the combined analysis of the 3 phases of SNO described in this Section is also shown.



(a) Day survival probability ($P_{ee}^D(E_\nu)$)



(b) Day/Night Asymmetry ($A^{DN}(E_\nu)$)

Figure 5.11: Best fit and RMS spread in the day ($P_{ee}(E_\nu)$) for both day and night survival probability functions and day/night asymmetry ($A^{\text{day-night}}(E_\nu)$). The curves were generated using the data from Tables 5.2 and 5.3.

also interesting to notice the large anti-correlation between the slope parameter of the day survival probability (c_1) and the slope parameter of the day-night asymmetry (a_1). This result is consistent with the conclusion of the absence of spectral distortion, where both slope parameters compete with each other in the shape of the

survival probability.

In the next Chapter these results will be used in the context of a phenomenological study of neutrino oscillations, aiming to extract the most precise estimate of the neutrino oscillation parameters.

Chapter 6

Neutrino Oscillation Analysis

The remaining of this thesis covers the interpretation of the properties of solar neutrinos based on the experimental data, in the context of matter induced neutrino oscillations. This work represents the totality of the neutrino oscillation analysis in [127], plus some further analyses which were not included in the final paper. Some of the concepts and verifications described in this chapter were also used in [70].

The presented results are obtained from the combined 3-phase signal extraction results described in Chapter 5. Section 6.1 is a review of the phenomenology of neutrino oscillations. A description of the different inputs necessary to obtain the survival probability of an electron neutrino at a given location in the Earth is described in Section 6.2, along with a demonstration of their respective effects on the survival probability. Section 6.3 gives a description of the analysis methods employed in the determination of the neutrino oscillation parameters. Finally in Section 6.5 the results of a neutrino oscillation analysis with SNO data are shown. An oscillation analysis combining all solar neutrino experimental data up to date is also presented, which allows a further improvement on the oscillation parameters and an attempt to constrain the currently unknown parameter θ_{13} . A global analysis combining the reactor experiment KamLAND [61] and the θ_{13} constrain of several other accelerator and reactor experiments are shown which allows not only to demonstrate the confirmation of the neutrino oscillation phenomenon by combining results from different types of experiments, but also to obtain the best possible constraint in θ_{13} .

The mechanism at the source of neutrino oscillations has been briefly described in Chapter 1 and is explained in the following sections in more detail.

6.1 Phenomenology of Neutrino Oscillations

The heart of the phenomenological study of neutrino oscillations is the calculation of the electron flavour neutrino survival probability (P_{ee}) for a given detector location and a set of oscillation parameter values. In the following sections the phenomenology of neutrino oscillations will be revisited and the theoretical derivation of the survival probability using different approaches will be covered.

6.1.1 Introduction

Neutrino oscillations are a direct result of the quantum interference patterns of the neutrino mass eigenstates. Neutrinos are produced in weak eigenstates which are a quantum mixture of mass eigenstates. If the masses differ, interference patterns arise from the evolution of the neutrino states in time resulting in an oscillatory pattern in its composition in terms of weak eigenstates. This mixing effect is governed by the mixing matrix, U , which can be parameterised in terms of three angles ($\theta_{12}, \theta_{13}, \theta_{23}$), that govern the amplitude of the oscillations, and a complex phase (δ) that allows the possibility of CP violation:

$$\begin{aligned}
U &= \begin{pmatrix} U_{e1} & U_{e2} & U_{e3} \\ U_{\mu1} & U_{\mu2} & U_{\mu3} \\ U_{\tau1} & U_{\tau2} & U_{\tau3} \end{pmatrix} \\
&= R_{23} \times R_{13} \times R_{12} \\
&= \begin{pmatrix} 1 & 0 & 0 \\ 0 & c_{23} & s_{23} \\ 0 & -s_{23} & c_{23} \end{pmatrix} \times \begin{pmatrix} c_{13} & 0 & s_{13}e^{-i\delta} \\ 0 & 1 & 0 \\ -s_{13}e^{i\delta} & 0 & c_{13} \end{pmatrix} \times \begin{pmatrix} c_{12} & s_{12} & 0 \\ -s_{12} & c_{12} & 0 \\ 0 & 0 & 1 \end{pmatrix} \\
&= \begin{pmatrix} c_{12}c_{13} & s_{12}c_{13} & s_{13}e^{-i\delta} \\ -s_{12}c_{23} - c_{12}s_{23}s_{13}e^{i\delta} & c_{12}c_{23} - s_{12}s_{23}s_{13}e^{i\delta} & s_{23}c_{13} \\ s_{12}s_{23} - c_{12}c_{23}s_{13}e^{i\delta} & -c_{12}s_{23} - s_{12}c_{23}s_{13}e^{i\delta} & c_{23}c_{13} \end{pmatrix}. \tag{6.1}
\end{aligned}$$

where $c_{ij} = \cos \theta_{ij}$ and $s_{ij} = \sin \theta_{ij}$ and R_{12} , R_{23} and R_{13} correspond to the three rotation matrices in which the mixing matrix can be parameterised. The only constraint on the mixing matrix is that it has to be unitary.

There are several references in literature covering the formalism of neutrino oscillations [2, 19, 20, 144–146], but most only cover the calculation in a two flavour scenario. The two neutrino state model assumes two flavour ($\nu_e, \nu_{a=\mu,\tau}$) and mass (ν_1, ν_2) eigenstates. In this context the parameter θ_{13} is set to zero, decoupling R_{12} and R_{23} , reducing the mixing matrix in Equation 6.1 to the rotation matrix R_{12} . This common approximation is due to the simpler calculations, but mostly because only recently the precision of the solar neutrino experimental results was enough to study the second order effects of θ_{13} . The calculations in this thesis will all be carried in a three flavour framework, keeping in mind that one can at any point recover a two flavour scenario by eliminating the oscillation angle θ_{13} by fixing its value to zero.

The following sections will review the formalism of the survival probability calculation in vacuum and matter, in order to better understand its implementations explained later on.

6.1.2 Oscillations in Vacuum

Following up from the derivation described in Section 1.2.1 and considering that neutrinos are produced in the Sun replacing the flavour states $\alpha, \beta \equiv e$ we can obtain an explicit form for the vacuum electron neutrino survival probability as:

$$\begin{aligned}
P_{ee} &= \left| U_{ei} U_{ie}^* e^{-i \frac{\Delta m_{i1}^2 L}{2E_\nu}} \right|^2 \\
&= \left| |U_{e1}|^2 + |U_{e2}|^2 e^{-i \frac{\Delta m_{21}^2 L}{2E_\nu}} + |U_{e3}|^2 e^{-i \frac{\Delta m_{31}^2 L}{2E_\nu}} \right|^2 \\
&= (|U_{e1}|^4 + |U_{e2}|^4 + |U_{e3}|^4) + 2|U_{e1}|^2 |U_{e2}|^2 \cos\left(\frac{\Delta m_{21}^2 L}{2E_\nu}\right) \\
&\quad + 2|U_{e1}|^2 |U_{e3}|^2 \cos\left(\frac{\Delta m_{31}^2 L}{2E_\nu}\right) + 2|U_{e2}|^2 |U_{e3}|^2 \cos\left(\frac{\Delta m_{21}^2 + \Delta m_{31}^2}{2E_\nu} L\right). \quad (6.2)
\end{aligned}$$

Replacing the matrix terms U_{ei} by the angle dependent terms the resulting survival probability is:

$$\begin{aligned}
P_{ee} &= 1 - \frac{1}{2} \cos^4 \theta_{13} \sin^2(2\theta_{12}) \left(1 - \cos\left(\frac{\Delta m_{21}^2 L}{2E_\nu}\right) \right) \\
&\quad - \frac{1}{2} \sin^2(2\theta_{13}) \left(1 - \cos\left(\frac{\Delta m_{31}^2 L}{2E_\nu}\right) \right) \\
&\quad - \frac{1}{2} \sin^2 \theta_{12} \sin^2(2\theta_{13}) \left(\cos\left(\frac{\Delta m_{31}^2 L}{2E_\nu}\right) - \cos\left(\frac{\Delta m_{21}^2 + \Delta m_{31}^2}{2E_\nu} L\right) \right). \quad (6.3)
\end{aligned}$$

6.1.3 Oscillations in Matter

In the context of solar neutrinos it is important to consider the matter effects in neutrino oscillations, where the flavour states are affected by effective potentials caused by matter, that alter the evolution equation.

Following the discussion in Section 1.2.2, by considering the effect of charged current interactions, the total Hamiltonian in the flavour basis becomes the sum of

a vacuum part H^0 and a matter part H^1 , both of which are described in different bases:

$$\begin{aligned}
H^f &= UH^0U^\dagger + H^1 \\
&= \frac{1}{2E} \begin{pmatrix} U_{e1} & U_{e2} & U_{e3} \\ U_{\mu1} & U_{\mu2} & U_{\mu3} \\ U_{\tau1} & U_{\tau2} & U_{\tau3} \end{pmatrix} \begin{pmatrix} 0 & 0 & 0 \\ 0 & \Delta m_{21} & 0 \\ 0 & 0 & \Delta m_{31} \end{pmatrix} \begin{pmatrix} U_{e1}^* & U_{\mu1}^* & U_{\tau1}^* \\ U_{e2}^* & U_{\mu2}^* & U_{\tau2}^* \\ U_{e3}^* & U_{\mu3}^* & U_{\tau3}^* \end{pmatrix} \\
&\quad + \frac{1}{2E} \begin{pmatrix} A_{CC} & 0 & 0 \\ 0 & 0 & 0 \\ 0 & 0 & 0 \end{pmatrix},
\end{aligned} \tag{6.4}$$

where $A_{CC} = 2\sqrt{2}E_\nu G_F N_e$ is the matter potential already described in Section 1.2.2. The mixing matrix U is used to perform a transformation to convert the vacuum Hamiltonian into the flavour basis.

There exists now a new basis, $\{|\nu_i^m\rangle\}_{i=1,2,3}$, the matter eigenstate basis, where the Hamiltonian is diagonal. In this new basis the time evolution of the eigenstates is just $e^{-i\frac{E_i}{\hbar}t}$, where E_i are the eigenvalues of the total Hamiltonian including the matter term. By diagonalising this Hamiltonian one can solve for this basis and then find the transformation T that transforms back to the flavour basis:

$$\begin{aligned}
T^\dagger H^f T |\nu_i^m\rangle &= E_i |\nu_i^m\rangle \\
|\nu_f\rangle_{f=e,\mu,\tau} &= T |\nu_i^m\rangle_{i=1,2,3}.
\end{aligned} \tag{6.5}$$

As solar neutrinos are produced close to the core of the Sun, they experience large and varying electron densities, which affect the Hamiltonian at any point of the neutrino propagation making the determination of an analytical solution for the oscillation probabilities extremely difficult without using several assumptions and approximations. Therefore the most general calculation of the electron survival probability

involves a numerical integration of a system of coupled differential equations:

$$i \frac{d}{dx} \psi_\alpha(x) = H^f \psi_\alpha(x), \quad (6.6)$$

where x is the position along the propagation direction and $\psi_\alpha(x)$ is a vector containing the real and imaginary coefficients of the wave function in flavour space. This system is then solved for each point x as the wave function is propagated from the starting point to the end point.

Within the allowed range of the oscillation parameters, it is possible to derive analytically the survival probability in matter through an adiabatic approximation. This calculation is explained in more detail below.

Adiabatic Approximation

The present allowed range on the oscillation parameters constrain the θ_{12} mixing angle to be large, but not maximal; while the solar neutrino dominant mass splitting, Δm_{21}^2 has a value on the order of 10^{-5} eV^2 . In this region of the MSW parameter space, it has been shown [23, 146–148] that the evolution of the neutrino states in the Sun can be described by an adiabatic approximation to a precision of better than 10^{-5} , well below the present solar neutrino experimental sensitivity.

In the adiabatic approximation, it is assumed that the mass eigenstate of the produced neutrinos remains unchanged through its propagation in the Sun, with only its flavour content being changed as it travels through regions of different densities. Therefore, under the adiabatic approximation, the neutrino flavour component at the exit from the Sun only depends on the conditions of the location where it was produced.

Let us then consider the neutrino evolution equation in the flavour basis described by Equation 1.17 :

$$i \frac{d}{dt} |\nu_\alpha\rangle = H^f |\nu_\alpha\rangle. \quad (6.7)$$

If we let T be the transformation from the matter eigenstate basis $|\nu_m\rangle$ to the flavour basis ($|\nu_\alpha\rangle = T|\nu_m\rangle$) we can write the propagation equation as

$$\begin{aligned} i\frac{d}{dt}|\nu_\alpha\rangle &= TH^mT^\dagger|\nu_\alpha\rangle \\ i\frac{d}{dt}T|\nu_m\rangle &= TH^m|\nu_m\rangle \\ iT\frac{d}{dt}|\nu_m\rangle + i\left(\frac{d}{dt}T|\nu_m\rangle\right) &= TH^m|\nu_m\rangle \end{aligned} \quad (6.8)$$

where $H^f = TH^mT^\dagger$ and H^m is the Hamiltonian in the mass eigenstate basis which can be written explicitly as:

$$H^m = \begin{pmatrix} c_{12}^2c_{13}^2V(t) & s_{12}c_{12}c_{13}^2V(t) & c_{12}s_{13}c_{13}V(t) \\ s_{12}c_{12}c_{13}^2V(t) & s_{12}^2c_{13}^2V(t) + 2\delta & s_{12}s_{13}c_{13}V(t) \\ c_{12}s_{13}c_{13}V(t) & s_{12}s_{13}c_{13}V(t) & 2\Delta + s_{13}^2V(t) \end{pmatrix}, \quad (6.9)$$

with $\delta = \frac{\Delta m_{21}^2}{4E}$, $\Delta = \frac{\Delta m_{31}^2}{4E}$ and $V(t) = \sqrt{2}G_F N_e(t)$ is the matter-induced potential of neutrinos that depends on the electron density, as described in Section 1.2.2. Finally, as $TT^\dagger = 1$, one can rewrite Equation 6.8 as :

$$i\frac{d}{dt}|\nu_m\rangle = \left(H^m - iT^\dagger\left(\frac{d}{dt}T\right)\right)|\nu_m\rangle. \quad (6.10)$$

Under the adiabatic approximation we consider that the electron density in the Sun varies smoothly and therefore the oscillation wavelength is much smaller than the length-scale of the variation of matter density in the Sun. Therefore we can drop the term with the derivative over T in Equation 6.10. Under this approximation the determination of the survival probability becomes a question of determining the matter eigenstates by diagonalising the Hamiltonian H^m at the point where the neutrino is produced. As neutrinos are only produced in the electron flavour in the Sun, the determination of the matter eigenvalues and eigenvectors becomes a matter of algebra, since the initial condition is known.

The matter eigenvectors of the resulting diagonalisation are the columns of the unitary matrix T , mentioned previously, which relates the flavour eigenstates and the matter eigenstates and has the form:

$$T = \begin{pmatrix} c_{13}^M c_{12}^M & c_{13}^M s_{12}^M & s_{13}^M \\ -s_{12}^M & c_{12}^M & 0 \\ -s_{13}^M c_{12}^M & -s_{13}^M s_{12}^M & c_{13}^M \end{pmatrix}, \quad (6.11)$$

where $c_{ij}^M \sim \cos \theta_{ij}^M$ and $s_{ij}^M \sim \sin \theta_{ij}^M$ and θ_{ij}^M are the matter oscillation angles which can be easily converted to their vacuum counterparts by using Equations 1.22.

The electron neutrino survival probability is then given by :

$$P_{\nu_e \rightarrow \nu_e} = \sum_{i,j=1}^3 |U_{ei}|^2 |T_{ej}|^2 |\langle \nu_i | \nu_j \rangle|^2, \quad (6.12)$$

where $|\langle \nu_i | \nu_j \rangle|^2$ is the probability that the j th matter eigenstate evolves into the i th vacuum eigenstate. Under the assumption of the adiabatic approximation this means that

$$|\langle \nu_i | \nu_j \rangle|^2 = \delta_{ij}. \quad (6.13)$$

Finally we reach an explicit formulation for the electron neutrino survival probability, under the adiabatic approximation:

$$P_{\nu_e \rightarrow \nu_e} = \cos^2 \theta_{13} \cos^2 \theta_{13}^M (\cos^2 \theta_{12} \cos^2 \theta_{12}^M + \sin^2 \theta_{12} \sin^2 \theta_{12}^M) + \sin^2 \theta_{13} \sin^2 \theta_{13}^M. \quad (6.14)$$

In the following sections the effective inputs necessary to perform the calculation of the survival probability are described, as well as their effective effect in the calculations.

6.2 Calculation of the Survival Probability

The calculations presented in the previous sections explain the behaviour of the neutrino from its source of production until it is detected. These sections explain the dependence of the neutrino survival probability on the oscillation parameters and how they are suitable to use in the interpretation of the experimental data. However, in order to obtain a numerical value for the survival probability of a neutrino detected at a given detector d , additional information is necessary in order to properly characterise the conditions of neutrino production and propagation. In this section these inputs will be explained.

6.2.1 Propagation in the Sun

In order to obtain the survival probability at the surface of the Sun of an electron neutrino produced in its interior, two properties are necessary, which are detailed below.

Solar Electron Density

The electron density as a function of the solar radius, $n_e(r)$, is a necessary element to describe the matter potential A_{CC} responsible for the matter effects on the neutrino propagation. In Figure 6.1 the electron density as a function of the solar radius r/R_\odot is shown for the considered SSMs in logarithmic scale. The total radius of the Sun is measured to be $R_\odot = 6.9551 \times 10^8 m$ [12]. Figure 6.1(b) shows the relative difference between each model and BS05(OP), which in this thesis is considered as the reference model. As it can be observed from the figure, the electron density has approximately a linear variation in logarithmic scale. Considering this smooth variation, the electron density values for which there is no numerical data available were obtained by performing a linear interpolation of the available data.

The differences of the electron density between models are at most 5%, which is virtually irrelevant in the context of solar neutrino analysis. Furthermore, all solar neutrinos are produced close to the core of the Sun, where the difference is even smaller.

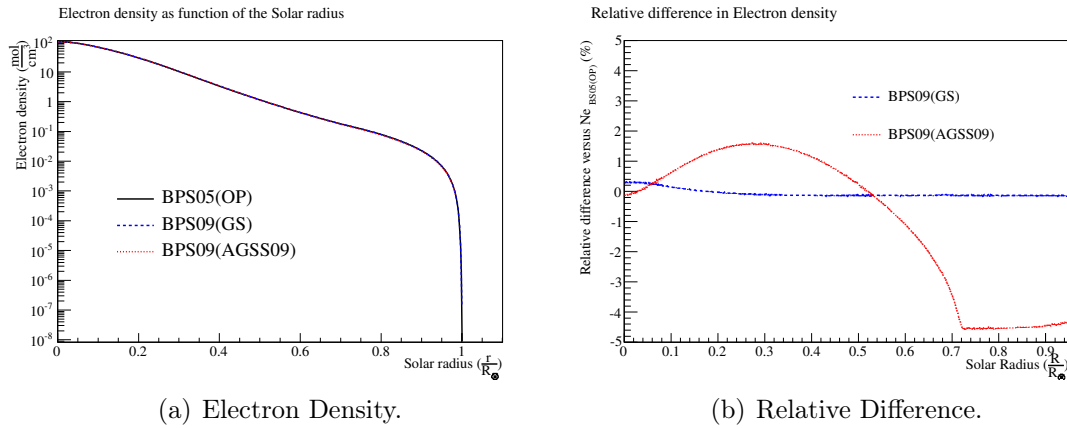


Figure 6.1: (a) Radial profile of the electron density as a function of solar radius for the solar models considered in this thesis. (b) Differences between each model against BS05(OP).

The most significant difference relates to the BPS09(AGSS09) solar model, because it assumes a considerably different solar composition.

Neutrino Production Regions

The distribution of the neutrino reaction source in the Sun is the other key element in the calculation of the survival probability. This is usually parameterised as a radial profile of intensity of neutrino production rate as a function of the Solar radius r/R_{\odot} . In Figure 6.2 the radial profile of neutrino production from each reaction is shown for all the considered solar models. For SNO, the most relevant profiles are the $\nu(^8\text{B})$ and $\nu(\text{hep})$, which are identified with filled regions. The differences in the solar models are minimal with slight variations mostly in the CNO fluxes (^{13}N , ^{15}O , and ^{17}F), especially in the BPS09(AGSS09) solar model, which differentiates most from the other models by considering a lower heavy element density in the Sun [28].

From Figure 6.2 it is visible that all neutrinos are produced close to the core of the Sun ($r < 0.35R_{\odot}$). In fact, this distribution has a strong effect on the survival probability, as neutrinos produced closer to the centre of the Sun will have a longer distance with a high density of electrons to cross. This effect is clearly illustrated in Figure 6.3(a) where the survival probability as a function of the neutrino energy E_{ν} is shown for the neutrino reactions relevant for SNO (^8B and hep) for a fixed set of oscillation parameters inside the presently allowed limits. Incidentally these reactions

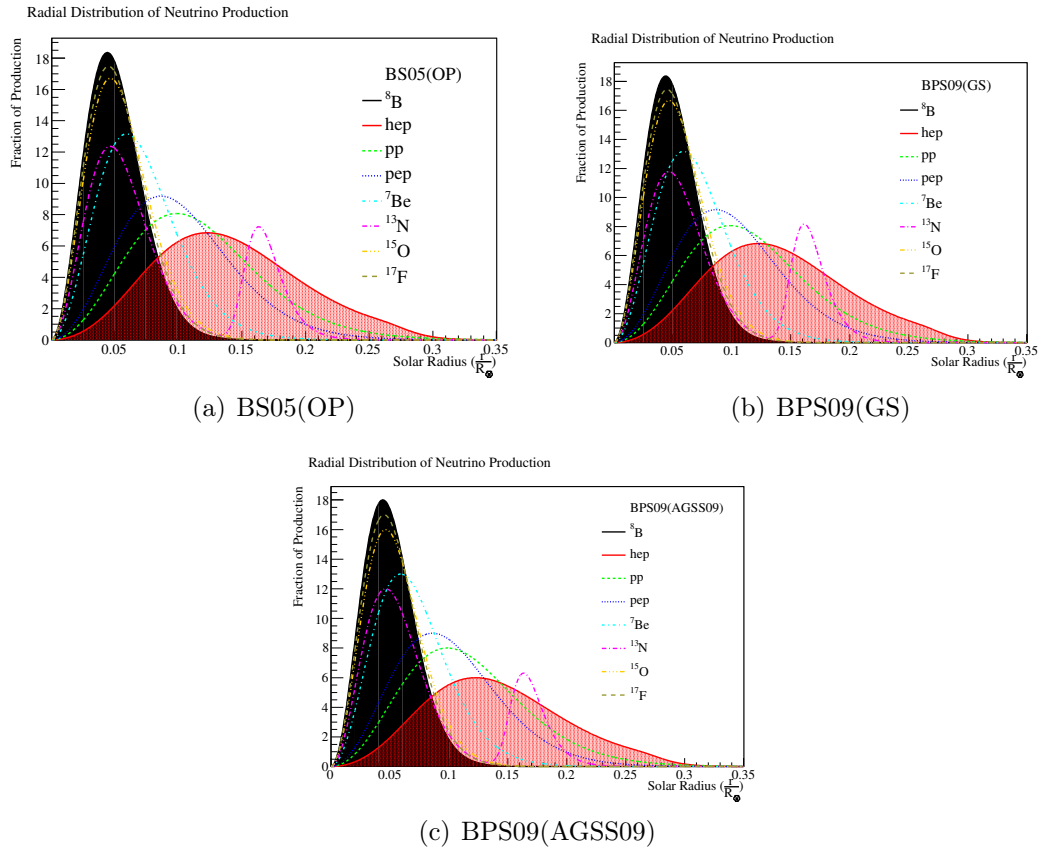


Figure 6.2: Radial profiles of the neutrino production regions for each reaction as function of the solar radius for different solar models.

have a different solar radial distribution, which translates into the differences observed in the survival probability curves.

On the other hand, Figure 6.3(b) shows the survival probability of ^8B neutrinos at the surface of the Sun obtained by using the inputs from different solar models. In this case it is clear that the difference is much smaller. In fact, the black line consists in fact of three lines superimposed where the survival probability was obtained for a common set of oscillation parameters but different solar model inputs. Clearly the curves cannot be differentiated. In blue the relative difference is shown, in percent, of the BPS09 solar models with respect to BS05(OP). The scale of these lines are shown on the right side of the figure.

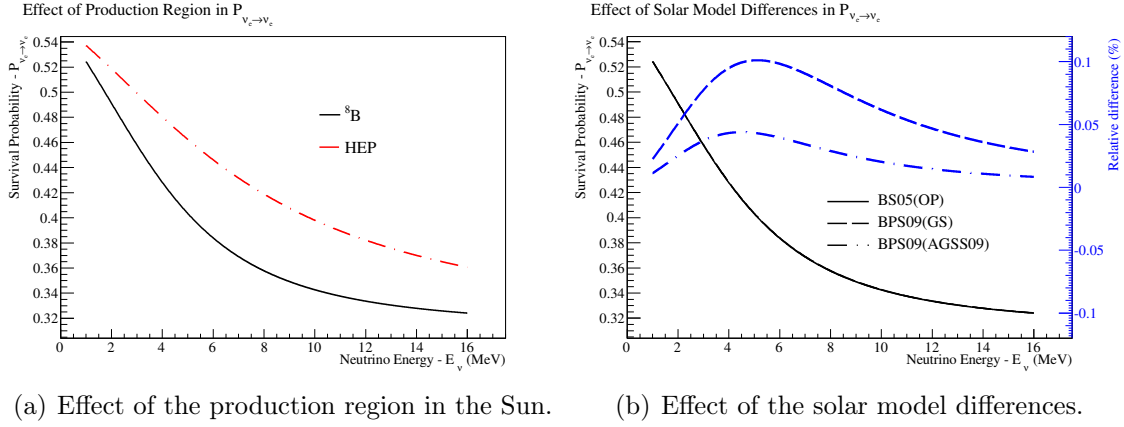


Figure 6.3: Survival probabilities of ${}^8\text{B}$ and hep neutrinos at the surface of the Sun as a function of the neutrino energy for different solar models. The oscillation parameters used were $\tan^2 \theta_{12} = 0.469$, $\Delta m_{21}^2 = 7.9 \times 10^{-5} eV^2$, $\sin^2 \theta_{13} = 0.01$ and $\Delta m_{21}^2 = 2.46 \times 10^{-3} eV^2$, the best fit points from [72]. The blue curves on Figure 6.3(b) give the relative difference in the survival probability between the BPS09 solar models and BS05(OP).

Although these parameters are key components in the determination of the survival probability, their variation is small for different solar models. This is particularly noticeable for the neutrino production regions, which are virtually unchanged from model to model. Therefore, the stability of the solar properties relevant to the calculation of the survival probabilities could allow us to use the same survival probabilities for all standard models. However, for the sake of precision, the survival probabilities in this thesis were calculated independently for each solar model.

6.2.2 Propagation in the Earth

While passing through Earth, neutrinos can again experience enhanced oscillations due to its matter potential.

When studying matter effects in the Earth it is usual to use the angle between the detector-centre of the Earth axis and detector-Sun axis to describe the path traveled by the neutrino through the Earth. There are two commonly used concepts when describing this angle:

Zenith angle (θ_z) Refers to the angle between the detector-Earth core and detector-Sun axes counting from the detector-Sun axis.

Nadir angle (η) Refers to the angle between the detector-Earth core and detector-Sun axes counting from the detector-earth core.

Both definitions provide the same information, but from different reference frames with $\eta = \pi - \theta_z$.

Although the matter effects are expected to be small in the Earth, due to its lower matter density, it is nonetheless relevant to account for this effect. Unlike the Sun, the different layers of the Earth have considerably different densities, and therefore a model for the matter density at each layer is necessary.

In most publications, the matter density in the Earth is taken from the *Preliminary Reference Earth Model (PREM)* [149], which is inferred from seismological considerations. However, there is a particular feature in this model that makes it sub-optimal for a precision analysis. The model performs an average of the Earth's matter density at each point of its radius, imposing a spherical isotropy in the matter density. Thus, the upper three kilometres of the Earth are set to a matter density close to the one in water (1.0 g/cm^3), as it covers most of the planet at these radii. This is not optimal for studying the matter effects in the Earth in the context of neutrino oscillations, as the location of most of the present solar neutrino experiments (especially SNO) is far enough from the ocean, and thus have a considerably larger matter density in their vicinity. Despite the small effect of Earth density, this discrepancy can be potentially misleading considering that, due to the phase transitions in the different layers of the Earth, the matter effects are dominated by the transitions in the vicinity of the detector [137].

Thus, the alternative *Continental Parametric Earth Model (PEM-C)* [150] was selected to be used as an input for the calculation of the survival probability in the Earth. This model was published by the same authors of PREM and describes in detail the density profile of the continental part of the Earth. Figure 6.4(a) show the distribution of matter density of both models as a function of the Earth radius r/R_\oplus , where $R_\oplus = 6371 \text{ km}$ is the mean radius of the Earth.

Both models have the same description in the core and mantle of Earth. However, the description of the upper crust differs quite significantly between the models. This is illustrated in Figure 6.4(b), where a detail of the models in the upper layers of the Earth is shown. As it can be observed from the figure, the PREM model has a much

lower matter density in this region, which is caused by the dominance of water in the upper radii of Earth.

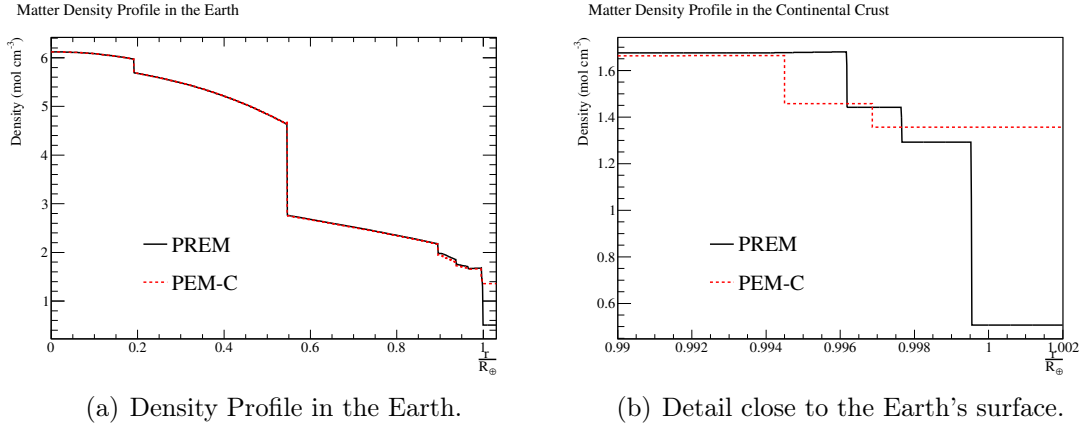


Figure 6.4: Radial profiles of matter density in the Earth.

This situation is particularly relevant in the calculation of the survival probabilities using the adiabatic approximation, where the accuracy of the calculation is strongly dependent on the description of the detector vicinity, where the matter effects are most relevant.

In order to illustrate the importance of an accurate description of the matter density in the detector vicinity, Figure 6.5 shows the survival probability of neutrinos arriving at the detector at the horizon ($\eta = \theta_z = \pi/2$). At this angle, and in the particular case of the SNO detector (although it is equally valid for most solar neutrino experiments), neutrinos go through approximately 200 km of Earth crust, and never at a depth lower than 2 km (which is the depth at which SNO is located). Therefore, by using the PREM model, one is considering a matter density closer to that of water. However, for most solar neutrino experiments at this angle, neutrinos go through continental crust, which is considerably more dense and therefore causes a higher regeneration of the electronic flavour.

By using the PEM-C model, one obtains a higher electron neutrino regeneration at high energies. As it can be observed in Figure 6.5, there is a difference of approximately 3% in the survival probability at this zenith angle. However, this effect is smeared by averaging the survival probabilities calculated for all paths through the

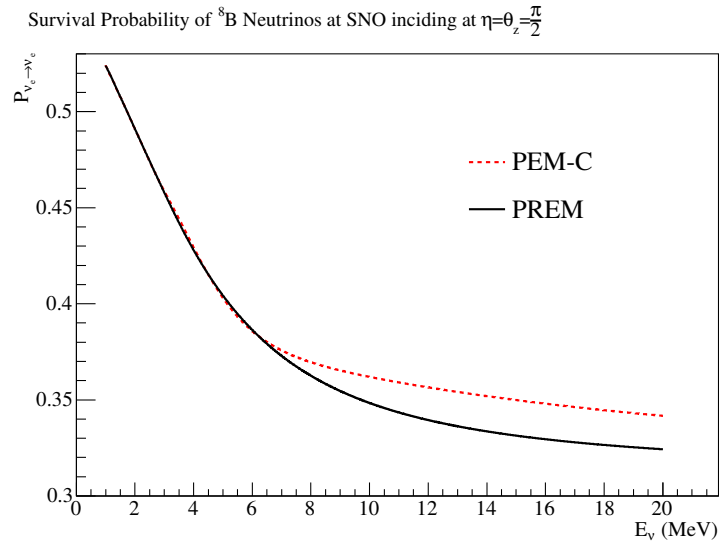


Figure 6.5: Effect of the survival probability calculated at the horizon ($\eta = \theta_z = \frac{\pi}{2}$). The oscillation parameters used were $\tan^2 \theta_{12} = 0.469$, $\Delta m_{21}^2 = 7.9 \times 10^{-5} eV^2$, $\sin^2 \theta_{13} = 0.01$ and $\Delta m_{31}^2 = 2.46 \times 10^{-3} eV^2$.

Earth. Nonetheless, by updating the model we ensure that we are using the most accurate description of the neutrino propagation path.

6.2.3 Integration over zenith-angle exposure

After performing the propagation of the neutrino states both in the Sun and in the Earth, it is necessary to integrate the survival probability over the different calculated paths in order to obtain a final curve of the survival probability, as a function of the neutrino energy, at the detector. This is achieved by performing a weighted average of the different paths, taking into account the live-time distribution $L(\theta_z)$ of the detector.

For each experiment, a series of paths along the Earth were defined as a function of the zenith angle (θ_z), for which the survival probabilities were calculated. Therefore, the survival probability at a detector "det" was obtained by the weighted sum of N_z

survival probabilities calculated for the different angles :

$$P_{ee}(E_\nu)^{det} = \frac{1}{\sum_{z=1}^{N_z} L(\theta_z)} \sum_{z=1}^{N_z} L(\theta_z) P_{ee}^{z,det}(E_\nu), \quad (6.15)$$

where $L(\theta_z)$ is taken from the live-time distributions such as the ones shown in Figure 6.6.

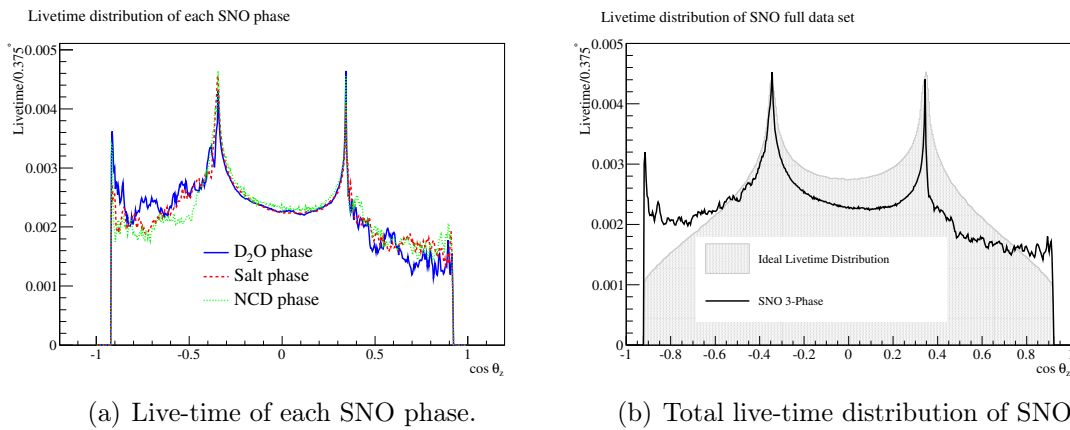


Figure 6.6: Live time distributions of individual SNO phases and the final live-time distribution of the combined three phases. The ideal live-time distribution is also shown in Figure 6.6(b). The shapes of each phase and the total live-time distributions are scaled to the same maximum. $\cos \theta_z < 0$ corresponds to the paths that cross the Earth below the horizon (night) and $\cos \theta_z > 0$ corresponds to trajectories crossing the Earth above the horizon (day).

In the case of SNO, the live-time distributions were taken directly from the data run lists. It allowed to account for patterns in the detector live-time that were not easily seen if a geometrical calculation was performed. Figure 6.6 shows the live-time distributions for the three phases of SNO and the resulting distribution obtained by combining the data from the three phases. The live-time distributions in the figure are scaled to have the same maximum, as the different phases have different total live-times (quoted in Section 2.2). The total live-time distribution of the full SNO data set is shown in Figure 6.6(b), together with the ideal distribution that would be obtained in case SNO was acquiring neutrino data without any interruption. The later was obtained by performing a geometrical calculation considering the detector coordinates in the Earth and the position of the Sun relatively to the detector for a whole year.

The differences between the curves express not only the different time patterns in data taking, but also dead time due to calibrations, commissioning and other activities that required interruption of collection of neutrino data. In fact, it should be noted that most of the neutrino data was taken during the night ($\cos\theta_z < 0$), as most of the maintenance and calibration activities were performed during the day shifts. It is also important to remark the absence of live-time for the very low and very high zenith angles. That is due to the geographic location of the detector, which means that the Sun is never aligned with the detector-Earth core axis.

For all other solar neutrino experiments used in the oscillation analysis discussed in this thesis, a geometrical calculation was performed considering the detector location, as the detailed live-time information is not publicly available. In this case, the Earth was assumed as having spherical symmetry with a mean radius $R_{\oplus} = 6371$ km [151].

In fact, the averaging of the survival probability over different sampled paths through the Earth makes the effect of using an updated Earth model to be less significant than the effect shown in Figure 6.5, which was the situation where the effect was more significant. By looking at the live-time distributions of SNO (Figure 6.6) one can see that, at $\theta_z = \pi/2$, the fraction of live-time is small, meaning that the effect will be significantly suppressed. The sampled paths where the live-time is considerably higher correspond in large majority to the regions where both Earth models agree. After calculating the weighted average over the sampled paths, the effect of the new Earth model in the survival probability in the detector was of about 0.2%, down from the 3% observed at $\theta_z = \pi/2$.

This averaging of a finite sample of paths through the Earth can lead to one problem that is easily overlooked: aliasing effects caused by the number of sampled paths with respect to the value of Δm_{31}^2 ¹. The neutrino mixing angles are responsible for defining the amplitude of the oscillations, while the mass square differences define the frequency of such oscillations. In the case of Δm_{31}^2 , the present best fit value ($\Delta m_{31}^2 = 2.36 \times 10^{-3} eV^2$) yields an associated wavelength of approximately 20 km for a neutrino with energy of the order of 10 MeV .

¹Aliasing effects are unphysical interferences that can appear from sampling a periodic function with a frequency smaller than the function's own frequency.

If one samples a relatively small value of neutrino paths over the Earth, say 60, the difference in length for each path will be $\Delta l = 2R_{\oplus}/N_z \approx 212\text{km}$ which is roughly ten times larger than the Δm_{31}^2 wavelength. Therefore unphysical interferences could arise at specific energies. Figure 6.7 shows this effect by demonstrating the resulting survival probability at the SNO detector by sampling 60, 90, 180 and 480 paths.

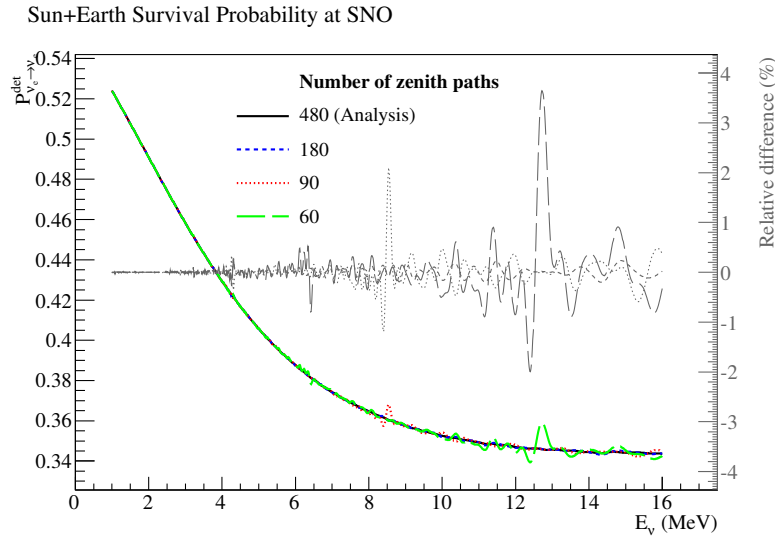


Figure 6.7: Survival probabilities of ${}^8\text{B}$ neutrinos at SNO using different number of sampled paths in the Earth. The grey lines show the relative difference with respect to the number of paths sampled in this thesis and the scale is shown on the right side of the figure. The survival probabilities were weighted with the combined 3-phase analysis live-time distribution. The oscillation parameters used were $\tan^2 \theta_{12} = 0.469$, $\Delta m_{21}^2 = 7.9 \times 10^{-5} \text{eV}^2$, $\sin^2 \theta_{13} = 0.01$ and $\Delta m_{31}^2 = 2.46 \times 10^{-3} \text{eV}^2$.

In this analysis, the live-time distribution was sectioned into $N_{\theta_z} = 480$ equal bins, corresponding to the amount of sampled neutrino propagation paths through the Earth. For each path a Sun+Earth survival probability was obtained as a function of the θ_z angle $P_{ee}^z(\theta_{12}, \Delta m_{21}^2, \theta_{13}, \Delta m_{31}^2, E_{\nu}, \theta_z)$.

Using the live-time distribution, the final Sun+Earth survival probability at a defined detector was obtained by performing the weighted average of the survival probability using Equation 6.15.

It is easy to understand that the effect of matter enhanced oscillation in the Earth will vary from detector to detector due to the different locations (both depth and live-time distribution). However, the matter effects on the Earth do not depend on the neutrino source, unlike the calculation in the Sun which is independent of the

detector location but depends on the source of neutrinos that are detected by the experiment.

In order to better match the experimental outputs, the survival probabilities were averaged using different day/night considerations. In the case of SNO, the outputs are separated into a day and night survival probability, and thus two sets of survival probabilities P_{ee}^D and P_{ee}^N are obtained using the corresponding portion of the live-time distribution. The day survival probability is almost undisturbed as the amount of matter above the detectors is small and thus causes a negligible effect in the survival probability. On the other hand the night survival probability changes quite considerably, especially at higher energies², as it weighs the paths that cross the dense layers of the Earth. Figure 6.8 shows the difference between day and night survival probabilities for ^8B neutrinos in the 3-phase analysis. For reference, the Sun survival probability is also shown. In the same figure, the relative differences calculated with respect to the Sun-only survival probability are also shown in grey. In this case, the scale is shown on the right side of the figure.

At this point all the inputs necessary to obtain a survival probability at a given detector have been presented, as well as their effects on the survival probability at the detector. The following section will describe the method employed to analyse the experimental results in the context of neutrino oscillations.

6.3 Neutrino Oscillation Analysis Method

The neutrino oscillation analysis consists of the estimation of the neutrino oscillation parameters that better describe the experimental data. In this section this process will be described in more detail, explaining how it is possible to interpret the experimental outputs.

As described in Chapter 5, the experimental outputs of SNO previously consisted in a reconstructed energy spectrum of the detected neutrino events, or the equivalent integral of the number of events detected above a given threshold, which is also the output format for the other solar neutrino experiments. In the SNO 3-phase

²For the presently allowed range of oscillation parameters. For smaller values of Δm_{21}^2 the day-night effect is visible at lower energies.

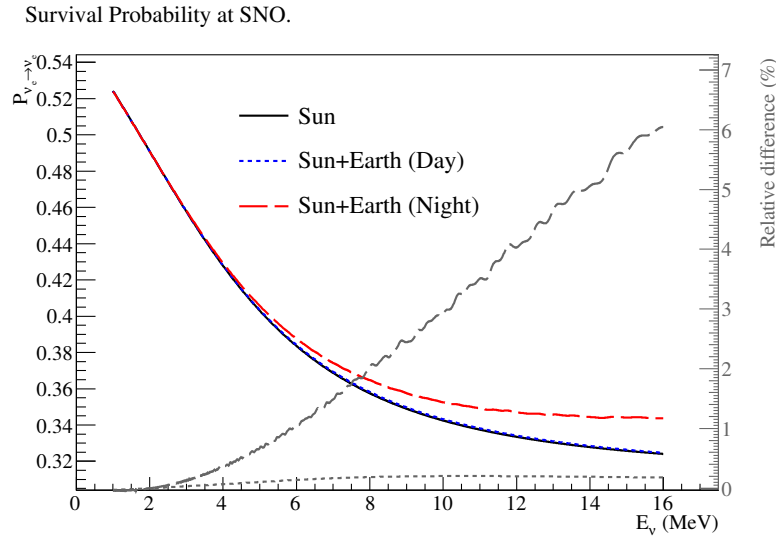


Figure 6.8: Survival probability curves of ${}^8\text{B}$ neutrinos for day and night including the propagation in both earth and Sun. The survival probability at the surface of the Sun is also shown. The relative difference between the calculations including Earth effects and the survival probability on the Sun are also shown in gray with the scale represented on the right side of the figure. The oscillation parameters used were $\tan^2 \theta_{12} = 0.469$, $\Delta m_{21}^2 = 7.9 \times 10^{-5} eV^2$, $\sin^2 \theta_{13} = 0.01$ and $\Delta m_{31}^2 = 2.46 \times 10^{-3} eV^2$.

analysis, the output of the SigEx analysis is a parametrisation of the electron survival probability and corresponding asymmetry between day and night periods. In this section the analysis of both types of outputs will be described, since both are needed for a full analysis of all solar neutrino experiments.

In the following sections, the term *MSW space* is used frequently to describe the range of the oscillation parameters $(\theta_{12}, \theta_{13}, \Delta m_{21}^2)$, which are the parameters aimed to be determined. Two oscillation parameters are implicitly fixed in the analysis: $\theta_{23} = \pi$ and $\Delta m_{31}^2 = 2.46 \times 10^{-3} eV^2$. This is due to the extremely low sensitivity of solar neutrinos to these parameters. Considering the energy range of solar neutrinos (1-20 MeV) and the distribution of the neutrino source (radial profile of neutrino production), the survival probability becomes virtually unaffected by varying θ_{23} and Δm_{31}^2 within their present uncertainties. Furthermore, the phase averaging performed in the Sun calculation further smears the effects of varying these parameters and therefore in this thesis they are fixed to their current best fit points, as even propagating their uncertainties do not show any effect in the neutrino oscillation analysis [143, 152].

6.3.1 Calculation of Expected Event Rates

Besides the combined analyses of SNO data, the output of the signal extraction from the solar neutrino experiments, although varied in the specific format, usually consist of a measurement of detected events (or a fraction compared to the SSM prediction), as explained in Section 1.4. Specifically, the radiochemical solar neutrino experiments (Homestake, SAGE and Gallex) [38, 43], being unable to tag the time or energy of the detected event, presented their experimental result in the form of an integrated number of detected events. Real-time experiments, Čerenkov or scintillation, being able to reconstruct the energy of the events, usually produced their result in the form of a number of detected events as a function of the reconstructed energy (T_{eff}) (SK [50, 51, 53], Borexino [55–57] and previous SNO CC and ES measurements [14, 36, 64, 65, 69, 153]).

However, in general, all these measurements are similar in the way that the output consists in one or more experimental observations (R_n^{exp}) $_{n=1,\dots,N}$ of detected events which do not directly describe the incoming neutrino flux. Thus, the most common implementation of the neutrino oscillation analysis for this type of outputs consists in building a figure of merit that evaluates the match between an estimate of the theoretical oscillated prediction R_n^{theo} against a corresponding experimental observable R_n^{exp} , for a given point in the MSW space.

Solar Neutrino Spectrum and Survival Probability

These quantities directly characterise the solar neutrinos, and thus are expressed as a function of the neutrino energy (E_ν). Each of the eight types of solar neutrinos ($pp, pep, hep, {}^7\text{Be}, {}^8\text{B}, {}^{13}\text{N}, {}^{15}\text{O}, {}^{17}\text{F}$) has its own flux scale Φ_{ν_i} and spectra shapes as a function of neutrino energy $\phi(E_\nu)$. In the case of the pep and ${}^7\text{Be}$ neutrinos the shape corresponds to one and two spectral lines, respectively.

For a detector d and neutrino type ν_i , the solar neutrino spectrum shape at the detector is given by

$$\phi_{\nu_i}^d(E_\nu) = \phi_{\nu_i}(E_\nu) \times P_{ee,\nu_i}(E_\nu), \quad (6.16)$$

where $P_{ee,\nu_i}(E_\nu)$ is the Sun+Earth survival probability at the detector for the selected neutrino type. It should be noted that ϕ_{ν_i} is only the neutrino spectrum shape, whose normalisation Φ_{ν_i} , is the total neutrino flux for the considered neutrino type.

In this thesis, three different solar models are tested, each having their own flux normalisation Φ_{ν_i} . The spectrum shapes, however, are independent of the solar model and therefore are the same for all models. Figure 1.3 (Chapter 1) shows the un-oscillated neutrino spectra for each solar neutrino type.

Interaction Cross Sections

Since the detectors do not directly detect neutrinos, but rather the byproducts of their interactions, the different interaction cross sections are another important input in the determination of the event rates. The neutrino interaction cross section is specific for each detection medium and reaction. In the particular case of SNO, four different cross sections have to be considered: $\sigma_{CC}, \sigma_{NC}, \sigma_{ES_{\mu,\tau}}$ and σ_{ES_e} . Although the ES interaction is sensitive to all flavours, σ_{ES_e} is approximately six times higher than $\sigma_{ES_{\mu,\tau}}$.

In Figure 6.9, these four cross sections are shown as a function of the neutrino energy (integrated over the recoil energies).

The cross section for the CC and NC reactions are taken from the calculation of Butler-Chen-Kong (BCK) [154], which includes radiative corrections. The ES cross sections were originally calculated by Bahcall [155–157], which also includes radiative corrections. These calculations have an associated uncertainty, but they are much smaller than the uncertainties of the solar model neutrino flux and therefore negligible in the calculation of the expected rate.

Detector Response Function

The detector response function $R(T_e, T)$ describes the detector resolution. This function evaluates the probability of an electron with a true kinetic energy T_e to be detected with an energy $T \equiv T_{eff}$. It is roughly Gaussian with additional tails.

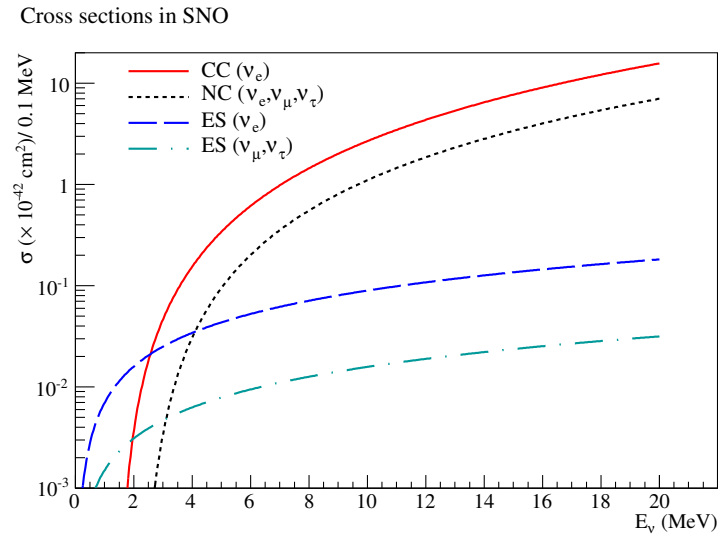


Figure 6.9: Cross sections of the possible neutrino interactions in the SNO experiment.

Therefore this function is specific to each experimental result. For SNO, each data taking phase had a different detector response function [64, 65, 69].

Usually an average of the response function is obtained through Monte Carlo simulations, tuned and validated with calibrations, as both the true and the reconstructed energies are known. In the case of other neutrino experiments the detector response functions are usually provided by the respective collaborations along with their experimental results.

Expected Event Rates in the Detector

Using the inputs described in the previous sections the predicted event rates are calculated by the means of an analytic convolution of the original neutrino spectrum in neutrino energy through the reaction energy thresholds, cross sections and detector responses.

Where there is an ability to discriminate the energy of a detected event, the number of expected events for a given reconstructed energy interval from a neutrino

type ν_i is then given by:

$$R_{T,\nu_i} = N_e \Phi_{\nu_i} \int_0^\infty \phi_{\nu_i}(E_\nu) P_{ee,\nu_i}(E_\nu) \int_0^\infty \frac{d\sigma}{dT_e}(E_\nu, T_e) \int_T^{T+\Delta T} \frac{dR}{dT'}(T_e, T') dT' dT_e dE_\nu, \quad (6.17)$$

where ΔT is the bin width in T_{eff} . When there is no possibility to discriminate the energy of the event, such as the neutron events of SNO (NC), the number of events for a neutrino type ν_i will be simply given by:

$$R_{\nu_i} = N_n \Phi_{\nu_i} \int_0^\infty \phi_{\nu_i}(E_\nu) \sigma(E_\nu) dE_\nu. \quad (6.18)$$

Note that in this case the response function was also dropped as the detected neutrons are thermalised and thus contain no history of their initial energy, nor of the incoming neutrino. In both cases, to obtain the total expected rate at the detector, it is only necessary to sum the rates obtained for each neutrino type.

Using these equations it is then possible to obtain a theoretical predicted event rate for a specific set of oscillation parameters, which can then be compared to the effective experimental measurement. The terms N_e and N_d include other factors such as live-time, neutrino flux normalisation, target volume and neutron capture efficiency, which are needed to effectively determine the number of events.

Figure of Merit

Upon building the model prediction of the observable R , one can build a figure of merit which evaluates the goodness-of-fit between the specific set of oscillation parameters and the experimental data.

The definition of the figure of merit in this section presents a general formalism which is used to analyse the output from other solar neutrino experiments and the combined analysis of all experiments. For the specific case of the output of the 3-phase analysis of SNO the figure of merit is constructed in a slightly different manner, which is described in Section 6.3.2. As the output consists in a functional parameterisation

of the survival probability, the determination of the figure of merit is considerably simpler.

In the following, the fractional rates mentioned previously are indexed with n , carrying statistical uncertainty u_n and total uncertainty σ_n . To each rate is assigned a set of k systematic uncertainties c_{nk} . Correlated systematic uncertainties can take different numerical values depending on the rates they affect.

The predicted values of the rates, R^{theo} , may hide dependences on additional parameters, f_i , which in general are allowed to vary away from their best estimates f_i^0 with constraints σ_{f_i} . For instance, when the parameter f_i describes a given systematic uncertainty, the associated systematic errors c_{nk} may also depend on f_i .

The figure of merit consists of a χ^2 calculation through the *covariance method* which was originally proposed in [158] and is the method widely used in neutrino oscillation analysis. The covariance method consists in building the following χ^2 function from the measured (R_n^{exp}) and predicted ($R_n^{theo}(f_i)$), fractional observables:

$$\chi_{covar}^2 = \sum_{n,m} (R_n^{exp} - R_n^{theo})^2 [\sigma_{total}^{-2}]_{nm} (R_m^{exp} - R_m^{theo})^2 + \sum_i \left(\frac{f_i - f_i^0}{\sigma_{f_i}} \right)^2. \quad (6.19)$$

The χ^2 is minimised with respect to the parameters f_i with penalty terms in the second sum. The inverse total error matrix $[\sigma_{total}^{-2}]_{nm}$ is composed of the statistical and systematic uncertainties, and includes the statistical correlations between the observables and systematic uncertainties:

$$\sigma_{total,nm}^2 = \rho_{nm}^{stat} u_n u_m + \sum_{h,k} \rho_{hk}^{syst} c_{nh}(f_i) c_{mk}(f_i), \quad (6.20)$$

where the correlation coefficients $\rho_{ij} \in [-1; +1]$. The matrix $\sigma_{total,nm}^2$ also depends on the f_i even though it is not shown explicitly. Among the solar neutrino experiments studied in this thesis, SNO is the only experiment where ρ_{ij}^{stat} is used because of the strong correlations inherent to the specific SigEx output. Furthermore, the other solar neutrino experiments usually shape their output so that the correlations between

different bins can be neglected and therefore these are not provided by the original publications.

6.3.2 Analysis of SNO 3-phase Output

As described in Chapter 5, the SNO 3-phase signal extraction procedure provides the results of the ${}^8\text{B}$ neutrino signal measurements in the form of six parameters: $f_{8\text{B}}$, the normalization scale of the ${}^8\text{B}$ solar neutrino flux (with respect to $5.69 \times 10^6 \text{ cm}^{-2}\text{s}^{-1}$, the prediction of the BPS05(OP) solar model), three parameters of a second order polynomial describing the day ν_e survival probability (c_0, c_1, c_2), and two parameters describing a linear day-night asymmetry (a_0, a_1). The correlation matrix between the parameters and the respective uncertainties (both statistical and systematic) are also provided (see Tables 5.2 and 5.3).

As the fit directly produces a description of the electron neutrino survival probability, it is possible to directly compare the model survival probability to the fit outputs. However, the fit results are coefficients of both a second and first order polynomials, while the model prediction is a general, numerically defined function of the oscillation parameters. Therefore, in order to construct a figure of merit for a set of oscillation parameters, it is necessary to convert the model prediction into the same parameterisation as the experimental fit result, *i.e.*, it is necessary to find the second order polynomial function (and the corresponding day-night asymmetry function) that best represents the particular model survival probability to be tested. For a given set of oscillation parameters ($\theta_{12}, \theta_{13}, \Delta m_{21}^2, \Delta m_{31}^2$), it is necessary to find the parameters of the second and first order polynomials that better approximate, respectively, the day survival probability P_{ee}^D and the day-night asymmetry A^{DN} .

This parameter transformation is dependent on detector effects, such as the analysis threshold, energy dependence of the cross sections and analysis cuts, and so the transformation must account for the sensitivity of the detector as a function of the neutrino energy. In order to account for these effects a Monte Carlo simulation was used to count the number of detected events of each neutrino energy that passed all the cuts³. In practice this corresponds to a MC generated “detected neutrino energy

³In fact, this simulation is obtained from the SigEx fit, as the scaled PDFs from the fit can be projected in neutrino energy, since this is a parameter of the SigEx

spectrum“, undistorted by neutrino oscillations.

Using a model predicted survival probability for the considered MSW parameters, the MC generated spectrum mentioned previously is distorted with the polynomial parameterisation allowing the polynomial parameters (c_0, c_1, c_2, a_0, a_1) to vary in the fit. This will effectively return the polynomial parameters that best represent the model, taking under consideration the detector effects.

Figure 6.10 shows the MC generated spectrum produced under the conditions described above in the analysis of the 3-phase data for both day and night. Each phase spectrum was rescaled so that the live-time scaling of each phase can be seen. In particular it is important to note the tail at lower neutrino energy caused by the fact that only the first two phases of SNO were analysed with an analysis threshold in reconstructed energy of $T_{eff} = 3.5$ MeV, while the third phase of SNO was analysed with a more conservative analysis threshold of $T_{eff} = 6$ MeV, as mentioned in Section 5.2.

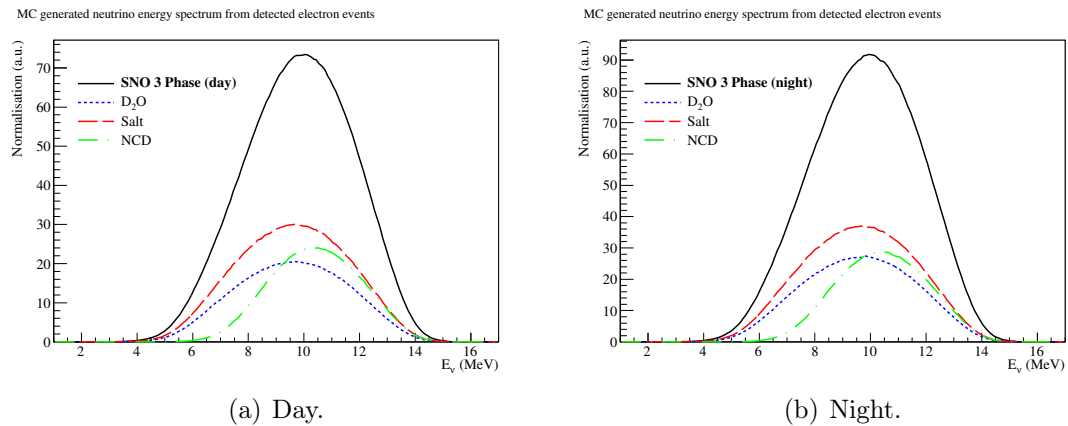


Figure 6.10: MC generated neutrino energy spectra of all electron events (CC and ES) that passed the analysis cuts in the SNO 3-phase data set, which is used to weigh the polynomial fit over the model survival probability.

Furthermore, it is also possible to notice the different detector responses of each phase, by comparing the green line with the blue and red lines. The sensitivity curve of the NCD phase is clearly shifted towards higher energies, which is caused not only by the higher analysis cut but also by a worse energy resolution in the NCD phase induced by the introduction of the proportional counters into the detector.

In practice, by the procedure described above, one obtains the polynomial parameterisation that the SNO experiment would be able to obtain for the considered set of oscillation parameters. Having the *polynomial parameterisation of the model survival probability*, it is now possible to test whether the oscillation parameters under consideration correctly describe the SigEx result. A χ^2 figure of merit is then calculated comparing the model polynomial parameterisation and the SigEx output, using the uncertainties and correlations produced by the SigEx fit:

$$\chi^2(\theta_{12}, \Delta m_{21}^2, \theta_{13}, \Delta m_{31}^2) = \sum_{m,n=0}^4 (p_n^{SigEx} - p_n^{model}) [\sigma_{SigEx}^{-2}]_{nm} (p_m^{SigEx} - p_m^{model}), \quad (6.21)$$

where p_i^{SigEx} are the polynomial parameters obtained from the SigEx fit ($p_{0,1,2} \sim c_{0,1,2}$ and $p_{3,4} \sim a_{0,1}$), p_i^{model} are the polynomial parameters obtained from the model survival probability, as described above, and σ_{nm} is the covariance matrix obtained from the SigEx fit including the correlations and the uncertainties on the parameters.

Repeating this procedure over all points in the MSW space, one can obtain a χ^2 map that describes how well SNO data adjusts to each point in the MSW parameter space.

It should be noted that this procedure completely disregards one of the outputs of SNO: f_{8B} . In fact, to extract the oscillation parameters only from SNO, this parameter is not needed as the survival probability is independent of the total neutrino flux. However, when combining the SNO results with other experiments, this output becomes necessary as it effectively is a measurement of the total neutrino flux and therefore it is correlated with the other experimental results.

The procedure to extract the oscillation parameters and their uncertainties is the same independently from the type of output used and is described in the following section.

6.3.3 Combination of SNO with other solar Experiments

By definition, the figures of merit in the previous subsections perform a comparison of each experimental observation (strictly speaking, each signal extraction output parameter) to the corresponding theoretical model prediction for a point in the MSW parameter space. In this context, the SNO SigEx outputs (polynomial coefficients and $f_{8\text{B}}$) are also considered an experimental observation $R^{expt} \equiv \{c_i, a_i, f_{8\text{B}}\}$, with the solar model prediction R^{theo} corresponding to the model survival probability polynomial coefficients obtained through the method explained in Section 6.3.2 for the polynomial coefficients (c_i, a_i) .

Therefore, for a neutrino oscillation analysis of all solar data there is no need to involve a special treatment for the SNO specific output, as the figure of merit corresponds simply to a comparison between a measured and a theoretically predicted observable. In this context all observables are the same, keeping in mind that the determination of the model predictions must remain consistent with the *form* in which the corresponding output parameter is shaped. A more detailed description of each experimental output will be provided in Section 6.5.3.

In the following subsections a description of some details of the analysis is presented, with particular emphasis to the most relevant improvements in this analysis, and the issues that was necessary to take into account while performing the combined analysis of data from multiple experiments.

Fractional Observables

The neutrino oscillation analysis depends on several inputs, both from the experiments themselves but also from the underlying physical model. As the experiments evolved through time, it is only natural that the different experimental outputs used different assumptions. One of the most common differences is the underlying solar model used in the SigEx analysis of each experiment. In the case of SNO, this is not particularly important, as the measurement of the NC event rate provides an almost direct measurement of ${}^8\text{B}$ flux. However, other neutrino experiments have to rely heavily on an assumed solar model to provide a scale of their event rates.

Together with the experimental observations R^{exp} , the solar neutrino experiments always provide the solar model used in their analysis. Furthermore, all experiments also provide their predicted rates in the case no oscillations were present $R^{pred}|_{P_{ee}=1}$. The superscript *pred* is used in order to distinguish the unoscillated prediction provided by the experiments from the model prediction calculated in the analysis (the superscript *theo* will be used in this case).

Thus, instead of using directly in the neutrino oscillation analysis the experimental outputs R^{exp} , one can use the ratio

$$R_f^{exp} \equiv \frac{R^{exp}}{R^{pred}|_{P_{ee}=1}}. \quad (6.22)$$

This normalises each experimental measurement to their solar model prediction, allowing the oscillation analysis to use any solar model of choice. In order to keep consistency in the calculation of the theoretical prediction R^{theo} to be used in the oscillation analysis, one should now replace R^{theo} with

$$R_f^{theo} \equiv \frac{R^{theo}}{R^{theo}|_{P_{ee}=1}}. \quad (6.23)$$

The major reasons for applying this normalisation to both the experimental and model predicted observables are not only to keep consistency of the analysis for a single solar model but also to eliminate unknown detector effects from the other experiments which are not publicly available, such as live-time distribution, making it difficult to determine exactly the model predicted number of events for each observable.

In the case of the SNO output, the polynomial coefficients are not fractional, as they are already treated differently and do not require any analytical convolution. The f_{8B} parameter, although being obtained independently of a specific solar model is presented as a fraction of the SSM 8B flux prediction that is used in the MC $(\Phi_{8B}^{SNO\text{MAN}})$ and therefore its normalisation is one. To perform a combined neutrino oscillation analysis using a different solar model than the one used by the SNO SigEx analysis, this normalisation has to be rescaled by the ratio of the solar model predicted

flux used in the analysis and the predicted flux used in the Monte Carlo simulation, $\Phi_{8B}^{SSM}/\Phi_{8B}^{SNOMAN}$, where Φ_{8B}^{SSM} is the total ${}^8\text{B}$ neutrino flux for the SSM under study.

Observable Rates

Most experiments are sensitive to more than one neutrino type leading to their experimental measurements of detected events to have multiple contributions from different neutrino types. For instance Gallium experiments (SAGE and Gallex) measurements [43] have contributions from all types of solar neutrinos.

Furthermore, SNO is able to perform a model independent measurement of the ${}^8\text{B}$ solar neutrino flux, which has always been more precise than the solar model [36, 65, 69, 70]. Thus, in a neutrino oscillation analysis, the SNO measurement of the neutral currents is usually used to constrain the ${}^8\text{B}$ solar neutrino flux, allowing the flux to be floated. In this case, the solar model uncertainties associated with the ${}^8\text{B}$ flux should no longer be applied to the prediction of the event rate.

In order to cope with this sensitivity to multiple neutrino sources, the number of expected events R^{theo} is not calculated directly through Equation 6.17 but by the sum of several specific *rates* ${}^A R_i$:

$$R^{theo} = \sum_i w_i {}^A R_i, \quad (6.24)$$

where the term w_i is a weighting factor which allows for different contributions from each individual neutrino reaction rate to the total observable.

For practical purposes, each rate is defined by the experiment, solar neutrino type ν_i , the detection reaction (CC, ES, NC) and the day-night orientation. For a point in the MSW space, the theoretical prediction of the number of events detected is given by the sum of the rates which contribute to that specific measurement. Similarly, systematic uncertainties that only affect a particular rate are only propagated into that rate, correctly affecting R^{theo} . Furthermore, each rate may affect differently a specific R^{theo} . For example, the output of the first analysis of SK [50] provides a reconstructed energy spectrum where some bins enumerate the number of detected events independently of the direction of the incoming neutrino (ES events are strongly

correlated with the direction of the neutrino), while other bins are constrained by a zenith angle range. In this case, the term w_i will be different for the individual rates, reflecting the different live-time fraction for each zenith angle range.

In the specific case of the SNO 3-phase analysis, due to the nature of its output, this feature is not so relevant as the polynomial coefficients do not use the analytical convolution, and the f_{8B} parameter is a direct measurement of the flux in the form of a fraction of the solar model prediction used in the Monte Carlo (BS05(OP)).

Improved precision on the survival probability calculation

In the past analyses of SNO, the survival probability calculation was performed through the numerical integration of the system of coupled differential Equations 6.6. This calculation is extremely CPU-intensive (in the order of several months of CPU time) and thus a prior calculation of the survival probability curves for each experiment was carried out and stored on tables for later access. The technical details of this procedure are described in [108]. In particular it is important to mention that in those tables the parameter Δm_{31}^2 was fixed to $2.3 \times 10^{-3} \text{ eV}^2$ [159]⁴ and the tables were built by sampling the remaining oscillation parameters in a logarithmic scale covering the range specified in Table 6.1.

Parameter	Limits	Number of Bins	Step Size
$\log_{10} \tan^2 \theta_{12}$	[-4 ; 1]	101	0.05
$\log_{10} \Delta m_{21}^2$	[-13 ; -2]	221	0.05
$\log_{10} \sin^2 \theta_{13}$	[-5 ; -0.6]	45	0.1

Table 6.1: Limits and dimensions of the survival probability calculated through numerical integration and stored into tables for later use. The step size is in logarithmic scale.

These tables were produced prior to the previous SNO analysis (LETA) and therefore the decision of its limits and achievable precision was based in the knowledge of the oscillation parameters at that time. This decision was further constrained by the large computing demands to perform the numerical integration in the Sun and therefore the range and precision of the tables was aimed more towards the

⁴ θ_{23} was previously fixed at $\pi/2$ and the CP violating phase was set to zero, assuming CPT invariance

practicalities than towards a precision measurement. With the results of the SNO LETA analysis [70] it was found that the pre-calculated tables limited the precision with which the oscillation parameters could be extracted, especially the mixing angle θ_{12} . However, due to time constraints in the schedule of the experiment, it was no longer feasible to recalculate these tables.

Thus for the 3-phase analysis an implementation of the analytical calculation described in 6.1.3 was carried out, taking care to avoid numerical limitations to the precision [160]. This implementation, which will be referred from now on as the *analytical calculation*, or PSelmaa⁵, was strongly optimised to be able to determine the model survival probability directly while running the neutrino oscillation analysis, and thus the only precision constraint comes from the precision of the approximation itself, which was shown to be better than the uncertainties imposed by the assumptions used in the construction of the tables used in the previous analyses [131]. Extensive tests were carried out, revealing that the analytical calculation is able to reproduce the results of the numerical integration to better than 0.1% [131], which is very good considering the experimental uncertainties of a few percent and the finite detector response.

This approximation however brings some limitations. In particular it is not possible to use it in the calculation of the survival probability for a range of oscillation parameters as large as the one calculated in the tables. In particular, the adiabatic approximation cannot be applied in a region where the parameters $\Delta m_{21}^2 < 10^{-8} eV^2$ [21]. However, this region has already been disfavoured by previous analyses both of SNO data and of other solar neutrino experiments [67, 69, 70, 72, 73].

In the present range of interest (the region of the MSW parameter space allowed by SNO alone), this calculation can be safely applied. This is demonstrated in Figure 6.11 where a coarse sample of survival probability curves covering a region larger than the region of interest for this analysis is compared with the results obtained by the particular implementation using the adiabatic approximation described in Section 6.1.3.

Considering the finite amount of survival probability points in neutrino energy

⁵This naming follows an internal convention of programming implemented on SNO and stands for Physics interpretation Sun-Earth Large Mixing Angle Adiabatic Approximation.

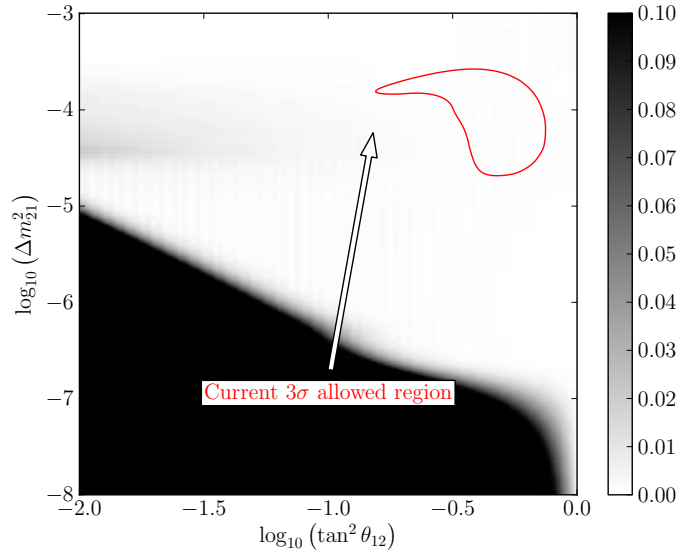


Figure 6.11: Comparison between the survival probability curves obtained by the adiabatic approximation and the numerical integration. The colour gradient represents the compatibility between the survival probability curves following the method described in Section 5.6.3.

that were calculated through the numerical integration and are stored in the lookup-tables, the comparison was performed following the same method as described in Section 5.6.3 where the difference in the curves is normalised by the area of the numerical integration curve. Therefore, Figure 6.11 represents the relative difference between the curves over the whole range of neutrino energies from 1.0 MeV to 16 MeV.

The figure shows a very good agreement of less than 1% in the LMA region. In fact, the range of oscillation parameters shown in the figure is already considerably larger than the current limits, which are also shown in the figure.

The analytical calculation is able to obtain the model survival probability for any set of oscillation parameters $(\theta_{12}, \theta_{13}, \Delta m_{21}^2, \Delta m_{31}^2)$ and neutrino energy E_ν , with no lower limit in the precision of the parameters, which largely compensates the intrinsic limitation imposed by the adiabatic approximation. An additional, independent, test of the analytical calculation was performed to validate the analytical calculation. The calculation was *downgraded* to include all limitations of the pre-calculated tables used in the previous analysis SNO LETA analysis which were generated through numerical integration and therefore are not affected by any limitation of the adiabatic

approximation. The data from LETA was then re-analysed with the downgraded analytical calculation algorithm. The results obtained showed no visible difference to the results published in [70], therefore demonstrating that any changes from using the new calculation are a result of the improvements rather than a limitation imposed by the adiabatic approximation or the algorithm itself.

Propagation of the systematic uncertainties

While performing the neutrino oscillation analysis, several sources of systematic uncertainties have to be considered since they can affect the experimental observables in different ways. In most cases the systematic uncertainties are specific to each experiment and therefore its treatment is usually carried out following the recipes provided by the respective experiments. However, some special cases exist and they have to be treated differently:

- The solar model uncertainties, which are common to all experiments and in some cases represent the major source of systematic error. These uncertainties affect the different neutrino sources, and therefore its effect varies from experiment to experiment. However, by using the concept of observable rates described above, the propagation of their effect is passed directly to the affected rate leading to a proper propagation of correlated uncertainty. More details about these uncertainties will be given below (Section 6.3.4).
- The ^8B neutrino spectrum shape affects almost all experiments (with the exception of Borexino) and its effect is strongly tied to the total ^8B neutrino flux. As it is explained further on, due to the NC measurement of SNO, this flux is allowed to vary in the fit, and therefore the contribution of this uncertainty has to be accordingly re-propagated to the predicted observables.
- For the remaining of the systematic uncertainties, the large majority are specific to each experiment and are propagated by the method previously described as *shift and refit*.
- The energy scale and resolution systematics for the experiments whose outputs are provided in the shape of an energy spectrum affect directly the detector

energy response and therefore it's propagation is performed dynamically when calculating the model predicted observables.

6.3.4 Solar Models and Propagation of their Uncertainties

In the analysis of solar neutrino oscillations, the solar model is one of the major components of the analysis. The solar model is a physical model which describes the Sun properties and therefore it is used not only to model the energy generation but also the particle propagation from its interior. These models are necessary not only to calculate the survival probability at the detector, but also the expected event rates for the different experiments.

These models are usually developed and later validated by comparing the model predictions for specific observables such as helium abundances at the surface of the Sun and the depth of the convective zone, with observations, such as helioseismological measurements. These models not only provide a series of parameters necessary to calculate the survival probabilities, such as the electron density and the radial distribution of the neutrino production reactions, but are also defined by a large amount of parameters which affect the model predictions, such as the heavy elements abundances, luminosity and radius. The solar models are usually quite complex and depending on numerous parameters, of which several cannot be directly measured. Nowadays, the solar models are defined as a function of 20 major parameters, which have different correlations with the neutrino production reactions and therefore their uncertainties are included in the oscillation analysis. These uncertainties are used in the form of partial derivatives which consist in a set of model systematic uncertainties affecting the predicted flux separately for each neutrino type. They correspond to uncertainties on the model input parameters propagated to the neutrino fluxes as a function of the neutrino energy.

Due to the limited amount of data available to develop the solar models, different models have emerged, which can be separated into two major groups based on the predicted metallicity (relative abundance of elements heavier than Helium): the high and low metallicity models. Although most of the solar model parameters relevant for the calculation of the neutrino survival probability are very similar for all solar

models, the predicted neutrino fluxes at the Earth can vary considerably from model to model.

In the context of this thesis three models have been tested: the *conservative* BS05(OP) [25] and the two more recent BPS09(GS) [26, 27] and BPS09(AGSS09) [26, 28]. The BS05(OP) model is considered conservative as the uncertainties on the 21 solar model input parameters are defined by taking the difference between the central values of the high and low metallicity models. The parameterisation of the more recent solar models are considered optimistic because the uncertainty in solar model parameters are defined by using considerably smaller uncertainties associated to the specific abundance model used. While the usage of any of these solar models in the neutrino oscillation analysis is valid, it is considered more appropriate to use the conservative approach due to the limited amount of experimental data used to develop these models. Therefore, it is widely considered that the *optimistic* uncertainties are in general underestimated and could potentially overconstrain the extracted neutrino oscillation parameters.

In this thesis the results are primarily shown for the BS05(OP) solar model, with a specific section (Section 6.5.4) dedicated to compare the results obtained by using the more optimistic models. It should be noted though that, besides the yet unmeasured fluxes from the CNO cycle, the major difference between the models is in fact in the ^8B flux thus the constraint by SNO removes one of the major differences between the models.

The different uncertainties of the solar model are propagated in the analysis as systematic uncertainties directly affecting the rates composing the theoretical predictions. However, as the total ^8B flux is directly measured by SNO's NC measurement ($f_{^8\text{B}}$), the solar model uncertainties are not applied to the rates involving the ^8B neutrinos. In this case, the only *model* uncertainty applied is the $\phi_{^8\text{B}}$ spectrum shape uncertainty, which was taken from [161]. Furthermore, in the case of the solar neutrino analysis, the absolute scale of the ^8B neutrino flux was treated as a free parameter in the fit. By using the SNO measurement as a constraint, it is possible to perform a simultaneous fit of the neutrino oscillation parameters and the flux normalisation reflecting the different contributions from all experimental data. This procedure has already been employed in the past and is explained in great detail in [158]. It is commonly referred as a free-flux fit, where the only assumption about the

^8B neutrino flux is the shape of its spectrum.

The solar model inputs were all taken from the original publications where the model was published. The sole exception is the ^8B neutrino spectrum shape $\phi_{8\text{B}}(E_\nu)$, for which an independent, and more accurate, measurement is used [161].

The solar model parameters and the corresponding partial derivatives are listed in Tables C.2, C.3 and C.4 of Appendix C.2. A more detailed description of these parameters and their effect on the neutrino fluxes is provided in [25]. The terms S_{11} , S_{33} , S_{34} , S_{114} , S_{17} and S_{hep} correspond, respectively, to pp , ^3He - ^3He , ^3He (^4He , γ) ^7Be , ^{14}N (p , γ) ^{15}O , ^7Be (p , γ) ^8B and hep low energy cross section uncertainties that directly affect these nuclear reactions. The terms L_\odot , Age , $Op.$ and $Diff.$ correspond to the uncertainty on the Sun luminosity, age, opacity and the uncertainty on the diffusion model. The term $Be7e$ defines the uncertainty on the theoretical rate of the electron capture reaction ^7Be (e^- , ν) ^7Li . Finally, the remaining input parameters of the solar model describe the uncertainty on heavy element composition for the more abundant elements.

The parameter partial derivatives α_{ki} are propagated by applying them directly to the individual fractional rates F_n^i and therefore build the SSM part of the error matrix:

$$F_n^{th} = \sum_{i=1}^8 F_n^i \quad (6.25)$$

$$\sigma_{SSM}^2 = \sum_{i=1}^8 F_n^i \sum_{j=1}^8 F_n^j \sum_{k=1}^{20} (\Delta p)^2 \alpha_{ki} \alpha_{kj}, \quad (6.26)$$

where Δp is the 1σ value of the k^{th} systematic uncertainty.

6.4 Validation of the Method

While the procedure described above is common for this type of analysis [158], the extraction of the oscillation parameters from an output defined as a polynomial

parametrisation of the survival probability is a novelty and therefore the method had to be further tested.

A series of ensemble tests were carried out to assess the capability of recovering the true oscillation parameters from a SigEx output. Using Monte Carlo simulations, the different types of events in SNO were simulated, producing a simulated version of the 3-phase data sample. This pool of data was then statistically separated into 250 fake sets, each one containing a portion of each event type following a Poisson distribution of the expected number of events of that type.

Using a randomly chosen set of oscillation parameters a survival probability curve was calculated and a distortion was applied to spectra of neutrino events in the simulated data, producing 250 fake sets mimicking the 3-phase data with a known solar neutrino oscillation effect. The aim of this procedure was to be able to test each stage of the analysis chain (both the SigEx and neutrino oscillation analyses), as the output of each step should be compatible with the conditions in which the data was generated.

The SigEx fit was run over each of the produced data sets, returning a total of 250 outputs. Each of these outputs was then used to run a SNO-only neutrino oscillation analysis, trying to recover the original set of oscillation parameters that were used to produce the simulated data sets. Considering the 250 outputs obtained by performing the neutrino oscillation analysis on each fake data set, one can calculate the biases and pulls of each extraction, for each oscillation parameter θ

$$Bias = \frac{N(\theta) - E(\theta)}{E(\theta)} \quad (6.27)$$

$$Pull = \frac{N(\theta) - E(\theta)}{\sigma(\theta)}, \quad (6.28)$$

where $N(\theta)$ and $E(\theta)$ are, respectively, the extracted oscillation parameter obtained from each data set and the true value for that same parameter used to generate the distorted set. The term $\sigma(\theta)$ is the fitted statistical uncertainty on the parameter θ .

The accuracy of the analysis could then be evaluated based on the mean biases

and pulls of all fake data sets. In this context the bias is the fractional difference between the fitted and expected values, while the pull is the significance of the shift in terms of the fit uncertainty. After a large number of ensembles are fitted, the distribution of the biases should be centred around zero and the distribution of the pulls should be normal $N(0, 1)$, if the extraction method is unbiased. Therefore the biases test the accuracy in recovering the central values and the pulls check both the fitted mean and uncertainty.

Figure 6.12 shows the distributions of the fitted best fit points for the 250 fake data sets. In Figures 6.12(a) and 6.12(b) the original oscillation parameter used to produce the sets is shown with the label "Truth value". It should be mentioned that the analysis was performed only in the context of two effective neutrino flavours ($\theta_{13} = 0$). The reason lies in the fact that SNO alone is only weakly sensitive to this parameter.

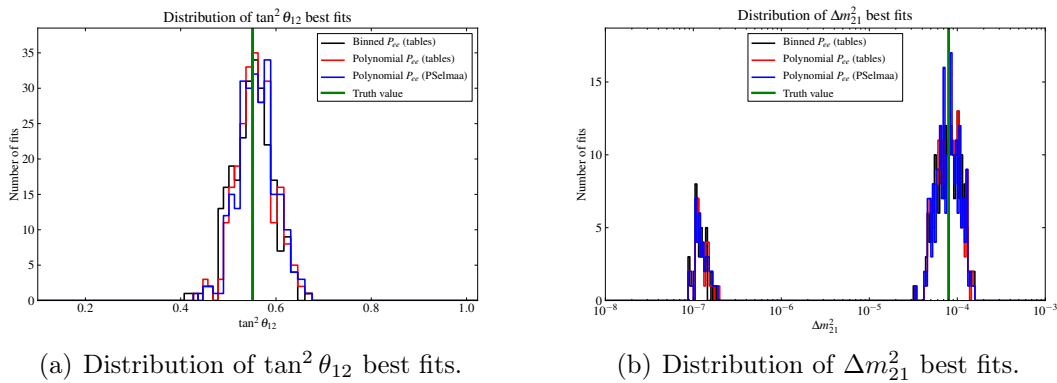


Figure 6.12: Distribution of the best fit points for fitted 250 fake data sets. The original oscillation parameter is also shown.

As it can be observed in Figure 6.12(b), a part of the fake data sets yielded a Δm^2_{21} best fit in the so called LOW region, which has a typical value of $\Delta m^2_{21} \sim 1 \times 10^{-7}$ eV², approximately three orders of magnitude lower than the true value. This is due to the lower sensitivity of SNO to this parameter. By looking at Figure 5.6, SNO has difficulty in distinguishing between the LMA and the LOW regions and therefore approximately 20% of the fits yield a LOW best fit point, as expected. Therefore, in the validation tests, we will always use the best fit point in the LMA region, independently of the *true* best fit point being located in the LOW region. Additional tests demonstrated that this procedure does not affect the best fit point

in $\tan^2 \theta_{12}$, which is the parameter to which SNO is most sensitive. Furthermore, the LOW region is already excluded with high confidence by the KamLAND reactor experiment and also by combined analyses of all solar neutrino data.

Figure 6.13 shows the mean bias and pulls, obtained after extracting the neutrino oscillation parameters from each of the 250 SigEx outputs. The figures show the results for three different methods characterised by the parameterisation of the SigEx output (binned or polynomial) and the survival probability calculation used (PSelmaa or tables). As mentioned in Section 5.6.3 different parameterisations of the SigEx output were initially considered. Results using a binned parameterisation of the survival probability are represented in the figure with black markers. Similarly, the polynomial parameterisation of the survival probability result with pre-calculated survival probability tables (used in the previous analysis) were also tested (red markers) along with the new survival probability calculation implemented (PSelmaa) whose results are shown with blue markers.

Figure 6.13(a) shows that the mean bias on the extraction of $\tan^2 \theta_{12}$ is consistent with zero for the polynomial parameterisation. From this figure it is also clear why the binned survival probability parameterisation was abandoned. From these tests it was observed that this parameterisation was intrinsically biased mostly due to the very limited amount of bins necessary for the fit to converge, which resulted in a distortion of the survival probability shape, which later could not be properly recovered when performing the neutrino oscillation analysis. On the other hand, by comparing the results obtained with the pre-calculated survival probability tables and the new analytical calculation, a very good agreement was found, demonstrating that the adiabatic approximation did not impose any bias in the extracted parameters. The results of a series of bias tests using the same polynomial SigEx parameterisation, but using the survival probability tables used in the previous analyses was also performed, yielding unbiased results. Considering the results shown here, the survival probability calculation (PSelmaa) and analysis method employed in this thesis was shown to be the less biased of the different analysis models under consideration.

The bias in the extraction of Δm_{21}^2 is still consistent with zero, but slightly shifted towards a higher value of the parameter. The errors shown in the figure correspond to the error on the mean.

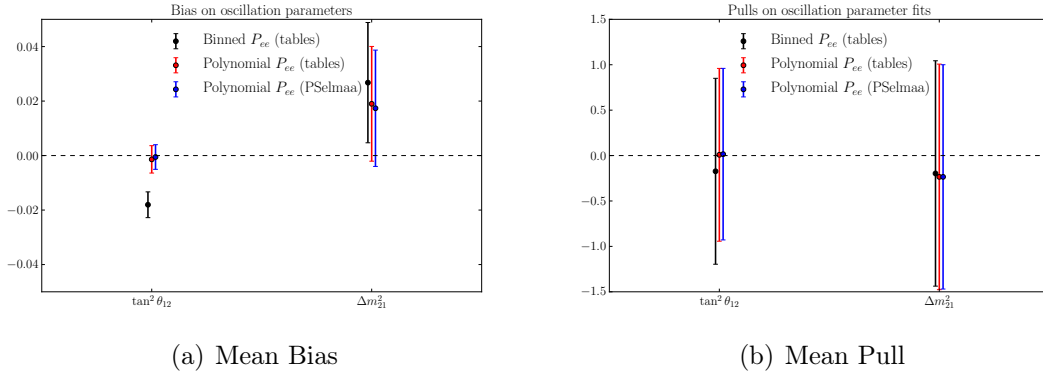


Figure 6.13: Mean bias and pull of neutrino oscillation analysis performed from the results of the signal extraction of 250 ensemble data sets.

This result is not entirely surprising, as the SNO experiment is sensitive only to *High Energy (HE)* solar neutrinos and thus has a very weak sensitivity to the parameter Δm_{21}^2 . In fact, the solar neutrino experiments in general have a lower sensitivity to Δm_{21}^2 than to the mixing angle, as this parameter reflects the oscillatory pattern of the neutrino flavour transitions and thus is very sensitive to the distance travelled by the neutrino. As all solar neutrinos are produced in about $1/3$ of the Solar radius, the precision to Δm_{21}^2 is considerably degraded by the phase averaging at the surface of the Sun. By looking at the sensitivity of SNO in terms of neutrino energy in Figure 5.6 it is easy to understand that the sensitivity does not allow to obtain a definite handle on the exact shape of the survival probability, which resulted in the slight shift on the bias of Δm_{21}^2 shown in Figure 6.13.

Figure 6.13(b) shows that the mean pulls have width of 1σ , meaning that the uncertainties have been properly propagated from the observables to the outputs. The error bars shown in the figure are the RMS of the pulls.

Considering these results, and keeping in mind the lower sensitivity of the solar neutrino experiments to the Δm_{21}^2 , it was demonstrated that the implemented method of extraction is well suited to perform the neutrino oscillation analysis. Concerning the lack of sensitivity of SNO in the extraction of the Δm_{21}^2 , it should also be kept in mind, that this parameter is extracted with very good accuracy by the reactor neutrino experiment KamLAND [59].

6.5 Oscillation Analysis Results

This Section presents the confidence intervals of the neutrino oscillation parameters based on the results of the SNO 3-phase combined analysis. Further studies considering other experimental results (such as other solar neutrino experiments and KamLAND) will also be performed demonstrating how the combination of the different experimental measurements can further constrain the limits on the oscillation parameters.

6.5.1 Estimation of the oscillation parameters

The technique employed to obtain the parameter best-estimate and corresponding uncertainties was a grid-scan on the MSW space. In this case the oscillation parameters are scanned over a very fine grid in linear scale. This was only possible with the analytic calculation of the survival probability implemented in this thesis, as the numerical integration tables had a maximal precision set beforehand. In Section 6.3.3 this implementation was shown to provide very good agreement in the survival probability curves when compared with the numerical integration results. As the analytic calculation was considerably faster than the numerical interaction of the neutrino wave functions, it was possible to optimise the step size in the grid so that it could be adjusted until no further improvement was obtained on the uncertainty of the estimated parameters. Furthermore, in order to obtain the best precision, instead of using a logarithmic scale grid spanning over a wide range of oscillation parameters, a linear scale grid was used using smaller steps.

The reason to perform a scan on the oscillation parameters, rather than a fit is purely technical. A fit on the oscillation parameters was also implemented using the same algorithms, but two reasons disfavoured this approach. As the survival probability curves vary considerably over the MSW space (as shown in Figure 5.6 of Section 5.6.3), it means that the χ^2 obtained as a function of the oscillation parameters can have several local minima. This requires a very robust fitting algorithm that can deal with multiple local minima. The second reason for choosing a parameter scan over a true fit of the oscillation parameters relies in the computation time required by this analysis. An analysis of the combined data from all solar neutrino experiments,

Parameter	Range	Step Size (linear scale)
$\tan^2 \theta_{12}$	$[1 \times 10^{-1}; 1]$	1×10^{-4}
Δm_{21}^2	$[1 \times 10^{-5}; 1 \times 10^{-3}]$	1×10^{-6}
$\sin^2 \theta_{13}$	$[1 \times 0.0; 0.25]$	5×10^{-3}

Table 6.2: Limits and step sizes of the MSW space tested in the neutrino oscillation parameter scan.

although having only a single minimum, contains more than a hundred observables. Performing the analysis as a simultaneous fit of the flux scale and the oscillation parameters implies that the fit cannot be parallelised, imposing an unreasonable requirement on the processing time for the analysis. For instance, the three-flavour neutrino oscillation analysis of all solar neutrino data discussed below would require a total of five years of processing time⁶. This would be absolutely impossible in a single fit without more advanced parallel analysis techniques.

On the other hand, by performing a scan the objective is to build a map of the χ^2 over the full region of interest in the MSW space. It is therefore possible to break the space into segments, analysing each segment independently and later joining the smaller maps into a full χ^2 map of the MSW space. Although this method implies a pre-set precision, by means of the grid stepping size, and requires the full space to be tested, the oscillation analysis can be performed considerably faster, depending on the number of available CPUs. Both methods have been tested in the same analysis yielding identical results, as expected [108]. The details of the MSW space sampled in this thesis is detailed in Table 6.2. The limits on the analysis region were set by extending to a range beyond 5σ significance in the present limits, and the precision (step size) was obtained by improving the precision below which no further improvement was obtained by re-running the analysis on the solar neutrino experimental results.

Having defined the region of interest and setting the intended precision, the MSW parameter space was scanned and the χ^2 values stored as a function of the oscillation parameters producing a χ^2 map. *Confidence Levels (CLs)* of the oscillation parameters were then obtained by projecting the map into one or two dimensions. The χ^2 differences $\Delta\chi^2 = \chi^2 - \chi_{min}^2$, listed in Table 6.3 were used as indicators of

⁶That particular analysis consumed approximately 4.3×10^4 h of processing time using approximately 1000 2.5 GHz, 64 bit, cores.

$N\sigma$	CL	$\Delta\chi^2$ 2D	$\Delta\chi^2$ 1D
1	68.27%	2.298	1.0
1.64	90.00%	4.605	2.706
1.96	95.00%	5.991	3.841
2.57	99.00%	9.210	6.635
3	99.73%	11.83	9.0

Table 6.3: Number of standard deviations ($N\sigma$) and confidence levels (CL) associated with the differences $\Delta\chi^2 - \chi^2_{min}$ in one and two dimensions.

the *Confidence Levels* (CLs) in one and two dimensional space. The definition of these values follow the prescription of [162] for construction of confidence intervals by performing a Gaussian approximation in order to avoid the full Neyman construction of the confidence region. In particular, the two-dimensional confidence intervals are obtained by selecting the region where the fit on the data yields a $\Delta\chi^2$ within the range that corresponds to the same two-sided confidence level for a standard χ^2 distribution with two degrees of freedom, which is quoted in the second column of the table. Similarly, the uncertainties on each individual oscillation parameter are determined by projecting the χ^2 obtained at each point as a function of the displayed parameter while marginalising all other parameters. Therefore, the confidence levels used to determine the uncertainties on each parameter are described in the third column of the table.

One special case to be taken under consideration is the determination of the upper limit on $\sin^2\theta_{13}$. Although $\tan^2\theta_{12}$ is known to be located in a physical region to more than 3σ , the parameter $\sin^2\theta_{13}$ is known to be very small and therefore close to an unphysical region. As the analysis algorithm restricts the fit to the physical region ($\sin^2\theta_{13} > 0$), one should not use the values quoted in Table 6.3 as they will potentially lead to wrong confidence limits [162]. Therefore, a one-sided 95% confidence level of $\Delta\chi^2 = 2.71$ is used to obtain the upper limit on the parameter.

6.5.2 Results from SNO

The results obtained for a SNO-only analysis were treated as described in Section 6.3.2. For each set of oscillation parameters, the model survival probability was transformed into the same polynomial parameterisation that was used in the SigEx

procedure, composed by three second order polynomial coefficients $\{c_0, c_1, c_2\}$ and two day-night asymmetry polynomial coefficients from a first order polynomial $\{a_0, a_1\}$. The additional $f_{8\text{B}}$ parameter is not used at this stage, as the polynomial coefficients already describe the survival probability, which does not depend on the specific scale of the ${}^8\text{B}$ neutrino flux. The χ^2 tables were built from the outputs of the SigEx procedure using the correlation matrix and total uncertainties on the coefficients.

Figure 6.14(a) shows the results obtained by analysing the SNO data considering a wide range of oscillation parameters in the context of two effective flavours (two flavour analysis). The results show the existence of a local minimum in the LOW region ($\Delta m_{21}^2 \approx 1 \times 10^{-7} eV^2$). As observed in the past [65, 69, 70] and in Figure 6.12(b), the SNO experiment alone is not able to distinguish between both solutions, having however a preference for the LMA solution with very small significance (0.2σ). The numerical results obtained from this analysis are quoted in Table 6.4, where both local minima are described. For the sake of comparison, the results obtained in the previous SNO analysis (LETA) are also quoted, as both analyses have the same data. The difference in the results reflects the improvements of the 3-phase analysis, both in terms of signal extraction and neutrino oscillation analysis. Here, the most important factor consists in the combination of the data from the 3 phases as a single data set, taking care of all correlations and common systematics. In the LETA analysis, the NCD phase was considered a separate and uncorrelated experiment without CC and ES spectral information.

For the sake of comparison, the same results are shown in Figure 6.14(b) together with the confidence intervals obtained by performing an oscillation analysis with three effective neutrino flavours (three flavour analysis). It permits to observe the effect of introducing the third mass eigenstate in the analysis. The results show a large loss of precision on the oscillation parameters, which is expected considering the low statistics provided by a single experiment and the low sensitivity of solar neutrino experiments to θ_{13} . Nonetheless it is important to remark how even in the context of a three flavour analysis, the allowed regions remain LMA and LOW with a small region at small mixing angle that is disfavoured at the 95% confidence level.

The effect of the θ_{13} mixing angle in the survival probability acts as an absolute scaling factor, whose effect increases with its absolute value. It is therefore much harder to distinguish from the dominant scaling effect of θ_{12} . In the context of solar

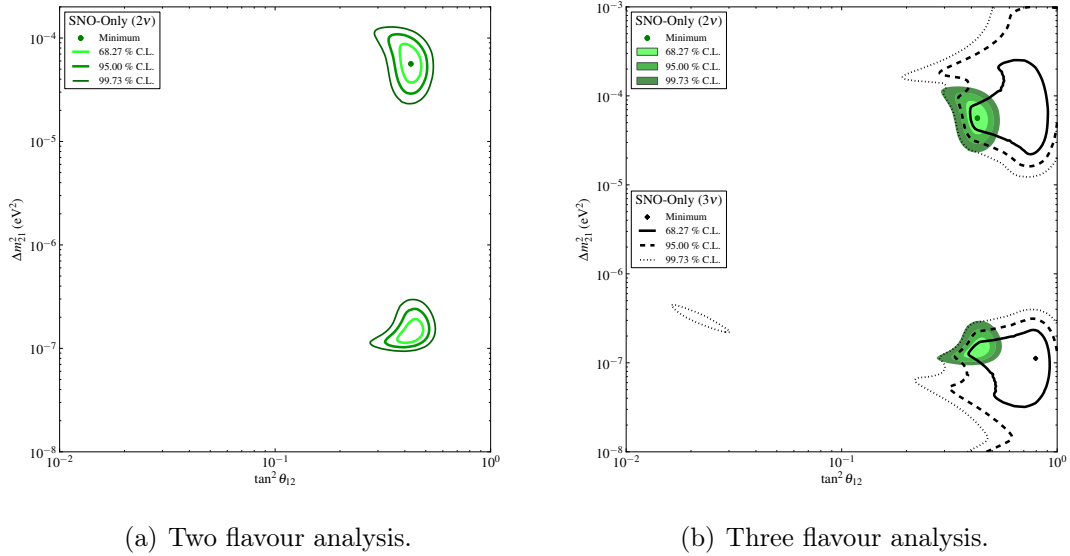


Figure 6.14: Confidence regions of the neutrino oscillation parameters obtained from the SNO only results by scanning a wide range of oscillation parameters. The numerical results are quoted in Table 6.4.

Oscillation analysis	$\tan^2 \theta_{12}$	$\Delta m_{21}^2 (eV^2)$	$\chi^2/n.d.f$
SNO 3-phase analysis			
Best fit (LMA)	$0.427^{+0.033}_{-0.029}$	$5.62^{+1.92}_{-1.36} \times 10^{-5}$	1.39/3
Best fit (LOW)	$0.427^{+0.043}_{-0.035}$	$1.35^{+0.35}_{-0.14} \times 10^{-7}$	1.41/3
SNO LETA analysis			
Best fit (LMA)	$0.437^{+0.038}_{-0.042}$	$5.50^{+2.21}_{-1.62} \times 10^{-5}$	8.20/9
Best fit (LOW)	$0.457^{+0.058}_{-0.058}$	$1.15^{+0.38}_{-0.18} \times 10^{-7}$	6.80/9

Table 6.4: Extracted neutrino oscillation parameters and corresponding uncertainty for a SNO-only result in a two-flavour analysis. As shown in Figure 6.14, SNO data alone is not enough to obtain a full constrain in a three flavour oscillation analysis. For comparison the results from the previous SNO analysis published in [70] are also shown.

neutrino experiments, a three flavour analysis is only relevant when a large amount of statistics is available, which is only achievable by combining several experimental results. In fact, since the effects of the oscillation parameters vary with energy, the sensitivity to the θ_{13} parameter is increased not only by increasing the statistics, but also by increasing the regions in neutrino energy being sampled. It is by comparing the low energy and high energy solar neutrino data that we can constrain θ_{13} .

6.5.3 Results from combining all solar neutrino data

The previous results showed that SNO alone is not able to constrain the oscillation parameters to a single solution, therefore a combined analysis of all solar neutrino data is needed. It is of major importance to perform a combined analysis of all solar neutrino data. While the SNO experiment is only sensitive to high energy neutrinos (${}^8\text{B}$ and *hep*), with a sensitivity above $E_\nu \sim 4.5\text{MeV}$, other experiments provide increased statistics and different sensitivities, as discussed in Section 1.5. Such are the cases of the radiochemical experiments that are sensitive to neutrino energies as low as 0.233 MeV, and the Borexino experiment that is sensitive mostly to the second energy line of ${}^7\text{Be}$ neutrinos ($E_\nu = 0.860\text{ MeV}$). Therefore, by combining all solar neutrino experiments, it is possible to sample a wide region of the solar neutrino spectrum, where different mixing effects interplay.

In this thesis the combined solar neutrino analysis includes the final results from the 3-phase combined analysis of SNO which were described in Chapter 5.

Besides the SNO results, the analysis also includes the integral rates from Homestake [38], a combined result of all Gallium based experiments [43], and the integral rate of the ${}^7\text{Be}$ measurement of Borexino [163]. Amongst these, the Homestake result incorporates contributions from all solar neutrino reactions with the exception of *pp* neutrinos, the rate being dominated mostly by the ${}^8\text{B}$ neutrinos. The Gallium results contain contributions from all solar neutrino reactions, including *pp*, which is the dominant component of the experimental observable. The Borexino result only accounts for the second line of the ${}^7\text{Be}$ shown in Figure 1.3.

Furthermore, all three reconstructed energy spectra of the ES rates published by the Super-Kamiokande experiment (SK-I, SK-II, SK-III) are also included [51–53]. The results from SK-I consist in 44 fractional rates⁷, which are separated not only in terms of total electron energy but also in terms of seven regions of zenith angle. The result from SK-II is represented in terms of 33 fractional rates separated into a day spectrum and a night spectrum⁸. Finally, the results from SK-III are provided in terms of 42 fractional rates broken into a day spectrum and a night spectrum.

⁷Fractional rates means that each rate is quoted in terms of a fraction of the solar model prediction in that energy range.

⁸With the exception of the rate at lowest energy that includes events from all orientations.

An additional experimental measurement was also included which consisted in 5 fractional rates of in reconstructed electron energy from ^8B neutrinos detected by Borexino [57].

These inputs represent a total of 133 observables and 57 systematic uncertainties, of which the ^8B spectrum shape uncertainty affects all observables, except the ^7Be Borexino rate. The list of all observables employed in the solar neutrino analysis are listed in appendix C.1. Besides scanning the oscillation parameters, the normalisation of the ^8B flux was allowed to float freely. Additionally, the hep flux normalisation was also allowed to vary, but constrained by the SSM uncertainty by means of a quadratic penalty term in the calculation of χ^2 , as shown in the last term of Equation 6.19.

Two flavour analysis

In Figure 6.15(a) the 2D contour of the oscillation parameters is shown over a wide region besides LMA in the context of a two flavour analysis. For comparison, the results obtained with SNO data alone are also shown. Unlike the results from SNO data alone, by combining all solar neutrino data, only the LMA solution becomes the only accepted at the 3σ level. In Figure 6.15(b), a more detailed comparison is shown focusing only on the LMA solution.

From these results it is easily noticed that by combining all solar neutrino data an enhanced sensitivity to the oscillation parameters is achieved. However, it is also clear that the results are strongly dominated by the SNO data, especially for θ_{12} . This is expected as SNO detects both CC events, sensitive only to ν_e , and NC events, equally sensitive to all flavours. In a two flavour analysis, the ratio $^{CC}/^{NC}$ events roughly corresponds to a direct measurement of the θ_{12} mixing angle (roughly $\sin^2 \theta_{12}$), and therefore SNO has a leading role in the determination of this parameter⁹.

The additional sensitivity achieved by combining all solar neutrino data reflects not only the increased statistics but mostly the additional neutrino energy information provided by measurements such as Borexino and the radiochemical experiments. The numerical results on the extracted oscillation parameters are quoted in Table 6.5.

⁹As ^8B neutrinos have a spectrum that is not fully detected by the experiments, this is just a rough estimate, since the survival probability has a dependence on neutrino energy. But at the neutrino energy range where SNO is sensitive, the survival probability is almost flat.

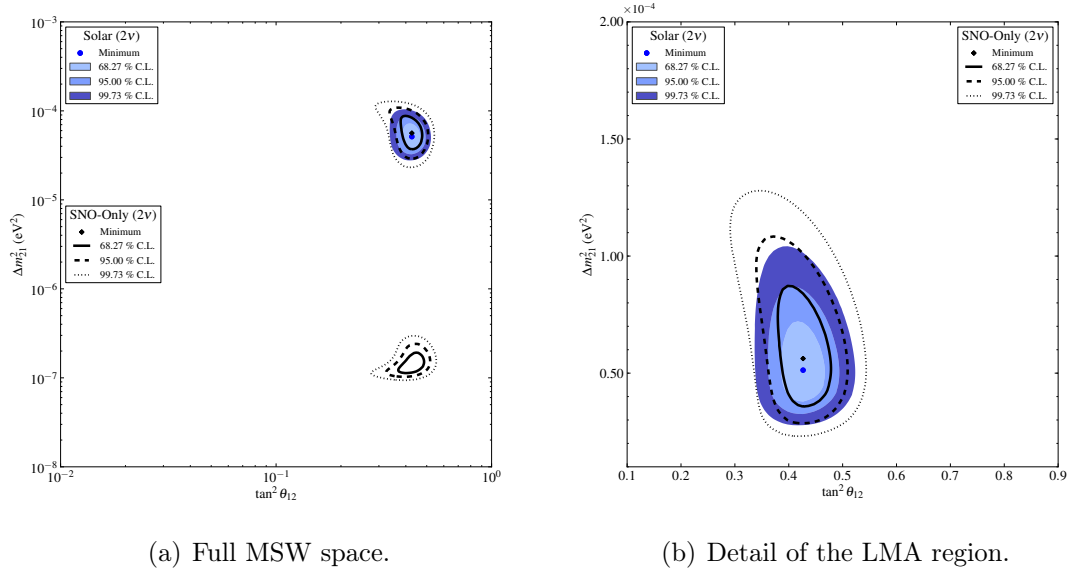


Figure 6.15: Confidence regions of the neutrino oscillation parameters obtained from a two flavour analysis of all solar neutrino data. The plot on the right shows a detail of the LMA region solutions, which is the only allowed by the solar analysis at the 3σ level. The numerical results are quoted in Table 6.10.

Three flavour analysis

By performing a three flavour analysis, the extracted uncertainties on the parameters becomes larger, as there is one additional degree of freedom to consider. However, unlike in the case of SNO, the allowed region of oscillation parameters is now fully contained to the LMA solution at the 3σ level. Figure 6.16 shows the confidence intervals obtained in the context of a three flavour analysis for all solar neutrino data. Figure 6.16(a) shows the projection over the plane $(\tan^2 \theta_{12}; \Delta m_{21}^2)$, while marginalising $\sin^3 \theta_{13}$. For comparison, the results from a solar two-flavour analysis from Figure 6.15 are also shown for comparison. In Figure 6.16(b) the allowed region in the plane $(\tan^2 \theta_{12}; \sin^2 \theta_{13})$ is shown, while marginalising Δm_{21}^2 . The best fit points in the extracted parameters and corresponding uncertainties are quoted in Table 6.5.

Figure 6.16(a) clearly shows the effect of considering three neutrino flavours in the analysis. As expected, there is a loss of precision on the oscillation parameters θ_{12} and Δm_{21}^2 which is due to the additional degree of freedom. However, there is

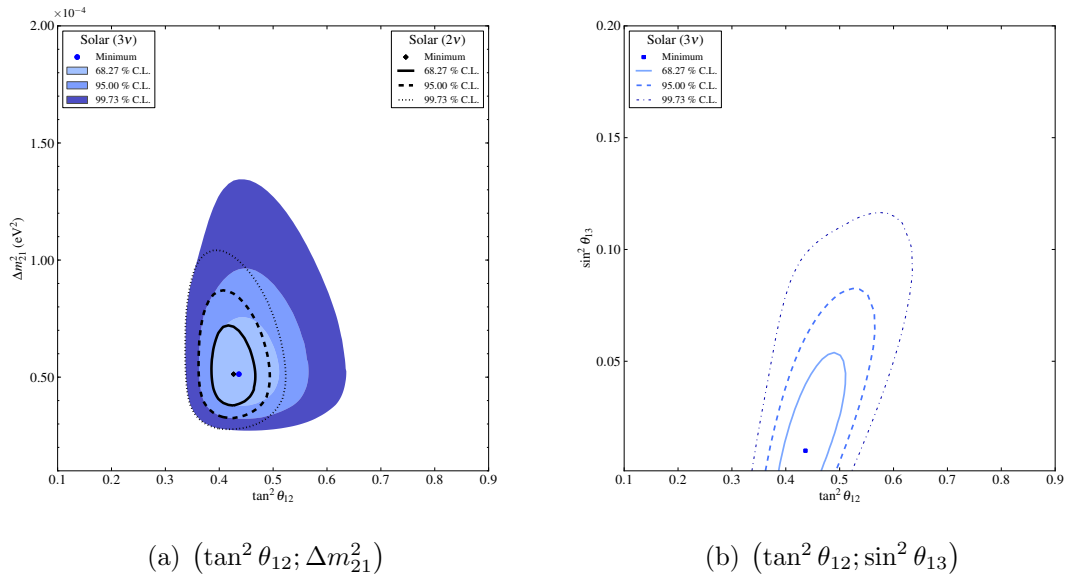


Figure 6.16: Confidence regions obtained from SNO data alone in the context of a two-flavour and three flavour analyses projected over two different planes in the MSW space.

an interesting observation from these results. Although there is effectively a loss in precision, this effect is not symmetric, *i.e.* the contours show a preferential direction in the broadening. For instance, by moving from a two-flavour analysis to a three flavour analysis the uncertainty in θ_{12} increases, but only for higher values of the mixing angle. This effect reflects the interdependence of the different mixing angles, as both affect the survival probability by means of a scaling factor. However, while the effect of θ_{12} is more predominant for higher neutrino energies, the effect of θ_{13} is most dominant on the low energy end. By allowing θ_{13} to vary freely, any tension between the low energy measurements such as Borexino and the rate experiments is reflected mostly in the θ_{13} parameter, allowing θ_{12} to reach higher values.

It is also important to notice a very large improvement on the limit in θ_{13} obtained by the analysis of the solar data. By comparing with the previous analysis of SNO data [70], a reduction of $\approx 30\%$ was achieved on the upper limit at the 95% C.L. The reason for this improvement is shared by several factors. For instance, the improvements added to this analysis were shown to expand the sensitivity on θ_{13} [143]. On the other hand, by properly combining all SNO phases into a single data set, the strong correlations between the different phases were taken into account,

Oscillation analysis	$\tan^2 \theta_{12}$	Δm_{21}^2 (eV^2)	$\sin^2 \theta_{13}$ ($\times 10^{-2}$)	$\chi^2/n.d.f$
Two flavour analysis				
SNO-only (LMA)	$0.427^{+0.033}_{-0.029}$	$5.62^{+1.92}_{-1.36} \times 10^{-5}$	1.39/3	
SNO-only (LOW)	$0.427^{+0.043}_{-0.035}$	$1.35^{+0.35}_{-0.14} \times 10^{-7}$	1.41/3	
Solar	$0.427^{+0.028}_{-0.028}$	$5.13^{+1.29}_{-0.96} \times 10^{-5}$		108.07/129
Three flavour analysis				
SNO 3-phase analysis				
Solar	$0.436^{+0.048}_{-0.036}$	$5.13^{+1.49}_{-0.98} \times 10^{-5}$	< 5.79 (95% <i>C.L.</i>)	107.92/128
SNO LETA analysis				
Solar	$0.468^{+0.052}_{-0.050}$	$6.31^{+2.49}_{-2.58} \times 10^{-5}$	< 8.10 (95% <i>C.L.</i>)	67.4/89
Solar+KamLAND	$0.468^{+0.042}_{-0.033}$	$7.59^{+0.21}_{-0.21} \times 10^{-5}$	$2.00^{+2.09}_{-1.63}$ < 5.7 (95% <i>C.L.</i>)	

Table 6.5: Extracted neutrino oscillation parameters and corresponding uncertainties in the oscillation analysis of all solar neutrino data in the two and three flavours framework.

which permitted to significantly improve the SNO results. Lastly, the inclusion of the most recent results from SK and Borexino further improved the analysis of solar neutrino data. Although weakly correlated, these improvements compete between themselves over the results and therefore it is hard to appoint a single dominant factor.

6.5.4 Effect of the Solar Model in the Oscillation Analysis

The results shown in the previous sections were all obtained using the BS05(OP) solar model and the corresponding uncertainties in its parameters. As described previously, the solar models affect the neutrino oscillation analysis in two ways: the parameters such as electron density and radial distribution of the neutrino reactions affect the survival probability directly, while the model predicted flux and corresponding uncertainties affect the theoretical prediction of event rates. The former has a negligible effect in the extraction of the oscillation parameters, as the differences are greatly overtaken by the experimental uncertainties. This was already shown in Section 6.2.1. The latter, however, can be relevant in the determination of the model predicted observables in the case of experimental data that relies on the solar model predicted flux. In fact, for the purposes of the neutrino oscillation analysis, most solar neutrino data are affected by this, with the exception of SNO which, by detecting

Oscillation analysis	$\tan^2 \theta_{12}$	Δm_{21}^2 (eV^2)	$\sin^2 \theta_{13}$ ($\times 10^{-2}$)	$\chi^2/n.d.f$
BS05(OP) [25]	$0.436^{+0.048}_{-0.036}$	$5.13^{+1.49}_{-0.98} \times 10^{-5}$	< 5.79 (95% <i>C.L.</i>)	107.92/128
BPS09(GS) [26, 27]	$0.447^{+0.049}_{-0.036}$	$4.90^{+1.34}_{-0.90} \times 10^{-5}$	< 5.47 (95% <i>C.L.</i>)	107.15/128
BPS09(AGSS09) [26, 28]	$0.447^{+0.040}_{-0.041}$	$5.13^{+1.50}_{-1.00} \times 10^{-5}$	< 5.74 (95% <i>C.L.</i>)	108.06/128

Table 6.6: Estimated neutrino oscillation parameters from analyses using different solar models.

neutrinos through NC, can perform a direct measurement of the solar ^8B neutrino flux and therefore do not depend on the solar model at all.

Therefore, in the context of a SNO-only analysis, as the only dependency on the solar model comes from the parameters that directly affect the shape of the survival probability, no visible effect was found when performing the analysis using different solar models. It is not the case for a combined solar neutrino analysis as the neutrino fluxes predicted by the solar model are necessary to perform the analytical convolution in order to estimate several theoretical event rates. Performing the oscillation analysis with different solar models can test if the solar neutrino data shows any preference for a particular solar model. Such a preference would have a strong impact in the comparison of the proposed solar models. In this case, one of the most relevant comparisons would be between the high and low metallicity solar models, as they show significant differences.

Therefore, the solar neutrino oscillation analysis was performed for three different solar models. Of these, BPS09(GS) and BPS05(OP) are very similar as both rely in the same heavy element abundance model (GS98 [27]) such that the only difference is an updated calculation of the total solar neutrino fluxes. BPS09(AGSS09), on the other hand, is a recently developed solar model, that uses the most recent calculation of heavy element abundance (AGSS09 [28]). In Figure 6.17 the confidence regions from a three-flavour solar analysis using three different solar models are shown, with the extracted values and uncertainties on the oscillation parameters quoted in Table 6.6.

The results show small differences between the solar models. In fact, considering the uncertainties, one can state that the solar neutrino data cannot make any statement in terms of distinguishing the tested solar models. It is surprising to note that, despite the consistency in the results, the BPS09(GS) solar model shows a larger

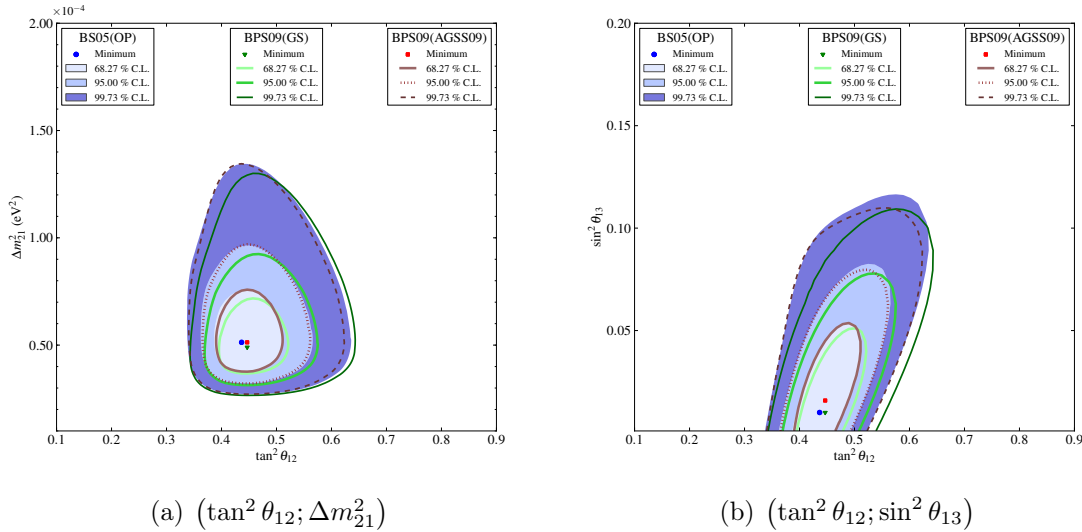


Figure 6.17: Confidence regions obtained from solar data in the context of a three-flavour analysis using different solar models.

deviation from the BS05(OP) solar model results than BPS09(AGSS09). Although the reason for this difference is not completely clear, one can postulate an hypothesis to justify this difference. Considering that, aside from integrated measurements from the radiochemical experiments (sensitive to multiple neutrino sources), the only neutrino fluxes that are effectively measured are ^8B and ^7Be . In the case of ^8B , the SNO measurement is independent of the solar model and therefore constrains the fit, discarding the difference between the solar models for this flux. This leaves only the ^7Be flux, measured by Borexino. Looking at the ^7Be neutrino fluxes predicted by each solar model, which are quoted in Table 1.2, one can see that BPS09(GS) and BPS09(AGSS09) solar models deviate from the BS05(OP) predicted flux by the same amount, but in different directions. Therefore, one hypothesis for the small discrepancy shown in the results might be a *preference* imposed by the Borexino data.

6.5.5 Probing the Neutrino Mass Hierarchy

One interesting feature of the analytical survival probability calculation used, it that unlike most adiabatic approximations, it did not discard the large mass splitting

Δm_{31}^2 . Although solar neutrinos are only weakly affected by this mass splitting, showing no difference in the survival probability inside the allowed range, one can however attempt to probe for its sign. As solar neutrino oscillations are dominated by matter effects, the sensitivity to the sign of Δm_{31}^2 is larger than the sensitivity to its absolute value. This is illustrated in Figure 6.18 where survival probability curves for different absolute values of ($\Delta m_{31}^2 \pm 1\sigma$) are shown against corresponding curves with different signs. Usually analyses of solar neutrino data assume *Normal Hierarchy (NH)* ($\Delta m_{31}^2 > 0$), although there is no imposition for this choice. In this section a comparison of the results under the assumption of both NH and *Inverted Hierarchy (IH)* ($\Delta m_{31}^2 < 0$) will be performed.

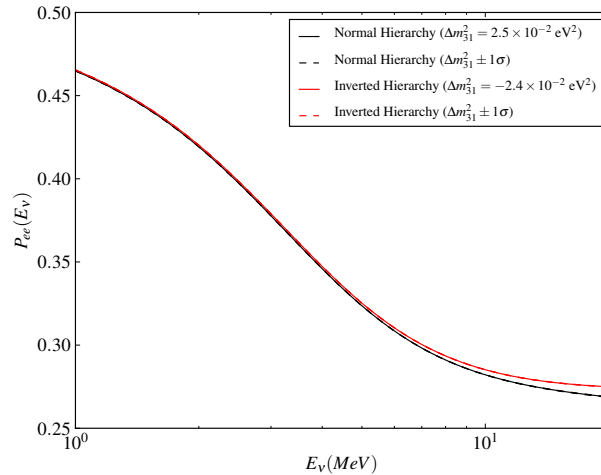


Figure 6.18: Comparison between the survival probability curves obtained by the analytic calculation for multiple values of Δm_{31}^2 . The black lines show the survival probability obtained under the assumption of Normal Hierarchy (NH) with $\Delta m_{31}^2 = 2.5 \times 10^{-3}$ and the red lines the corresponding survival probabilities under the assumption of Inverted Hierarchy (IH) with $\Delta m_{31}^2 = -2.4 \times 10^{-3}$. The remaining oscillation parameters were taken from the solar best fit point quoted in Table 6.10.

From this figure it is possible to note that the effect of the uncertainties is completely negligible, whereas the effect of the sign, despite being small, is more noticeable. It should be kept in mind that there is an intrinsic limitation to this test. The dependence of the survival probability on Δm_{31}^2 is strongly tied with the value of $\sin^2 \theta_{13}$ with the effect of Δm_{31}^2 (both sign and absolute value) scaling with increasing values of this mixing angle. Therefore, in Figure 6.11 the upper limit on $\sin^2 \theta_{13}$ from the solar analysis was used, to better illustrate the effect.

Oscillation analysis	$\tan^2 \theta_{12}$	Δm_{21}^2 (eV^2)	$\sin^2 \theta_{13}$ ($\times 10^{-2}$)	$\chi^2/n.d.f$
<i>Normal Hierarchy (NH)</i> ($\Delta m_{31}^2 = 2.5 \times 10^{-3} eV^2$)	$0.436^{+0.048}_{-0.036}$	$5.13^{+1.49}_{-0.98} \times 10^{-5}$	< 5.79 (95% C.L.)	$107.92/128$
<i>Inverted Hierarchy (IH)</i> ($\Delta m_{31}^2 = -2.4 \times 10^{-3} eV^2$)	$0.436^{+0.044}_{-0.036}$	$4.90^{+1.51}_{-0.97} \times 10^{-5}$	< 6.03 (95% C.L.)	$107.91/128$

Table 6.7: Estimated neutrino oscillation parameters from analyses under the assumption of normal (NH) and inverted (IH) hierarchies.

In Figure 6.19 the contour plots from this analysis are shown, with the corresponding numerical results are quoted in Table 6.7.

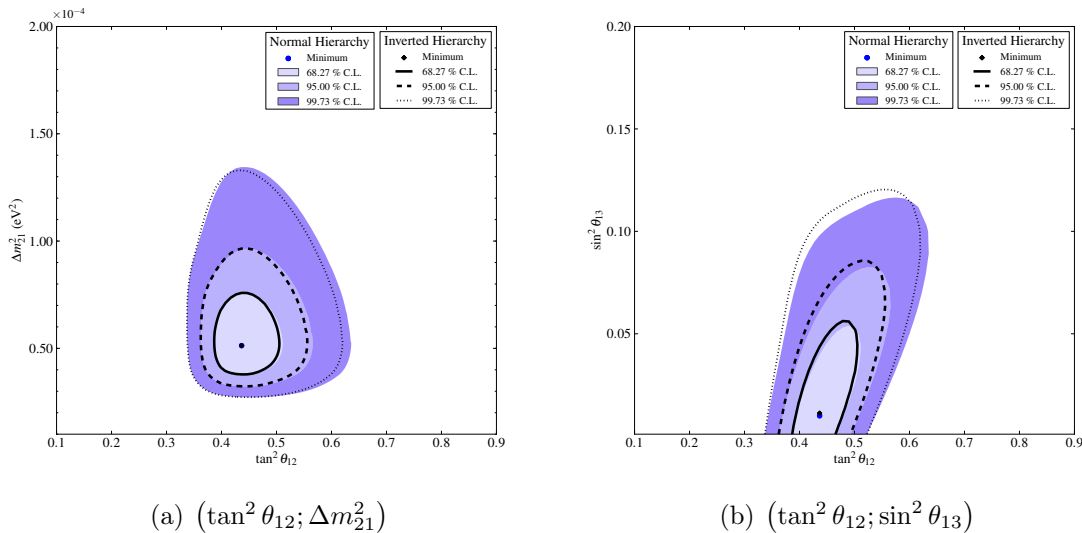


Figure 6.19: Confidence regions obtained from solar data in the context of a three-flavour analysis assuming NH and IH for neutrino masses.

The results of both analyses are completely consistent. However, despite having no statistical significance it is interesting to note that the analysis under the assumption of inverted hierarchy shows a slightly smaller uncertainty on $\tan^2 \theta_{12}$ and a higher limit on $\sin^2 \theta_{13}$. However the difference in the figure of merit has no statistical significance and therefore no conclusion can be drawn.

Nonetheless this demonstrates that despite the small effect of the sign of Δm_{31}^2 , it can be studied in the solar fits. This small effect is strongly constrained by the value of $\sin^2 \theta_{13}$, which scales down the global effect of the sign of Δm_{31}^2 .

6.6 Global Analysis of the Oscillation Parameters

In the previous Section a neutrino oscillation analysis of both SNO and all solar neutrino data was performed in order to obtain the most accurate limits on the mixing parameters relevant to solar neutrinos. However, these results can be further improved by considering other neutrino sources, such as reactor, atmospheric and accelerator data. These results can help to further constrain the oscillation parameters measured by the solar neutrino experiments due to the different sensitivities, both in flavour and energy. In this section data from such sources shall be used to further constrain the limits on the neutrino oscillation parameters.

The contributions of experimental data from non-solar neutrino sources can be separated into two different types according to the L/E_ν ratio relevant for the particular experiment, where L identifies the distance traveled by the neutrino and E_ν the neutrino energy range. Of all non-solar neutrino experiments, the most relevant to analyse along with the solar neutrino data is KamLAND, as it is sensitive to the same oscillation parameters.

The other types of experiments are generally not sensitive to the oscillation parameters relevant to solar neutrinos with the exception of the θ_{13} mixing angle. As in the case of KamLAND, these experiments are completely uncorrelated to solar neutrino experiments and therefore it is possible to obtain a global constraint on the common oscillation parameter of interest by joining the respective $\Delta\chi^2$ projections. More details about each of these limits are provided in the following subsections.

6.6.1 Combining Solar Data and KamLAND

The *Long Baseline Experiment (LBL)* reactor experiment KamLAND [59] studies antineutrinos produced in a series of reactors located mostly in Japan, having an average baseline of 180 km [59]. Reactor antineutrinos have an energy range of 1 to 10 MeV and therefore KamLAND is sensitive to the same oscillation parameters as the solar neutrino experiments, which makes this result the most interesting to combine with a solar data. As the distances traveled by the neutrinos are known to a much higher accuracy than solar neutrinos, this experiment is mostly sensitive to

the parameter Δm_{21}^2 . This sensitivity is further enhanced by the larger correlation between the energy of the positron produced by the antineutrino interaction when compared to the energy of the produced particles in the solar experiments.

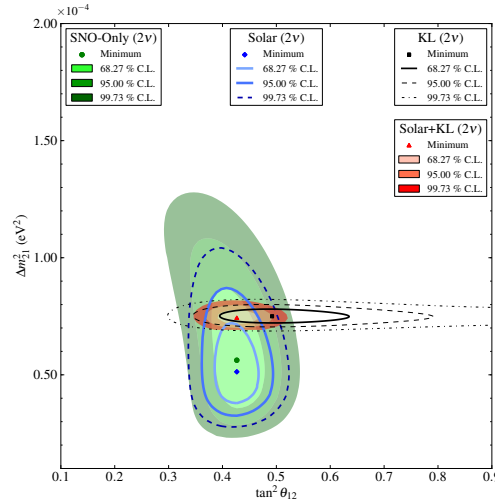


Figure 6.20: Confidence regions of the neutrino oscillation parameters obtained from a two flavour analysis of all solar neutrino data combined with the two-flavour analysis of KamLAND data. The allowed region from the combination of both data sets is shown in orange. The numerical results are quoted in Table 6.10.

As KamLAND is sensitive to antineutrinos, in order to combine both solar and reactor data one must assume that both neutrinos and antineutrinos must share the same oscillation parameters, as implied by CPT invariance. By the time the previous SNO result was published, the KamLAND experiment didn't perform a three flavour analysis of their data. Therefore in the context of this thesis an independent analysis was performed [164], which was used in [70] to perform a combined analysis. A brief description of this analysis is performed in C.3. Since then, an official three flavour analysis was published by the KamLAND collaboration [62], and therefore this result was used in the context of this thesis.

To perform the combined analysis the χ^2 map as a function of θ_{12} , Δm_{21}^2 and θ_{13} published by KamLAND [165] was added directly to the χ^2 map obtained from the solar analysis. This procedure is possible since both types of experiments are completely uncorrelated, with independent flux sources and systematic uncertainties. Therefore the respective χ^2 values constrain each other resulting in a region of allowed

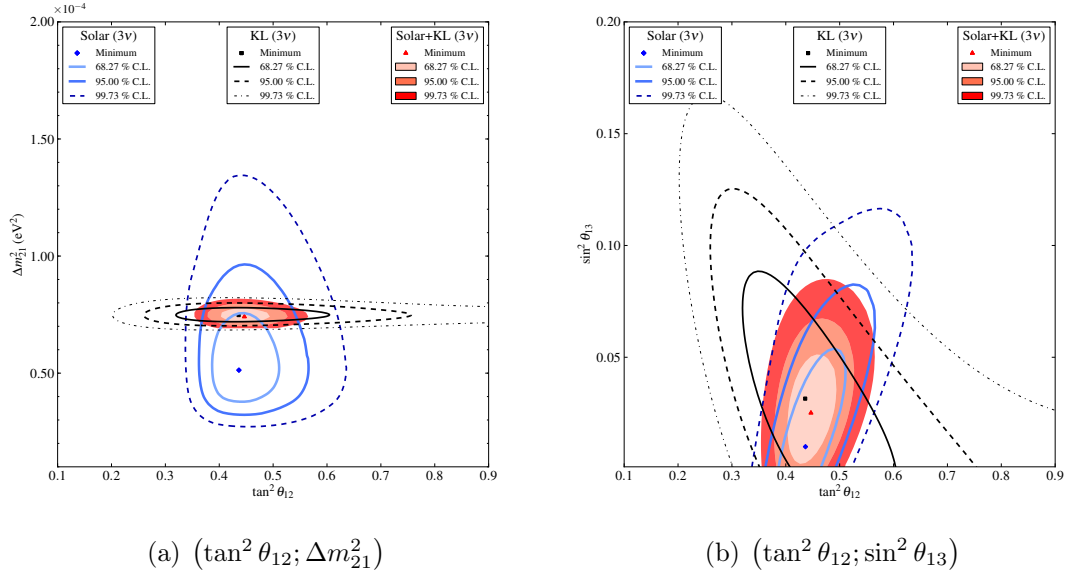


Figure 6.21: Confidence regions obtained from combining the solar neutrino analysis and the KamLAND analysis in the context of three neutrino flavours.

oscillation parameters that best adjust the data from both solar experiments and KamLAND.

Figure 6.20 shows the result of the global analysis on two flavours. The combined confidence regions are shown in a shaded colour. The numerical results are quoted in Table 6.8. From these results it is clear that the dominance of KamLAND over Δm_{21}^2 , while the solar neutrino experiments show a dominance in the determination of θ_{12} . In Figure 6.21 the confidence regions obtained from the same analysis but now considering three active neutrino flavours are shown. It is interesting to note that by comparing the confidence regions from Figures 6.20 and 6.21 there is a better agreement between the solar and KamLAND data if θ_{13} has a non-zero value with the best fit points becoming closer for a higher value of θ_{13} . This is further illustrated in Figure 6.21(b), where an anti-correlation between these two types of experiments is clearly noticed for the allowed values of θ_{13} . Nonetheless this *tension* between the experiments is still weak, providing a suggestion for non-zero θ_{13} with a statistical significance of 1.8σ . To further illustrate the dominance of each type of experiment (solar and reactor) the 1D projections of $\Delta\chi^2$ for each estimated parameter are shown in Figure 6.22 with the solar neutrino analysis, the KamLAND analysis and the final

combined results. From the figures it is noted the dominance of solar data over $\tan^2 \theta_{12}$, while KamLAND dominates over Δm_{21}^2 . Neither of the experiments has a strong bound on $\sin^2 \theta_{13}$, although a tension is visible between the corresponding confidence intervals.

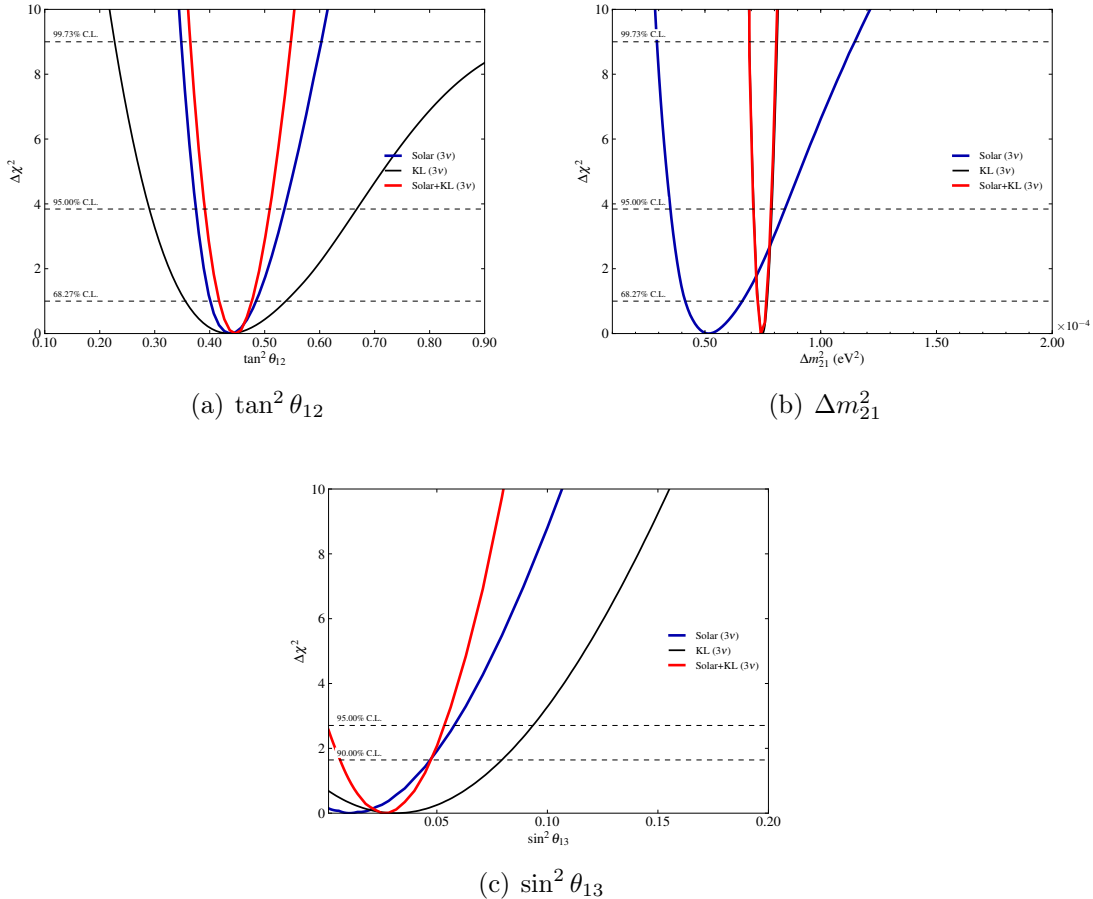


Figure 6.22: Confidence regions for the estimated oscillation parameters obtained from combining the solar neutrino analysis and the KamLAND analysis in the context of three neutrino flavours.

6.6.2 Further constrains from other neutrino sources

Unlike KamLAND, which is sensitive to the same neutrino oscillation parameters as the solar neutrino experiments, other neutrino sources are insensitive to both θ_{12} and Δm_{21}^2 . Therefore, by having only one mixing parameter with a non-negligible

Oscillation analysis	$\tan^2 \theta_{12}$	Δm_{21}^2 (eV^2)	$\sin^2 \theta_{13}$ ($\times 10^{-2}$)	$\chi^2/n.d.f$
Two flavour analysis				
Solar	$0.427^{+0.028}_{-0.028}$	$5.13^{+1.29}_{-0.96} \times 10^{-5}$		$108.07/129$
Solar+KamLAND	$0.427^{+0.027}_{-0.024}$	$7.46^{+0.20}_{-0.19} \times 10^{-5}$		
Three flavour analysis				
SNO 3-phase analysis				
Solar	$0.436^{+0.048}_{-0.036}$	$5.13^{+1.49}_{-0.98} \times 10^{-5}$	< 5.79 (95% <i>C.L.</i>)	$107.92/128$
Solar+KamLAND	$0.446^{+0.030}_{-0.029}$	$7.41^{+0.21}_{-0.19} \times 10^{-5}$	$2.51^{+1.76}_{-1.46}$ < 5.34 (95% <i>C.L.</i>)	
SNO LETA analysis				
Solar	$0.468^{+0.052}_{-0.050}$	$6.31^{+2.49}_{-2.58} \times 10^{-5}$	< 8.10 (95% <i>C.L.</i>)	$67.4/89$
Solar+KamLAND	$0.468^{+0.042}_{-0.033}$	$7.59^{+0.21}_{-0.21} \times 10^{-5}$	$2.00^{+2.09}_{-1.63}$ < 5.7 (95% <i>C.L.</i>)	

Table 6.8: Extracted neutrino oscillation parameters and corresponding uncertainties in the oscillation analysis of all solar neutrino data combined with KamLAND in the two and three flavours framework.

correlation, it is possible to apply a similar method as the one used when combining the KamLAND results but now using only a 1D projection of $\Delta\chi^2$ as a function of θ_{13} from other experiments in order to further constrain this parameter.

As examples of these sources one can consider the *Short Baseline Experiment (SBL)* reactor experiment Chooz [166], the atmospheric neutrino data from SK [46] and LBL accelerator experiments MINOS [159] and T2K [49]. Of particular relevance one can consider the latest results from T2K [167], where an independent indication of a non-zero value of θ_{13} was observed with a 2.7σ significance. Being completely uncorrelated between themselves, one can simply add the 1D projection over θ_{13} of each experiment in order to obtain a global constrain on this parameter.

Figure 6.23 shows the resulting confidence intervals obtained by combining the projection obtained in Section 6.6.1, with the contributions from all other experiments, as published in [168].

By combining all these results it is interesting to note that there is now an indication of 3.2σ for a non-zero value of θ_{13} . However, it should be noted that this procedure, although commonly used, must be considered simply as an indication, as

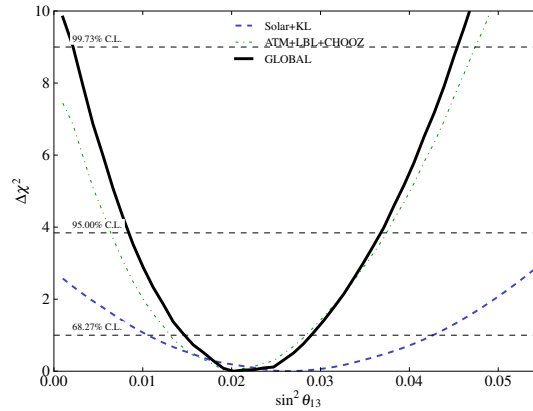


Figure 6.23: Unidimensional projection of $\Delta\chi^2$ as a function of $\sin^2 \theta_{13}$ demonstrating the resulting constrain in θ_{13} from combining all available neutrino data. The numerical results are quoted in Table 6.10.

the details of each individual analysis can affect the final results. For a more thorough analysis, all experimental data used in this subsection should be re-analysed ensuring the consistency on any assumptions used.

6.7 A Look Into the Future: SNO+

Considering the present measurements from solar neutrino data, one can readily observe that there isn't much more to improve by looking at the same neutrino sources, since the experimental uncertainties are now reaching a state where they compete with the solar model uncertainties. Thus, the best approach to further improve the solar neutrino picture, is by looking at other neutrino sources. In this section, an evaluation of the future improvements will be performed by determining the impact of a one and two year measurements of *pep* solar neutrinos neutrinos in the oscillation parameters.

The SNO+ experiment [74, 169–171] is a natural successor of SNO. By the end of SNO data taking, the heavy water was removed from the detector and returned back. SNO+ reuses the SNO detector and is planning to use liquid scintillator (Linear Alkyl Benzene - LAB) as the active medium. This change in the approach leads to two immediate consequences: SNO+ will use the same detection principle as

other liquid scintillation experiments, such as Borexino, *i.e.*, the neutrino events are detected through elastic scattering. As Borexino, by using liquid scintillator, SNO+ becomes sensitive to a lower energy range than SNO, making the two experiments complementary. SNO+ has a rich physics program, aiming to detect reactor, geo, atmospheric and solar neutrinos, and even studying neutrinoless double beta decay with ^{150}Nd [171]. For the purposes of this thesis the focus will be on the solar neutrino physics potential.

The large rock overburden of the SNO detector creates a great shield for cosmic rays, strongly reducing the cosmogenic background. In this context, SNO+ has the best possibility to perform a high precision measurement of *pep* neutrinos. The *pep* solar neutrino flux has the second best known flux, with an uncertainty of $\pm 1.5\%$, and being a mono-energetic line ($E_{\nu}^{pep} = 1.442$ MeV), its detection tests a very specific point of the solar neutrino spectrum. Furthermore, the energy of *pep* neutrinos lie precisely in the intermediate region between matter dominated and vacuum dominated oscillations. However *pep* neutrinos are not easy to detect, not only due to their low energy, but mostly due to the fact that its major background consists in the cosmogenic production of ^{11}C , which has a β^+ decay with a half life of $T_{1/2} = 29.4$ min and an energy deposition in the detector (both from the decay and the successive positron annihilation) between 1.02 and 1.98 MeV [172], partially covering the window for detection of *pep* neutrinos. In this context SNO+ has a unique possibility to perform the measurement, as the 6000 m.w.e. rock overburden reduce the amount of muons interacting with the detector to ≈ 80 per day. SNO+ will also be able to detect ^8B and ^7Be neutrinos. However, these have already been detected by other experiments with good statistics (SNO has measured ^8B with an uncertainty of 3.8% [127] and Borexino measured ^7Be with an uncertainty of 4.8% [163]). Therefore in this section, the focus will be on a SNO+ measurement of *pep*.

Therefore a model of SNO+ was constructed based on the properties of the SNO detector and the properties of LAB. Using this model, and the solar best fit oscillation parameters quoted in Table 6.5, the number of events expected for at the present best fit point and in the absence of oscillations was calculated. This value is different from the more simplistic approach of using directly the survival probability at 1.442 MeV¹⁰

¹⁰Since *pep* neutrinos are mono-energetic, a zeroth order approach could be to use the survival probability directly as an observable.

Oscillation analysis	$\tan^2 \theta_{12}$	$\Delta m_{21}^2 (eV^2)$	$\sin^2 \theta_{13} (\times 10^{-2})$	$\chi^2/n.d.f$
Solar (current data)	$0.436_{-0.036}^{+0.048}$	$5.13_{-0.98}^{+1.49} \times 10^{-5}$	$< 5.79 (95\% C.L.)$	107.92/128
Solar + 9% SNO+ pep	$0.436_{-0.034}^{+0.044}$	$5.13_{-0.96}^{+1.47} \times 10^{-5}$	$< 5.27 (95\% C.L.)$	107.92/129
Solar + 5% SNO+ pep	$0.436_{-0.031}^{+0.039}$	$5.13_{-0.95}^{+1.48} \times 10^{-5}$	$< 4.67 (95\% C.L.)$	107.92/129

Table 6.9: Estimated neutrino oscillation parameters from analyses using different solar models.

due to the fact that ES events can occur on two channels, one of which is sensitive to all neutrino flavours. In this analysis, two situations were considered: a one year measurement of pep, assuming a total uncertainty of 9%, and a two year measurement assuming a total uncertainty of 5%. These values are almost arbitrary, although some considerations were taken in their definition, such as live-time (80%), fiducial volume (50%), a data taking period of one and two years and an expected rate of ^{11}C events at the depth of SNOLAB. Using these data, two neutrino oscillation analyses were performed with the same inputs discussed in Section 6.5.3, plus our own estimate for a SNO+ pep measurement. The results obtained are shown in Figure 6.24. The obtained results in terms of oscillation parameters are quoted in Table 6.24.

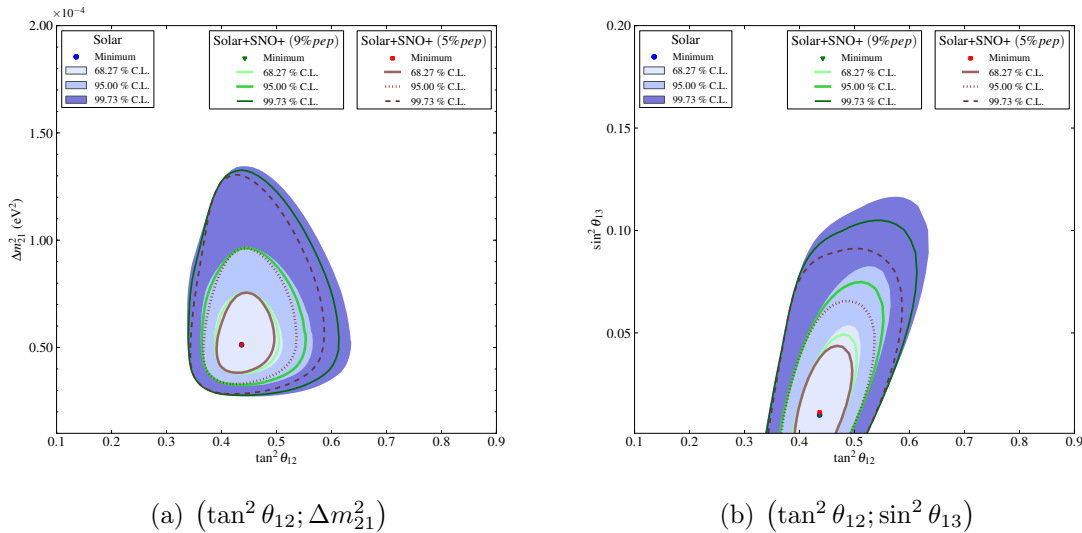


Figure 6.24: Confidence regions obtained from a solar neutrino analysis combining existing solar data with an expectation for a SNO+ measurement of pep neutrinos assuming an uncertainty of 5% and 9%.

These results show that SNO+ has a clear potential to further improve on the

precision of the neutrino oscillation parameters, especially on the mixing angles. The results show a reduction on the uncertainty of $\tan^2 \theta_{12}$ of about 1% per year of data. In terms of $\sin^2 \theta_{13}$, the effect is even more noticeable with a reduction on the limit of approximately 10% with each year of data. Although this analysis is based on a series of assumptions that need to be further developed and investigated, it shows nonetheless a great potential on SNO+ to further improve on the solar neutrino picture. The potential to measure CNO and pp solar neutrinos, as well as reactor neutrinos, makes SNO+ a very interesting experiment for any studies on the neutrino properties. A potential measurement of CNO neutrinos has the possibility to make a statement between the high and low metallicity solar models [173]. Being on the top of the pp fusion chain, pp neutrinos have the smallest of the solar model uncertainties and the highest flux, which by itself makes their detection a great challenge.

6.8 Summary

The parameters relevant for neutrino oscillations in the solar sector were extracted from a series of analyses which sequentially added further information to the study of neutrino properties. The results, shown in the previous section, demonstrated that the precision of the experimental measurement currently achieved allow the oscillation parameters to be determined with unprecedented precision.

Table 6.10 summarises the measurements of the neutrino oscillation parameters obtained in the different analyses described in this thesis. The results are presented in the form of a best fit parameter with 1σ uncertainties evaluated from marginalised 1D projections of the relevant parameter.

The precision on $\tan^2 \theta_{12}$ is primarily due to the SNO measurements, with further improvement added by data from experiments probing the lower neutrino energy regions, such as Borexino and the radiochemical experiments. This can be observed clearly in Figures 6.20 and 6.21, but most importantly by the numerical results quoted in Table 6.10.

A few observations can be made concerning $\tan^2 \theta_{12}$: comparing the current SNO results with the previously published results [70], it was verified a decrease in the central value of $\tan^2 \theta_{12}$ of approximately 1σ and a reduction in the uncertainty on the

Oscillation analysis	$\tan^2 \theta_{12}$	Δm_{21}^2 (eV^2)	$\sin^2 \theta_{13}$ ($\times 10^{-2}$)	$\chi^2/n.d.f$
Two flavour analyses				
SNO-only (LMA)	$0.427^{+0.033}_{-0.029}$	$5.62^{+1.92}_{-1.36} \times 10^{-5}$	1.39/3	
SNO-only (LOW)	$0.427^{+0.043}_{-0.035}$	$1.35^{+0.35}_{-0.14} \times 10^{-7}$	1.41/3	
Solar (BS05(OP),NH)	$0.427^{+0.028}_{-0.028}$	$5.13^{+1.29}_{-0.96} \times 10^{-5}$		108.07/129
Solar+KamLAND	$0.427^{+0.027}_{-0.024}$	$7.46^{+0.20}_{-0.19} \times 10^{-5}$		
Three flavour analyses				
SNO 3-phase analysis				
Solar	$0.436^{+0.048}_{-0.036}$	$5.13^{+1.49}_{-0.98} \times 10^{-5}$	< 5.79 (95% <i>C.L.</i>)	107.92/128
Solar+KamLAND	$0.446^{+0.030}_{-0.029}$	$7.41^{+0.21}_{-0.19} \times 10^{-5}$	$2.51^{+1.76}_{-1.46}$ < 5.34 (95% <i>C.L.</i>)	
Global			$2.02^{+0.88}_{-0.55}$	
Solar analysis with other solar models				
BPS09(GS)	$0.447^{+0.049}_{-0.036}$	$4.90^{+1.34}_{-0.90} \times 10^{-5}$	< 5.47 (95% <i>C.L.</i>)	107.15/128
BPS09(AGSS09)	$0.447^{+0.040}_{-0.041}$	$5.13^{+1.50}_{-1.00} \times 10^{-5}$	< 5.74 (95% <i>C.L.</i>)	108.06/128
Study of neutrino mass hierarchy				
IH	$0.436^{+0.044}_{-0.036}$	$4.90^{+1.51}_{-0.97} \times 10^{-5}$	< 6.03 (95% <i>C.L.</i>)	107.91/128

Table 6.10: Summary of the estimated neutrino oscillation parameters and corresponding uncertainties for the analyses described in the previous sections.

parameter from 13.3% down to 8%. This is a very interesting measurement, which clearly demonstrates the effect of adding the correlations between the phases. The decrease in the mixing parameter is mostly due to the inclusion of the NCD phase into the combined analysis, and the improvements that were added with it. The NC measurement of the NCD phase was considerably higher than in the previous phases [69]. By joining this phase with the first two phases, the normalisation of the total ^8B neutrino flux went up, which is also observable in the $f_{8\text{B}}$ parameter extracted in the SigEx analysis, causing $\tan^2 \theta_{12}$ to decrease. The improvement on the uncertainty, however, can be attributed to the improved oscillation analysis, where the principal improvement factor is the higher precision in the shape of the model survival probability, which is a critical component in the oscillation analysis. By performing a combined analysis of all solar neutrino data it was possible to further constrain $\tan^2 \theta_{12}$. Despite the precision being dominated by SNO, the higher precision measurement of the ^7Be neutrinos by Borexino, with 5% uncertainty in the low energy range of solar neutrinos also provides a significant improvement.

Concerning the parameter Δm_{21}^2 , although it was observed a considerable improvement both from SNO and solar neutrino analyses, in the context of a global measurement this parameter is completely dominated by KamLAND's measurements. The improvement observed with solar data is mostly due to the increased precision in the calculation of the survival probability, both for day and night. However, as KamLAND has a much better precision in the determination of both the baseline and has a higher correlation between the energy of the positron and the energy of the incoming antineutrino, the precision attainable from solar neutrino data cannot match.

Finally, the parameter $\sin^2 \theta_{13}$ could also be further constrained here in a combined analysis of solar neutrino data. However, due to its second order effect in the survival probability, the constrain is weak and cannot be interpreted as more than a hint for a non-zero value. In the context of a combined analysis of solar and reactor data from KamLAND this hint was found to have a significance of 1.64σ . However, it was also verified that by adding constrains obtained from other experiments this hint gained statistical significance of 3.2σ . In this case the constrain is clearly dominated by the accelerator results of T2K and MINOS, which alone provide approximately 2.7σ significance for a non-zero θ_{13} .

Analyses of other effects such as solar models and neutrino mass hierarchy were also carried out and, although in both cases the results don't have enough statistical significance to perform a statement, different effects were studied. In the comparison between solar models it was seen that the solar data is not able to distinguish between them, although their properties slightly change the limits on the oscillation parameters. When testing the neutrino mass hierarchies, a small effect on the mixing angles was observed, with the results under the assumption of IH yielding a slightly lower upper bound on $\tan^2 \theta_{12}$ and a higher limit on $\sin^2 \theta_{13}$. This result is understandable if one takes into account the effect of the sign of Δm_{31}^2 in the calculation of the solar neutrino survival probability. Under the assumption of IH the survival probability shows a rise at high neutrino energies. The difference in the allowed ranges of the mixing angles suggest that this increase causes a change in the tension between the mixing angles reducing the uncertainty of $\tan^2 \theta_{12}$ and increasing the upper limit on $\sin^2 \theta_{13}$.

Considering the motivations quoted in Section 1.6, the results shown in this chapter bring some very interesting information. For instance, the suggestion that the third mixing angle might not be zero is becoming more and more favoured, which will open the door for the study of CP violation in the lepton sector. Despite obtaining only an upper limit from the solar neutrino analysis, this limit was reduced, when comparing with the previous data, which increased the *tension* with the KamLAND results. This led to an increase in the significance of the non-zero θ_{13} hint from these two types of experiments and ultimately to a significance of more than 3σ from all neutrino data.

When interpreting the results from the point of view of the various symmetry models, these results also bring new information. For instance, considering the shift observed in the θ_{12} mixing angle, one of the most popular models - Tri-Bimaximal Mixing - is now becoming more disfavoured being now almost 2σ away from the present best fit point. Of course, the statistical significance is still low and therefore this cannot be taken as more than a hint. Nonetheless, considering the expectations in the mixing angles shown in Figure 1.15 for both θ_{12} and θ_{13} several models are now becoming disfavoured. Of course many more models exist, but these results are a strong motivation for searching for new solutions at the GUT scales.

Finally, casting an eye into the future, a simple sensitivity test was performed to determine the possible improvement of a potential *pep* measurement by the SNO+ experiment. Two scenarios were assumed, consistent with both a one and two years of solar neutrino data taking. Under the considered assumptions it was shown that SNO+ has a potential to further improve over the oscillation parameters, having a significant effect both in $\tan^2\theta_{12}$ and $\sin^2\theta_{13}$. This potential is not completely surprising, considering that *pep* solar neutrinos are mono-energetic and their energy places them in an energy region with a strong physics potential to investigate the transition between vacuum and matter induced neutrino oscillations.

Chapter 7

Conclusion

The search for understanding the properties of the neutrino is going on for almost 80 years, and yet it is a story that is far from its completion. Starting by simply testing the hypothesis of the existence of the neutrino, as some of its properties were unravelled along with the development of more advanced and precise detection and measurement techniques, further questions were raised. Even now, although much has been understood on the study of these light neutral leptons, there are yet several questions that wait to be answered, such as their role, nature and mass. It is therefore not surprising the amount and variety of experiments proposed by the scientific community to determine the properties of this elusive particle.

In this context, the SNO experiment provided a major contribution to both neutrino and astroparticle physics by clearly demonstrating the existence of solar neutrino oscillation phenomenon, explaining the problem of rate deficits observed by other experiments. The SNO experiment, and all other solar neutrino experiments, have since then turned their focus towards a precise characterisation of both the neutrino oscillation phenomenon and the measurement of the total flux of all active neutrino flavours, and thus testing the SSM.

This thesis contributed towards this goal in two ways: by improving the optical characterisation of the detector, which was described in Chapters 3 and 4, and by directly improving the oscillation analysis of neutrino data, described in Chapter 6.

The contribution to the optical calibration allowed to identify and further improve

the knowledge of the optical properties of the detector, which was demonstrated to have a direct impact in the energy reconstruction of the neutrino events. This contribution involved not only the direct participation in the calibration activities, but also in the analysis of the data to extract the best analytical description of the detector optics.

Although its origin could not be irrefutably found, the investigation of the detector asymmetries demonstrated its existence at the level of the optical calibration, which was then treated by the implementation of an additional systematic error in the optical parameters, and the implementation of a correction in the energy reconstruction algorithms. The development of additional optical cuts were demonstrated to have a direct impact on the optical characterisation of the detector, significantly improving the estimation of the media attenuation coefficients, and reducing their overall uncertainty.

A large part of the optical calibration developments concerned the third and last phase of SNO. The introduction of the NCDs posed a major challenge to the optical calibration, introducing new optical effects and strongly affecting the photon collection statistics of the PMTs. The studies performed on the optical effects caused by the NCDs allowed to retain a comparable precision in the oscillation parameters with respect with the previous phases, despite the added difficulties in the PMT data analysis caused by the shadows and reflections. Although not directly used in the processing of the neutrino data, a new method for correcting the reflections caused by the proportional counters was added to validate the previously implemented technique, and even improve it.

All the optical calibration activities were successful in the improvement of the optical characterisation of the detector and most of them were integrated in the analysis workflow having a direct impact on the analysis of the third phase of the experiment, and the two combined analyses that followed. Besides the direct impact in the SNO analyses, these activities were also of key importance to the development of the SNO+ experiment, which shall use the same detector as SNO, replacing the heavy water by liquid scintillator. Although the optics with liquid scintillator are different, the information collected by the SNO experiment serves as a starting point in the characterisation of the detector, especially in the development of the Monte

Carlo simulation and analysis algorithms, such as the optical calibration. Furthermore, in its commissioning phase, the SNO+ experiment shall use the detector filled with light water, for which the optical calibration algorithms from SNO can be used with minimal adaptations.

Besides the extensive work on the optics, a contribution to the extraction of the SNO signals was performed by determining the best parameterisation of the survival probability that should be used to describe the spectral distortion consistent with neutrino oscillations (Chapter 5). This study, although only a part of a larger analysis yielded results consistent with other independent checks and helped in the decision on how to best describe the data from SNO, avoiding the problems imposed by the different energy responses of the individual SNO data phases.

Using a three active flavour model of neutrino oscillations, a precision analysis was performed on SNO data, yielding the best precise measurement to date of the mixing angle θ_{12} , for the first time reducing the uncertainty below 10% in the context of two effective neutrino flavours analysis. Although the basic analysis algorithm was retained from prior work, a whole new set of improvements allowed to considerably improve the extraction of the oscillation parameters relevant for solar neutrinos.

A major part of this improvement was due to the implementation of a new survival probability calculation. Although it was limited to a subset of the MSW parameter space and it was based in a well known adiabatic approximation, the improvements both in speed of the calculation and precision of the oscillation parameters was greatly improved over the static nature of the previous calculation. Additional improvements in both the treatment of some systematic uncertainties, the cross-section calculations and a better description of the Earth further enhanced the analysis.

The results obtained from a combined analysis of all solar neutrino data also yielded a significant improvement in the precision of the extracted oscillation parameters over previous analyses. The limit on θ_{13} was the lowest ever achieved with solar data. By combining the solar analysis results with the external data from both KamLAND as well as with all neutrino data from other sources, a significant milestone was found reaching a 3.2σ significance for a non-zero θ_{13} that is dominated mostly by the LBL experimental data. However it was also found that the results obtained with both solar, and later by adding in the limit from KamLAND, are also consistent

with the LBL results. This indication of a non-zero value opens the door to new tests, like probing the effects of CP-violation in the lepton sector.

All these results now leave a paved way to a new generation of experiments and analyses, to further understand the physics of neutrinos.

Appendix A

Acronyms

SM	Standard Model of particle physics
SSM	Solar Standard Model
SK	Super-Kamiokande
K2K	KEK to Kamioka
T2K	Tokai to Kamioka
LS	Liquid Scintillator
CKM	Cabibbo-Kobayashi-Maskawa
PMNS	Pontecorvo-Maki-Nakagawa-Sakata
MSW	Mikheev-Smirnov-Wolfenstein
CNO	Carbon-Nitrogen-Oxygen cycle
SNU	Solar Neutrino Unit
SNO	Sudbury Neutrino Observatory
D₂O	heavy water
H₂O	light water
PMT	photomultiplier tube
NCD	neutral current detector

CC	charged current
NC	neutral current
ES	elastic scattering
LMA	Large Mixing Angle
m.w.e.	meter water equivalent
TBM	Tri-Bimaximal Mixing
GUT	Grand Unified Theory
AV	acrylic vessel
UV	Ultra-Violet
DCR	deck clean room
PSUP	PMT support structure
OWL	outward looking
FEC	Front End Card
DAQ	data acquisition system
ECA	Electronic Calibration
D-T	deuterium-tritium
PE	photo-electron
SNOMAN	SNO Monte Carlo and ANalysis software
OCA	optical calibration
MC	Monte Carlo
LB	laserball
QE	quantum efficiency
PMTR	PMT angular response
OccRatio	Occupancy-Ratio
Occupancy	Occupancy-Efficiency
PCA	PMT Calibration

MPE	multi photoelectron correction
SigEx	signal extraction
3-phase	three phase combined analysis
LETA	low energy threshold analysis
PDF	probability density function
PSA	pulse shape analysis
P_{ee}	electron neutrino survival probability
PREM	Preliminary Reference Earth Model
PEM-C	Continental Parametric Earth Model
HE	High Energy
CL	Confidence Level
LBL	Long Baseline Experiment
SBL	Short Baseline Experiment
RMS	root mean square
NH	Normal Hierarchy
IH	Inverted Hierarchy

Appendix B

More on Optical Calibration

B.1 Optical Calibration Systematics

The systematic uncertainties in the optical calibration were originally defined in [83] (systematics common to all phases) and [108] (NCD phase systematics). The complete list of systematic uncertainties is described in table 4.3 being briefly described below.

The systematics common to all phases were the following:

Radial Scale Shift (1): The source positions were moved radially by 1% towards the PMTs. This accounted for uncertainties in the detector size in time units, which could be caused by changes to the PMT calibration time slopes and also accounted for changes in assumed quantities such as group velocities and wavelength. A weight factor of $f_1 = 0.2$ was applied to reduce the effective shift to 0.2%. This systematic affected mostly the water attenuations, resulting in a change of 10% in the D₂O attenuation and 20% in H₂O attenuation. The observed effect in the PMTR was less than 1%.

Radial Position Shift (2): All runs were displaced radially by 5 cm outwards. Like the previous systematic, this shift affected mostly the water attenuations. Since the uncertainty in the source radial position is of 2cm, this systematic had a weighting factor of $f_2 = 0.2$ to reduce the effective shift to 1 cm shift. A

changes in the D₂O and H₂O attenuations was about 15% and 25%, respectively while the effect in the PMTR was below 1%.

Radial Position Smear (3): All runs were displaced radially by an amount sampled from a gaussian with $\sigma = 5$ cm. Unlike the previous systematics, this smear could be either positive or negative. Like the previous systematics the effect was observed mostly in the water attenuations. For the same reasons as before, this systematic was also scaled by a factor $f_3 = 0.2$, which resulted in a change in the water attenuations of 5%.

Source z position (4): All runs were displaced vertically by 5 cm. This systematic accounted for vertical shifts in the detector coordinates and differences between the nominal and fitted LB positions. This systematic was weighted by $f_4 = 0.4$ which resulted in an effective shift of 2 cm. The mean position shift between the manipulator and fitted source positions is $\sim 1 \pm 1.4$ in each coordinate[83]. This systematic only had a significant effect in the H₂O attenuation, where a change of 2.5% was observed.

Source x position (5): Like the shift along z , this systematic consisted in applying a shift of 5 cm outwards along the source x coordinate. The weight was reduced to $f_5 = 0.2$, in order to take into account correlations with the previous systematics. The effect in the media attenuations and PMTR was smaller than the statistical uncertainties.

Source size (6): The distance from the laserball to each PMT was decreased by 3 cm, to account for its finite size. The weighting factor of $f_6 = 0.5$ accounted for the fact that the uncertainty in the knowledge of the actual optical centre of the laserball is ~ 1 cm.

Laserball distribution variations (7 and 8): The effect of the laserball intensity was obtained by squaring the relative intensity obtained in the nominal fit, in order to increase the residual differences. The effect of the uniformity was obtained by forcing the laserball distribution to be flat in all directions. Although the laserball distribution is an output parameter, these changes were used to quantify the effects of the laserball distribution on the other output parameters of the optical model. Because the laserball distribution is an output of the optical model, and thus its effect is partially accounted in the statistical

uncertainties, a weighting factor of $f_{7,8} = 0.05$ was applied. In both cases, these changes only affected the water attenuations by less than 5%, while the effect in the PMTR was negligible.

PMT-PMT variability (9): The PMT variability was ignored by setting $\sigma_{PMT} = 0$ in χ^2 calculation of the optical fit described in equations 3.6 and 3.10. As the PMT variability was determined with an uncertainty of $\sim 20\%$, a weighting factor of $f_9 = 0.2$ was applied. This resulted in a change of 1% in the D₂O attenuation, 5% in the H₂O attenuation and less than 2% in PMTR.

χ^2 cuts (10 and 11): While the nominal fit results were obtained after applying a χ^2 cut of $\chi^2 < 25$, successive iterations were performed with cuts of $\chi^2 < 16$ and $\chi^2 < 9$, to better understand how the PMT selection affected the results. The weights are set to $f_{11,12} = 1.0$, as this systematic does not account for physical uncertainties. Each systematic resulted in changes up to 2% in both water attenuations and PMTR.

PMT z asymmetry (12): As discussed in section 4.4.2, this was addressed by fitting simultaneously for two PMTRs. A scale factor of $f_{13} = 0.5$ was applied to account for the larger statistical uncertainties resulting from the extraction of two independent PMTRs, specially in NCD phase where the statistics reduction due to the geometrical cuts was considerably larger. An overall effect of 3% was obtained only in the PMTR.

The systematics specific to the NCD phase were:

PMT Efficiencies (13): A scale of 10% was applied to the PMT efficiencies. As spread in the PMT efficiencies is half of the shift applied, a weighting factor of $f_{12} = 0.5$ was applied. This systematic was particularly important in the NCD phase as the PMT efficiencies are directly used with the Occupancy method. The effect in the D₂O attenuations were on the order of 6%, while an effect of 1% was observed in the PMTR, specially at high angles. Due to strong correlations between the H₂O attenuations and the PMTR at high angles, the effect of this systematic in the H₂O attenuations cannot be directly estimated.

NCD tolerance parameter (14): A change of half of the nominal value of ($\Delta L = 5\text{cm}$) was applied to show the effect of increased statistics. A weighting factor

of $f_{14} = 0.5$ was applied to account for the uncertainty in the NCD positions. This systematic affected mostly the D₂O attenuation by an amount of $\sim 3\%$.

NCD Reflections (15): This systematic aimed to evaluate the effect of the NCD reflections in the optical parameters. The systematic was evaluated by effectively removing the NCD reflection correction, leaving only the MPE correction. In order to fully evaluate the effect of the correction a weight of $f_{15} = 1.0$ was applied. The effect on the optical parameters was negligible, with observed changes smaller than the statistical uncertainties.

NCD Reflection probability(16): This systematic was only applied in case of using the analytical NCD reflection correction described in section 4.3.4. In this case the reflection probability was multiplied by a factor of 10 to account for uncertainties in the solid angles, time windows and NCD reflectivity. A weight factor of $f_{16} = 0.2$ was applied assuming that the errors associated with this shift could not be greater than an equivalent increase in the NCD reflectivity of 100%. This systematic affected only the D₂O attenuation, as expected, resulting in a change of 5%.

NCD Reflectivity (17): This systematic was only applied in case of using the Monte Carlo reflection correction discussed in section 4.3.4. In order to evaluate this systematic a new set of Monte Carlo simulations was generated with the NCD reflectivity tuned to be the double of the nominal value for each wavelength. A weighting factor of $f_{17} = 1.0$ was applied to observe the full extent of the effect of the NCD reflectivity in the optical parameters. The results were consistent with the NCD reflection probability systematic, observing a change of 5% in the D₂O attenuation.

Appendix C

Additional Information on Neutrino Oscillation Analysis

C.1 Inputs of the combined Solar Neutrino Analysis

For the Solar neutrino oscillation analysis besides the inputs for the SNO experiment which were already described in chapter 5, the inputs from other solar neutrino experiments are also used. In table C.1 a list of such inputs are listed. The inputs from Borexino ^8B are published as a plot in [57] but the actual bin values and uncertainties were provided by the collaboration upon request.

Table C.1: Inputs for the Solar neutrino analysis in 3-phase paper.

Experiment	Measurement	Reference
Ga Rate (SNU)	66.1 ± 3.1	[43]
Cl Rate (SNU)	2.56 ± 0.23	[38]
Borexino ^7Be Rate	46.0 ± 2.2 cpd/100tons	[163]
Borexino ^8B Spectrum	Counts/2MeV/345.3 days	[57]
[3.0; 5.0]	29 ± 8.5	
[5.0; 7.0]	26 ± 5.5	
[7.0; 9.0]	14 ± 3.8	
[9.0; 11.0]	5 ± 2.2	

[11.0; 13.0]	1 ± 1	
SK-I Zenith Spectrum (MeV)	Rate (SSM)	[50]
[5.0; 5.5]	0.467 ± 10.04	
[5.5; 6.5](<i>day</i>)	0.453 ± 0.020	
[5.5; 6.5](<i>M1</i>)	0.442 ± 0.053	
[5.5; 6.5](<i>M2</i>)	0.379 ± 0.049	
[5.5; 6.5](<i>M3</i>)	0.472 ± 0.045	
[5.5; 6.5](<i>M4</i>)	0.522 ± 0.045	
[5.5; 6.5](<i>M5</i>)	0.503 ± 0.049	
[5.5; 6.5](<i>Core</i>)	0.426 ± 0.052	
[6.5; 8.0](<i>day</i>)	0.474 ± 0.012	
[6.5; 8.0](<i>M1</i>)	0.530 ± 0.034	
[6.5; 8.0](<i>M2</i>)	0.506 ± 0.030	
[6.5; 8.0](<i>M3</i>)	0.438 ± 0.026	
[6.5; 8.0](<i>M4</i>)	0.478 ± 0.026	
[6.5; 8.0](<i>M5</i>)	0.451 ± 0.028	
[6.5; 8.0](<i>Core</i>)	0.439 ± 0.031	
[8.0; 9.5](<i>day</i>)	0.448 ± 0.013	
[8.0; 9.5](<i>M1</i>)	0.463 ± 0.036	
[8.0; 9.5](<i>M2</i>)	0.470 ± 0.033	
[8.0; 9.5](<i>M3</i>)	0.462 ± 0.029	
[8.0; 9.5](<i>M4</i>)	0.509 ± 0.029	
[8.0; 9.5](<i>M5</i>)	0.461 ± 0.032	
[8.0; 9.5](<i>Core</i>)	0.451 ± 0.035	
[9.5; 11.5](<i>day</i>)	0.453 ± 0.015	
[9.5; 11.5](<i>M1</i>)	0.449 ± 0.040	
[9.5; 11.5](<i>M2</i>)	0.502 ± 0.038	
[9.5; 11.5](<i>M3</i>)	0.451 ± 0.032	
[9.5; 11.5](<i>M4</i>)	0.473 ± 0.032	
[9.5; 11.5](<i>M5</i>)	0.477 ± 0.035	
[9.5; 11.5](<i>Core</i>)	0.483 ± 0.040	
[11.5; 13.5](<i>day</i>)	0.477 ± 0.025	
[11.5; 13.5](<i>M1</i>)	0.509 ± 0.067	
[11.5; 13.5](<i>M2</i>)	0.351 ± 0.055	

[11.5; 13.5] (<i>M3</i>)	0.391 ± 0.049	
[11.5; 13.5] (<i>M4</i>)	0.498 ± 0.053	
[11.5; 13.5] (<i>M5</i>)	0.434 ± 0.056	
[11.5; 13.5] (<i>Core</i>)	0.521 ± 0.064	
[13.5; 16.0] (<i>day</i>)	0.511 ± 0.054	
[13.5; 16.0] (<i>M1</i>)	0.570 ± 0.150	
[13.5; 16.0] (<i>M2</i>)	0.831 ± 0.167	
[13.5; 16.0] (<i>M3</i>)	0.694 ± 0.131	
[13.5; 16.0] (<i>M4</i>)	0.665 ± 0.127	
[13.5; 16.0] (<i>M5</i>)	0.441 ± 0.118	
[13.5; 16.0] (<i>Core</i>)	0.469 ± 0.131	
[16.0; 20.0]	0.555 ± 0.146	
SK-II day-night Spectrum (MeV)	Events/kton/year	[51]
[7.0; 7.5] (average)	43.7 ± 5.1	
[7.5; 8.0] (day)	36.4 ± 5.1	
[7.5; 8.0] (night)	43.6 ± 5.2	
[8.0; 8.5] (day)	34.4 ± 3.5	
[8.0; 8.5] (night)	35.5 ± 3.5	
[8.5; 9.0] (day)	27.0 ± 2.8	
[8.5; 9.0] (night)	33.0 ± 2.8	
[9.0; 9.5] (day)	23.9 ± 2.3	
[9.0; 9.5] (night)	25.0 ± 2.3	
[9.5; 10.0] (day)	20.7 ± 2.0	
[9.5; 10.0] (night)	23.3 ± 2.0	
[10.0; 10.5] (day)	15.4 ± 1.7	
[10.0; 10.5] (night)	17.6 ± 1.7	
[10.5; 11.0] (day)	13.5 ± 1.5	
[10.5; 11.0] (night)	14.2 ± 1.5	
[11.0; 11.5] (day)	11.3 ± 0.9	
[11.0; 11.5] (night)	9.4 ± 1.2	
[11.5; 12.0] (day)	7.11 ± 1.00	
[11.5; 12.0] (night)	8.96 ± 1.035	
[12.0; 12.5] (day)	6.82 ± 0.94	
[12.0; 12.5] (night)	5.79 ± 0.86	

[12.5; 13.0] (day)	4.18 ± 0.73	
[12.5; 13.0] (night)	3.97 ± 0.70	
[13.0; 13.5] (day)	2.95 ± 0.62	
[13.0; 13.5] (night)	3.66 ± 0.61	
[13.5; 14.0] (day)	2.95 ± 0.57	
[13.5; 14.0] (night)	1.59 ± 0.44	
[14.0; 15.0] (day)	2.99 ± 0.60	
[14.0; 15.0] (night)	2.58 ± 0.53	
[15.0; 16.0] (day)	1.37 ± 0.42	
[15.0; 16.0] (night)	2.08 ± 0.45	
[16.0; 20.0] (day)	1.11 ± 0.37	
[16.0; 20.0] (night)	1.60 ± 0.40	
SK-III day-night Spectrum (MeV)	Events/kton/year	[53]
[5.0; 5.5] (day)	94.600 ± 15.400	
[5.0; 5.5] (night)	73.500 ± 13.400	
[5.5; 6.0] (day)	75.200 ± 9.600	
[5.5; 6.0] (night)	61.500 ± 8.250	
[6.0; 6.5] (day)	55.900 ± 6.800	
[6.0; 6.5] (night)	71.000 ± 6.900	
[6.5; 7.0] (day)	51.300 ± 3.800	
[6.5; 7.0] (night)	59.100 ± 3.800	
[7.0; 7.5] (day)	55.900 ± 3.600	
[7.0; 7.5] (night)	52.300 ± 3.450	
[7.5; 8.0] (day)	39.900 ± 3.100	
[7.5; 8.0] (night)	41.200 ± 3.000	
[8.0; 8.5] (day)	37.500 ± 2.700	
[8.0; 8.5] (night)	35.900 ± 2.550	
[8.5; 9.0] (day)	28.700 ± 2.300	
[8.5; 9.0] (night)	32.900 ± 2.350	
[9.0; 9.5] (day)	20.000 ± 1.850	
[9.0; 9.5] (night)	25.200 ± 2.000	
[9.5; 10.0] (day)	18.000 ± 1.700	
[9.5; 10.0] (night)	20.800 ± 1.750	
[10.0; 10.5] (day)	15.200 ± 1.450	

[10.0; 10.5] (night)	13.800 ± 1.400	
[10.5; 11.0] (day)	15.200 ± 1.400	
[10.5; 11.0] (night)	13.000 ± 1.250	
[11.0; 11.5] (day)	9.670 ± 1.140	
[11.0; 11.5] (night)	9.560 ± 1.060	
[11.5; 12.0] (day)	5.330 ± 0.850	
[11.5; 12.0] (night)	6.170 ± 0.895	
[12.0; 12.5] (day)	4.200 ± 0.745	
[12.0; 12.5] (night)	5.770 ± 0.800	
[12.5; 13.0] (day)	2.740 ± 0.565	
[12.5; 13.0] (night)	3.470 ± 0.610	
[13.0; 13.5] (day)	1.630 ± 0.425	
[13.0; 13.5] (night)	2.300 ± 0.500	
[13.5; 14.0] (day)	1.170 ± 0.340	
[13.5; 14.0] (night)	1.530 ± 0.420	
[14.0; 15.0] (day)	2.080 ± 0.470	
[14.0; 15.0] (night)	2.350 ± 0.485	
[15.0; 16.0] (day)	0.394 ± 0.231	
[15.0; 16.0] (night)	1.266 ± 0.346	
[16.0; 20.0] (day)	0.252 ± 0.183	
[16.0; 20.0] (night)	0.000 ± 0.276	
SNO 3-Phase	P_{ee} Polynomial parameterisation	[131]
f_{8B}	0.9235 ± 0.0348	
c_0	0.3174 ± 0.0185	
c_1	0.0039 ± 0.0080	
c_2	-0.0010 ± 0.0033	
a_0	0.0464 ± 0.0335	
a_1	-0.0163 ± 0.0272	

C.2 Parameters of the Standard Solar Models

Tables C.2, C.3 and C.4 list the partial derivatives of the solar models studied in this thesis. The propagation of the solar model uncertainties is described in Section 6.3.4. The first column gives the name of the parameters, p , the second the uncertainty on the parameter, and the remaining columns the partial derivatives α_{ki} for each neutrino flux.

p	Δp	pp	pep	hep	${}^7\text{Be}$	${}^8\text{B}$	${}^{13}\text{N}$	${}^{15}\text{O}$	${}^{17}\text{F}$
S_{11}	1	0.001	-0.001	-0	-0.004	-0.01	-0.01	-0.011	-0.011
S_{33}	1	0.002	0.003	-0.024	-0.023	-0.021	0.001	0.001	0.001
S_{34}	1	-0.005	-0.007	-0.007	0.08	0.075	-0.004	-0.004	-0.004
S_{114}	1	-0.002	-0.002	-0.001	0	0.001	0.079	0.095	0.001
S_{17}	1	0	0	0	0	0.038	0	0	0
L_{\odot}	1	0.003	0.003	0	0.014	0.028	0.021	0.024	0.026
Age	1	-0	0	-0	0.003	0.006	0.004	0.006	0.006
$Op.$	1	0.003	0.005	0.011	-0.028	-0.052	-0.033	-0.041	-0.043
$Diff.$	1	0.003	0.004	0.007	-0.018	-0.04	-0.051	-0.055	-0.057
$Be7e$	1	0	0	0	0	-0.02	0	0	0
S_{hep}	1	0	0	0.151	0	0	0	0	0
C	0.297	-0.014	-0.025	-0.015	-0.002	0.03	0.845	0.826	0.033
N	0.32	-0.003	-0.006	-0.004	0.002	0.011	0.181	0.209	0.01
O	0.387	-0.006	-0.011	-0.023	0.052	0.121	0.079	0.093	1.102
Ne	0.539	-0.005	-0.005	-0.017	0.049	0.096	0.057	0.068	0.076
Mg	0.115	-0.005	-0.005	-0.018	0.051	0.096	0.06	0.07	0.078
Si	0.115	-0.011	-0.014	-0.037	0.104	0.194	0.128	0.15	0.164
S	0.092	-0.008	-0.017	-0.028	0.074	0.137	0.094	0.109	0.12
Ar	0.496	-0.002	-0.006	-0.007	0.018	0.034	0.024	0.028	0.031
Fe	0.115	-0.023	-0.065	-0.069	0.209	0.515	0.342	0.401	0.444

Table C.2: Systematic uncertainties of the BS05(OP) SSM in the form of partial derivatives. An uncertainty $\Delta p = 1$ means the derivative already includes the weight of the uncertainty.

p	Δp	pp	pep	hep	${}^7\text{Be}$	${}^8\text{B}$	${}^{13}\text{N}$	${}^{15}\text{O}$	${}^{17}\text{F}$
S_{11}	0.004	0.119	-0.194	-0.099	-1.052	-2.683	-2.139	-2.895	-3.066
S_{33}	0.06	0.033	0.048	-0.454	-0.428	-0.406	0.03	0.024	0.022
S_{34}	0.032	-0.065	-0.094	-0.081	0.858	0.813	-0.06	-0.051	-0.047
S_{114}	0.08	-0.007	-0.011	-0.006	-0.002	0.007	0.749	1.001	0.007
S_{17}	0.038	0	0	0	0	1	0	0	0
L_{\odot}	0.004	0.78	1.007	0.142	3.562	7.165	4.664	6.116	6.61
Age	0.0044	-0.074	0.008	-0.129	0.755	1.341	0.939	1.358	1.467
$Op.$	0.025	-0.099	-0.3	-0.398	1.267	2.702	1.433	2.06	2.27
$Diff.$	0.15	-0.012	-0.018	-0.04	0.131	0.278	0.352	0.398	0.422
$Be7e$	0.02	0	0	0	0	-1	0	0	0
S_{hep}	0.151	0	0	1	0	0	0	0	0
C	0.134	-0.006	-0.012	-0.008	-0.001	0.02	0.841	0.794	0.023
N	0.145	-0.002	-0.003	-0.002	0.001	0.006	0.155	0.206	0.006
O	0.13	-0.005	-0.01	-0.024	0.056	0.125	0.069	0.096	1.105
Ne	0.142	-0.004	-0.004	-0.018	0.05	0.099	0.052	0.072	0.079
Mg	0.141	-0.005	-0.004	-0.017	0.052	0.098	0.051	0.072	0.079
Si	0.139	-0.009	-0.012	-0.036	0.106	0.195	0.111	0.151	0.165
S	0.152	-0.005	-0.012	-0.026	0.07	0.13	0.079	0.105	0.114
Ar	0.179	-0.001	-0.004	-0.006	0.016	0.03	0.019	0.025	0.027
Fe	0.143	-0.02	-0.063	-0.071	0.219	0.53	0.307	0.415	0.457

Table C.3: Systematic uncertainties of the BPS09(GS) SSM in the form of partial derivatives.

p	Δp	pp	pep	hep	${}^7\text{Be}$	${}^8\text{B}$	${}^{13}\text{N}$	${}^{15}\text{O}$	${}^{17}\text{F}$
S_{11}	0.004	0.09	-0.236	-0.112	-1.07	-2.73	-2.09	-2.95	-3.14
S_{33}	0.06	0.029	0.043	-0.459	-0.441	-0.427	0.025	0.018	0.015
S_{34}	0.032	-0.059	-0.086	-0.072	0.878	0.846	-0.053	-0.041	-0.037
S_{114}	0.08	-0.004	-0.007	-0.004	-0.001	0.005	0.711	1	0.005
S_{17}	0.038	0	0	0	0	1	0	0	0
L_{\odot}	0.004	0.808	1.04	0.174	3.56	7.13	4.4	6	6.51
Age	0.0044	-0.067	0.017	-0.118	0.786	1.38	0.855	1.34	1.45
$Op.$	0.025	-0.099	-0.3	-0.398	1.27	2.7	1.43	2.06	2.27
$Diff.$	0.15	-0.011	-0.016	-0.037	0.136	0.28	0.34	0.394	0.417
$Be7e$	0.02	0	0	0	0	-1	0	0	0
S_{hep}	0.151	0	0	1	0	0	0	0	0
C	0.133	-0.005	-0.009	-0.007	0.004	0.025	0.861	0.81	0.024
N	0.147	-0.001	-0.002	-0.002	0.002	0.007	0.148	0.207	0.005
O	0.129	-0.005	-0.006	-0.02	0.053	0.111	0.047	0.075	1.08
Ne	0.145	-0.004	-0.003	-0.014	0.044	0.083	0.035	0.055	0.061
Mg	0.142	-0.004	-0.002	-0.017	0.057	0.106	0.051	0.076	0.084
Si	0.139	-0.009	-0.012	-0.036	0.116	0.211	0.109	0.158	0.174
S	0.153	-0.006	-0.014	-0.028	0.083	0.151	0.083	0.117	0.128
Ar	0.188	-0.001	-0.003	-0.005	0.014	0.027	0.015	0.021	0.023
Fe	0.144	-0.016	-0.054	-0.064	0.217	0.51	0.262	0.386	0.428

Table C.4: Systematic uncertainties of the BPS09(Asplund:2009fu) SSM in the form of partial derivatives.

C.3 KamLAND

At the time the results from [70] were obtained, no three flavour analysis of KamLAND data was publicly available. Therefore, an independent analysis was performed in the context of this thesis with the publicly available data. The details of the analysis are described in [164]. A brief explanation shall be presented here.

The analysis follows the same lines as the method used in the analysis of other solar neutrino experiments besides SNO, described in section 6.3.1, that consists in an analytical convolution of the produced neutrino spectrum, cross sections and detector response, by performing the appropriate modifications to these elements.

The KamLAND Collaboration provided the data from figure 1 of [59], which includes both the reconstructed energy spectrum of reactor anti-neutrino events, and the corresponding expected spectrum without oscillations. Following a similar procedure as the one described in section 6.3.1, the analysis was performed by constructing an expected reconstructed energy spectrum for each point in a grid of oscillation parameters and obtaining a figure of merit by comparing the expected spectrum to the one reconstructed by KamLAND.

Unlike the Sun where there is a single source and spectrum for a given reaction, the neutrino flux at KamLAND is contributed by 75 reactors at distances below 1000 km. Each of these reactors have their own fuel composition, which is not publicly known. Furthermore, each reactor has different thermal powers and operating periods, which translates into different anti-neutrino fluxes over time.

The neutrino spectrum at the detector without oscillations was then determined based on the average duty cycle and thermal power of the reactors collected from [174], and the average fuel composition quoted by KamLAND in [59]. It is important to note that the normalisation of the spectrum, i.e., the total flux of neutrinos is of no importance. Only the shape of the reconstructed spectrum contains information concerning the neutrino oscillations and therefore the un-oscillated spectra predicted by KamLAND and calculated in this analysis were important milestones to verify the accuracy of the expected observables.

The KamLAND survival probabilities of $\bar{\nu}_e$ were calculated using a simplified

version of the vacuum survival probability of equation 1.12, taking into account the characteristics of KamLAND[18]:

$$P(\bar{\nu}_e \rightarrow \bar{\nu}_e) = \sin^4 \theta_{13} + \cos^4 \theta_{13} P^{2\nu}(\bar{\nu}_e \rightarrow \bar{\nu}_e) \quad (\text{C.1})$$

with

$$P^{2\nu}(\bar{\nu}_e \rightarrow \bar{\nu}_e) = 1 - \sin^2 2\theta_{12} \sin^2 \frac{\Delta m_{21}^2 L}{4E} \quad (\text{C.2})$$

At the average baseline of KamLAND, the matter effects are negligible and therefore these equations were shown to be very fast and accurate. An energy resolution of $6.5\%/\sqrt{E}$ was applied in the response function, and two systematic uncertainties were propagated: the reactor rates (4%), and the energy scale (2%).

Bibliography

- [1] B. Pontecorvo, “Inverse beta processes and nonconservation of lepton charge,” *Sov.Phys.JETP* **7**, 172 (1958).
- [2] J. N. Bahcall and J. R. Davis, “An account of the development of the solar neutrino problem.” (Cambridge University Press, 1982) Chap. ch. 12, pp. 243-285.
- [3] J. N. Bahcall, “Solar neutrinos. I: Theoretical,” *Phys.Rev.Lett.* **12**, 300 (1964).
- [4] R. Davis, “Solar neutrinos. II: Experimental,” *Phys.Rev.Lett.* **12**, 303 (1964).
- [5] C. Jensen, *Controversy and Consensus: Nuclear Beta Decay 1911 - 1934*, edited by F. Aaserud, H. Kragh, E. Rüdinger, and R. Stuewer, *Science Networks. Historical Studies.*, Vol. 24 (Birkhäuser, Basel, 2000).
- [6] W. Pauli, “On the Earlier and more recent history of the neutrino,” *Camb.Monogr.Part.Phys.Nucl.Phys.Cosmol.* **14**, 1 (2000).
- [7] J. Chadwick, “Possible Existence of a Neutron,” *Nature* **129**, 312 (1932).
- [8] E. Fermi, “Trends to a Theory of beta Radiation. (In Italian),” *Nuovo Cim.* **11**, 1 (1934).
- [9] H. Bethe and R. Peierls, “The ‘neutrino’,” *Nature* **133**, 532 (1934).
- [10] F. Reines, C. Cowan, F. Harrison, A. McGuire, and H. Kruse, “Detection of the free anti-neutrino,” *Phys.Rev.* **117**, 159 (1960).
- [11] S. Weinberg, “A Model of Leptons,” *Phys.Rev.Lett.* **19**, 1264 (1967).

-
- [12] K. Nakamura *et al.* (Particle Data Group), “Review of particle physics,” *J.Phys.G* **G37**, 075021 (2010).
- [13] Y. Fukuda *et al.* (Super-Kamiokande Collaboration), “Evidence for oscillation of atmospheric neutrinos,” *Phys.Rev.Lett.* **81**, 1562 (1998), arXiv:hep-ex/9807003 [hep-ex].
- [14] Q. Ahmad *et al.* (SNO Collaboration), “Measurement of the rate of $\nu/e + d \rightarrow p + p + e^-$ interactions produced by B-8 solar neutrinos at the Sudbury Neutrino Observatory,” *Phys.Rev.Lett.* **87**, 071301 (2001), arXiv:nucl-ex/0106015 [nucl-ex].
- [15] Z. Maki, M. Nakagawa, and S. Sakata, “Remarks on the unified model of elementary particles,” *Prog.Theor.Phys.* **28**, 870 (1962).
- [16] S. M. Bilenky, C. Giunti, and W. Grimus, “Phenomenology of neutrino oscillations,” *Prog.Part.Nucl.Phys.* **43**, 1 (1999), arXiv:hep-ph/9812360 [hep-ph].
- [17] E. Majorana, “Theory of the Symmetry of Electrons and Positrons,” *Nuovo Cim.* **14**, 171 (1937).
- [18] C. Giunti and C. Kim, *Fundamentals of Neutrino Physics and Astrophysics* (Oxford University Press, USA, 2007).
- [19] L. Wolfenstein, “Neutrino Oscillations in Matter,” *Phys.Rev.* **D17**, 2369 (1978).
- [20] S. Mikheev and A. Smirnov, “Resonance Amplification of Oscillations in Matter and Spectroscopy of Solar Neutrinos,” *Sov.J.Nucl.Phys.* **42**, 913 (1985).
- [21] S. Mikheev and A. Smirnov, “Resonant amplification of neutrino oscillations in matter and solar neutrino spectroscopy,” *Nuovo Cim.* **C9**, 17 (1986).
- [22] S. Mikheev and A. Smirnov, “Neutrino oscillations in a medium with variable density,” *Sov.Phys.Usp.* **29**, 1155 (1986).
- [23] T. K. Kuo and J. Pantaleone, “Neutrino oscillations in matter,” *Rev. Mod. Phys.* **61**, 937 (1989).

- [24] J. N. Bahcall, M. Pinsonneault, and S. Basu, “Solar models: Current epoch and time dependences, neutrinos, and helioseismological properties,” *Astrophys.J.* **555**, 990 (2001), arXiv:astro-ph/0010346 [astro-ph].
- [25] J. N. Bahcall, A. M. Serenelli, and S. Basu, “New solar opacities, abundances, helioseismology, and neutrino fluxes,” *Astrophys.J.* **621**, L85 (2005), arXiv:astro-ph/0412440 [astro-ph] .
- [26] A. Serenelli, S. Basu, J. W. Ferguson, and M. Asplund, “New Solar Composition: The Problem With Solar Models Revisited,” *Astrophys.J.* **705**, L123 (2009), * Brief entry *, arXiv:0909.2668 [astro-ph.SR] .
- [27] N. Grevesse and A. J. Sauval, “Standard Solar Composition,” *Space Sci.Rev.* **85**, 161 (1998).
- [28] M. Asplund, N. Grevesse, A. Sauval, and P. Scott, “The chemical composition of the Sun,” *Ann.Rev.Astron.Astrophys.* **47**, 481 (2009), arXiv:0909.0948 [astro-ph.SR] .
- [29] L. W. Alvarez, *A Proposed Experimental Test of the Neutrino Theory*, Tech. Rep. UCRL-328 (University of California, Berkeley, California, USA, 1949).
- [30] B. Pontecorvo, “Inverse beta process,” *Camb.Monogr.Part.Phys.Nucl.Phys.Cosmol.* **1**, 25 (1991).
- [31] J. Bahcall, W. A. Fowler, J. Iben, I., and R. Sears, “Solar neutrino flux,” *Astrophys.J.* **137**, 344 (1963).
- [32] J. Davis, Raymond, D. S. Harmer, and K. C. Hoffman, “Search for neutrinos from the sun,” *Phys.Rev.Lett.* **20**, 1205 (1968).
- [33] K. Hirata *et al.* (Kamiokande-II Collaboration), “Observation of a small atmospheric muon-neutrino / electron-neutrino ratio in Kamiokande,” *Phys.Lett.* **B280**, 146 (1992).
- [34] D. Casper, R. Becker-Szendy, C. Bratton, D. Cady, R. Claus, *et al.*, “Measurement of atmospheric neutrino composition with IMB-3,” *Phys.Rev.Lett.* **66**, 2561 (1991).

- [35] Y. Fukuda *et al.* (Super-Kamiokande Collaboration), “Study of the atmospheric neutrino flux in the multi-GeV energy range,” *Phys.Lett.* **B436**, 33 (1998), arXiv:hep-ex/9805006 [hep-ex].
- [36] B. Aharmim *et al.* (SNO Collaboration), “Measurement of the $\nu(e)$ and total B-8 solar neutrino fluxes with the Sudbury neutrino observatory phase I data set,” *Phys.Rev.* **C75**, 045502 (2007), arXiv:nucl-ex/0610020 [nucl-ex].
- [37] A. Serenelli, “Standard Solar Model and Solar Neutrinos,” (2010), <http://www.mpa-garching.mpg.de/~aldos/>.
- [38] B. Cleveland, T. Daily, J. Davis, Raymond, J. R. Distel, K. Lande, *et al.*, “Measurement of the solar electron neutrino flux with the Homestake chlorine detector,” *Astrophys.J.* **496**, 505 (1998).
- [39] P. Anselmann *et al.* (GALLEX Collaboration), “Solar neutrinos observed by GALLEX at Gran Sasso.” *Phys.Lett.* **B285**, 376 (1992).
- [40] M. Altmann *et al.* (GNO COLLABORATION), “Complete results for five years of GNO solar neutrino observations,” *Phys.Lett.* **B616**, 174 (2005), arXiv:hep-ex/0504037 [hep-ex] .
- [41] J. Abdurashitov *et al.* (SAGE Collaboration), “Measurement of the solar neutrino capture rate in SAGE,” *Nucl.Phys.Proc.Suppl.* **118**, 39 (2003).
- [42] W. Hampel *et al.* (GALLEX Collaboration), “GALLEX solar neutrino observations: Results for GALLEX IV,” *Phys.Lett.* **B447**, 127 (1999).
- [43] J. Abdurashitov *et al.* (SAGE Collaboration), “Measurement of the solar neutrino capture rate with gallium metal. III: Results for the 2002–2007 data-taking period,” *Phys.Rev.* **C80**, 015807 (2009), arXiv:0901.2200 [nucl-ex] .
- [44] M. Koshiba, “Observational neutrino astrophysics,” *Phys.Rept.* **220**, 229 (1992).
- [45] Y. Fukuda, T. Hayakawa, E. Ichihara, M. Ishitsuka, Y. Itow, *et al.*, “The Super-Kamiokande detector,” *Nucl.Instrum.Meth.* **A501**, 418 (2003).

- [46] R. Wendell *et al.* (Kamiokande Collaboration), “Atmospheric neutrino oscillation analysis with sub-leading effects in Super-Kamiokande I, II, and III,” *Phys.Rev.* **D81**, 092004 (2010), arXiv:1002.3471 [hep-ex] .
- [47] D. Kielczewska (SUPER-KAMIOKANDE and K2K Collaborations), “Neutrino oscillations in Super-Kamiokande and K2K experiments,” *Nuovo Cim.* **B120**, 877 (2005).
- [48] M. Ahn *et al.* (K2K Collaboration), “Measurement of Neutrino Oscillation by the K2K Experiment,” *Phys.Rev.* **D74**, 072003 (2006), arXiv:hep-ex/0606032 [hep-ex] .
- [49] D. Wark, “The T2K experiment,” *Nucl.Phys.News* **19**, 26 (2009).
- [50] S. Fukuda *et al.* (Super-Kamiokande Collaboration), “Determination of solar neutrino oscillation parameters using 1496 days of Super-Kamiokande I data,” *Phys.Lett.* **B539**, 179 (2002), arXiv:hep-ex/0205075 [hep-ex].
- [51] J. Cravens *et al.* (Super-Kamiokande Collaboration), “Solar neutrino measurements in Super-Kamiokande-II,” *Phys.Rev.* **D78**, 032002 (2008), arXiv:0803.4312 [hep-ex] .
- [52] J. Hosaka *et al.* (Super-Kamkiokande Collaboration), “Solar neutrino measurements in super-Kamiokande-I,” *Phys.Rev.* **D73**, 112001 (2006), arXiv:hep-ex/0508053 [hep-ex] .
- [53] K. Abe *et al.* (Super-Kamiokande Collaboration), “Solar neutrino results in Super-Kamiokande-III,” *Phys.Rev.* **D83**, 052010 (2011), arXiv:1010.0118 [hep-ex] .
- [54] G. Alimonti *et al.* (Borexino Collaboration), “The Borexino detector at the Laboratori Nazionali del Gran Sasso,” *Nucl.Instrum.Meth.* **A600**, 568 (2009), * Brief entry *, arXiv:0806.2400 [physics.ins-det] .
- [55] C. Arpesella *et al.* (Borexino Collaboration), “First real time detection of Be-7 solar neutrinos by Borexino,” *Phys.Lett.* **B658**, 101 (2008), arXiv:0708.2251 [astro-ph] .

- [56] C. Arpesella *et al.* (The Borexino Collaboration), “Direct Measurement of the Be-7 Solar Neutrino Flux with 192 Days of Borexino Data,” *Phys.Rev.Lett.* **101**, 091302 (2008), arXiv:0805.3843 [astro-ph].
- [57] G. Bellini *et al.* (The Borexino Collaboration), “Measurement of the solar 8B neutrino rate with a liquid scintillator target and 3 MeV energy threshold in the Borexino detector,” *Phys.Rev.* **D82**, 033006 (2010), arXiv:0808.2868 [astro-ph].
- [58] J. Busenitz, “The KamLAND experiment,” *Int.J.Mod.Phys.* **A16S1B**, 742 (2001).
- [59] S. Abe *et al.* (KamLAND Collaboration), “Precision Measurement of Neutrino Oscillation Parameters with KamLAND,” *Phys.Rev.Lett.* **100**, 221803 (2008), arXiv:0801.4589 [hep-ex].
- [60] T. Araki *et al.* (KamLAND Collaboration), “Measurement of neutrino oscillation with KamLAND: Evidence of spectral distortion,” *Phys.Rev.Lett.* **94**, 081801 (2005), arXiv:hep-ex/0406035 [hep-ex].
- [61] K. Eguchi *et al.* (KamLAND Collaboration), “First results from KamLAND: Evidence for reactor anti-neutrino disappearance,” *Phys.Rev.Lett.* **90**, 021802 (2003), arXiv:hep-ex/0212021 [hep-ex].
- [62] A. Gando *et al.* (The KamLAND Collaboration), “Constraints on θ_{13} from A Three-Flavor Oscillation Analysis of Reactor Antineutrinos at KamLAND,” *Phys.Rev.* **D83**, 052002 (2011), arXiv:1009.4771 [hep-ex].
- [63] H. Chen, “Direct Approach to Resolve the Solar Neutrino Problem,” *Phys.Rev.Lett.* **55**, 1534 (1985).
- [64] Q. Ahmad *et al.* (SNO Collaboration), “Measurement of day and night neutrino energy spectra at SNO and constraints on neutrino mixing parameters,” *Phys.Rev.Lett.* **89**, 011302 (2002), arXiv:nucl-ex/0204009 [nucl-ex].
- [65] B. Aharmim *et al.* (SNO Collaboration), “Electron energy spectra, fluxes, and day-night asymmetries of B-8 solar neutrinos from measurements with NaCl dissolved in the heavy-water detector at the Sudbury Neutrino Observatory,” *Phys.Rev.* **C72**, 055502 (2005), arXiv:nucl-ex/0502021 [nucl-ex].

- [66] G. Fogli, E. Lisi, A. Marrone, and A. Palazzo, “Solar neutrinos: With a tribute to John. N. Bahcall,” , 69 (2006), arXiv:hep-ph/0605186 [hep-ph] .
- [67] M. Maltoni and T. Schwetz, “Three-flavour neutrino oscillation update and comments on possible hints for a non-zero theta (13),” PoS **IDM2008**, 072 (2008), arXiv:0812.3161 [hep-ph] .
- [68] G. Fogli, E. Lisi, A. Marrone, A. Palazzo, and A. Rotunno, “SNO, KamLAND and neutrino oscillations: theta(13),” , 81 (2009), arXiv:0905.3549 [hep-ph] .
- [69] B. Aharmim *et al.* (SNO Collaboration), “An Independent Measurement of the Total Active B-8 Solar Neutrino Flux Using an Array of He-3 Proportional Counters at the Sudbury Neutrino Observatory,” Phys.Rev.Lett. **101**, 111301 (2008), arXiv:0806.0989 [nucl-ex] .
- [70] B. Aharmim *et al.* (SNO Collaboration), “Low Energy Threshold Analysis of the Phase I and Phase II Data Sets of the Sudbury Neutrino Observatory,” Phys.Rev. **C81**, 055504 (2010), arXiv:0910.2984 [nucl-ex] .
- [71] G. Fogli, E. Lisi, A. Marrone, and A. Palazzo, “Global analysis of three-flavor neutrino masses and mixings,” Prog.Part.Nucl.Phys. **57**, 742 (2006), arXiv:hep-ph/0506083 [hep-ph] .
- [72] M. Gonzalez-Garcia, M. Maltoni, and J. Salvado, “Updated global fit to three neutrino mixing: status of the hints of theta13 > 0,” JHEP **1004**, 056 (2010), arXiv:1001.4524 [hep-ph] .
- [73] T. Schwetz, M. Tortola, and J. Valle, “Global neutrino data and recent reactor fluxes: status of three-flavour oscillation parameters,” New J.Phys. **13**, 063004 (2011), * Temporary entry *, arXiv:1103.0734 [hep-ph].
- [74] M. Chen *et al.*, “A letter expressing interest in staging an experiment at sno-lab involving filling sno with liquid scintillator plus double beta decay candidate isotopes,” Online: <http://www.sno.phy.queensu.ca/~alex/SNOLab.pdf> (2004).
- [75] P. Harrison, D. Perkins, and W. Scott, “Tri-bimaximal mixing and the neutrino oscillation data,” Phys.Lett. **B530**, 167 (2002), arXiv:hep-ph/0202074 [hep-ph].

- [76] C. I. Low and R. R. Volkas, “Tri-bimaximal mixing, discrete family symmetries, and a conjecture connecting the quark and lepton mixing matrices,” *Phys.Rev.* **D68**, 033007 (2003), arXiv:hep-ph/0305243 [hep-ph].
- [77] S. K. Agarwalla, M. Parida, R. Mohapatra, and G. Rajasekaran, “Neutrino Mixings and Leptonic CP Violation from CKM Matrix and Majorana Phases,” *Phys.Rev.* **D75**, 033007 (2007), arXiv:hep-ph/0611225 [hep-ph].
- [78] R. Mohapatra, M. Parida, and G. Rajasekaran, “High scale mixing unification and large neutrino mixing angles,” *Phys.Rev.* **D69**, 053007 (2004), arXiv:hep-ph/0301234 [hep-ph] .
- [79] C. H. Albright, A. Dueck, and W. Rodejohann, “Possible Alternatives to Tri-bimaximal Mixing,” *Eur.Phys.J.* **C70**, 1099 (2010), arXiv:1004.2798 [hep-ph] .
- [80] J. Boger *et al.* (SNO Collaboration), “The Sudbury neutrino observatory,” *Nucl.Instrum.Meth.* **A449**, 172 (2000), arXiv:nucl-ex/9910016 [nucl-ex].
- [81] J. F. Amsbaugh, J. Anaya, B. J.b, T. Bowles, M. Browne, *et al.*, “An Array of low-background He-3 proportional counters for the Sudbury neutrino observatory,” *Nucl.Instrum.Meth.* **A579**, 1054 (2007), arXiv:0705.3665 [nucl-ex] .
- [82] P. Vogel and J. F. Beacom, “Angular distribution of neutron inverse beta decay, $\bar{\nu}_e + p \rightarrow e^+ + n$,” *Phys.Rev.* **D60**, 053003 (1999), arXiv:hep-ph/9903554 [hep-ph].
- [83] B. A. Moffat, *The Optical Calibration of the Sudbury Neutrino Observatory*, Phd thesis, Queen’s University, Kingston, Canada (2001).
- [84] M. Moorhead (SNO Collaboration), *Reflectors in Cherenkov Detectors*, Ph.D. thesis, Oxford University, Oxford, UK (1992).
- [85] J. Klein, M. Neubauer, M. Newcomer, and R. V. Berg, *The SNO Trigger System*, SNO Technical Report SNO-STR-97-035 (University of Pennsylvania, 1997).

- [86] S. Seibert and C. Tunnel, *Measuring the Trigger Efficiency in the NCD-Phase and the All-Phase Implications.*, SNO Technical Report (University of Texas at Austin, 2006).
- [87] B. Beltran *et al.*, “A Monte Carlo simulation of the Sudbury Neutrino Observatory proportional counters,” (2011).
- [88] SNO Collaboration, *The NCD unidoc v8*, Tech. Rep. (SNO Internal Note, 2002) mANN-5D54GA.
- [89] B. Aharmim *et al.* (SNO Collaboration), “High sensitivity measurement of Ra-224 and Ra-226 in water with an improved hydrous titanium oxide technique at the Sudbury Neutrino Observatory,” *Nucl.Instrum.Meth.* **A604**, 531 (2009), arXiv:0803.4162 [nucl-ex] .
- [90] T. Andersen *et al.* (SNO Collaboration), “A Radium assay technique using hydrous titanium oxide adsorbent for the Sudbury Neutrino Observatory,” *Nucl.Instrum.Meth.* **A501**, 386 (2003), arXiv:nucl-ex/0208015 [nucl-ex] .
- [91] T. Andersen *et al.* (SNO Collaboration), “Measurement of radium concentration in water with Mn coated beads at the Sudbury Neutrino Observatory,” *Nucl.Instrum.Meth.* **A501**, 399 (2003), arXiv:nucl-ex/0208010 [nucl-ex] .
- [92] B. Moffat, R. Ford, F. Duncan, K. Graham, A. Hallin, *et al.*, “Optical calibration hardware for the sudbury neutrino observatory,” *Nucl.Instrum.Meth.* **A554**, 255 (2005), arXiv:nucl-ex/0507026 [nucl-ex].
- [93] R. Ford, *Nitrogen/dye laser system for the optical calibration of SNO*, Master’s thesis, Queen’s University, Kingston, Canada (1993).
- [94] M. Dragowsky, A. Hamer, Y. Chan, R. Deal, E. Earle, *et al.*, “The N-16 calibration source for the Sudbury Neutrino Observatory,” *Nucl.Instrum.Meth.* **A481**, 284 (2002), arXiv:nucl-ex/0109011 [nucl-ex].
- [95] N. Tagg, A. Hamer, B. Sur, E. Earle, R. Helmer, *et al.*, “The Li-8 calibration source for the Sudbury Neutrino Observatory,” *Nucl.Instrum.Meth.* **A489**, 178 (2002), arXiv:nucl-ex/0202024 [nucl-ex].

- [96] A. W. Poon, R. Komar, C. Waltham, M. Browne, R. Roberston, *et al.*, “A Compact H-3(p, γ)He-4 19.8-MeV gamma-ray source for energy calibration at the Sudbury Neutrino Observatory,” Nucl.Instrum.Meth. **A452**, 115 (2000), arXiv:physics/9910011 [physics].
- [97] S. Brice *et al.*, *First Generation Acrylic Encapsulated U/Th Sources*, SNO Technical Report SNO-STR-99-023 (SNO, 2000).
- [98] C. Howard, *Injection of a Uniform ^{24}Na Radioactive Source into the Sudbury Neutrino Observatory*, Master’s thesis, Queen’s University, Kingston, Canada (2006).
- [99] SNO collaboration, *The SNOMAN User Manual* (2008), internal reference manual.
- [100] W. R. Nelson, H. Hirayama, and D. W. O. Rogers, *The EGS4 code system*, sLAC-0265.
- [101] E. Briesmeister and F. Judith, *MCNP: A General Monte Carlo N-Particle Transport Code*, 1A-12625-M.
- [102] A. E. G. Ingelman and J. Rathsman, *LEPTO version 6.3 – The Lund Monte Carlo for Deep Inelastic Lepton-Nucleon Scattering*. (1995).
- [103] *FLUKA Online Manual*, <http://www.fluka.org>.
- [104] C. Zeitnitz and T. Gabriel, “The geant-calor interface and benchmark calculations of zeus test calorimeters,” Nuclear Instruments and Methods in Physics Research Section A: Accelerators, Spectrometers, Detectors and Associated Equipment **349**, 106 (1994).
- [105] J. N. Bahcall, P. I. Krastev, and A. Y. Smirnov, “SNO: Predictions for ten measurable quantities,” Phys.Rev. **D62**, 093004 (2000), arXiv:hep-ph/0002293 [hep-ph] .
- [106] C. V. Ouellet, *A Study of Relative Efficiencies of Photomultiplier Tubes in the Sudbury Neutrino Observatory*, Master’s thesis, Queen’s University, Kingston, Canada (2003).

-
- [107] R. D. Grant, *Optical Calibration of the Sudbury Neutrino Observatory and Determination of the ^8B Solar Neutrino Flux in the Salt Phase*, Phd thesis, Carleton University, Ottawa, Canada (2004).
- [108] O. Simard, *Measurement of the Survival Probability and Determination of the Three-Flavour Neutrino Oscillation Parameters at the Sudbury Neutrino Observatory*, Phd thesis, Carleton University, Ottawa, Canada (2008).
- [109] P.-L. Drouin, *FTN: A Time Fitter for the NCD Phase*, SNO Internal Note MANN-78VP3B (Carleton University, 2007).
- [110] W. Press, S. Teukolsky, W. Vetterling, and B. Flannery, *Numerical Recipes 3rd Edition: The Art of Scientific Computing*, 3rd ed. (Cambridge University Press, 2007).
- [111] O. Simard, *Low Statistics Effects on Optical Constants Fits*, SNO Internal Note (Carleton University, 2005) mANN-6HWSMQ.
- [112] J. Cameron, *The Photomultiplier Tube Calibration in the Sudbury Neutrino Observatory*, Phd thesis, Oxford University, Oxford, UK (2001).
- [113] N. Barros, O. Simard, J. Maneira, C. Kraus, and P.-L. Drouin, *Optical Calibrations in the NCD Phase*, SNO Internal Note MANN-6YSTJB (SNO, 2007).
- [114] N. Barros, *First look at late light for NCD reflectivity studies*, SNO Internal Note MANN-7GBPW5 (LIP, 2007).
- [115] R. MacLellan, *The Energy Calibration for the Solar Neutrino Analysis of All Three Phases of the Sudbury Neutrino Observatory*, Phd thesis, Queens University, Kingston, Canada (2009).
- [116] P. Doe, "Composition of the NCD attachment anchors," (2006), Private Communication.
- [117] N. Barros, *Checks on Optical constants in the reprocessed NCD scans*, SNO Internal Note MANN-72UEK4 (LIP, 2007).
- [118] M. Dunford, *Measurement of the (^8B) solar neutrino energy spectrum at the Sudbury Neutrino Observatory*, Ph.d. thesis, University of Pennsylvania (2005).

-
- [119] S. Seibert, *Optical Effects of the NCD Anchors*, SNO Internal Note MANN-6HWSMQ (2006).
- [120] N. Barros, *Preliminary Results on PMTR Asymmetry in the Batch III concentrators*, SNO Internal Note MANN-6R2PH6 (SNO, 2006).
- [121] N. Barros, *Preliminary optics fits with two angular responses*, SNO Internal Note MANN-6RFLAV (LIP, 2006).
- [122] N. Barros, *Z bias and Anchors in the optical calibration*, SNO Internal Note MANN-6UHKU4 (SNO, 2006).
- [123] O. Simard, *A New Laserball Model for the Optics in the NCD Phase*, SNO Internal Note MANN-6RTNUE (Carleton University, 2006).
- [124] SNO E&O Working Group, *Energy and Optics Measurements for the Salt phase of SNO*, Tech. Rep. MANN-5M6QZ3 (SNO, 2003).
- [125] X. Dai, *Chemical Explanation of Heavy Water Attenuation*, SNO Internal Note MANN-5ARRUP (SNO, 2002).
- [126] C. Waltham, *Concentrator Reflectometry*, SNO Internal Note MANN-59339D (SNO, 2002).
- [127] B. Aharmim *et al.* (SNO Collaboration), “Combined Analysis of all Three Phases of Solar Neutrino Data from the Sudbury Neutrino Observatory,” (2011), * Temporary entry *, arXiv:1109.0763 [nucl-ex] .
- [128] S. Habib, *A Combined Three-Phase Signal Extraction of the Sudbury Neutrino Observatory Data Using Markov Chain Monte Carlo Technique*, Ph.D. thesis, University of Alberta, Edmonton, Canada (2010).
- [129] C. Howard, *A Search for hep Neutrinos with the Sudbury Neutrino Observatory Detector*, Phd thesis, University of Alberta, Edmonton, Canada (2010).
- [130] P.-L. Drouin, *Three-Phase Extraction of the Electron Neutrino Survival Probability at the Sudbury Neutrino Observatory*, Ph.D. thesis, Carleton University, Ottawa, Canada (2011).

-
- [131] SNO Collaboration, *SNO Three-Phase Combined Analysis Unidoc*, SNO Internal Note (SNO 3-Phase Working Group, 2010).
- [132] M. Neubauer, *Evidence for Electron Neutrino Flavour Change Through Measurement of $8B$ Solar Neutrino Flux at the Sudbury Neutrino Observatory*, Phd thesis, University of Pennsylvania, Philadelphia, USA (2001).
- [133] M. Boulay, *Direct Evidence for Weak Flavor Mixing with the Sudbury Neutrino Observatory*, Phd thesis, Queen's University, Kingston, Canada (2001).
- [134] J. Dunmore, *The Separation of CC and NC Events in the Sudbury Neutrino Observatory*, Phd thesis, Oxford University, Oxford, UK (2004).
- [135] M. Abramowitz and I. A. Stegun, *Handbook of Mathematical Functions with Formulas, Graphs, and Mathematical Tables*, ninth dover printing, tenth gpo printing ed. (Dover, New York, 1964).
- [136] SNO Collaboration, *SNO LETA Unidoc*, SNO Internal Note (SNO LETA Working Group, 2009).
- [137] R. Martin, *An Analysis of the $3He$ Proportional Counter Data from the Sudbury Neutrino Observatory Using Pulse Shape Discrimination*, Phd thesis, Queens University, Kingston, Canada (2009).
- [138] N. Oblath, *A Measurement of Neutral-Current Neutrino Interactions at the Sudbury Neutrino Observatory with an Array of $3He$ Proportional Counters*, Ph.D. thesis, University of Washington, Seattle, USA (2009).
- [139] S. Seibert, *A Low Energy Measurement of the $8B$ Solar Neutrino Spectrum at the Sudbury Neutrino Observatory*, Phd thesis, University of Texas at Austin, Austin, USA (2008).
- [140] G. Orebi-Gann, *An Improved Measurement of the $8B$ Solar Neutrino Energy Spectrum at the Sudbury Neutrino Observatory*, Phd thesis, University of Oxford, Oxford, UK (2008).
- [141] F. Zhang, *MC Study of Atmospheric Neutrino Backgrounds for LETA*, SNO Internal Note MANN-73PL4B (SNO, 2007).

-
- [142] N. Barros, *Accuracy of Polynomial Parameterisations to characterise the Survival Probability in SNO*, SNO Internal Note (LIP, 2008).
- [143] N. Barros, *Neutrino Oscillation Analysis Documentation*, SNO Internal Note MANN-89JHK8 (LIP, 2009).
- [144] H. Bethe, “A Possible Explanation of the Solar Neutrino Puzzle,” *Phys.Rev.Lett.* **56**, 1305 (1986).
- [145] J. N. Bahcall and H. Bethe, “A Solution of the solar neutrino problem,” *Phys.Rev.Lett.* **65**, 2233 (1990).
- [146] H. Bethe and J. N. Bahcall, “Solar neutrinos and the Mikheev-Smirnov-Wolfenstein theory,” *Phys.Rev.* **D44**, 2962 (1991).
- [147] D. Harley, T.-K. Kuo, and J. T. Pantaleone, “Solar neutrinos with three flavor mixings,” *Phys.Rev.* **D47**, 4059 (1993), arXiv:hep-ph/9208241 [hep-ph].
- [148] E. K. Akhmedov, M. Tortola, and J. Valle, “A Simple analytic three flavor description of the day night effect in the solar neutrino flux,” *JHEP* **0405**, 057 (2004), arXiv:hep-ph/0404083 [hep-ph].
- [149] A. Dziewonski and D. Anderson, “Preliminary reference earth model,” *Phys.Earth Planet.Interiors* **25**, 297 (1981).
- [150] A. M. Dziewonski, A. L. Hales, and E. R. Lapwood, “Parametrically simple earth models consistent with geophysical data,” *Physics of The Earth and Planetary Interiors* **10**, 12 (1975).
- [151] H. Moritz, “Geodetic reference system 1980,” *Journal of Geodesy* **74**, 128 (2000), 10.1007/s001900050278.
- [152] M. Chen, *PhysInt Unidoc v2.1*, SNO Internal Note (SNO, 2002).
- [153] B. Aharmim *et al.* (SNO Collaboration), “Measurement of the ν_e and Total ^8B Solar Neutrino Fluxes with the Sudbury Neutrino Observatory Phase-III Data Set,” (2011), * Temporary entry *, arXiv:1107.2901 [nucl-ex] .

- [154] M. Butler, J.-W. Chen, and X. Kong, “Neutrino deuteron scattering in effective field theory at next-to-next-to-leading order,” *Phys.Rev.* **C63**, 035501 (2001), arXiv:nucl-th/0008032 [nucl-th] .
- [155] J. N. Bahcall, “Neutrino Opacity 1. Neutrino-Lepton Scattering,” *Phys.Rev.* **136**, B1164 (1964).
- [156] J. N. Bahcall, “Neutrino - Electron Scattering and Solar Neutrino Experiments,” *Rev.Mod.Phys.* **59**, 505 (1987).
- [157] J. N. Bahcall, M. Kamionkowski, and A. Sirlin, “Solar neutrinos: Radiative corrections in neutrino - electron scattering experiments,” *Phys.Rev.* **D51**, 6146 (1995), arXiv:astro-ph/9502003 [astro-ph].
- [158] G. Fogli, E. Lisi, A. Marrone, D. Montanino, and A. Palazzo, “Getting the most from the statistical analysis of solar neutrino oscillations,” *Phys.Rev.* **D66**, 053010 (2002), arXiv:hep-ph/0206162 [hep-ph] .
- [159] D. Michael *et al.* (MINOS Collaboration), “Observation of muon neutrino disappearance with the MINOS detectors and the NuMI neutrino beam,” *Phys.Rev.Lett.* **97**, 191801 (2006), arXiv:hep-ex/0607088 [hep-ex].
- [160] B. Nickel, “Development of a three-flavour adiabatic approximation for SNO.” (2009), Private Communication.
- [161] W. Winter, S. Freedman, K. Rehm, and J. Schiffer, “The B-8 neutrino spectrum,” *Phys.Rev.* **C73**, 025503 (2006), arXiv:nucl-ex/0406019 [nucl-ex] .
- [162] G. J. Feldman and R. D. Cousins, “A Unified approach to the classical statistical analysis of small signals,” *Phys.Rev.* **D57**, 3873 (1998), arXiv:physics/9711021 [physics.data-an] .
- [163] G. Bellini *et al.* (The Borexino Collaboration), “Precision measurement of the ${}^7\text{Be}$ solar neutrino interaction rate in Borexino,” (2011), * Temporary entry *, arXiv:1104.1816 [hep-ex] .
- [164] N. Barros, *Update of Kamland oscillation analysis for LETA and 3-phase*, SNO Internal Note MANN-7VPL6L (LIP, 2009).

- [165] “Data Release Accompanying the 4th KamLAND Reactor Result,” Online: http://www.awa.tohoku.ac.jp/KamLAND/4th_result_data_release/4th_result_data_release.html (2010).
- [166] M. Apollonio *et al.* (CHOOZ Collaboration), “Search for neutrino oscillations on a long baseline at the CHOOZ nuclear power station,” *Eur.Phys.J.* **C27**, 331 (2003), arXiv:hep-ex/0301017 [hep-ex].
- [167] K. Abe *et al.* (T2K Collaboration), “Indication of Electron Neutrino Appearance from an Accelerator-produced Off-axis Muon Neutrino Beam,” *Phys.Rev.Lett.* **107**, 041801 (2011), arXiv:1106.2822 [hep-ex].
- [168] G. Fogli, E. Lisi, A. Marrone, A. Palazzo, and A. Rotunno, “Evidence of $\theta_{13} > 0$ from global neutrino data analysis,” (2011), arXiv:1106.6028 [hep-ph].
- [169] M. C. Chen and S. collaboration, “The SNO+ experiment,” (2008), 0810.3694v1.
- [170] M. Picariello, J. Pulido, S. Andringa, N. Barros, and J. Maneira, “SNO+: Predictions from standard solar models and spin flavour precession,” *JHEP* **0711**, 055 (2007), arXiv:0705.4070 [hep-ph] .
- [171] J. Maneira, “Status and prospects of SNO+,” *Nuclear Physics B - Proceedings Supplements* **217**, 50 (2011), proceedings of the Neutrino Oscillation Workshop (NOW 2010).
- [172] H. Back *et al.* (Borexino Collaboration), “CNO and pep neutrino spectroscopy in Borexino: Measurement of the deep-underground production of cosmogenic ^{11}C in an organic liquid scintillator,” *Phys. Rev. C; Physical Review C* **74** (2006), 10.1103/PhysRevC.74.045805.
- [173] W. C. Haxton and A. M. Serenelli, “Cn-cycle neutrinos and solar metallicity,” (2009), 0902.0036v1 .
- [174] “Japanese Reactors operational records,” Online : <http://www.jaif.or.jp/english/aij/index2.html> (2009).